UC Berkeley
UC Berkeley Electronic Theses and Dissertations

Title

Structural Divergence and Adaption in Prokaryotic Ribosomes

Permalink

https://escholarship.org/uc/item/9x06t63x

ISBN

9798276023847

Author

Nissley, Amos James

Publication Date

2025-12-06

Peer reviewed|Thesis/dissertation

eScholarship.org Powered by the California Digital Library
University of California

Structural Divergence and Adaption in Prokaryotic Ribosomes

By

Amos James Nissley

A dissertation submitted in partial satisfaction of the

requirements for the degree of

Doctor of Philosophy

in

Chemistry

in the

Graduate Division

of the

University of California, Berkeley

Committee in charge:

Professor Jamie H. D. Cate, Chair
Professor Alanna Schepartz
Professor Eva Nogales

Fall 2025

Abstract

Structural Divergence and Adaption in Prokaryotic Ribosomes

By

Amos James Nissley

Doctor of Philosophy in Chemistry

University of California, Berkeley

Professor Jamie H. D. Cate, Chair

Ribosomes are macromolecular machines that catalyze cellular protein synthesis. While ribosome structure is well understood in model organisms, we lack a holistic understanding of how ribosome structure and adaptation has changed across divergent organisms. This thesis investigates structural changes in ribosomes and ribosome-binding proteins across prokaryotic species. Chapter 1 reviews our current understanding of ribosome structure, function, and adaption and their relevance in ribosome engineering.

Chapter 2 examines rare rRNA sequence variation in the A loop, the binding site for the A-site tRNA in the LSU, found in a subset of hyperthermophilic archaea. In organisms from the archaeal phylum Thermoproteota, two highly conserved uridines in the A loop are instead cytosines. Substitution of these two positions with cytosines in the *E. coli* ribosome globally increased the stability of the LSU compared to wild type (WT), without affecting the activity of *E. coli* ribosomes. This sequence variation provides a strategy to stabilize the ribosome for future ribosome engineering efforts.

Chapter 3 identifies and addresses a folding defect in ribosomes caused by a common rRNA tagging strategy in the LSU. Insertion of an MS2 tag into 23S rRNA helix H98 disrupts a key tertiary RNA contact, destabilizing the LSU. Guided by this insight, we designed a modified MS2 tag that restores H98 tertiary contacts. An analysis of ribosome structures revealed that many bacterial species form tertiary contacts between 23S rRNA helices near the 5′ and 3′ ends, which likely aid the stability of ribosomes across species.

Chapter 4 explores divergent peptidyl transferase center (PTC) sequences in archaeal ribosomes. We found that archaeal PTC sequences are less conserved than those of bacteria. We determined the cryo-EM structure ribosomes from an archaeon with a divergent PTC, *Pyrobaculum calidifontis*. This structure revealed how divergent PTC sequences are accommodated, enabled by differences in bacterial and archaeal rProteins. We also identified a previously undescribed ribosome hibernation factor bound to the *P. calidifontis* ribosome, which we named Dri. Dri comprises a family of archaeal-specific ribosome hibernation factors distributed across multiple archaeal phyla.

Chapter 5 continues the investigation of archaeal ribosome hibernation factors. We investigated divergent Dri homologs from the methanogenic archaeon *Methanosarcina acetivorans*. In the *M. acetivorans* genome, there are four archaeal ribosome hibernation factors encoded by adjacent genes and named them SriA-D. Cryo-EM structures of the *M. acetivorans* ribosome showed that SriA and SriB bind to the LSU and SriC and SriD bind to the SSU to inactivate the ribosome. A phylogenetic analysis revealed that Sri proteins broadly co-occur across archaea phyla.

Finally, Chapter 6 presents the conclusion and outlines future directions for ribosomal structural biology across the tree of life.

Acknowledgements

During my time at Berkeley, I have received help and support from many people. I would first like to thank my advisor, Jamie Cate. Jamie, you have consistently encouraged my scientific curiosity and enabled me to pursue science even when it led down unexpected paths. I am grateful for the opportunities you have provided me and for the collaborative environment that you foster in the lab. I thank the members of the Cate lab for creating a supportive space in which to carry out my PhD. To the C-GEM subgroup, Zoe, Chandrima, Kristina, Alexandra, and Kate, I am grateful to have worked alongside you. You are remarkable colleagues, and I learned so much from each of you. I thank my bay-mates, Das, Angélica, Conner, and Haley. I learned a lot from you, and you all made the lab supportive and entertaining. In my PhD, I was fortunate to work with three extremely talented and motivated undergraduate students, Tammam, Tara, and Roan. Your enthusiasm always inspired me and you three made the work not only easier but also very fun. I am deeply thankful to my mom, dad, and Alia for supporting me throughout my scientific career, even though it took me far from home. Jenna, I feel incredibly fortunate to have shared this experience with you. I have always been able to count on you for support and advice. I'm very excited to see where our journey takes us next.

Table of Contents

Abstract.....1
Acknowledgements.....i
Table of Contents.....ii

Chapter 1: Introduction
- 1.1: Overview of ribosome structure and function.....1
- 1.2: Ribosomes are adapted to function in diverse organisms.....2
- 1.3: Ribosome hibernation factors protect ribosomes during stress.....3
- 1.4: Ribosome engineering for new function.....4

Chapter 2: Rare ribosomal RNA sequences from archaea stabilize the bacterial ribosome
- 2.1: Abstract.....5
- 2.2: Introduction.....5
- 2.3: Material and methods.....6
- 2.4: Results.....12
    - Sequence conservation in the A loop
    - A loop mutations in the *E. coli* 50S ribosomal subunit
    - Structure of the CC 70S ribosome
    - CC mutations stabilize the 50S ribosomal subunit
    - Additional mutations at the base of the A loop RNA hairpin
    - CC mutations stabilize *E. coli* ribosomes with PTC mutations
- 2.5: Discussion.....20
- 2.6: Supplementary information.....23

Chapter 3: Interactions between terminal ribosomal RNA helices stabilize the *E. coli* large ribosomal subunit
- 3.1: Abstract.....37
- 3.2: Introduction.....37
- 3.3: Material and methods.....38
- 3.4: Results.....41
    - H1, H94, and H98 interact in the *E. coli* LSU
    - MS2-V3 restores stability to the *E. coli* LSU
    - Nucleotide bridges between H1, H94, and H98 are required for full LSU stability
- 3.5: Discussion.....47
- 3.6: Supplementary information.....49

Chapter 4: Structure of an archaeal ribosome reveals a divergent active site and hibernation factor
- 4.1: Abstract.....56
- 4.2: Introduction.....56
- 4.3: Material and methods.....57
- 4.4: Results.....65
    - Cryo-EM structures of the *P. calidifontis* ribosome
    - Highly divergent PTCs from a subset of archaea

    - Differences in archaeal uL3 enable PTC sequence variation
    - Dri is an archaeal ribosome hibernation factor
- 4.5: Discussion**.....73**
- 4.6: Extended Figures and Tables**.....76**
- 4.7: Supplementary information**.....83**

Chapter 5: Broadly distributed factors work in tandem to mediate ribosome hibernation in Archaea

- 5.1: Abstract**.....98**
- 5.2: Introduction**.....98**
- 5.3: Material and methods**.....99**
- 5.4: Results**.....103**
    - Ribosome hibernation factors in *M. acetivorans*
    - SriA and SriB bind to the large ribosomal subunit
    - SriC and SriD bind to the small ribosomal subunit
    - Sri gene clusters are broadly distributed in Archaea
- 5.5: Discussion**.....108**
- 5.6: Supplementary information**.....111**

Chapter 6: Conclusion and Outlook.....126

References.....127

Chapter 1: Introduction

1.1 Overview of ribosome structure and function

The ribosome is the universally conserved translator of the genetic code. Ribosomes are large ribonucleoprotein complexes responsible for synthesizing proteins from messenger RNAs (mRNA). The ribosome consists of two subunits, the large ribosomal subunit (LSU) and the small ribosomal subunit (SSU). The ribosomal catalytic center, called the peptidyl transferase center (PTC), is in the LSU and catalyzes peptide bond formation during translation elongation. The SSU binds to the mRNA and contains the mRNA decoding center (DC), where mRNAs are decoded by the ribosome using cognate transfer RNAs (tRNA). The ribosome is unique among macromolecular complexes as both of its functional sites, the PTC and the DC, are formed primarily from ribosomal RNA (rRNA) rather than ribosomal proteins (rProteins). This observation inspired the hypothesis that the ribosome is an ancient machine that formed in the "RNA-world" during the emergence of life on early Earth.[1] Under this hypothesis, early ribosomes were small ribozymes that evolved through accretion of RNA elements and rProteins.[2] Modern ribosomes share a nearly universal core, but also include a wide array of diverse rRNA expansions and rProteins, which provide platforms for specialized functions and regulation.[3,4]

Ribosomes facilitate translation by binding to mRNAs, tRNAs, and protein translation factors. They contain three canonical tRNA sites, called the aminoacyl (A), peptidyl (P), and exit (E) sites. Protein translation proceeds through three phases: initiation, elongation, and termination. Translation initiation is the process through which ribosomes and initiation factors recognize and assemble a 70S ribosome at the start codon of an mRNA. The mechanism of translation initiation is not conserved and occurs via different pathways in Bacteria[5], Archaea[6], and Eukaryotes[7]. Here, I will briefly highlight the common features of translation initiation across Prokaryotes. Recognition of the start codon during translation initiation occurs mainly through one of two pathways: Shine-Dalgarno (SD)-dependent initiation and leaderless initiation.[8] In SD-dependent initiation, the mRNA sequence upstream of the start codon, called the SD-sequence, forms a duplex with the 3′-end of the 16S rRNA in the SSU, called the aSD-sequence. This interaction places the start codon in the P site of the SSU. Some prokaryotic mRNAs, termed leaderless mRNAs, lack a 5′-untranslated region (UTR) and instead place a start codon near the 5′-end of the mRNA. Translation initiation of leaderless mRNAs relies on weak mRNA secondary structure surrounding the start codon[8], and interactions between the mRNA 5′-end and the SSU[9], which positions the start codon in the P site of the SSU. After mRNA binding, initiator tRNA is delivered to the P site by an initiation factor (IF2 in Bacteria and aIF2 in Archaea) and the LSU is recruited to form a 70S ribosome.

During translation elongation, the nascent polypeptide chain is extended by sequential incorporation of amino acids specified by the mRNA coding sequence. The first stage of translation elongation involves the delivery of an aminoacyl-tRNA to the A site of the ribosome by an elongation factor (EF-Tu in Bacteria and aEF1α in Archaea). After delivery, the codon in the mRNA and anticodon in the tRNA form a complex, which stimulates GTP hydrolysis by EF-Tu or aEF1α. During tRNA binding to the A site, the ribosome employs kinetic proofreading to ensure that the correct tRNA-mRNA pair is accommodated.[10–12] After accommodation of the aminoacyl-tRNA, peptidyl transfer is catalyzed by the PTC. In the second stage of elongation, tRNAs are translocated by an elongation factor (EF-G in Bacteria and aEF2 in Archaea), such that the P-site tRNA shifts to the E site and the A-site tRNA shifts to the P site.[13,14] The elongation cycle repeats until a termination codon enters the A site, which promotes binding of release factors

that catalyze release of the polypeptide chain from the P-site tRNA, completing the translation cycle.

1.2 Ribosomes are adapted to function in diverse organisms

Although ribosomes are universally conserved, they also exhibit structural and compositional variation. Recent advances in cryogenic electron-microscopy (cryo-EM) have enabled the determination of numerous ribosome structures from a wide array of organisms and organelles at high resolution.[15] These structures demonstrate that ribosomes are adapted to function in specialized environments and support the unique lifestyles of divergent forms of life. Variation in ribosome structure enables organisms to optimize protein synthesis in response to environmental and evolutionary pressures. Understanding how changes to ribosome structure shapes function provides a molecular basis for adaptation and a framework for exploring the evolutionary trajectories underlying the complexity of life.

One of the most pronounced differences between the ribosomes from Bacteria, Archaea, and Eukaryotes is their size. Most eukaryotic ribosomes have acquired additional rProteins and expansions in their rRNA.[3,4] While ribosome expansion is considered an evolutionary adaptation for increased regulation, many organisms and organelles possess compacted ribosomes that have lost rProteins and sections of rRNA. Ribosome compaction reflects selective pressure for genome minimization in organelles, like mitochondria, and obligate symbiotes and parasites. For instance, mammalian mitochondrial ribosomes exhibit extremely reduced rRNA, which is encoded by the minimized mitochondrial genome.[16] rRNA reduction is compensated by increasing the number and size of mitochondrial rProteins, which are predominantly encoded in the nuclear genome.[17] Similarly, the transition to symbiotic or parasitic lifestyles is accompanied by a reduction in genome size and, in many of these organisms, ribosome compaction.[18] This reduction is exemplified by the ribosomes from parasitic microsporidia, which, despite their eukaryotic origin, have shed many rRNA expansions and rProteins, resulting in a size smaller than some bacterial ribosomes.[19,20] Genome compaction can also lead to the loss of core ribosomal proteins, such as in the obligate symbiotic CPR bacteria, which have lost otherwise universal rProteins.[21]

While many rProteins are universally conserved, there are rProteins specific to the three domains of life.[22] Overall, archaeal ribosomes have rProteins that are homologous to those in eukaryotes. Differences in bacterial and archaeal/eukaryotic rProteins affect the function of the ribosome and the mechanisms of translation. For instance, bS1 is an essential rProtein that facilitates mRNA delivery to the ribosome during translation initiation in bacteria.[23] Another example is eS26, which is an rProtein found in eukaryotes and some archaea. eS26 sequesters the 16S rRNA 3′-end and was shown to reorganize the SSU during SD-dependent and leaderless translation initiation in Archaea.[9] Binding of eS26 to the ribosome is also dynamic in yeast where it regulates the translation of certain mRNAs, highlighting the roles of rProteins in both ribosome structure and function.[24]

In addition to changes in ribosome composition, organisms have also adapted conserved rProteins to function in diverse environments. Halophiles are organisms adapted to grow in high salt environments. One challenge for protein folding in high salt environments is protein hydration. Therefore proteins from halophiles generally have lower isoelectric points, as acidic amino acids on the protein surface help maintain protein solvation.[25] This presents a challenge for ribosomal proteins, which are predominantly basic because of the need to interact with negatively charged rRNA. To balance these pressures, rProteins in halophiles are more acidic overall than those in mesophiles, with acidic patches distributed across the surface of halophilic ribosomes, while they

remain basic in regions that interact with rRNA.[26,27] rProteins are also adapted in thermophiles, which are organisms that grow at high temperatures. For instance, rProteins from thermophiles are more likely to have metal binding sites and exhibit different amino acid content compared to those from mesophiles.[28] These features improve protein folding and stability at high temperatures.

rRNA forms the core of ribosomes and is also adapted to function across a range of environmental conditions. One example of an extreme change in rRNA composition is found in the rRNA from mitochondrial ribosomes. Metabolic proteins on the inner mitochondrial membrane produce reactive oxygen species that can damage RNA, specifically guanine bases, which have the lowest redox potential among the RNA bases[29]. To prevent oxidative damage, mitochondrial rRNAs are severely depleted of guanine bases, especially at solvent exposed positions on the ribosomal surface.[30] rRNAs have also been adapted in the ribosomes from thermophiles. Thermophilic rRNAs have a higher number of GC base pairs, which are more stable due to base stacking, and a lower abundance of uracil bases than mesophilic rRNAs.[28,31,32] The importance of GC base pairs in stabilizing rRNA is exemplified by the rRNAs from the halophilic archaeon *Haloarcula marismortui*. *H. marismortui* has three rRNA operons; two that are identical and a third that contains a higher number of GC base pairs. The third rRNA is critical for growth of *H. marismortui* at high temperatures.[33] Beyond changes in sequence, rRNA from thermophiles is post-transcriptionally modified to a greater extent than in most mesophiles.[34] Chemical modifications such as N^4-acetylation of cytosines and 5-methylation of cytosines and uridines can increase hydrogen bonding and hydrophobic interactions, which stabilizes the ribosome. These modifications are critical for the growth of some hyperthermophiles at high temperatures.[35,36] Overall, the structural and compositional variation of ribosomes underscores their adaptability, enabling protein synthesis across diverse environments and illuminating the evolutionary strategies that sustain life.

1.3 Ribosome hibernation factors protect ribosomes during dormancy

Organisms have also adapted their translation machinery to respond to environmental stress. These stresses can include changes in nutrient availability, salt concentration, temperature, or oxidative stress. Protein synthesis is an energetically demanding process, consuming a large fraction of the cell's energy. To save energy during stress conditions, many organisms induce a global translation shutdown and inactivation of ribosomes through a process called ribosome hibernation. Ribosome hibernation is mediated by protein factors, known as hibernation factors, which inhibit translation by occluding functional sites on the ribosome or by promoting ribosome dimerization.[37,38] In addition to suppressing protein synthesis, ribosome hibernation protects ribosomes from damage by endogenous RNases during stress.[39] Thus, hibernation preserves an intact pool of ribosomes that remain poised to resume translation once growth conditions become favorable. Ribosome preservation during dormancy is especially important in microbes, as up to 60% of the microbial biomass exists in a state of dormancy.[40]

While the process of ribosome hibernation is conserved across life, hibernation factors from different organisms differ greatly in their structure and modes of ribosome inactivation. Multiple ribosome hibernation factors are known in bacteria. RMF, HPF, and RaiA (also known as protein Y) are bacterial ribosome hibernation factors that bind to the small ribosomal subunit (SSU) and block mRNA and tRNA binding sites.[41,42] RMF and HPF also promote the formation of inactive 100S ribosome dimers.[43–45] A family of bacterial hibernation factors, Balon, was recently discovered, that is composed of distant homologs of the archaeal/eukaryotic release

factor.[46] Balon factors are unique among hibernation factors in their ability to bind to actively translating ribosomes that are still bound to peptidyl-tRNA.

Similar to their bacterial counterparts, eukaryotic ribosome hibernation factors, such as Stm1/Serbp1[47], IFRD2[48], and MDF1[19] occlude tRNA binding sites on the ribosome. Ribosome hibernation in higher eukaryotes also differs between cell types. For example, factors that control ribosome hibernation in the egg, such as Dapl1[49], illustrate cell-type specificity. In addition to hibernation factors, ribosome hibernation states can also involve translation factors such as tRNAs and elongation factors.[49,50] Ribosome dimerization, while initially thought to be limited to bacteria, has also been observed in eukaryotes, mediated by the microsporidian hibernation factor MDF2.[50] Ribosome hibernation factors exemplify an evolutionarily conserved adaptation that safeguards ribosomes during stress and enables cells to resume protein synthesis when conditions improve.

1.4 Ribosome engineering for new function

While ribosomes have evolved to polymerize the 20 canonical α-amino acids, there has been growing interest in engineering ribosomes beyond their natural function for use in biotechnology and the synthesis of unnatural sequence-defined polymers.[51,52] Examples of ribosome engineering that enhance function include changes in rRNA to achieve increased protein synthesis[53], translation kinetics[54], or tolerance to organic solvents and varied buffer conditions[55]. *In vivo* ribosome engineering of endogenous ribosomes is limited to small changes, because ribosomes are still needed for cellular protein synthesis. Additionally, some changes to ribosomes are dominant-lethal, where the modified ribosome exhibits a toxic phenotype that is lethal even in the presence of WT ribosomes. To mitigate these issues, orthogonal ribosomes have been developed, in which the aSD in the SSU has an altered sequence so it only targets orthogonal mRNAs with the cognate orthogonal SD sequence.[56] To apply this orthogonality to the LSU, tethered ribosomes were developed in which the 23S and 16S rRNAs are covalently joined so that both subunits only translate mRNAs with an orthogonal SD sequence.[57,58] Orthogonal ribosomes hold promise for future *in vivo* high-throughput screening of mutant ribosome libraries.

Changes have also been made to the ribosomal PTC to engineer ribosomes capable of utilizing non-α-L-amino acids in translation. These include changes for incorporating β-amino acids[59,60], D-amino acids[61], and dipeptide mimetics[62]. These examples demonstrate that ribosome engineering is a promising avenue for the synthesis of sequence-defined polymers with monomors that differ from α-amino acids. One of the challenges in engineering the PTC is that it is nearly universally conserved across life. Because of its conservation, there is little information in natural rRNA sequences about what changes can be made to the PTC, unlike in protein engineering where multiple sequence alignments can reveal variable sites that tolerate mutations.[63,64] Additionally, even single PTC mutations can inactivate ribosomes or are toxic *in cellulo*.[65] An example of the challenges is the P7A7 ribosome, which was engineered to incorporate β-amino acids *in vivo* but is inactive and exhibited a major folding defect *in vitro*.[59,66] Some of these challenges have been addressed in protein engineering by using thermostable proteins. It has been shown that thermostable proteins are better able to accommodate destabilizing mutations required to achieve new function.[67] A possible solution for the challenges in ribosome engineering is to use thermostable ribosomes or other features of divergent ribosomes from across the tree of life. Ultimately, studying ribosomes from divergent organisms may reveal design principles that enable more effective ribosome engineering.

Chapter 2: Rare ribosomal RNA sequences from archaea stabilize the bacterial ribosome

Reproduced from: Nissley, A. J., Penev, P. I., Watson, Z. L., Banfield, J. F. & Cate, J. H. D. Rare ribosomal RNA sequences from archaea stabilize the bacterial ribosome. *Nucleic Acids Res.* **51**, 1880–1894 (2023).

2.1 Abstract

The ribosome serves as the universally conserved translator of the genetic code into proteins and supports life across diverse temperatures ranging from below freezing to above 120 °C. Ribosomes are capable of functioning across this wide range of temperatures even though the catalytic site for peptide bond formation, the peptidyl transferase center, is nearly universally conserved. Here we find that Thermoproteota, a phylum of thermophilic Archaea, substitute cytidine for uridine at large subunit rRNA positions 2554 and 2555 (*Escherichia coli* numbering) in the A loop, immediately adjacent to the binding site for the 3′-end of A-site tRNA. We show by cryo-EM that *E. coli* ribosomes with uridine to cytidine mutations at these positions retain the proper fold and post-transcriptional modification of the A loop. Additionally, these mutations do not affect cellular growth and protect the large ribosomal subunit from thermal denaturation. This work identifies sequence variation across archaeal ribosomes in the peptidyl transferase center that likely confers stabilization of the ribosome at high temperatures and develops a stable mutant bacterial ribosome that can act as a scaffold for future ribosome engineering efforts.

2.2 Introduction

Ribosomes are ribonucleoprotein complexes that carry out protein synthesis through the translation of genetic information into polypeptides. The ribosome consists of a large subunit (LSU) which contains the catalytic peptidyl transferase center (PTC) and the small subunit where messenger RNA (mRNA) is decoded. Nucleotides in the PTC critical for peptide bond formation are universally or highly conserved, and mutation of these nucleotides often results in severe growth defects or lethal phenotypes[68–70]. However, some mutational flexibility exists in the PTC beyond the core nucleotides that are directly involved in catalysis[65]. Sequence variation at these sites, as well as post-transcriptional modification, are known to afford resistance to certain antibiotics targeting the ribosome[71]. However, the functional impact of natural variation in the PTC on translation remains to be determined.

During translation elongation, an incoming aminoacyl transfer RNA (aa-tRNA) docks in the A site of the ribosome. For proper tRNA substrate positioning to occur, the tRNA anticodon must base pair with the mRNA in the small subunit decoding site while the tRNA 3′-CCA nucleotides interact with the A loop, an RNA hairpin in the ribosomal RNA (rRNA) of the large subunit[72]. Proper orientation of the 3′-CCA end of the A-site tRNA by the A loop is necessary for correct positioning of the linked amino acid and subsequent peptide bond formation. In the *E. coli* ribosome, the interaction between the A-site tRNA 3′-CCA end and the A loop is formed in part by base pairing between universally conserved nucleotides C75 in the tRNA and G2553 in 23S rRNA (*E. coli* numbering)[73]. Mutation of either of these residues leads to a complete loss of activity that can be recovered by compensatory mutations that restore base pairing, establishing this interaction as vital to translation[73,74].

While some sequence variability exists within the A loop, its structure is universally conserved due to its critical role in translation elongation[75]. Additionally, 2′-*O*-methylation of U2552 is a conserved post-transcriptional modification that enables the proper folding of the A

loop and ensures residues in the apical loop can interact with the A-site tRNA[76]. In *E. coli*, loss of U2552 2′-*O*-methylation leads to severe growth defects and ribosome misfolding[77]. Positions 2554 and 2555 in the A loop are conserved as uridines in eukaryotes and bacteria. U2554 forms a non-canonical base pair with C74 of the A-site tRNA and the base of U2555 stacks with C74[78]. These interactions help to further stabilize the 3′-CCA end of the A-site tRNA upon docking in the ribosome. Previously, point mutations have been made at positions 2554 and 2555 in the bacterial ribosome with varying functional effects. U2555 mutations to adenine or guanine increase +1/-1 frameshifting and stop codon readthrough[79]. In *in vitro* assembled ribosomes, a U2554C mutation decreased translation activity while a U2555C mutation had no effect[65]. Despite previous functional studies of ribosomes with mutations in the A loop and PTC, there have been no investigations into how rRNA sequences in these regions affect the thermodynamic stability of the ribosome.

Interestingly, positions 2554 and 2555 are sometimes found as cytidines in Archaea[73,79]. It is known that thermophilic organisms stabilize their rRNA by increasing its GC content, which stabilizes secondary structure[80]. Additionally it has been shown that thermophilic organisms have higher levels of post-transcriptional rRNA modification, including N^4-acetylcytidine[35] and 2′-*O*-methylation[81], and that the extent of these modifications is correlated with growth temperature. Here, we find that organisms in archaeal phylum Thermoproteota have cytidines at positions 2554 and 2555 in the A loop (*E. coli* numbering). Using archaeal sequences as a guide, we show that U to C mutations at positions 2554 and 2555 in 23S rRNA of the *E. coli* ribosome have a stabilizing effect on the 50S ribosomal subunit. This work identifies rare sequence variation in ribosomal RNA that likely leads to thermostability in the archaeal ribosome and describes how the specific stabilization of A loop structure can lead to global ribosome stabilization. These insights into how thermophilic organisms can stabilize their ribosomes provide a foundation for engineering ribosomes with increased mutational robustness and evolvability.

2.3 Materials and methods

Archaeal rRNA sequence alignment and tree visualization

To investigate sequences within the A loop we aligned archaeal 23S rRNA sequences from the SILVA database[82] to a manually curated sequence alignment of large subunit (LSU) rRNA[75] using mafft with the option –add[83,84]. We used a custom python script (https://github.com/petaripenev/A-loop_sequence_analysis) to identify relevant positions, and correlate data for average optimal living temperature from the TEMPURA database[85] with the alignment and a phylogenetic tree retrieved from SILVA. For several new Nitrososphaerota taxa missing from the TEMPURA database, we searched published articles to identify likely ranges of optimal living temperature (**Table S2.1**). The nucleotide identity and average optimal living temperature were mapped on the tree with iTOL[86]. Phyla were indicated following the latest GTDB taxonomy[87].

Cloning and plasmid design

A modified version of the pLK35[88] plasmid, which encodes 5S, 16S, and MS2-tagged 23S rRNA[89], with an IPTG inducible tac promoter was used for ribosome mutagenesis. Point mutations were introduced using the Q5 mutagenesis kit (NEB) and appropriate primer sets (**Table S2.2**). All plasmid sequences were verified by Sanger sequencing (ElimBio).

E. coli growth assays

E. coli strain SQ171 (Δ7rrn), which harbors a pCsacB plasmid containing the *rrnB* operon, the Kan^R gene, and the sucrose counter-selectable *sacB* marker, was used to examine *E. coli* growth supported by mutant ribosomes. Replacement of the pCsacB plasmid with the modified pLK35 plasmid was achieved as described with adaptions[90,91]. An A2058G erythromycin resistance mutation[92] was introduced into pLK35 plasmids to improve the selection of clones containing the pLK35 plasmid. Competent SQ171 cells were transformed with a pLK35 plasmid containing the desired 23S rRNA mutations and an MS2 tag, diluted to 1 mL in SOC media (NEB), and grown at 37 °C for 6 hours. 200 µL of culture was then added to 2 mL of SOC media with 100 µg/mL ampicillin, 25 µg/mL spectinomycin, and 0.25% (w/v) sucrose and incubated for 18 hours at 37 °C. Cells were pelleted, resuspended in 100 µL of media, and spread on an LB agar plate with 100 µg/mL ampicillin, 25 µg/mL spectinomycin, 1 mg/mL erythromycin, and 5% sucrose. Plates were incubated at 37 °C for 24 hours and 6 colonies were replica plated onto LB agar plates with 100 µg/mL ampicillin or 50 µg/mL kanamycin to confirm the loss of the pCsacB plasmid. Plasmids from colonies that did not grow on plates with kanamycin were isolated and sequenced to further confirm the loss of the pCsacB plasmid. To study *E. coli* growth supported by a mixed population of mutant and WT ribosomes, NEB Express I^q cells were transformed with each modified pLK35 plasmid with the desired 23S rRNA mutations, but without the A2058G erythromycin resistance mutation.

Liquid cultures of each transformant were grown overnight and then were diluted to OD 0.01 in LB media containing 100 µg/mL ampicillin and 25 µg/mL spectinomycin (SQ171) or 100 µg/mL ampicillin and 500 µM IPTG (NEB Express I^q). 200 µL of each dilution was then pipetted into wells of a sterile 96-well plate. The OD_{600} was measured every 15 minutes using a Spark Plate Reader (Tecan) at 37 °C with constant shaking. Doubling times were calculated by fitting the initial region of exponential growth to a Malthusian growth model in Prism.

To determine the ratio of MS2-tagged plasmid encoded ribosomes to untagged WT genomically encoded ribosomes present during the growth experiments, 200 µL of culture from each sample was pelleted. Total RNA was extracted from cell pellets using the RNeasy Mini Kit (Qiagen). Semiquantitative PCR was used to determine the ratio of tagged 23S rRNA to WT 23S rRNA as previously described[66]. Briefly, primer MS2_quant_R was used to reverse transcribe a portion of 23S rRNA. A region containing the sequence for the MS2 tag was amplified via PCR using primers MS2_quant_F and MS2_quant_R (**Table S2.2**). PCR products were run on a 10% polyacrylamide-TBE gel (Invitrogen) and visualized with SYBR gold stain (ThermoFisher). DNA bands were quantified using ImageJ software[93].

Crude ribosome preparation

Crude ribosomes were isolated as previously described with several adaptations[94]. NEB Express I^q cells were transformed with the corresponding pLK35 plasmid carrying a tac promoter, MS2-tagged 23S rRNA, and the desired mutations. Overnight cultures of the transformants were diluted 1:100 into 2-3 L of LB broth containing 100 µg/mL ampicillin and grown at 37 °C. Upon growth to OD_{600}=0.6, rRNA transcription was induced with 0.5 mM IPTG and the cultures were grown for 3 hours at 37 °C. Cells were then pelleted, resuspended in 50-100 mL buffer A (20 mM Tris-HCl pH 7.5, 100 mM NH_4Cl, 10 mM $MgCl_2$, 0.5 mM EDTA, 2 mM DTT), and lysed by sonication. The lysate was then clarified by centrifugation at 14,000 rpm (34,000 xg) for 45 minutes in a F14-14x50cy rotor (ThermoFisher). Clarified lysate was then loaded onto a sucrose cushion containing 24 mL of buffer B (20 mM Tris-HCl pH 7.5, 500 mM NH_4Cl, 10 mM $MgCl_2$,

0.5 mM EDTA, 2 mM DTT) with 0.5 M sucrose and 17 ml of buffer C (20 mM Tris-HCl pH 7.5, 60 mM NH_4Cl, 6 mM $MgCl_2$, 0.5 mM EDTA, 2 mM DTT) with 0.7 M sucrose in Ti-45 tubes (Beckman-Coulter). The tubes were then placed in a Ti-45 rotor and spun at 27,000 rpm (57,000 xg) for 16 hours at 4 °C. The next day, ribosome pellets were resuspended in dissociation buffer (buffer C with 1 mM $MgCl_2$).

MS2-tagged ribosome purification

The MBP-MS2 fusion protein was purified as previously described[66]. 10 mg of MBP-MS2 protein was diluted to 1 mg/mL in MS2-150 buffer (20 mM HEPES pH 7.5, 150 mM KCl, 1 mM EDTA, 2 mM 2-mercaptoethanol) for a 5 mL column preparation. For each 1 mL column prep, 4 mg of MBP-MS2 protein was used. The 5 mL or 1 mL MBP Trap column (Cytiva) was washed with 5 column volumes (CV) of MS2-150 buffer and then the MBP-MS2 protein was loaded slowly onto the column. The column was then washed with 5 CV of buffer A-1 (buffer A with 1 mM $MgCl_2$). Crude tagged ribosomes (~100-200 mg) were diluted to 15 mg/mL in buffer A-1, which dissociates 70S ribosomes into 30S and 50S subunits and decreases WT ribosome contamination. The diluted crude ribosomes were loaded slowly onto the MBP-trap column, which was then washed with 5 CV of buffer A-1 followed by 5 CV of buffer A-250 (buffer A with 250 mM NH_4Cl and 1 mM $MgCl_2$). Ribosomes were eluted with a 10 CV gradient of buffer A-1 containing 0-10 mM maltose. Fractions containing tagged ribosomes were concentrated in 100 kDa cut off spin filters (Millipore) and washed with buffer A-1. 50S ribosomal subunits were quantified using the approximation of 1 A_{260}= 36 nM and were stored at -80 °C.

Untagged subunit purification

Overnight cultures of *E. coli* strain MRE600 were diluted 1:100 into 2-3 L of LB broth and grown to an OD_{600}=0.6. Cells were then pelleted and lysed by sonication. Ribosomes were pelleted and resuspended as described above for crude ribosome preparations. After resuspension in dissociation buffer, the 30S and 50S subunits were separated on a 15-35% (w/v) sucrose gradient in dissociation buffer on a SW-32 rotor (Beckman-Coulter) spun at 28,000 rpm (97,000 xg) for 16 hours. Fractions containing the 50S and 30S subunits were collected separately, washed with dissociation buffer, and concentrated in a 100 kDa cut off spin filter. To increase purity, concentrated subunits were separately run on second 15-35% sucrose gradients and appropriate fractions were washed with dissociation buffer and concentrated.

Nanoluciferase 11S fragment purification

A plasmid encoding 8xHis-tagged 11S was transformed into BL21 (DE3) Rosetta2 pLysS cells (Macrolab, UC Berkeley). An overnight culture was diluted (1:100) into LB media with 100 µg/mL ampicillin and grown at 37 °C. When the culture reached OD_{600}=0.4, cells were induced with 1 mM IPTG for three hours. Cells were then pelleted at 4,000 xg for 15 minutes and resuspended in ~20 mL 11S lysis buffer (20 mM HEPES pH 7.5, 50 mM KCl, 10% glycerol, and 10 mM imidazole). Cells were lysed by sonication and the lysate was clarified by centrifugation at 18,000 rpm (25,000 xg) for 30 minutes (JA-20 rotor, Beckman). Supernatant was then applied to a 1 mL HisTrap column (Cytiva). The column was washed with 10 CV of 11S lysis buffer and eluted with a 20 CV linear gradient form 20-500 mM imidazole in lysis buffer. Protein fractions were dialyzed against 11S lysis buffer without imidazole overnight at 4 °C. The protein was then concentrated and stored at -80 °C.

HiBit translation assay

50S ribosomal subunits were diluted to 1.4 μM in buffer A with a final concentration of 10 mM $MgCl_2$. This mixture was then incubated at the desired temperature for 30 minutes on a ProFlex (ThermoFisher) PCR cycler with a heated lid. After incubation, tubes containing the 50S subunits were placed on the bench and allowed to cool slowly to room temperature for 30 minutes. The cooling method influenced the return of mutant ribosome activity. Slow cooling at room temperature returned higher levels of activity as compared to snap-cooling on ice for the CC mutant ribosome (**Figure S2.1**). It is possible that snap-cooling leads to a less active conformation in the mutant ribosome. Due to this observation, a slow-cooling method was utilized. After cooling, an *in vitro* translation mixture was assembled using a ΔRibosome PURExpress kit (NEB). The mixture was assembled with the following: 3.2 μL solution A (NEB), 1 μL factor mix (NEB), 250 nM pre-incubated 50S ribosomal subunits, 500 nM WT untagged 30S ribosomal subunits, 1U/μL Murine RNAse inhibitor (NEB), 100 nM 11S NanoLuc protein[95], 1:50 (v/v) dilution of Nano-Glo substrate (Promega), and 10 ng/μL of DNA template containing a T7 promoter, ribosome binding site, and the coding sequence for the HiBit peptide[95] (final volume of 8 μL). 2 μL of the *in vitro* translation mixture was placed in a 384 well plate, and luminescence was measured as a function of time in a Spark Plate Reader (Tecan). Ribosome activity was calculated by determining the slope of the initial linear region of each *in vitro* translation reaction. Each reported activity is the average from three separate HiBit reactions.

In vitro nLuc translation endpoint assay

An *in vitro* translation reaction was assembled with the following: 6.4 μL solution A (NEB), 2 μL factor mix (NEB), 250 nM pre-incubated 50S subunit, 500 nM WT untagged 30S subunit, 1U/μL Murine RNAse inhibitor (NEB), and 10 ng/μL of a plasmid encoding a T7 promoter followed by the nLuc gene (final volume of 16 μL). This reaction was then incubated at 37 °C for 1 hour. After incubation, 5 μL from the reaction was mixed with 30 μL of 11S buffer (20 mM HEPES pH 7.5, 50 mM KCl, and 10% glycerol) and a 1:50 dilution of Nano-Glo substrate (Promega). This mixture was placed in a 384 well plate and luminescence was measured in a Spark Plate Reader (Tecan). Triplicate readings were measured and averaged for each *in vitro* translation reaction.

Sucrose gradients

For heat treated 50S subunits, 10 pmol 50S subunit was diluted in buffer A with 10 mM $MgCl_2$ to a final volume of 20 μL. This mixture was then incubated at the desired temperature for 30 minutes on a ProFlex (ThermoFisher) PCR cycler with a heated lid and placed on the bench for 30 minutes to cool slowly to room temperature. For 70S formation assays, 10 pmol 50S subunit and 20 pmol WT untagged 30S subunit were diluted in buffer A with 15 mM $MgCl_2$ to a final volume of 20 μL. These samples were then incubated at 37 °C for 30 minutes. Samples were loaded onto a 15-40% sucrose gradient in buffer A with 10 or 15 mM $MgCl_2$. Gradients were then placed in a SW-41 Ti rotor (Beckman-Coulter) and centrifuged at 29,000 rpm (100,000 xg) for 13 hours. An ISCO gradient fractionation system was used to measure A_{254} traces.

CD spectroscopy

RNA oligonucleotides were purchased from IDT (**Table S2.3**) and resuspended into RNAse-free water. RNA was incubated at 95 °C for 3 minutes and then immediately snap-cooled in an ice water bath. After cooling, the RNA concentration was adjusted to 100 μM and the buffer

concentration was adjusted to 20 mM $K_xH_yPO_4$ pH 6.5. Low ionic buffer conditions were used to shift the melting temperature to a value where both the initial and final baselines could be more accurately modeled. CD experiments were conducted in a 1-mm path-length cuvette with an Aviv 410 CD spectropolarimeter. For thermal melting experiments, CD at 262 nm was recorded in 2 °C intervals from 5 °C to 95 °C. The temperature was moved to the target value, and the system was allowed to equilibrate for one minute before a measurement was taken. Thermal melting data was fit to a two-state model with sloping baselines[96] (**Equation 2.1**) in Prism 9. All RNAs tested exhibited reversible thermal melting profiles. Each RNA construct was measured in duplicate.

$$f(T) = \frac{(m_u T + b_u) + (m_f T + b_f) e^{\left(\frac{\Delta H}{R}\right)\left(\frac{1}{T_m + 273.15} - \frac{1}{T_m + 273.15}\right)}}{1 + e^{\left(\frac{\Delta H}{R}\right)\left(\frac{1}{T_m + 273.15} - \frac{1}{T_m + 273.15}\right)}} \quad \textbf{(2.1)}$$

Where T is temperature in Celsius, m_u and m_f are the slopes of the unfolded and folded baselines, respectively, b_u and b_f are the y-intercepts of the unfolded and folded baselines, respectively, ΔH is the Vant Hoff enthalpy of unfolding, R is the gas constant, and T_m is the melting temperature in Celsius.

Methionyl-tRNA synthetase purification

A plasmid encoding 6xHis-tagged methionyl-tRNA synthetase (MetRS) was transformed into BL21 (DE3) Codon+ RIL cells (Agilent). Overnight cultures were diluted (1:100) into ZYM-5052 autoinducing media[97] and grown overnight at 37 °C. Cells were pelleted at 4,000 xg for 15 minutes and resuspended in 50 mL of MetRS lysis buffer (20 mM Tris pH 7.5, 150 mM NaCl, 5 mM imidazole, and 0.5 mM EDTA). Cells were lysed by sonication and the lysate was clarified by centrifugation at 18,000 rpm (25,000 xg JA-20 rotor, Beckman-Coulter) for 30 minutes. The supernatant was applied to a 5 mL HisTrap column (Cytiva), washed with 5 CV of MetRS lysis buffer with 23 mM imidazole and eluted with a 20 CV linear gradient from 23-500 mM imidazole. Protein fractions were pooled and dialyzed overnight against MetRS buffer (50 mM HEPES pH 7.5, 100 mM KCl, 10 mM $MgCl_2$, 7 mM BME and 30% glycerol). The protein was concentrated and stored at -80 °C.

tRNA preparation

A single stranded DNA template encoding a T7 promoter and $tRNA^{fMet}$, with a C1G mutation to increase transcription yield and deletion of the 3′-terminal adenosine (C1G -A), was amplified via PCR, yielding a double stranded DNA template. $tRNA^{fMet}$ was *in vitro* transcribed with transcription buffer (50 mM Tris pH 7.5, 15 mM $MgCl_2$, 5 mM DTT, 2 mM spermidine), 2.5 mM NTPs, 1 U/µL Murine Rnase inhibitor (NEB), 0.5 U/µL T7 polymerase (NEB), and 0.5 U/mL YIPP (NEB). *In vitro* transcription reactions were incubated for 16 hours at 37 °C and then treated with 45 U/mL of RQ1 Dnase (Promega) at 37 °C for 30 minutes. Reactions were ethanol precipitated and then resolved on a 12% denaturing polyacrylamide gel. Gel slices containing the tRNA were excised, crushed, and soaked in 300 mM sodium acetate pH 5.2 overnight at 4 °C. The RNA was then ethanol precipitated, resuspended in water, and stored at -80 °C.

$tRNA^{fMet}$ lacking the 3′-terminal adenosine (A76) was then treated with the tRNA nucleotidyl transferase from *Archeoglobus fulgidus* (*Af*) and 3′-NH_2-ATP (nATP) (Axxora) in the following conditions: 100 mM glycine pH 9.0, 10 mM $MgCl_2$, 2 µM nucleotidyl transferase, 2 µM tRNA(-A), 0.5 mM nATP, 1 mM DTT, and 2 U/mL YIPP (NEB)[98]. *Af* tRNA nucleotidyl transferase was purified with the same method and buffers as the MBP-MS2 fusion protein[66]. The

reaction was incubated at 37 °C for 2 hours. The tRNA was then phenol-chloroform extracted, ethanol precipitated, and resuspended in water.

E. coli methionyl-tRNA synthetase (MetRS) was used to charge 3′-amino $tRNA^{fMet}$ in the following conditions: charging buffer (50 mM HEPES pH 7.5, 10 mM KCl, 20 mM $MgCl_2$, 2 mM DTT), 10 µM $tRNA^{fMet}$-NH_2, 10 mM methionine, 1 µM MetRS, 10 mM ATP, 1 U/µL Murine Rnase inhibitor. The reaction was incubated at 37 °C for 30 minutes. Charged tRNA was phenol-chloroform extracted, ethanol precipitated, resuspended in water, and stored at -80 °C.

Cryo-EM sample preparation

To assemble 70S ribosomes, 0.5 mg of U2554C U2555C (CC) mutant 50S subunit and 0.6 mg of WT untagged 30S subunit were incubated in buffer C with 10 mM $MgCl_2$ at 37 °C for 45 minutes. The ribosome mixture was then loaded onto a 15-40% (w/v) sucrose gradient in buffer C with 10 mM $MgCl_2$. Gradients were centrifuged at 28,000 rpm (97,000 xg) for 16 hours in a SW-32 rotor (Beckman-Coulter). An ISCO gradient fraction system was used to isolate the 70S fraction (**Figure S2.2**).

Ribosome-tRNA-mRNA complexes were prepared as previously described[99] with modifications. Complexes were formed non-enzymatically by combining 2 µM Met-$tRNA^{fMet}$, 5 µM mRNA, and 100 nM ribosomes in buffer AC (20 mM Tris pH 7.5, 100 mM NH_4Cl, 15 mM $MgCl_2$, 0.5 mM EDTA, 2 mM DTT, 2 mM spermidine, and 0.05 mM spermine). Paromomycin at a concentration of 100 µM was used to ensure nonenzymatic A-site tRNA binding. The complex was incubated at 37 °C for 30 minutes and then held at 4 °C. The mRNA sequence was 5′-GUAUAAGGAGGUAAA<u>AUGAUG</u>UAACUA-3′ (IDT). Met codons are underlined. This mRNA sequence placed Met-$tRNA^{fMet}$ in both the A and P sites. Cryo-EM grids were prepared and samples were frozen as previously described[99].

Cryo-EM data acquisition, image processing, and modeling

Movies were collected on a 300 kV Titan Krios microscope with a GIF energy filter and a Gatan K3 camera, and data was acquired as described (**Table S2.4**)[99]. Raw movies were binned to the physical pixel size (0.8279 Å) in RELION 3.1[100] and motion corrected with MotionCor2[101]. The CTFs of micrographs were estimated using CTFFind4[102]. The estimated CTFs of micrographs were visually inspected, and micrographs with poor CTF fit were manually rejected. Particles were picked using the RELION implementation with a Laplacian of Gaussian method, and then extracted and binned 4x for classification steps. 2D classification was performed in RELION using 150 classes. Junk particles were rejected and a second round of 2D classification was performed. 3D classification was performed with a cryoSPARC heterogeneous refinement[103] with 10 classes using an initial model generated in EMAN2[104] from PDB 1VY4[105]. Classes containing features consistent with well-ordered 70S particles were combined and a local refinement on the 50S subunit was carried out. The aligned particles were then transferred back to RELION. A 3D classification without alignment was performed in RELION to separate classes with slightly rotated 30S subunits. This procedure yielded a junk class, a rotated 30S subunit that had no A-site tRNA density, and a class that had P-site and A-site tRNA density. The latter class was then subjected to an additional classification without alignment using a mask on the A-site tRNA. Interestingly, this step yielded two slightly shifted A-site tRNA classes that were equally populated (**Figure S2.3**). The separation of multiple A-site tRNA classes with a masked 3D classification has been observed with the WT ribosome[106]. Upon closer examination, one of these classes had clear density for the CCA-end of the A-site tRNA and was processed further. These particles were

re-extracted at full size and subjected to CTF Refinement[100] and Bayesian polishing[107] in RELION. A focus refinement was performed separately on the 50S and 30S subunits and the resulting focus refined maps were aligned and combined to generate a final composite map. PDB 7K00 was used as an initial 70S ribosome model[99] and the 'Fit to Map' function in ChimeraX[108] was used to align the cryo-EM map to the initial model. The 70S model was refined using real space refinement in PHENIX (**Table S2.5**)[109]. The model and cryo-EM map were inspected in COOT[110] and manual adjustments to the model were made as needed.

2.4 Results

Sequence conservation in the A loop

To investigate sequence diversity in the A loop, we aligned archaeal 23S rRNA sequences from the SILVA database[82] to a structurally guided sequence alignment of LSU rRNA[75], identifying nucleotide variation at positions 2554 and 2555 (*E. coli* numbering) (**Figure 2.1A**). Both positions are almost universally uridine residues (UU), except for sequences from the Thermoproteota phylum, which includes a variety of organisms from high and low temperature environments (**Figure 2.1B**). Class Nitrososphaeria (Thaumarchaeota) from this phylum generally includes mesophilic organisms that are prevalent in cold marine environments, while class Thermoprotei (Crenarchaeota) includes hyperthermophilic organisms that grow at high temperatures[111]. We find that Nitrososphaeria tend to have a cytidine at position 2554 (CU) while Thermoprotei more often have cytidines at both positions (CC) (**Figure 2.1B**). Organisms within Thermoproteota, such as *Pyrolobus fumarii* and *Geogemma barossii*, have extreme growth temperatures (up to 121 °C), even among thermophiles, suggesting that this change may play a role in ribosome stability[112,113]. However, there are some hyperthermophiles in Thermoproteota that have either CU or UU sequences in the A loop. Additionally, other thermophilic Archaea, such as organisms in Thermoplasmatota and Euryarchaeota, have uridines instead of cytidines at these positions, suggesting that the CC mutation is one of multiple evolutionary strategies to confer heat resistance.

A loop mutations in the E. coli 50S ribosomal subunit

Since nucleotides 2554 and 2555 in 23S rRNA are conserved as uridines in bacteria and eukaryotes, we studied the effects of U to C mutations observed in archaeal A loop sequences in the context of the *E. coli* ribosome. We first assessed whether mutations in the A loop influence bacterial growth. *E. coli* strain SQ171, which does not contain genomically encoded rRNA and requires a plasmid containing an rRNA operon[114], was transformed with a plasmid (pLK35) harboring either a wild-type (WT) 23S rRNA sequence, a U2554C (CU) point mutation, or a U2554C-U2555C (CC) double mutation. These transformants were then counter selected to cure the original pCsacB plasmid, encoding the WT rRNA operon, so that selected colonies are only supported by ribosomes encoded by the pLK35 plasmid (methods). *E. coli* SQ171 containing the WT, CU, or CC plasmids all grew and indicates that the mutant ribosomes can support life, which is in line with a previous study of growth supported by ribosomes with these mutations[115]. Growth of these strains in liquid media revealed that all transformants have similar doubling times (**Figure 2.2A, Table S2.6**), although bacteria supported by the CU and CC ribosomes had slightly longer lag phases. These trends in growth and lag time were also observed in bacteria that expressed mixed populations of mutant and WT ribosomes (**Figure S2.4, Table S2.6**). Taken together, these results indicate that ribosomes with CU and CC A loop mutations function nearly indistinguishably from WT ribosomes *in vivo*.

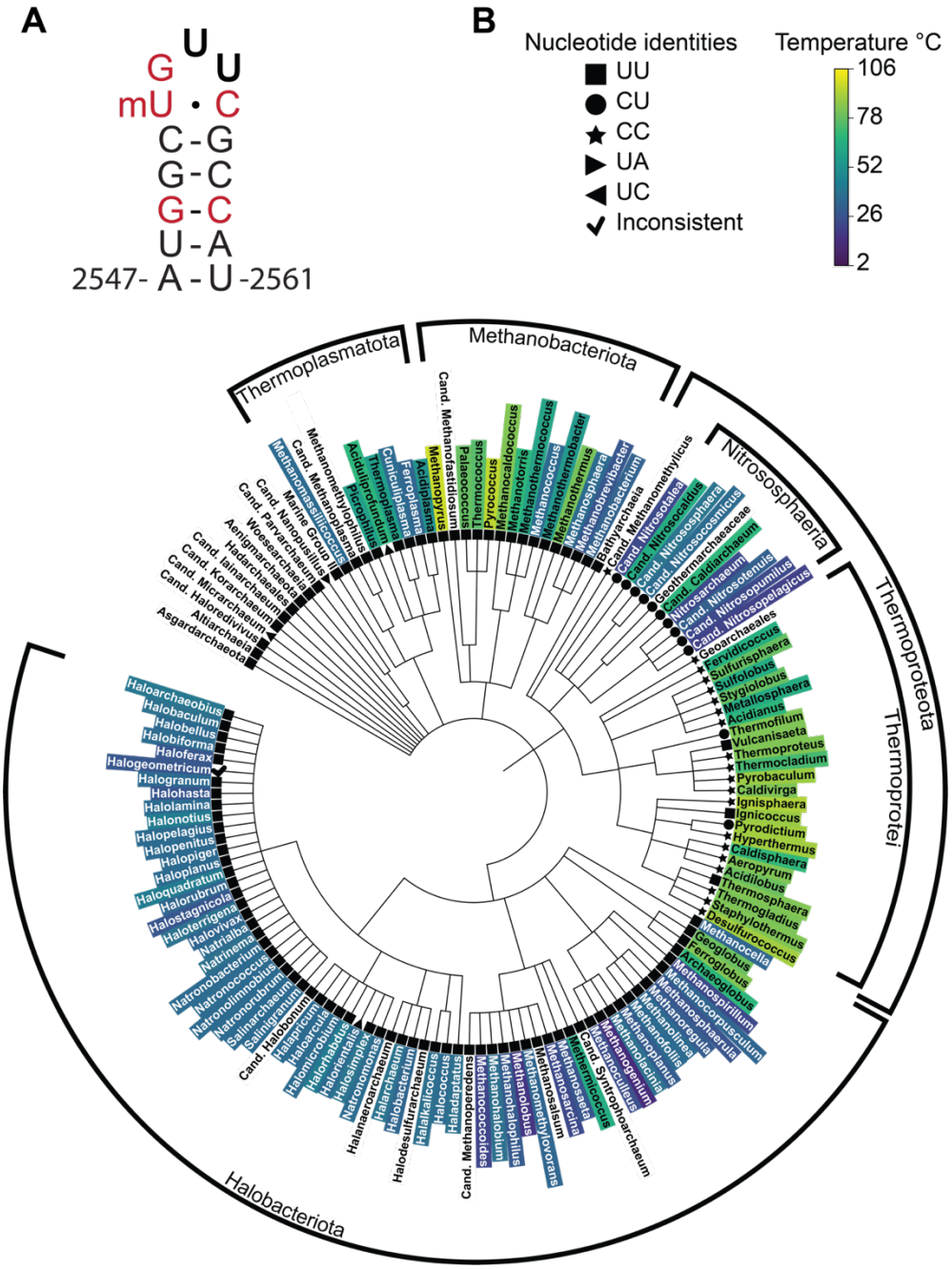


Figure 2.1 Distribution of nucleotide sequence variation in the A loop across Archaea. A) RNA secondary structure of the *E. coli* A loop. Red nucleotides are universally conserved. Positions 2554 and 2555 are in bold. B) Phylogenetic tree of archaeal large ribosomal subunit (LSU) rRNA in the SILVA database[82]. Coloring at the genus level is based on optimal growth temperatures. Nucleotide sequences at the equivalent positions to 2554 and 2555 in *E. coli* 23S rRNA are indicated by geometric symbols. CU and CC variations at these positions are found mainly in Thermoproteota (Nitrososphaeria and Thermoproteotei).

Having established the tolerance of U to C A-loop mutations *in vivo*, we further characterized the mutational effects *in vitro*. Three forms of the *E. coli* 50S ribosomal subunit were purified using an MS2 tag[89]: WT, U2554C (CU) and U2554C-U2555C (CC) (**Figure S2.5**). We

first examined whether these mutations influence bacterial ribosome activity at normal growth temperatures using an *in vitro* translation endpoint assay in which full length nLuc protein (171 amino acids) is translated. At 37 °C, both the CU and CC ribosomes produce similar levels of active nLuc protein compared to WT ribosomes (**Figure 2.2B**), indicating that the U to C mutations do not cause translation defects *in vitro*.

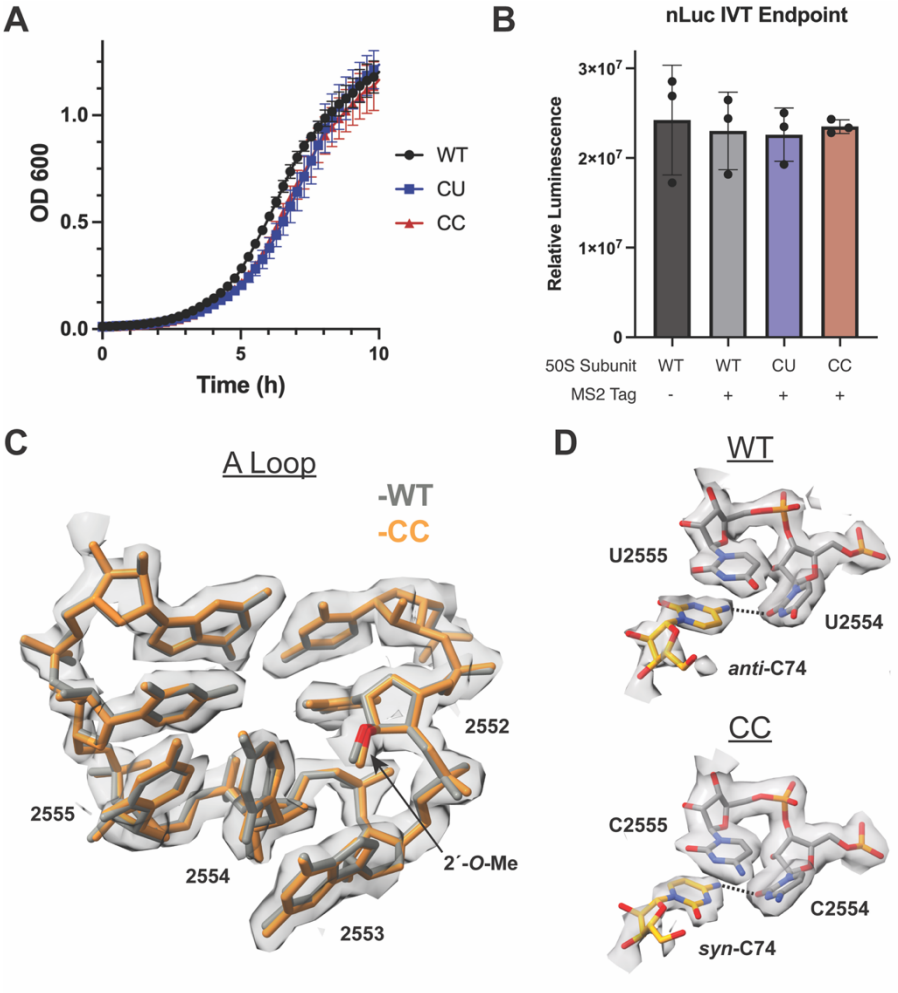


Figure 2.2 Effects of CU and CC mutations on the A loop. A) Growth curves of *E. coli* strain SQ171 expressing plasmid-encoded ribosomes (data and error bars are represented as the mean and standard deviation of 4 replicates respectively). The plasmid-encoded 23S rRNA harbors an MS2 tag. B) Nanoluciferase *in vitro* translation endpoint assay for mutant ribosomes at 37 °C (data is represented as the mean of 3 replicates). Error bars represent the standard deviation of three reactions. C) Cryo-EM density and model for the CC mutant ribosome are shown in grey and orange respectively. The model from a WT ribosome structure[106] is shown in grey. D) (Top) Cryo-EM density and model for C74 in the A-site tRNA and U2554 and U2555 in the A loop from[106]. (Bottom) Cryo-EM density and model for C74 in the A-site tRNA and C2554 and C2555 in the A loop in the CC mutant ribosome. The C74 (N4)-U2554 or C2554 (O2) hydrogen bonds are represented by dashed lines. A *B*-factor of 30 Å^2 was applied to the CC mutant ribosome cryo-EM map.

Structure of the CC 70S ribosome

To probe the structural effects of the A loop mutants, we solved the cryo-EM structure of the CC mutant 70S ribosome in a complex with mRNA and aminoacyl-tRNAs in the P site and A site (non-hydrolysable Met-tRNA^{fMet}, see methods) to a global resolution of 2.2 Å (**Figure S2.6**). The structure reveals that, in the presence of the U to C mutations at positions 2554 and 2555, the A loop fold is indistinguishable from the WT A loop (**Figure 2.2C**). This result is in line with the observations that the CC ribosome has WT (UU) levels of activity at 37 °C *in vitro* and has no impact on cellular growth rates. In addition, the A loop in the CC mutant also contains the proper 2′-O-methylation of U2552, as evidenced by clear density for the 2′-*O*-methyl group on the ribose of U2552 (**Figure 2.2C**). Mutations at positions 2554 and 2555 thus do not affect the 2′-*O*-methylation of the nearby residue U2552 by *E. coli* methyltransferase RrmJ. The proper fold of the A loop in the CC structure is also indicative of the correct modification, as loss of U2552 2′-*O*-methylation has been shown to change the fold of the A loop[76].

While the structure of the A loop itself is not altered by the CC mutations, the positioning of the A-site tRNA and its interaction with the A loop is altered in two ways compared to WT ribosomes. First, C74 of the A-site tRNA adopts a *syn* conformation, in contrast to the *anti*-conformation observed in the WT ribosome (**Figure 2.2D**)[105,106]. The *syn* conformation is highly disfavored thermodynamically for pyrimidines and therefore, *syn* pyrimidines are not frequently found in RNA[116]. In the WT ribosome, C74 of the A-site tRNA is held in its position in part through hydrogen bonding between the exocyclic amine of C74 (N4) and the O2 carbonyl oxygen of U2554 (O2) in the A loop and by base stacking with U2555 in the A loop and C75 in the tRNA. In the CC mutant ribosome, hydrogen bonding between N4 of C74 and the O2 of C2554 is preserved with a *syn*-C74 (**Figure 2.2D**). No new hydrogen bonds are formed that stabilize this conformation and no conformational change in the ribosome occurs that would disfavor the *anti* conformation. It Is possible that either a change In the local electronic environment In the CC mutant or transient solvent interactions work to stabilize the *syn* conformation of C74. Despite this change, the C75-G2553 base pair is preserved and A76 and the linked methionine are in their canonical positions[105,106].

Second, during cryo-EM data processing, a masked classification of the A site yielded two slightly shifted tRNA classes that were equally populated (**Figure S2.3**), one of which had clear density for the 3′-CCA end of the A-site tRNA that was further processed to yield the final high-resolution structure. The second A-site tRNA class identified in the cryo-EM data (class 2) lacks density for most of the tRNA acceptor stem (including the 3′-CCA) but contains density for the anticodon and weak density for the rest of the tRNA (**Figure S2.7**). This contrasts with the WT *E. coli* ribosome structure, where all A-site tRNA classes had density for the CCA-end[106]. The structure of the WT ribosome used for comparison contains the same tRNAs in the P-site and A-site as in the CC ribosome structure, and both structures used paromomycin to favor A-site tRNA binding, which facilitates the direct comparison (methods). These results suggest that the U to C mutations in the A loop interfere with docking of the A-site tRNA's 3′-CCA end, possibly due to the *syn*-C74 conformation favored by the mutation.

CC mutations stabilize the 50S ribosomal subunit

Since CC variation in the A loop is found in hyperthermophilic Archaea, we sought to assess whether it stabilizes the 50S ribosomal subunit. To further examine ribosome activity in this context, we used a Nanoluc (nLuc) luciferase complementation assay, in which a truncated and catalytically inactive form of nLuc, termed 11S, is complemented by an *in vitro* translated peptide

with high affinity for 11S, termed HiBit, to restore luciferase activity (**Figure 2.3A**)[95]. This assay enables the close monitoring of translation rates, rather than the endpoint detection of translated protein as in the nLuc assay and is able to detect low levels of ribosome activity. We find that ribosomes with U to C mutations at positions 2554 and 2555 are as active as WT ribosomes at 37 °C in the HiBit assay (**Figure 2.3A**), which is consistent with the nLuc endpoint assay (**Figure 2.2B**).

E. coli protein components of an *in vitro* translation reaction are not thermostable[117], and rather than conducting *in vitro* translation assays at temperatures above 37 °C, we sought to decouple the thermostability of the 50S subunit and the translation reaction mixture. To do this, 50S subunits were first incubated at high temperatures, cooled slowly, and then added to *in vitro* translation reactions. Using this experimental design, we tested the thermostability of 50S subunits with the HiBit assay. WT ribosome activity begins to decrease after incubation at 60 °C, which suggests that this is the temperature at which 50S subunit denaturation begins (**Figure S2.8**). Surprisingly, we found that the MS2 tag inserted into 23S rRNA helix 98 (H98) affects ribosome stability, as the tagged WT ribosome has considerably lower levels of activity than the untagged WT ribosome after 50S subunit incubation at 60 °C (**Figure 2.3A** and **Figure S2.8**). MS2 tags in H98 have been used extensively as they do not affect cellular growth or ribosome assembly and function[89,118,119]. In further experiments, we sought to assess if CC mutations could recover activity of MS2-tagged 50S subunits after incubation at 60 °C.

Comparison of the MS2-tagged WT ribosomes and the tagged mutant ribosomes shows that both the CU and CC mutants have higher levels of activity than the tagged WT ribosome after 60 °C incubation of the 50S subunit, with the CC mutant retaining the highest levels of activity (**Figure 2.3A**). The higher activity retained by the CC ribosome compared to WT suggests that these mutations stabilize the ribosome. Notably, as in the HiBit assay, we also see increased protein output from the CC mutant compared to the tagged WT 50S subunits after pre-incubation at 60 °C in a full length nLuc endpoint assay (**Figure S2.9**).

To assess whether the effects on ribosome activity observed in the HiBit assay were due to possible folding defects in the PTC after heat treatment, or due to global misfolding of the 50S subunit, 50S subunits were resolved on sucrose gradients. Consistent with the HiBit assay, untagged WT 50S subunits are well folded after heat treatment at 60 °C with only a slight loss of folded 50S subunits (**Figure 2.3B**). The addition of an MS2 tag into H98 (WT-MS2 Tag 50S) leads to global ribosome unfolding after heat treatment. The peak height of the tagged WT 50S is decreased and broadened compared to the untagged 50S, consistent with a heterogeneous population of 50S subunits, likely due to degradation. While the CU 50S subunit shows slightly higher activity in the HiBit assay than the tagged WT subunit, the CU mutation does not improve global 50S subunit stability substantially, as determined with sucrose gradients (**Figure 2.3B**). This matches the full length nLuc endpoint assay where the CU subunit has low activity after heat treatment (**Figure S2.9**). In contrast, as demonstrated with *in vitro* translation assays, the CC 50S subunits remain more homogeneous on sucrose gradients, indicating they are better folded after heat treatment than the tagged WT subunit and that CC mutations globally stabilize the 50S subunit.

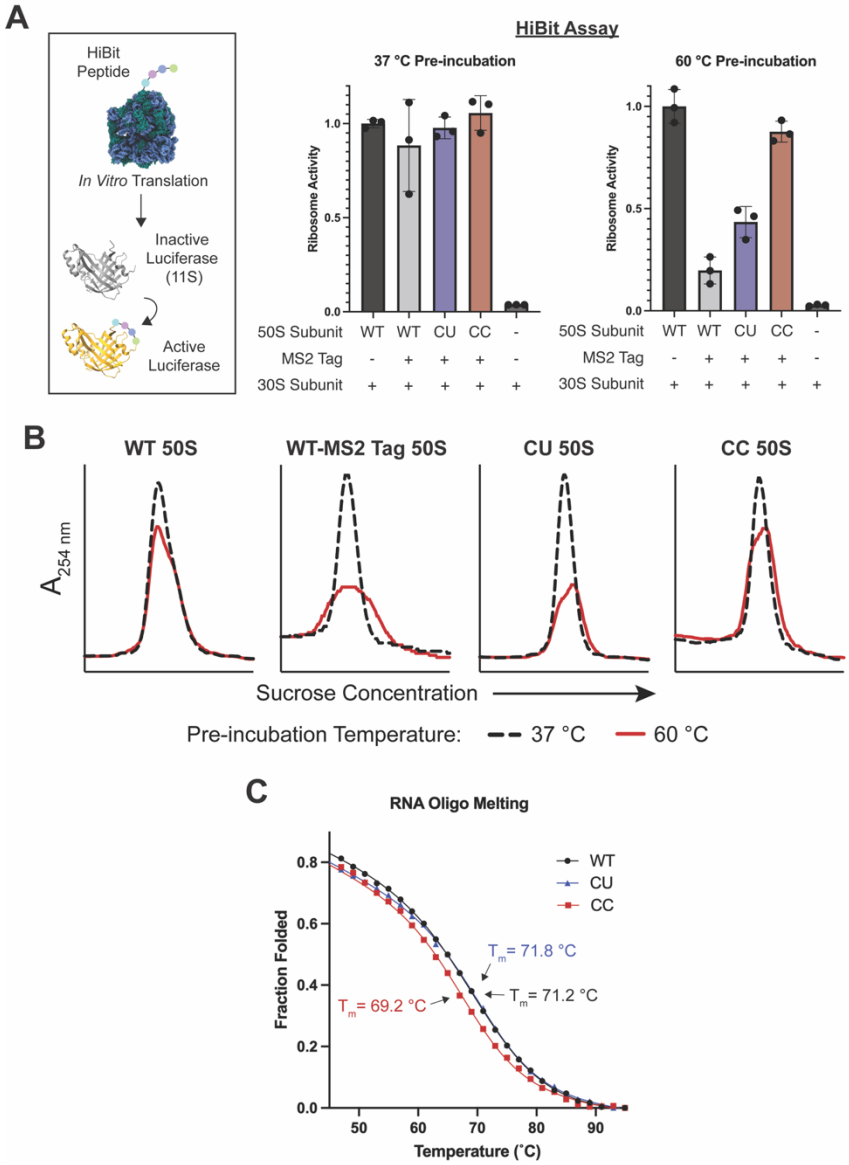


Figure 2.3. Stability of 50S subunits with A loop mutations at positions 2554-2555. A) In the HiBit assay, the 12 amino acid HiBit peptide is translated by the ribosome, which activates a truncated nanoluciferase (11S). 50S subunits were pre-incubated at 37 °C or 60 °C and then their relative activities were determined with the HiBit assay (data is represented as the mean of 3 replicates). Both untagged and MS2-tagged WT 50S subunits were used as controls. Error bars represent the standard deviation of three independent reactions. B) 50S subunits were heat treated at 37 °C (black dash) or 60 °C (red) and then resolved on a 15-40% sucrose gradient. C) RNA oligonucleotides (15 nucleotides) containing the WT A loop sequence (2547-2561), the CU, or CC mutant sequences were melted on a CD spectrometer. The melting temperature I was calculated for each construct using a two-state model.

To further probe the basis for ribosomal stabilization by U to C mutations in the A loop, we conducted thermal melting experiments of isolated rRNA hairpins comprising the A loop. We used RNA oligonucleotides of WT and mutant A loop sequences (CU and CC), all of which contained 2′-O-methylation of U2552. In circular dichroism (CD) thermal melting experiments, the RNA constructs demonstrated cooperative and reversible unfolding (**Figure S2.10**). The WT, CU, and CC A loop constructs had melting temperatures of 71.2 °C, 71.8 °C, and 69 °C, respectively (**Figure 2.3C** and **Table S2.7**) in low ionic conditions (methods). The slight decrease

in melting temperature in the CC oligo could be explained by increased base stacking between cytosine residues in the unfolded state[120]. Further, this data indicates that cytosine resides are only stabilizing when the A loop is in its mature conformation in the ribosome. The high melting temperatures also suggest that the A loop may retain its secondary structure in the ribosome at the high temperatures used for the heat treatment experiment, regardless of whether nucleotides 2554-2555 are UU, CU, or CC.

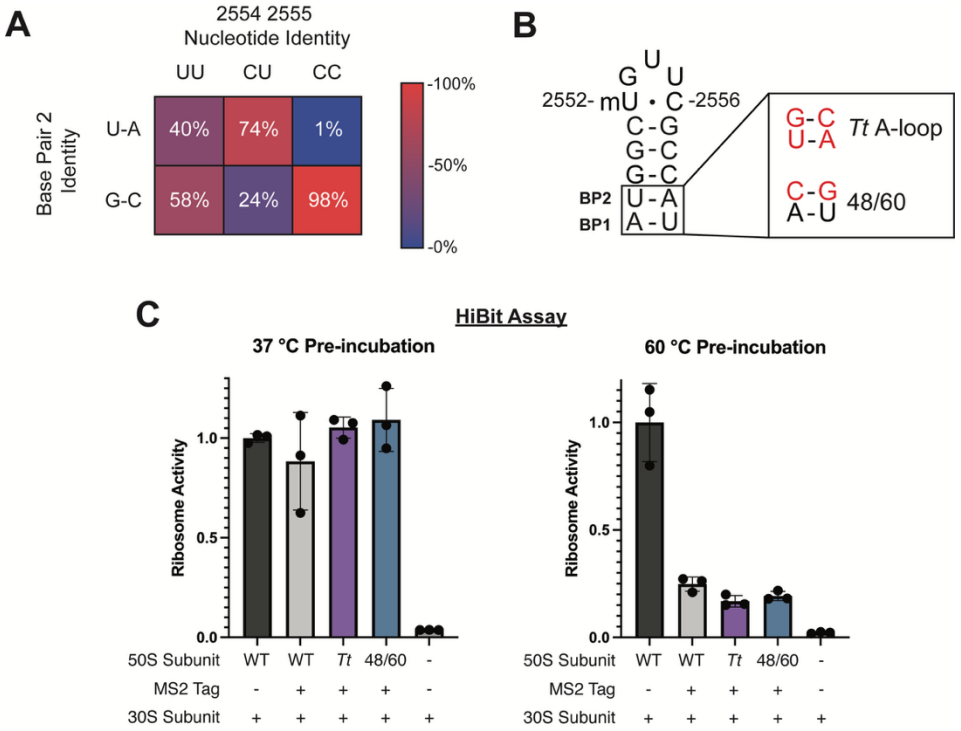


Figure 2.4. Effects of A-loop secondary structure variation on global 50S subunit stability. A) Distribution of archaeal 23S sequences from the SILVA database[82] based on nucleotide identity at positions 2554 and 2555 (top) and the identity of the base pair at position 2 (2548-2560) (left). The heatmap is colored to represent the percentage of each column that has either a U-A or G-C base pair. B) The helix of the *E. coli* A-loop was mutated to match that of *T. thermophilus* (top). A second A loop mutant (48/60) was designed to maintain interactions between the A-loop RNA stem and *E. coli* ribosomal protein uL14. C) 50S subunits were pre-incubated at 37 °C or 60 °C and then their relative activities were determined with the HiBit assay (data is represented as the mean of 3 replicates). WT and WT-Tag data (37 °C pre-incubation) is reproduced from Figure 3A. Error bars represent the standard deviation of three independent reactions.

Additional mutations at the base of the A loop RNA hairpin

In view of the global ribosomal stabilization conferred by CC mutations in the A loop, we also searched archaeal rRNA sequences for additional A loop sequence variation at other positions in the RNA hairpin. We found that most Archaea with the CC variation have a GC base pair between nucleotides 2548 and 2560 (base pair 2) (**Figure 2.4A** and **Figure S2.11**). This GC base pair is also present in over half of Archaea with uridines at positions 2554 and 2555, whereas *E. coli* has a less stable AU base pair at this position. As thermophilic organisms have increased rRNA GC content[80], we hypothesized that secondary structure variation at the base of the A loop might also serve to stabilize the ribosome. The base of the A-loop RNA helix interacts with ribosomal protein uL14, which varies significantly between Bacteria and Archaea in this region

and complicates incorporation of an Archaeal A loop helical sequence into the *E. coli* ribosome. Because of this, we also looked at the A loop of the thermophilic bacterium *Thermus thermophilus*. The *T. thermophilus* A loop also has a GC base pair at base pair 2, and the uL14-rRNA contacts in *E. coli* and *T. thermophilus* are more similar[105].

Based on Archaeal and *T. thermophilus* A-loop sequences, we designed two mutant *E. coli* 50S ribosomal subunits to test for global stability. The first incorporates the A-loop sequence from *T. thermophilus* (*Tt* A loop), which swaps the order of the A and U at base pair 1 and changes base pair 2 to a GC base pair. These changes are predicted to stabilize the secondary structure of the A loop hairpin (**Figure S2.12**). To maintain native uL14 interactions with the A loop, a second ribosome mutant, U2548C-A2560G (48/60), was prepared. With this design, base pair 2 of the A loop is changed to a GC base pair but pyrimidine bases are kept at positions 2548 and 2561 (**Figure 2.4B**). *E. coli* uL14 interacts with the pyrimidine O2 at those positions and the 48/60 mutant should preserve the native contacts. While the 48/60 mutant is predicted to be less stable than the *Tt* A loop mutant, it is predicted to afford more stability than the WT *E. coli* sequence (**Figure S2.12**). We assayed the thermostability of these mutants using the HiBit assay. As expected, these mutant ribosomes have full activity after pre-incubation at 37 °C indicating that the mutations do not affect the fold of the A loop (**Figure 2.4C**). After pre-incubation of the 50S subunits at 60 °C, the *Tt* A loop and 48/60 mutant ribosomes exhibit low activity, similar to that of the MS2-tagged WT ribosome control. These results indicate that these mutations in the RNA helix adjacent to the A loop do not confer additional stability to the WT ribosome on their own, in contrast to the stability afforded by U to C mutations in the apical loop.

CC mutations stabilize E. coli ribosomes with PTC mutations

Stabilization of the PTC could have utility in ribosome engineering where mutations are made in and around the PTC to allow for the incorporation of nonnatural amino acids or other monomers into proteins[59,61]. As CC mutations stabilize the 50S subunit from thermal denaturation, we posited that they could stabilize the PTC in the presence of other mutations. To investigate whether CC mutations stabilize ribosomes with PTC mutations, 50S ribosomal subunits carrying an A2451C point mutation or U2554C-U2555C-A2451C mutations (CC-A2451C) were purified using the MS2-tag purification. The A2451C point mutation was chosen because A2451 is a core PTC nucleotide that interacts directly with A76 of the P-site tRNA[121] and mutations at this position have been shown to greatly decrease the rate of peptide bond formation[122]. We found that the ribosomes with an A2451C mutation in the 23S rRNA have roughly 55% of WT activity (**Figure 2.5A**). We additionally find that subunits with CC-A2451C mutations are slightly less active than subunits with an A2451C mutation. However, after heat treatment at 60 °C, CC-A2451C subunits are more active than A2451C subunits and have roughly the same activity as WT subunits with an MS2 tag. This indicates that while the CC mutations do not increase the activity of A2451C subunits at 37 °C, they stabilize the A2451C 50S subunit. Additionally, we find that both A2451C and CC A2451C subunits form 70S subunits, in line with *in vitro* translation assays (**Figure 2.5B**).

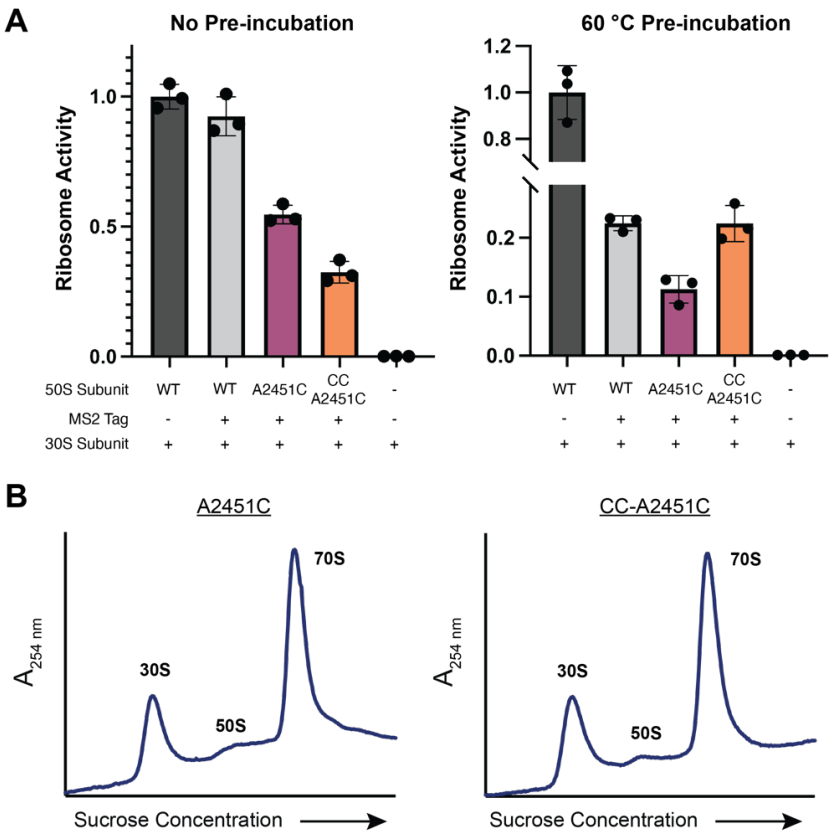


Figure 2.5. Robustness of the PTC in CC ribosomes. A) The relative activities of 50S subunits with an A2451C mutation or the triple mutation CC-A2451C were determined using the HiBit assay (data is represented as the mean of 3 replicates). Subunits were added directly (left) or pre-incubated at 60 °C (right) before addition to the HiBit assay. Error bars represent the standard deviation of three independent reactions. C) 70S formation by A2451C (left) and CC-A2451C 50S subunits (right).

2.5 Discussion

While the ribosome is highly conserved and contains universally conserved elements across all domains of life, hyperthermophiles have adapted their ribosomes to function at extreme temperatures. Here we find that the hyperthermophilic Archaea of the Thermoprotei class have adapted rare rRNA sequence variation in the catalytic center of the ribosome, in which cytidines are found at positions 2554 and 2555 in the A loop of 23S rRNA. Grafting U to C mutations at positions 2554 and 2555 in *E. coli* 23S rRNA stabilizes the 50S ribosomal subunit from thermal inactivation, consistent with CC variation serving a stabilizing role in certain hyperthermophilic Archaea. Consistent with our findings, some organisms in Thermoproteota have recently been shown to stabilize their tRNA through 2′ phosphorylation of a uridine residue, which highlights the need for stabilized translation machinery at high temperature[123].

CC sequence variation is only observed in the Thermoprotei class. This can be explained phylogenetically if the common ancestor of Nitrososphaeria and Thermoprotei developed the CC modification. This modification was advantageous for thermophilic Thermoprotei, while it may have slowly reverted in the mesophilic Nitrososphaeria to CU. It is notable that not all thermophilic Archaea and no thermophiles in the other domains of life acquired this variation. This suggests that there may be an evolutionary disadvantage of the CU and CC variation.

The cryo-EM structure of the CC mutant ribosome at 2.2 Å resolution revealed an unexpected change in the interaction between the mutant A loop and the A-site tRNA. In contrast to UU ribosomes, nucleotide C74 in the tRNA adopts the disfavored *syn* conformation when bound to the CC mutant ribosome, which may be a side effect of a change in the local electronic environment by the U to C mutations. *Syn* pyrimidines are exceptionally rare and are more commonly found in the aptamer binding domains and catalytic sites of RNAs[116]. The *syn*-C74 in the A-site tRNA, at lower temperatures such as those tested with the *E. coli* ribosome, may lead to slight translation defects, which we were unable to detect in bulk translation assays, and could explain why CC A loop mutations are not more prevalent. Additionally, it is possible that the *syn* conformation is less populated at the high growth temperatures of Thermoproteota and therefore less problematic for hyperthermophiles. During cryo-EM processing we identified a highly populated A-site tRNA class that has a disordered acceptor stem. This may indicate that the CC ribosome is deficient in A-site tRNA binding. In yeast, a pseudouridine to cytidine mutation at nucleotide 2554 (*E. coli* numbering) decreased tRNA binding to the ribosome[124]. It is also possible that a *syn*-C74 may interfere with tRNA translocation after peptide bond formation. When tRNA docks in the ribosomal P site, C74 directly base pairs with G2252 in the large subunit rRNA P loop. This base pair would require the *syn*-C74 in the A site tRNA to flip back to the *anti*-conformation when it translocates to the P site, which could present a hurdle for proper P-site docking. However, tRNAs with mutations at position 74 are still accepted as substrates by the ribosome, which indicates that the C74-G2552 interaction is not essential for translation[74,125]. This suggests that a tRNA containing a *syn*-C74 could be translocated by the ribosome with little difficulty.

It is striking that modest pyrimidine to pyrimidine substitutions at only two positions can globally stabilize the 50S ribosomal subunit, a 1.5 Mda particle. CD melting experiments demonstrate that the secondary structure of the RNA hairpin containing the A loop is not stabilized by U to C mutations. Therefore, the observed stabilization of the mutant 50S subunit likely arises from enhanced tertiary interactions in the A loop that only form within the ribosome. This is consistent with a prior structural analysis of an isolated A loop RNA hairpin, which differs from the structure of the A loop within the 50S ribosomal subunit, especially in the apical loop[126]. The A loop rRNA helix has a high melting temperature outside of the ribosome (71.2 °C), which suggests that the A loop helix may stay folded in the ribosome even at high temperatures. Additionally, mutations in the A loop predicted to stabilize the secondary structure of the rRNA helix had no additional impact on the global thermal stability of the 50S subunit. Taken together, these data suggest that the stability of A-loop secondary structure may not be as important for global ribosome stability as its tertiary structure. It has been shown that residues in cytosine-rich RNA loops remain partially stacked[120]. Therefore, cytosine base stacking may lead to tertiary stabilization of the mature A loop as cytosine residues have lower base stacking free energies than uracil residues[127,128]. Since the A loop is part of the last region of 23S rRNA to fold during 50S subunit maturation[129], this region could be involved in the initial stages of unfolding of 50S subunits. Consequently, the stability of the A loop would in part define the stability of the PTC and the 50S subunit globally.

Protein engineering can benefit from a thermostable scaffold, which can better withstand the incorporation of destabilizing mutations that are needed to evolve new functionality[67]. For example, chimeric proteins that incorporate protein domains from thermophilic archaea have been used to improve engineering of *E. coli* aminoacyl-tRNA synthetases[130]. Here, we show that rare sequence variation in highly conserved regions of rRNA from thermophilic organisms can stabilize

the *E. coli* ribosome. The CC mutant *E. coli* ribosome does not have an observable growth defect *in vivo* and is able to translate both small peptides and full proteins *in vitro*. Previous computationally designed ribosomes with mutations in the A loop had severe defects in ribosome activity[131]. In contrast, the mutations examined here, including those in the stem of H92, lead to highly functional ribosomes, which is likely due to the preservation of conserved A loop nucleotides. The use of natural rRNA sequence variation to engineer beneficial properties into the bacterial ribosome could be a useful strategy as these sequences are known to lead to robust ribosomes that function in diverse environments. While mutating the PTC has allowed for the incorporation of non-proteinogenic monomers by the ribosome, PTC mutations can have a severely destabilizing effect[65,91]. We show that CC mutations stabilize ribosomes at high temperatures in the context of a destabilizing MS2 tag. The CC mutations in the A loop may therefore have utility in future engineering of ribosomes capable of improved synthesis of non-proteinogenic polymers[51,132].

2.6 Supplementary Information

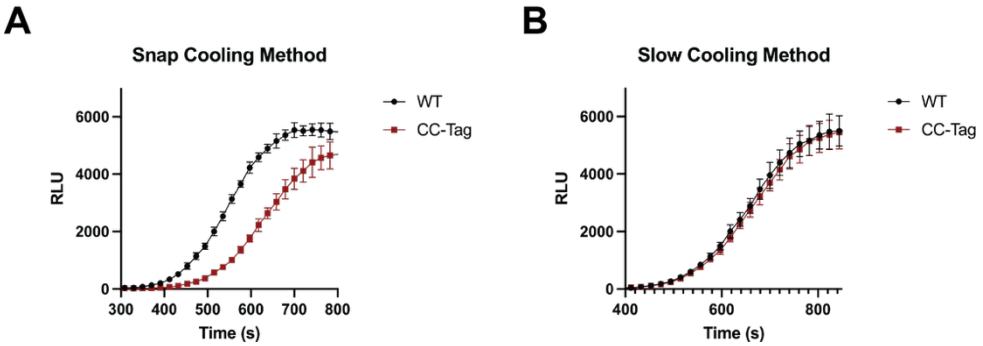


Figure S2.1. HiBit translation assay for untagged WT and MS2-tagged CC 50S ribosomes. Ribosomes were pre-incubated at 50 °C for 30 minutes and then cooled quickly on ice (left) or allowed to cool more slowly by incubating at room temperature for an additional 30 minutes (right).

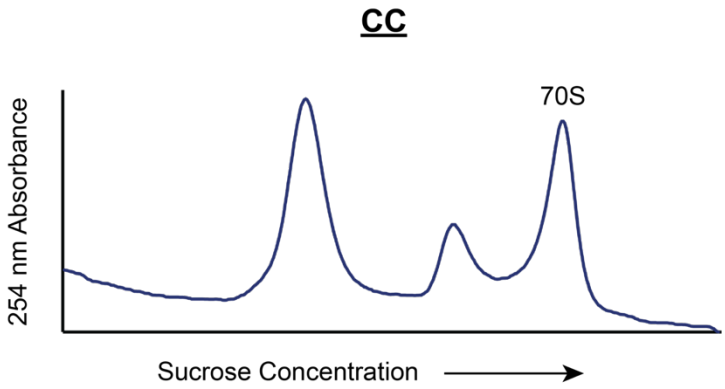


Figure S2.2. Association gradient of CC mutant 50S and WT *E. coli* 30S subunits. 30S subunits (2 equiv.) and 50S subunits (1equiv.) were incubated with 10 mM $MgCl_2$ and resolved on a 15-40% sucrose gradient. 70S fractions were collected for cryo-EM analysis.

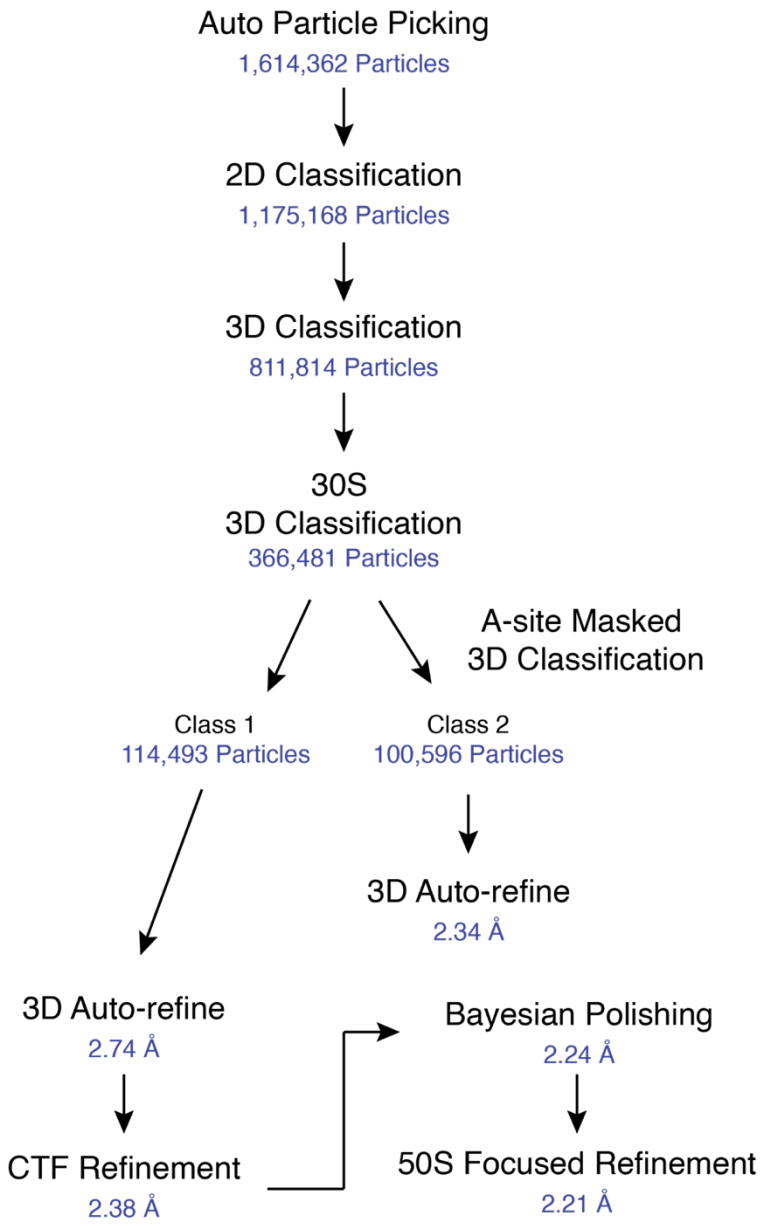


Figure S2.3. Cryo-EM processing workflow. A-site Class 1 had density for the tRNA 3′-CCA end and was further refined. Class 2 lacked density for the A-site tRNA 3′-CCA end.

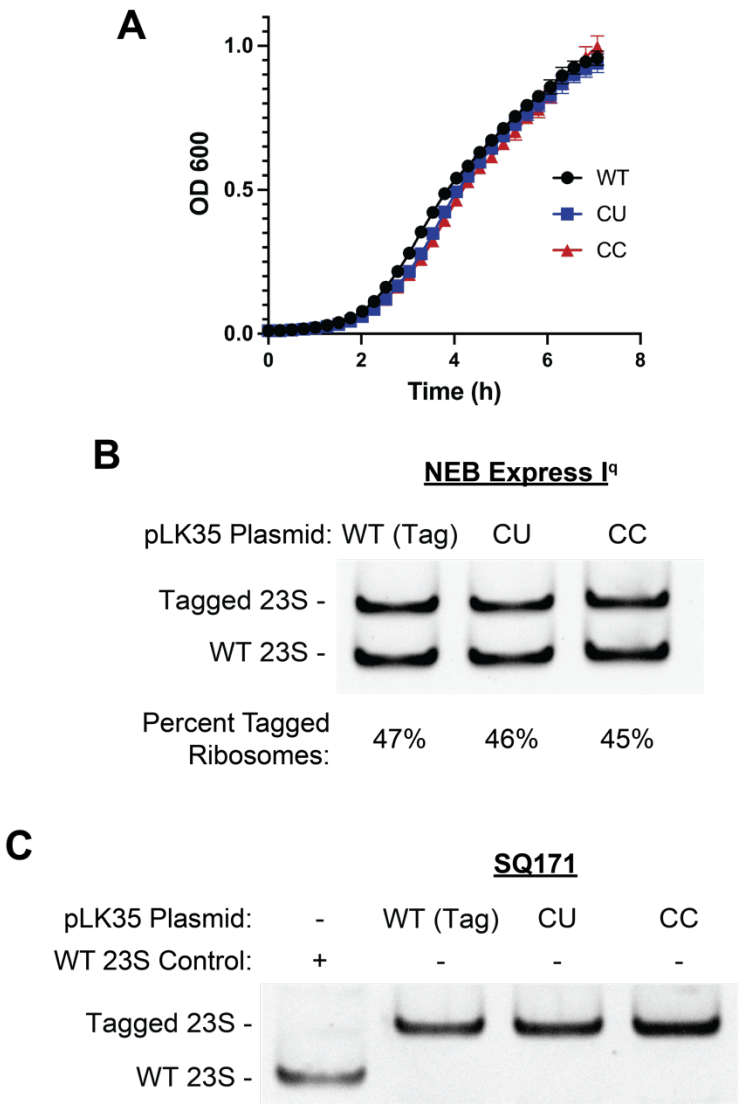


Figure S2.4. Effects of Mutant A loop Sequences on *E. Coli* Growth. A) Growth curves of *E. coli* Express I^q cells which express both plasmid encoded and genomically encoded ribosomes (data is represented as the mean of 3 replicates). Error bars represent the standard deviation of three independent replicates. The plasmid-encoded 23S rRNA harbors an MS2 tag. B) Following *E. coli* growth assays, the ratio of MS2-tagged ribosomes to WT endogenous ribosomes was determined. RT-PCR samples were run on a 10% polyacrylamide-TBE gel. DNA containing an MS2 tag sequence is 32 bp larger than DNA with the native 23S sequence. Amplified bands were quantified to determine the percent of MS2-tagged ribosomes. C) Ribosomes from *E. coli* strain SQ171 were subjected to RT-PCR to confirm that only plasmid encoded (MS2 tag) ribosomes were expressed during growth experiments (**Figure 2.2A**).

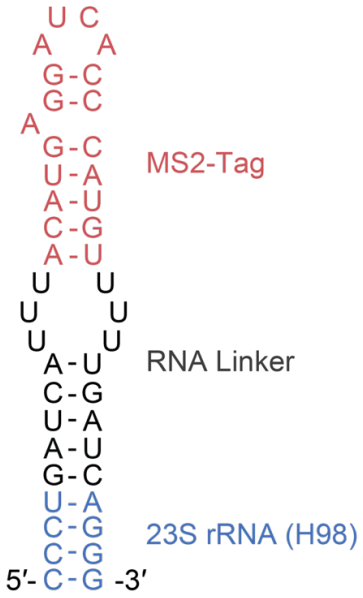


Figure S2.5. MS2-Tag design used in this study. The MS2 tag is inserted into rRNA helix H98 in the 50S *E. coli* ribosome. The H98 stem is elongated and the MS2 stem loop is attached with a poly-U linker.

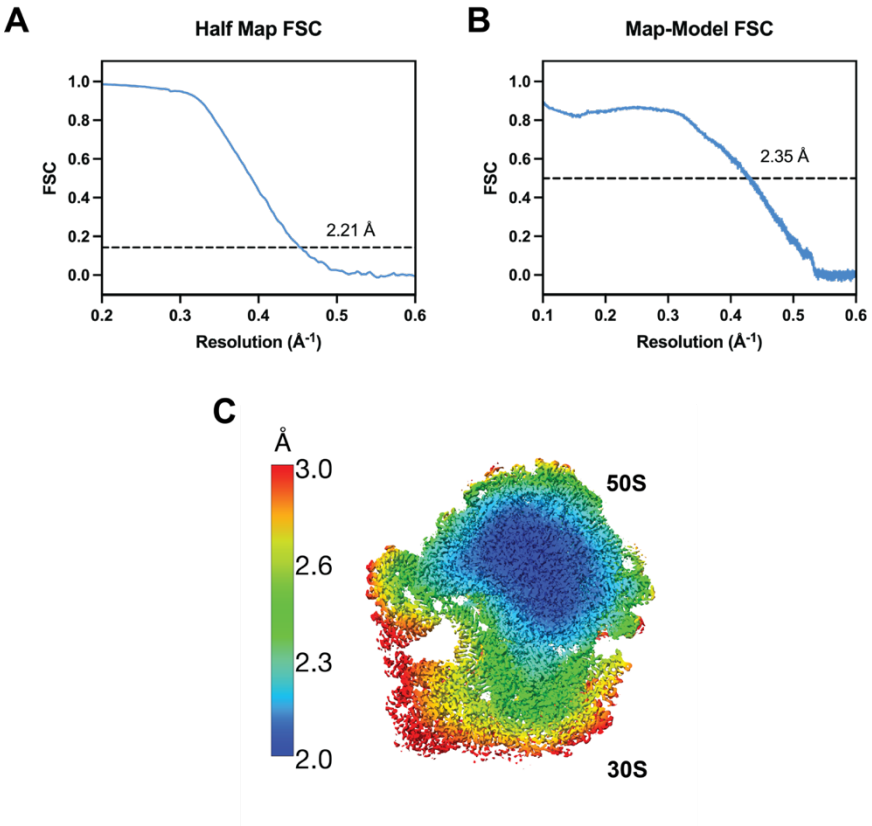


Figure S2.6. Resolution of the cryo-EM map generated from the particles in Class I. The global 70S ribosome A) half map FSC resolution is 2.21 Å and B) map to model FSC resolution is 2.35 Å. C) Local resolution is plotted on the 70S ribosome map.

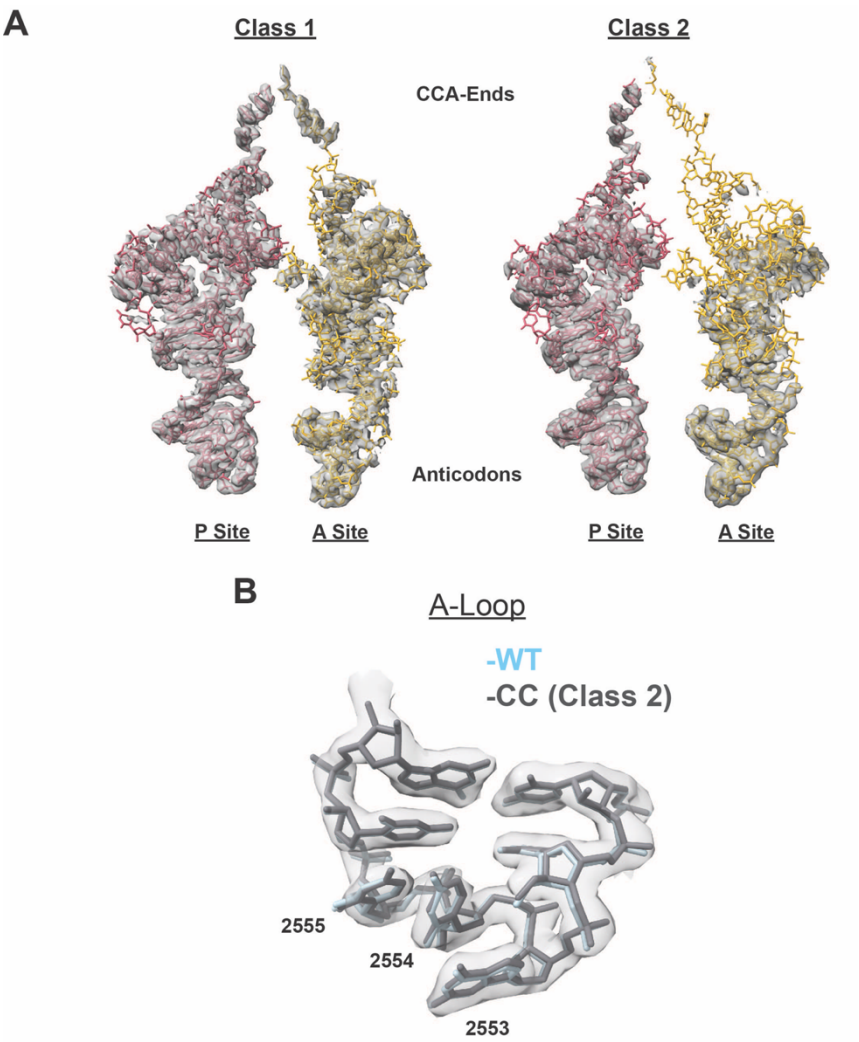


Figure S2.7. Features of the tRNAs in A-site classes 1 and 2. A) P-site and A-site tRNA model and cryo-EM density for A-site class 1 (left) and class 2 (right). Class 2 corresponded to an A-site tRNA class that lacked density for most of the acceptor stem. A B-factor of 30 $Å^2$ was applied to the cryo-EM maps. B) Cryo-EM density and model for the A-loop from Class 2 are shown in grey. The model from a WT ribosome structure[106] is shown in light blue.

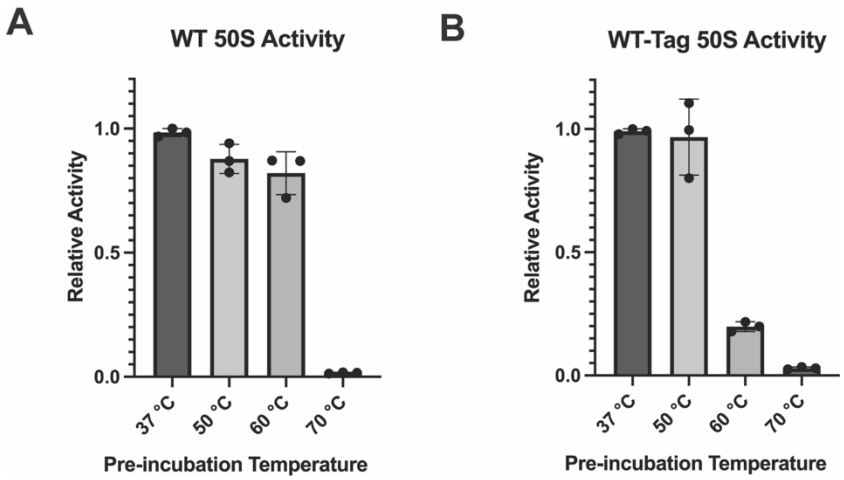


Figure S2.8. Activity of heat-treated 50S subunits without and with the MS2 tag. A) Untagged and B) MS2-tagged WT 50S ribosomes were pre-incubated at the indicated temperatures for 30 minutes and then slow cooled for 30 minutes. The 50S ribosomes were then used in the HiBit translation assay (data is represented as the mean of 3 replicates). Error bars represent the standard deviation of three reactions.

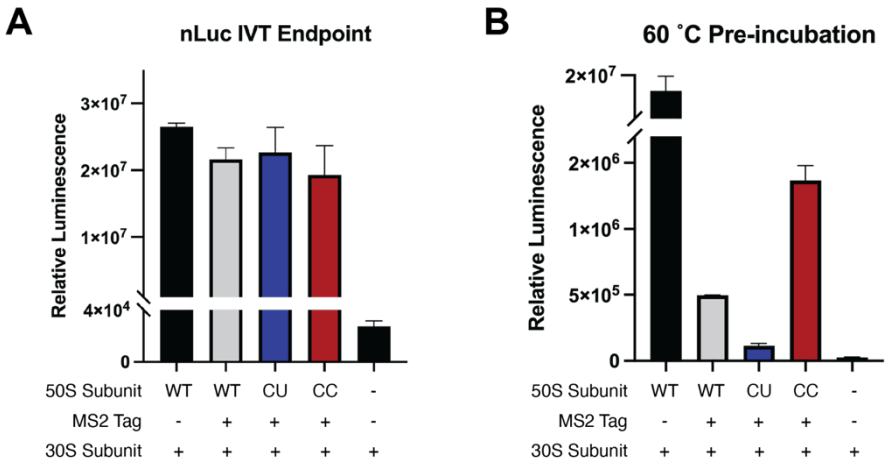


Figure S2.9. Activity of ribosomes in nLuc translation endpoint assays. A) Replicate of an nLuc IVT endpoint assay at 37 °C for CU and CC ribosomes. B) 50S ribosomes were preincubated at 60 °C and cooled slowly. Their relative activities were then determined with the nLuc endpoint assay.

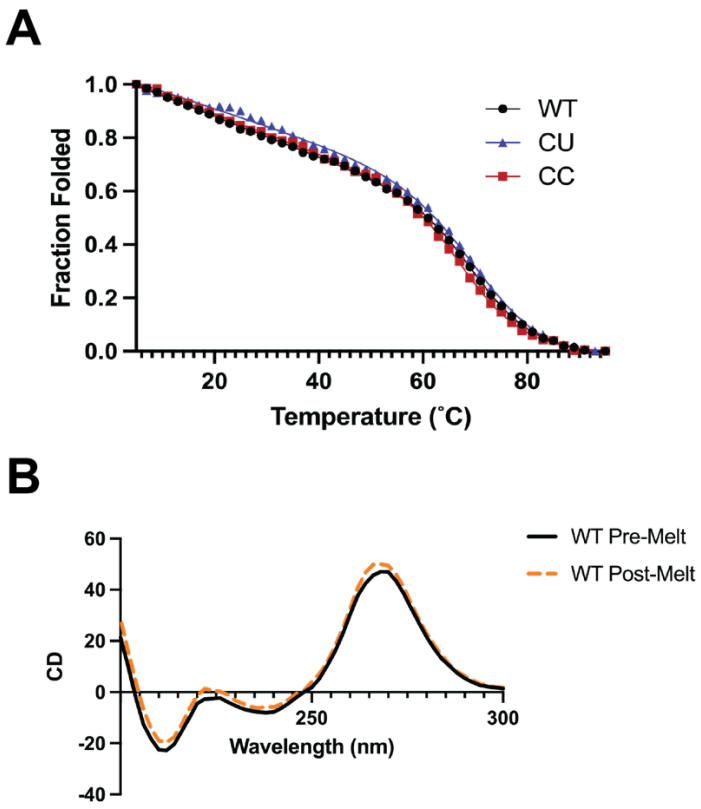


Figure S2.10. CD unfolding of A-loop RNA constructs. A) Full CD unfolding data from 5 to 95 °C. RNA constructs demonstrated cooperative two-state unfolding. B) CD wavelength scans from 300 to 200 nm of the WT A-loop construct before the melting experiment (black) and after the melting experiment (orange). The similarity of the curves implies reversible unfolding of the RNA during melting experiments.

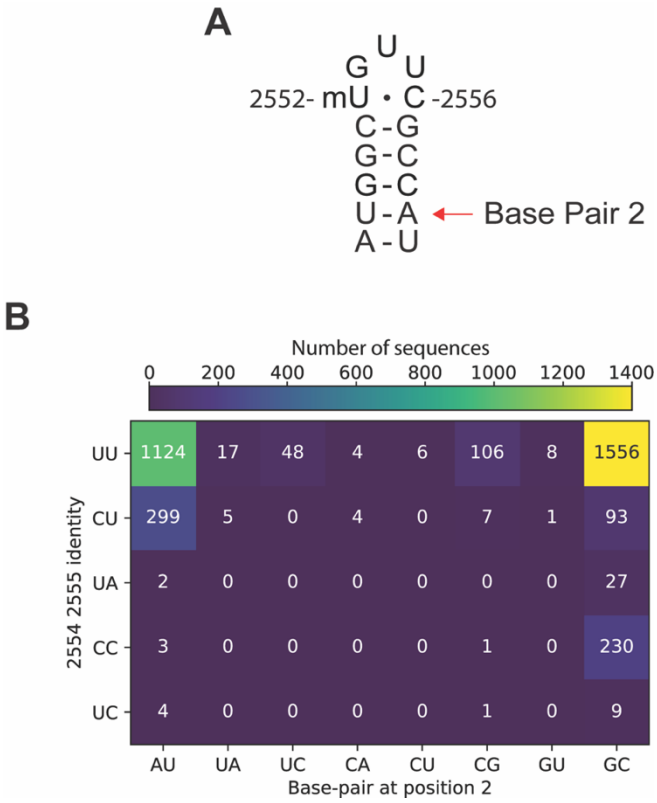


Figure S2.11. Archaeal sequences at the base of their A-loop. A) Base pair 2 (2548-2560) is highlighted on the secondary structure of the *E. coli* A-loop. B) Distribution of archaeal sequences in the SILVA database based on 2554/2555 and base pair 2 identity. The left axis classifies Archaea based on the identity of nucleotides at positions 2554 and 2555. The main populations are UU, CU, and CC. The bottom axis classifies Archaea based on the nucleotide identity at base pair 2 in the A-loop. Almost all Archaea with cytidines at positions 2554 and 2555 have a GC base pair at position 2. Around half of Archaea with uridines at positions 2554 and 2555 also have a GC base pair at position 2.

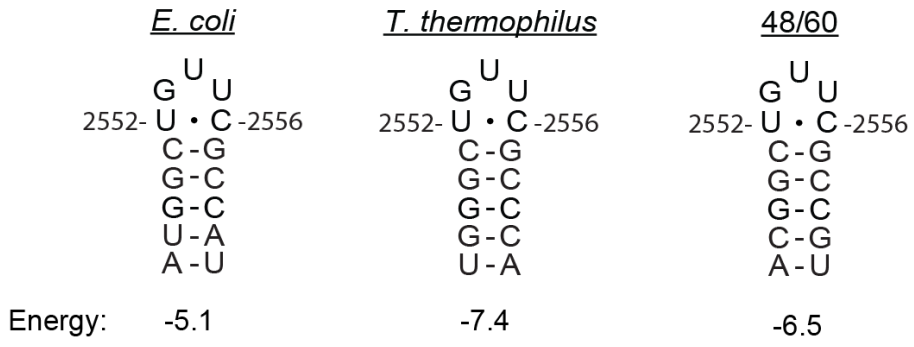


Figure S2.12. Secondary structures and predicted minimum free energies of A-loop mutants. *T. thermophilus* has variation at the base of the A-loop that stabilize its secondary structure. The 48/60 mutant was designed to stabilize the base of the A-loop while leaving pyrimidine bases at positions 2548 and 2561 to maintain contacts with ribosomal protein uL14. Relative minimum free energies were calculated in RNAstructure[133].

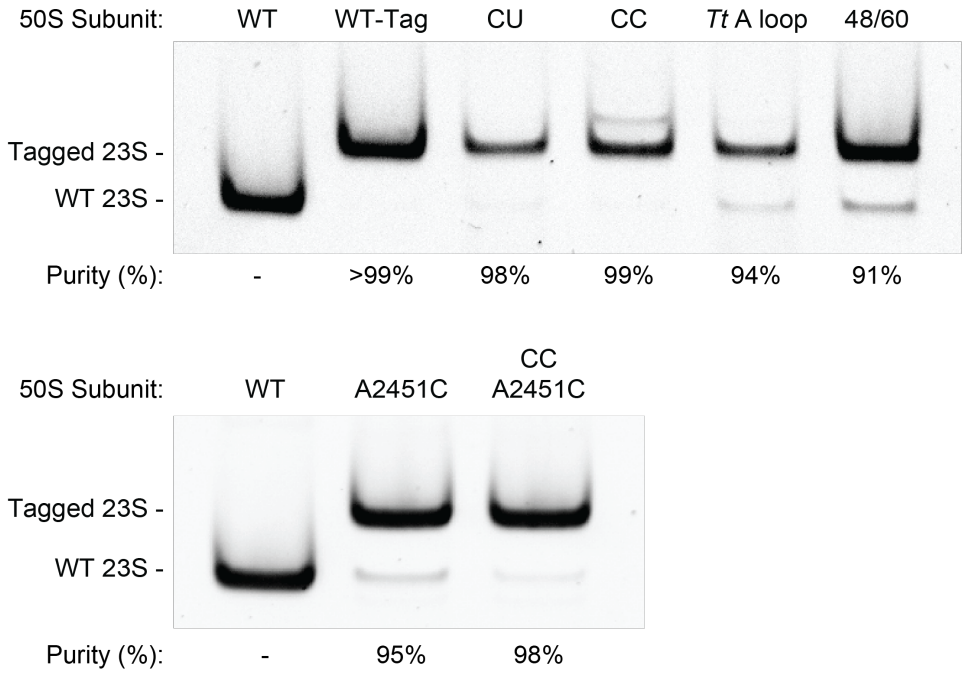


Figure S2.13. Purity of 50S subunits used for *in vitro* assays. After MS2 purification, 23S rRNA was isolated from 50S subunits and used for RT-PCR analysis. DNA containing an MS2 tag sequence is 32 bp larger than DNA with the native 23S sequence. RT-PCR products were run on a 10% polyacrylamide-TBE gel, and band intensities were used to quantify ribosome purity.

Table S2.1. Additional growth temperatures for archaeal taxa

Name	Strain	TaxID	Taxonomy	Growth Temperature	Source
Nitrosopelagicus brevis	CN25	1410606	Archaea;Thaumarchaeota	22 °C	[134]
Nitrosotalea devanaterra	-	1078905	Archaea;Thaumarchaeota	25 °C	[135]
Nitrosotenuis aquarius	-	1846278	Archaea;Thaumarchaeota	33 °C	[136]
Nitrosocaldus islandicus	-	1846278	Archaea;Thaumarchaeota; Nitrososphaeria	65 °C	[137]
Nitrosocosmicus franklandus	C13	1798806	Archaea;Thaumarchaeota; Nitrososphaeria; Nitrososphaerales; Nitrososphaeraceae	37.5 °C	[138]
Caldiarchaeum subterraneum	-	1798806	Archaea;Thaumarchaeota	70 °C	[139]

Table S2.2. DNA primers used in chapter 2
(m denotes 2'-O-Me; lowercases in the sequence indicate sites where mutations are introduced)

Primer name	Sequence	Comment
U2554C_F	GGTATGGCTGcTCGCCATTTA	Forward primer for U2554C 23S rRNA mutagenesis
U2554C_R	CTTGGGACCTACTTCAGC	Reverse primer for U2554C 23S rRNA mutagenesis
U2554/5C_F	GGTATGGCTGccCGCCATTTAAAG	Forward primer for U2554C U2555C 23S rRNA mutagenesis
U2554/5C_R	CTTGGGACCTACTTCAGC	Reverse primer for U2554C U2555C 23S rRNA mutagenesis
A2058G_F	GGCAAGACGGgAAGACCCCGT	Forward primer for A2058G 23S rRNA mutagenesis
A2058G_R	GCGGGTACACTGCATCTTC	Reverse primer for A2058G 23S rRNA mutagenesis
Tt_Aloop_F	TCGCCcaTTAAAGTGGTACGCGAGC	Forward primer for A2547U U2548G A2560C U2561A 23S rRNA mutagenesis (*Tt* A loop)
Tt_Aloop_R	ACAGCCcaACCCTTGGGACCTACTTC	Reverse primer for A2547U U2548G A2560C U2561A 23S rRNA mutagenesis (*Tt* A loop)
48/60_Aloop_F	TCGCCgTTTAAAGTGGTACGCGAG	Forward primer for U2548C A2560G 23S rRNA mutagenesis (48/60)
48/60_Aloop_R	ACAGCCgTACCCTTGGGACCTACTT	Reverse primer for U2548C A2560G 23S rRNA mutagenesis (48/60)
A2451C_F	TCCGGGGATAcCAGGCTGATA	Forward primer for A2451C 23S rRNA mutagenesis
A2451C_R	GTACCTTTTATCCGTTGAGC	Reverse primer for A2451C 23S rRNA mutagenesis
MS2_quant_F	CTTGCCCCGAGATGAGTTCTCCC	RT-PCR primer for the ribosome purity assay
MS2_quant_R	GTACCGGTTAGCTCAACGCATCGCT	Primer for amplification of cDNA in the ribosome purity assay
HiBit Template	GCGAATTAATACGACTCACTATAGGGTTAACT TTAACAAGGAGAAAAACATGGTGAGCGGCTG GCGCCTGTTTAAAAAAATTAGCTAACTAGCAT AACCCCTCTCTAAACGGAGGGGTTTAGTCA	DNA template for the HiBit peptide
HiBit_amp_F	GCGAATTAATACGACTCACTATAG	Forward amplification primer for the HiBit template
HiBit_amp_R	AAACCCCTCCGTTTAGAG	Reverse amplification primer for the HiBit template
$tRNA^{fMET}$ Template (C1G)	AATTCCTGCAGTAATACGACTCACTATAGGCG GGGTGGAGCAGCCTGGTAGCTCGTCGGGCTC ATAACCCGAAGGTCGTCGGTTCAAATCCGGC CCCCGCAACC	DNA template for $tRNA^{fMet}$ C1G -A
fMet_amp_F	AATTCCTGCAGTAATACGACTCAC	Forward amplification primer for the $tRNA^{fMet}$ template
fMet-A_amp_R	mGmGTTGCGGGGGCC	Reverse amplification primer for the $tRNA^{fMet}$ template

Table S2.3. RNA oligos (IDT) used in chapter 2. (m denotes 2'-*O*-Me)

Name	Sequence
WT A loop	AUGGCmUGUUCGCCAU
CU A loop	AUGGCmUGCUCGCCAU
CC A loop	AUGGCmUGCCCGCCAU

Table S2.4. Cryo-EM data collection and processing

Magnification	105,000
Voltage (kV)	300
Electron Exposure ($e^-/Å^2$)	40
Defocus Range (μm)	-0.5/-1.5
Pixel Size (Å)	0.8279
Symmetry Imposed	C1
Initial Particle Images	1,614,362
Final Particle Images	114,493
Map Resolution (Å)	2.21
FSC Threshold	0.143

Table S2.5. Model refinement statistics

Model component	
Model resolution (Å)	2.35
FSC threshold	0.5
Map sharpening *B* factor (Å^2)	-38.8
Model composition	
Non-hydrogen atoms	148866
Mg^{2+} ions	268
Zn^{2+} ions	2
Polyamines	17
Waters	6756
Ligands (paromomycin)	1
Mean *B* Factors (Å^2)	
RNA	15.98
Protein	15.81
Waters	8.73
Other	10.56
R.m.s. deviations from ideal values	
Bond (Å)	0.005
Angle (°)	0.762
Molprobity all-atom clash score	8.93
Ramachandran plot	
Favored (%)	96.37
Allowed (%)	3.58
Outliers (%)	0.05
RNA validation	
Angles outliers (%)	0.004
Sugar pucker outliers (%)	0.2
Average suiteness	0.587

Table S2.6. Doubling times for *E. coli* expressing plasmid encoded ribosome mutants

***E. coli* Strain**	**pLK35 Plasmid Sequence**	**Doubling Time (m)**
NEB Express I^q	WT	36.0 ± 0.6
NEB Express I^q	CU	35.7 ± 0.3
NEB Express I^q	CC	38.4 ± 0.6
SQ171	WT	60 ± 1
SQ171	CU	66 ± 3
SQ171	CC	61 ± 2

Table S2.7. Thermodynamic parameters derived from CD melting experiments for A-loop RNA constructs.[+]

Construct	T_m (° C)	ΔH_{unfold} (kJ/mol)	ΔG_{25}[++] (kJ/mol)
WT	71.8 ± 0.6	197 ± 9	26.8 ± 0.9
CU	71.8 ± 0.1	189 ± 2	25.7 ± 0.3
CC	69.0 ± 0.2	183 ± 8	23.6 ± 1.2

+ Errors are reported as the S.D. of two experimental replicates.
++ ΔG_{25} is the Gibbs free energy of unfolding at 25 °C.

Chapter 3: Interactions between terminal ribosomal RNA helices stabilize the *E. coli* large ribosomal subunit

Reproduced from: Nissley, A. J., Kamal, T. S. & Cate, J. H. D. Interactions between terminal ribosomal RNA helices stabilize the *E. coli* large ribosomal subunit. *RNA* **29**, 1500–1508 (2023).

3.1 Abstract

The ribosome is a large ribonucleoprotein assembly that uses diverse and complex molecular interactions to maintain proper folding. *In vivo* assembled ribosomes have been isolated using MS2-tags installed in either the 16S or 23S ribosomal RNAs (rRNAs), to enable studies of ribosome structure and function *in vitro*. RNA tags in the *Escherichia coli* 50S subunit have commonly been inserted into an extended helix H98 in 23S rRNA, as this addition does not affect cellular growth or *in vitro* ribosome activity. Here, we find that *E. coli* 50S subunits with MS2 tags inserted in H98 are destabilized compared to wild type (WT) 50S subunits. We identify the loss of RNA-RNA tertiary contacts that bridge helices H1, H94, and H98 as the cause of destabilization. Using cryogenic electron microscopy (cryo-EM), we show that this interaction is disrupted by the addition of the MS2 tag and can be restored through the insertion of a single adenosine in the extended H98 helix. This work establishes ways to improve MS2 tags in the 50S subunit that maintain ribosome stability and investigates a complex RNA tertiary structure that may be important for stability in various bacterial ribosomes.

3.2 Introduction

The ribosome is a large ribonucleoprotein assembly responsible for protein synthesis in the cell. Due to its complexity, the ribosome is composed of intricate networks of RNA-protein and RNA-RNA interactions[140]. These complex interactions are formed during ribosome assembly, which is a process requiring ribosomal RNA (rRNA), ribosomal proteins (rProteins), and many auxiliary assembly factors[141]. In *Escherichia coli* (*E. coli*), the three rRNAs–5S, 16S, and 23S–are all transcribed as a single transcript. During the early stages of ribosomal large subunit (LSU) assembly, sequences flanking the 5′ and 3′ ends of the pre-23S rRNA transcript base-pair to form the leader trailer (LT) helix[142]. The LT helix is then subsequently cleaved by several Rnases, and the remaining RNA helix comprises helix 1 (H1) of the pre-23S rRNA[143–145]. Additionally, it has been shown that some bacteria remove H1 post-assembly and this removal is correlated with the evolutionary loss of H98[146], which suggests a synergistic role between the two helices.

The use of affinity tags in the 23S rRNA has enabled the *in vitro* study of *in vivo*-assembled LSUs with mutations in 23S rRNA. This has commonly been achieved through the insertion of an RNA helix from the genome of the MS2 bacteriophage into helix H98 of the 23S rRNA on the surface of the ribosome[89]. Tagged mutant ribosomal subunits can then be purified using the MS2 coat protein dimer that selectively binds to the MS2 RNA helix[147]. MS2 tags inserted in H98 of 23S rRNA have been used extensively to enable the investigation of rRNA function[119,122], in engineered ribosomes[66], and for *in vivo* ribosome tracking[118]. Although *E. coli* 50S ribosomal subunits with MS2 tags inserted into H98 retain wild-type (WT) *in vivo* and *in vitro* function, we previously showed that these 50S subunits have lower thermostability compared to WT 50S subunits[148].

Here we Investigate the loss of thermostability In the *E. coli* LSU upon addition of an MS2 tag into H98. We find that RNA contacts between nucleotides at the interface of rRNA helices H1, H94, and H98 are important for the stability of the *E. coli* 50S ribosomal subunit. Using cryo-EM, we show that this interaction is disrupted by the addition of previous MS2 tag designs in H98 and

that the addition of a single adenosine residue in the tag can restore the tertiary interaction and WT levels of stability. The MS2-tags described herein offer an improved method for studying mutant and engineered ribosomes without the introduction of additional instability. Moreover, tertiary interactions between helices at the terminal ends of 23S rRNA corresponding to H1, H94, and H98 are found in many bacteria and these likely play stabilizing roles in a variety of bacterial ribosomes.

3.3 Materials and methods

Cloning and plasmid design

A modified pLK35 plasmid[88], containing a tac promoter followed by the rrnB operon, which encodes the MS2-tagged 23S rRNA, was used for mutagenesis. Point mutations, insertions, and deletions were made using either the Q5 mutagenesis kit (NEB) or the InFusion cloning kit (Takara Bio) and the corresponding primer sets (**Table S3.1**). MS2 tags inserted in H98 were placed between 23S rRNA bases 2796 and 2800, with the concomitant removal of nucleotides 2797-2799. To insert an MS2 tag into H25, the MS2-V2 sequence was placed between 23S rRNA bases 544 and 549, with the removal of nucleotides 545-548. The following DNA sequences were inserted for each tag design:

MS2-V1: 5′-ACTAGTTTTGATGAGGATTACCCATCTTTACTAGT-3′
MS2-V2: 5′-GATCATTTACATGAGGATCACCCATGTTTTTGATC-3′
MS2-V3: 5′-GATCATTTACATGAGGATCACCCATGTTTTTGATCA-3′

Ribosome expression and purification

Mutant *E. coli* 50S ribosomal subunits were expressed and purified as previously described[148]. Briefly, *E. coli* NEB Express I^q cells were transformed with the corresponding pLK35 plasmid. Transformants were grown in 3 L of LB broth containing 100 μg/mL ampicillin at 37°C. Cultures were induced with 0.5 mM isopropyl β-D-1-thiogalactopyranoside once they reached OD_{600}=0.6 and were incubated for an additional 3 hours. Cells were pelleted, resuspended in 50 mL buffer A (20 mM Tris-HCl pH 7.5, 100 mM NH_4Cl, 10 mM $MgCl_2$, 0.5 mM EDTA, 2 mM dithiothreitol (DTT)) with Pierce protease inhibitor (ThermoFisher), and lysed by sonication. The lysate was clarified by centrifugation and then loaded onto a sucrose cushion containing 24 mL of buffer B (20 mM Tris-HCl pH 7.5, 500 mM NH_4Cl, 10 mM $MgCl_2$, 0.5 mM EDTA, 2 mM DTT) with 0.5 M sucrose and 17 mL of buffer C (20 mM Tris-HCl pH 7.5, 60 mM NH_4Cl, 6 mM $MgCl_2$, 0.5 mM EDTA, 2 mM DTT) with 0.7 M sucrose in Type 45 Ti tubes (Beckman-Coulter). Ribosomes were pelleted by centrifugation at 27,000 rpm (57,000 xg) for 16 hours at 4°C. The pellets were then resuspended in dissociation buffer (buffer C with 1 mM $MgCl_2$), which dissociates 70S ribosomes into 30S and 50S subunits.

MS2-tagged 50S subunits were then purified using a maltose binding protein (MBP)-MS2 fusion protein, which was purified as previously described[66]. A 5 mL MBP Trap column (Cytiva) at 4°C was washed with 5 column volumes (CV) of MS2-150 buffer (20 mM HEPES pH 7.5, 150 mM KCl, 1 mM EDTA, 2 mM 2-mercaptoethanol) and then 10 mg of MBP-MS2 protein was loaded slowly onto the column. The column was then washed with 5 CV of buffer A-1 (buffer A with 1 mM $MgCl_2$), and crude ribosomes were loaded onto the column. The column was washed with 5 CV of buffer A-1, 10 CV of buffer A-250 (buffer A with 250 mM NH_4Cl and 1 mM $MgCl_2$), and then tagged ribosomal subunits were eluted with a 10 CV gradient of 0-10 mM maltose in buffer A-1. The purified 50S subunits were concentrated in 100 kDa cut off spin filters (Millipore), quantified with an approximation of 1 A_{260}= 36 nM, and flash frozen in liquid nitrogen. WT untagged 30S and 50S ribosomal subunits were purified as previously described[148].

Mutant ribosome purity assay

To determine the levels of WT untagged 50S subunit contamination after mutant ribosome purification, semiquantitative PCR was utilized as previously described[66] with adaptations. Roughly 50 pmol of purified mutant ribosomes were denatured at 95°C for 3 minutes. LiCl was added to a final concentration of 5 M to precipitate the rRNA, which was subsequently resuspended in Rnase-free water. Primers MS2_H98_quant_R or MS2_H25_quant_R, for mutant ribosomes with MS2 tags in either H98 or H25 respectively, were used to reverse transcribe a region of 23S rRNA using AMV reverse transcriptase (Promega). The region of cDNA containing the MS2 tag was amplified via PCR using primer pairs MS2_H98_quant_F and MS2_H98_quant_R or MS2_H25_quant_F and MS2_H25_quant_R. PCR products were resolved on a 10% polyacrylamide-TBE gel (Invitrogen) and visualized with SYBR gold stain (ThermoFisher). DNA bands were quantified with ImageJ software[93].

In vitro nanoluciferase translation endpoint assay

50S subunits were diluted to 1.4 μM in buffer A with a final concentration of 10 mM $MgCl_2$. The diluted subunits were incubated for 15 minutes at the indicated temperature and then incubated for an additional 15 minutes at room temperature to cool. An *in vitro* translation reaction was then assembled using the PURExpress system (NEB) with the following: 3.2 μL solution A (NEB), 1 μL factor mix (NEB), 250 nM pre-incubated 50S subunit, 500 nM WT 30S subunit, 1 U/μL Rnase inhibitor (NEB), and 10 ng/μL of a plasmid containing a T7 promoter followed by the nanoluciferase (nLuc) gene (final volume of 8 μL). The reaction was incubated for 1 hour at 37°C and then 2 μL of the reaction was mixed with 30 μL of nLuc buffer (20 mM HEPES pH 7.5, 50 mM KCl, and 10% glycerol) and a 1:50 dilution of Nano-Glo substrate (Promega). All 32 μL were then placed in a 384 well plate and luminescence was measured in a Spark Plate Reader (Tecan). Experimental triplicates were measured and averaged for each *in vitro* translation reaction.

MetRS and MTF expression and purification

Plasmids containing a T7 promoter followed by the gene for *E. coli* methionyl-tRNA synthetase (MetRS) or methionyl-tRNA formyltransferase (MTF) and a 6x-His tag were transformed into *E. coli* BL21 (DE3) Codon+ RIL cells. Overnight cultures were diluted in ZYM-5052 autoinducing media[97] and grown overnight at 37°C. Cells were then pelleted by centrifugation, resuspended in lysis buffer (20 mM Tris pH 7.8, 150 mM NaCl, 5 mM imidazole, 0.5 mM EDTA), and lysed by sonication. The lysate was clarified by centrifugation at 25,000 xg (JA-20 rotor, Beckman) at 4°C for 30 minutes. The supernatant was applied to a 5 mL HisTrap column (Cytiva) at 4°C and the column was washed with 5 CV of lysis buffer with 23 mM imidazole. Protein was eluted from the column using a linear gradient of 20 CV lysis buffer from 23-500 mM imidazole. The eluted protein was then dialyzed against 50 mM HEPES pH 7.5, 100 mM KCl, 10 mM $MgCl_2$, 7 mM β-mercaptoethanol (BME), and 30% glycerol, concentrated, and stored at -80°C.

fMet-tRNA^{fMet} preparation

$tRNA^{fMet}$ with a C1G mutation and a modified terminal 3′-NH_2-ATP was *in vitro* transcribed and modified as previously described[148]. fMet-$tRNA^{fMet}$ was prepared enzymatically as described[149]. Briefly, a charging reaction was prepared with the following: 10 μM NH_2-

$tRNA^{fMet}$, 10 mM methionine, 300 μM N10-formyl-tetrahydrofolate, 10 mM ATP, 1 U/μL Rnase inhibitor (NEB), 1 μM (MetRS), and 1 μM MTF in AA buffer (50 mM HEPES pH 7.5, 10 mM KCl, 20 mM $MgCl_2$, and 2 mM DTT). This reaction was incubated at 37°C for 30 minutes. The tRNA was then phenol-chloroform extracted, ethanol precipitated, and resuspended in water.

Cryo-EM sample preparation

40 pmol of MS2-V3 50S subunit and 80 pmol WT untagged 30S subunit were incubated at 37°C in buffer C with a total of 10 mM $MgCl_2$ for 45 minutes. This mixture was then split and loaded on to four 15-40% (w/v) sucrose gradients in buffer D (20 mM HEPES pH 7.5, 100 mM KCl, 10 mM $Mg(OAc)_2$). Gradients were centrifuged at 97,000 xg for 16 hours in a SW-41 rotor (Beckman-Coulter). An ISCO fractionation system was used to isolate the 70S fraction from each gradient (**Figure S3.1**). 70S factions were then combined, washed in buffer D, and concentrated in a 100 kDa cut off spin filter (Millipore).

100 nM 70S ribosome, 1 μM fMet-$tRNA^{fMet}$, and 5 μM mRNA with the sequence 5′-GUAUAAGGAGGUAAAAUGUUCUAACUA-3′ (IDT), were combined in Buffer D with 15 mM MgOAc and incubated at 37°C for 45 minutes. The fMet codon is underlined in the mRNA sequence. 300 mesh R1.2/R1.3 UltraAu foil grids with a deposited layer of amorphous carbon were glow discharged in a PELCO easiGlow for 12 seconds under 0.37 mBar vacuum and with 25 mA current. 4 μL of the complex was then added to the grid, incubated for 1 minute, and then the grid was touched to three successive 100 μL drops of buffer D. Grids were plunge-frozen in liquid ethane using a Vitrobot Mark IV at 4°C with 100% humidity and the settings blot force 4 and blot time 2 s.

Cryo-EM data acquisition, image processing, and modeling

Data was acquired as previously described[99] with adaptations (**Table S3.2**). Briefly, movies were collected on a 300 kV Titan Krios microscope with a BIO-energy filter and Gatan K3 camera. The super-resolution pixel size was set to 0.405 (physical pixel size of 0.81) and SerialEM[150] was used to automate data collection. Movies were collected over a defocus range of -0.5 to -1.5 μm with an electron dose of 40 $e^-/Å^2$ split over 40 frames. Image shift was used to collect movies in a 3x3 grid of holes with two movies collected per hole.

Raw movies were Fourier-cropped to the physical calibrated pixel size (0.8248 Å) and patch motion corrected in cryoSPARC 3[103]. CTFFind4[102] was used to estimate the CTFs of micrographs and ones with poor estimated CTF fit were manually excluded. Micrographs were then split into exposure groups based on the 3x3 groups during image-shift collection. Particles were picked using the cryoSPARC template picker with 70S ribosome 2D templates generated in cryoSPARC. Particles were then extracted and Fourier-cropped to 1/8 of the box size and 2D classification was performed in cryoSPARC using 100 classes. Junk particles were rejected and a second round of 2D classification was performed to further remove the remaining junk particles. Selected particles were re-extracted and Fourier-cropped to ¼ of the box size and 3D classification was performed with heterogeneous refinement in cryoSPARC using a 70S ribosome map from[148]. Classes containing features consistent with 70S ribosomes were combined and subjected to another round of 3D classification. Classes from the second round of 3D classification that refined to high resolution were combined and particles from these classes were extracted at the full box size. The particles were then subjected to homogeneous refinement in cryoSPARC with per-particle defocus optimization, per-group CTF parameter optimization, and Ewald sphere correction. Focus refinements were run separately on the 50S and 30S subunits with local refinement in cryoSPARC

(**Figure S3.2**). For modeling, a composite map was constructed by combining the maps from the 50S and 30S focused refinements. PDB 7K00[99], which was used as an Initial 70S ribosome model, was aligned to the composite map In ChimeraX[108]. Real space refinement in PHENIX[109] was used to refine the model, and the manual adjustments were made to the model as needed in COOT[110] (**Table S3.3**). To better model the MS2 tag, particles were Fourier-cropped to ½ the box size and the region containing H1 and H98 was masked and subjected to 3D variability analysis in cryoSPARC (**Figure S3.2**). Each of the volume series were inspected and the map which contained the best density for the MS2 tag and showed characteristics of an RNA helix was selected. The MS2 tag was modeled into this map using secondary structure constraints in PHENIX.

3.4 Results

H1, H94, and H98 interact in the E. coli LSU

To better understand the architecture of the region surrounding H98, we examined the structure of the *E. coli* ribosome[99]. Helices H1, H94, and H98 reside on the surface of the 50S ribosomal subunit, and the apical regions of H1 and H98 extend away from the ribosome (**Figure 3.1A**). H1 is formed through base pairing between the 5′ and 3′ ends of the 23S rRNA (nucleotides 1-8 and 2895-2904 respectively). The 3′ end of 23S rRNA comprises Domain VI of the LSU which contains RNA helices H94-H101. In the *E. coli* ribosome, H1, H94, and H98 are in close proximity (**Figure 3.1B**), and nucleotides at the base of H1 (G9, A10), the base of H94 (U2629), and in the apical loop of H98 (A2800) form tertiary interactions.

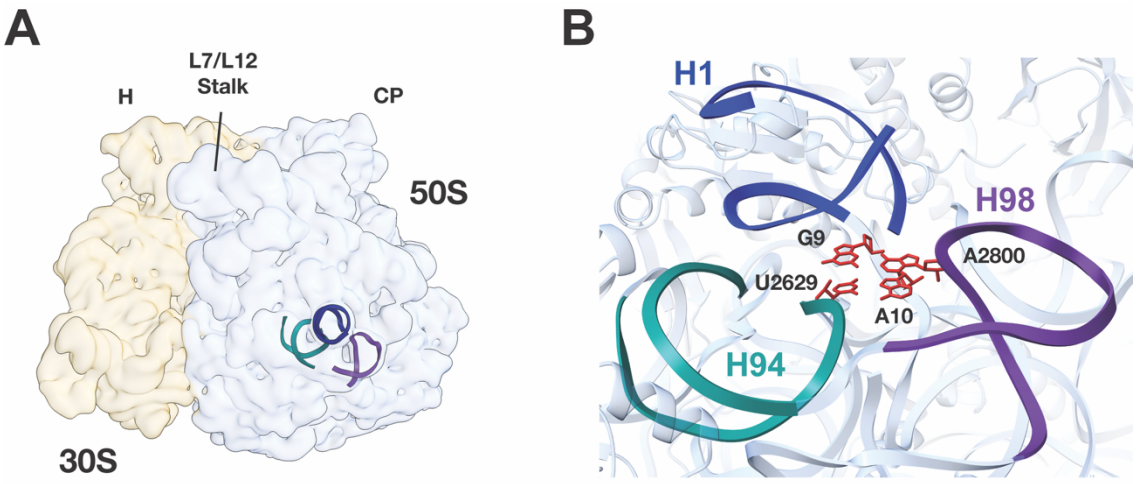


Figure 3.1. Location and overview of the region surrounding 23S rRNA helix H1. A) Location of helices H1 (dark blue), H94 (teal), and H98 (purple) in the *E. coli* LSU. The locations of the Central Protuberance of the 50S subunit (CP) and Head of the 30S subunit (H) are marked. B) Structural model of the *E. coli* 70S ribosome (PDB:7K00) highlighting interactions between H1, H94, and H98. Nucleotides that form the interaction between these helices are colored red.

The purification of *E. coli* LSUs with mutations in 23S rRNA has commonly been achieved through the insertion of MS2 tags into H98. The original sequence of the MS2 tag from[89] is shown in **Figure 3.2A** (referred to here as MS2-V1). The tag is inserted into H98 by extension of the helix, which culminates with a poly-uridine stretch (RNA linker). The MS2 helix is then inserted at the end of the RNA linker to ensure that it is accessible to the MS2 coat protein. A second tag design, which includes a different linker sequence and mutations in the MS2 stem loop that increase the MS2 coat protein's affinity for the RNA[151], was used more recently[66] (referred to here as MS2-V2).

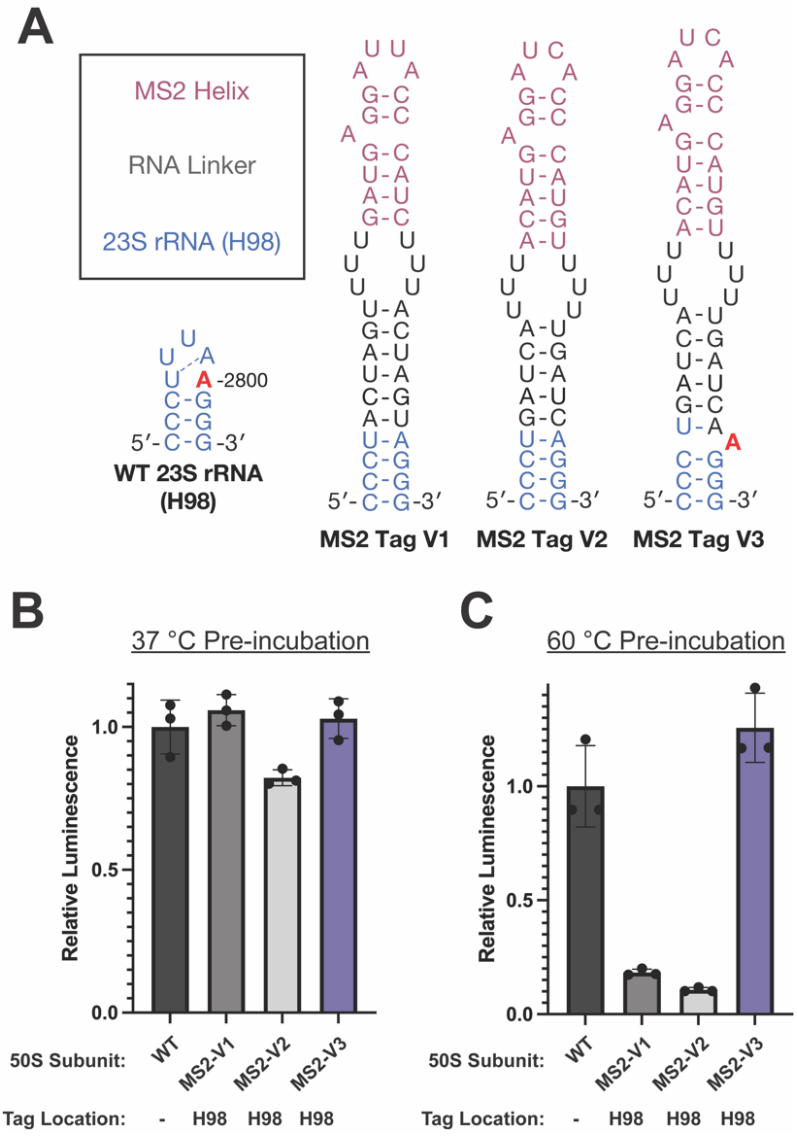


Figure 3.2. Design and activity of 50S subunits with MS2 tags inserted into H98. A) The secondary structure of H98 in WT 23S rRNA or ribosomes with MS2 tags. The sequence of MS2-V1 and MS2-V2 are from[89] and[66] respectively. Addition of an adenosine in MS2-V3 at a position equivalent to A2800 is proposed to mimic the sequence of the WT 23S rRNA (A2800 in red). 50S subunits were preincubated at B) 37°C or C) 60°C before their addition to the nanoLuciferase *in vitro* translation assay. Data is normalized to WT subunits with no MS2 tag. All error bars are the standard deviation of three experimental replicates.

It was previously shown that 50S s"buni's with an MS2-V2 tag inserted into H98 are destabilized compared to WT subunits[148]. We hypothesized that the insertion of an MS2 tag into H98 disrupts the tertiary interactions between H1, H94, and H98 and causes global destabilization of the 50S subunit. In the WT ribosome structure, nucleotide A2800 in H98 interacts with bases near H1, bridging H1 and H98. Although A2800 is not removed during the insertion of MS2-V1 or V2, the extension of the helix and the loss of A2799 in the H98 apical loop could drive A2800 into a Watson-Crick base pair with U2796 in the H98 helix rather than remaining flipped out to interact with H1 and H94. To test whether we could improve the MS2 tag design, we added an additional adenosine into a position synonymous to A2800 (MS2-V3). This design would allow the additional unpaired adenosine to interact with H1 nucleotides and restore the canonical structure of this region.

MS2-V3 restores stability to the E. coli LSU

To test whether the loss of A2800 in MS2 tags was the cause for destabilization of the 50S subunit, we tested the activity of 50S subunits with MS2-V1, V2, or V3 tags using an *in vitro* nanoluciferase (nLuc) translation assay. As was shown previously, the insertion of an MS2-V1 tag does not affect *in vitro* ribosome activity at 37°C[66,89] (**Figure 3.2B**). We do observe a slight decrease in the activity of 50S subunits with MS2-V2 tags, however this may be due to the additional incubation step at 37°C before the *in vitro* translation assay (Methods). Notably, 50S subunits with a MS2-V3 insertion have similar levels of activity to untagged WT 50S subunits.

While ribosome activity at 37°C is not affected by the insertion of MS2 tags in H98, we also investigated the ability of 50S subunits to withstand a heat treatment step before the *in vitro* translation assays. After pre-incubation at 60°C, subunits with MS2-V1 and V2 inserted in H98 exhibit only 18% and 11%, respectively, of the activity of untagged WT subunits (**Figure 3.2C**). This indicates that subunits with MS2-V1 and V2 tags are destabilized compared to WT subunits. In contrast, 50S subunits with MS2-V3 tags demonstrate WT levels of activity after incubation at 60°C (**Figure 3.2C** and **Figure S3.3**). This suggests that loss of the A2800 interaction plays a role in the destabilization of subunits with MS2-V1 and MS2-V2 tags.

We examined the H1-H94-H98 interaction in the cryo-EM structures of a WT 70S ribosome[99] and ribosomes with an MS2-V2 tag[148]. In the WT ribosome, there is clear density for G9 (H1), A10 (H1), and U2629 (H94) sugars and bases. There is also clear density for the A2800 (H98) base despite poor density for the rest of the apical region of H98 (**Figure 3.3A**), indicating that while H98 is dynamic on the surface of the ribosome, A2800 is rigidly docked through contacts with H1 nucleotides. In contrast, the ribosome with MS2-V2 inserted in H98, lacks density for A2800 and displays weak density for A10 suggesting that this nucleotide is more dynamic. While A2800 is not deleted in the MS2-V2 tag, the lack of density at its canonical position suggests that the adenosine forms a Watson-Crick base pair with U2796 in the H98 helix. The RNA helical extension of H98 in the MS2-V2 tag may energetically favor the A2800-U2796 base pair and force A2800 out of its canonical flipped position observed in the WT structure.

To determine how the addition of an adenosine residue in MS2-V3 affects the structure of the H1-H94-H98 region, we determined the structure of an MS2-V3 tagged *E. coli* 70S ribosome with fMet-tRNA^{fMet} in the P site to a global resolution of 1.8 Å resolution. This high-resolution structure enabled the visualization of individual nucleotides on the surface of the ribosome, including some of those in H1 and H98 where local resolutions range from 2.2-2.4 Å (**Figure S3.4**). Additionally, we utilized 3D-variability analysis in cryoSPARC to better resolve the

extended MS2 tag and could model the helix into lower-resolution helical density through the poly-uridine stretch.

Although the apical MS2 helix and MS2 coat protein are likely too dynamic to be visualized, H98 with the MS2-V3 insertion adopts roughly the same conformation as WT H98, with the linker helix extending away from the surface of the 50S subunit (**Figure 3.3B**). Importantly, there is clear density for both A10 and the additional adenosine at a position equivalent to 2800 in the WT ribosome (2833 with the MS2-V3 tag) (**Figure 3.3A**). The additional adenosine is in a similar position to A2800 in the WT structure and forms similar hydrogen bonds with the other quartet nucleotides (**Figure 3.3B** and **Figure S3.5**).

To further understand how the addition of the adenosine affects the extended H98, we looked at low-pass filtered maps for ribosomes with MS2-V2 and MS2-V3 tags (**Figure 3.3C**). With MS2-V2 tags, there is a lack of density around canonical location of A2800 and much of the linker helix, suggesting that once H1-H98 contacts are lost, H98 becomes highly dynamic. Upon the addition of an adenosine in MS2-V3 tags, there is a recovery of density for the extended H98. Thus, in the ribosome with an MS2-V3 tag, addition of an adenosine into the MS2 tag restores the H1-H94-H98 tertiary interaction and this recovers ribosome stability.

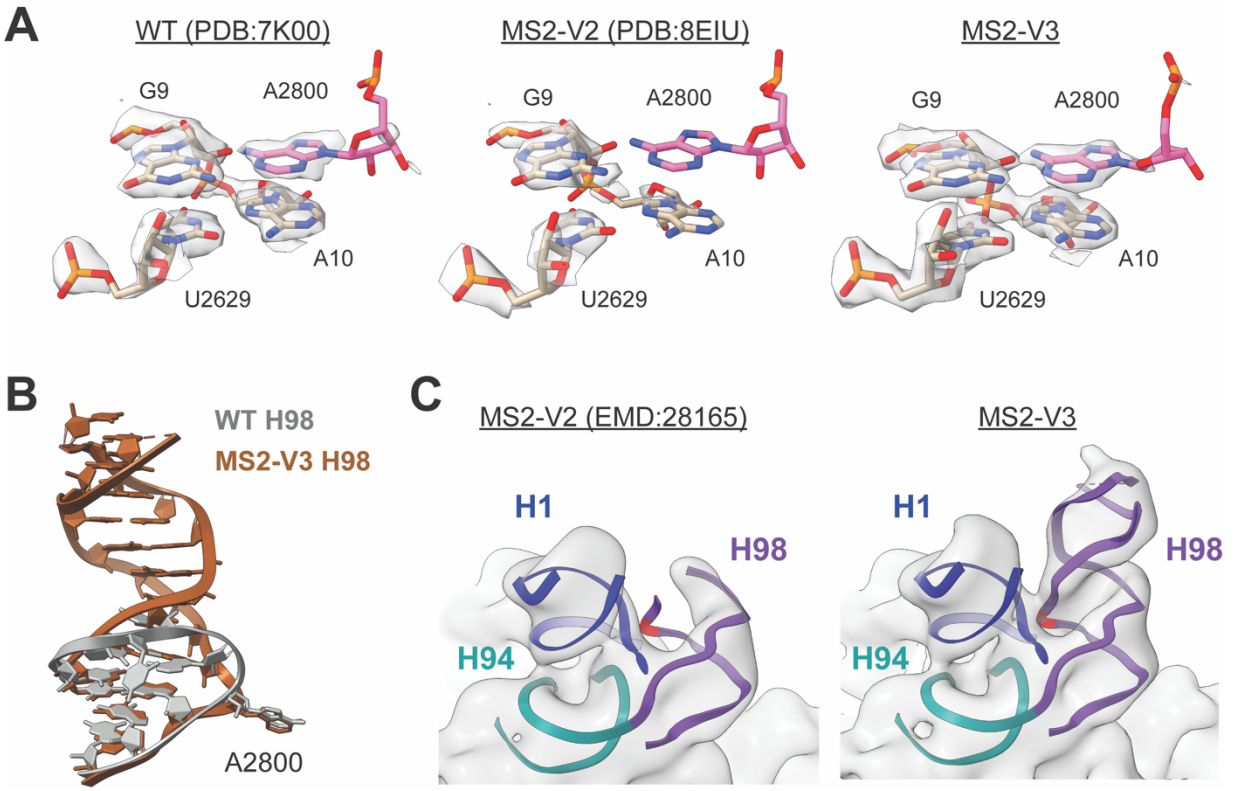


Figure 3.3. Structure of the *E. coli* 70S ribosome with MS2-V3 inserted in H98. A) Model and density for the H1-H94-H98 nucleotide quartet in the WT 70S ribosome (left, PDB:7K00 EMD:22586), 70S ribosome with MS2-V2 inserted in H98 (middle, PDB:8EIU EMD:28165), and 70S ribosome with MS2-V3 inserted in H98 (right). Nucleotide A2800 is shown in pink and an additional *B*-factor of 15 Å^2 was applied to the cryo-EM maps. B) Overview of H98 in the WT 70S ribosome (grey, PDB:7K00) and the helix upon insertion of MS2-V3 in H98 (brown). C) Low-pass filtered cryo-EM maps for MS2-V2 (EMD:28165) and MS2-V3 overlayed on the MS2-V3 model for H1, H94, and H98. Cryo-EM maps were low-pass filtered to 10 Å. The nucleotide equivalent to A2800 (A2833) is marked in red.

Nucleotide bridges between H1, H94, and H98 are required for full LSU stability

Since the interaction between H1, H94, and H98 plays a role in ribosome stability, we carefully examined the structure of this region. The nucleotide quartet is composed of two sets of base pairs which stack on one another: a type X *trans* Watson-Crick—sugar edge base pair between G9 and A2800 and a type XXIV *trans* Watson-Crick—Hoogsteen base pair between U2629 and A10. Additionally, N1 of G9 and N6 of A2800 interact with the 2′-OH of U2629 and G9, respectively (**Figure 3.4A**).

To further interrogate the interactions between H1, H94, and H98, we inserted the MS2-V2 tag into H25, as a streptavidin binding aptamer was previously placed in H25 for the affinity purification of *E. coli* ribosomes[152]. By moving the MS2 tag into H25, we were able to maintain the WT sequence of H98 to determine how the native contacts in this region affect the stability of the LSU. The insertion of an MS2 tag into H25 has a slight negative effect on ribosome stability but no effect on activity at 37°C (**Figure 3.4B** and **Figure S3.6**). This result suggests that the extension of solvent accessible helices on the surface of the ribosome can have unexpected effects on ribosome folding and stability. Utilizing the MS2 tag inserted into H25, the following 50S mutant subunits were purified: G9U, A10U, U2629C, A2800U, and A2800G. Purine to uridine mutations (G9U, A10U, and A2800U) were made to disrupt base pairing and base stacking in the H1-H94-H98 tertiary contact as uridine has higher (less favorable) base stacking free energies than purine nucleotides[127,128]. A U2629C mutation was hypothesized to make minor perturbations to the U2629-A10 pair while maintaining the smaller pyrimidine ring size.

Mutations in the quartet nucleotides did not decrease ribosome activity at 37°C but negatively affected ribosome stability (**Figure 3.4C** and **Figure S3.6**). The G9U and A10U mutant subunits had the highest stability compared to the other quartet mutations. It is likely that both nucleotides work together to fully link H1 to H94 and H98, and that the mutation of one residue does not completely abolish the interaction. Mutations to U2629 and A2800 led to the largest negative effects on ribosome stability. The mutation of these residues would prevent H94 or H98 from interacting with H1, which indicates that the loss of either of these contacts decreases ribosome stability. Subunits with an A2800U mutation had the lowest activity after pre-incubation at 60°C, suggesting that the H98-H1 interaction plays an important role in the stability of the *E. coli* LSU. When the nucleotides that base-pair (G9U) or base stack (A10U) with A2800 are mutated, there is also a loss in ribosome stability. Additionally, a subunit with an A2800G mutation displayed slightly higher levels of activity after pre-incubation at 60°C than one with an A2800U mutation. The guanosine at position 2800 would still be able to form a purine-purine base stack with A10 but would not be able base-pair with the sugar edge of G9, indicating that base-stacking in this region likely plays an important role in nucleotide engagement.

H98 is a poorly conserved helix in 23S rRNA that is absent in ribosomes from many organisms[153]. Since H1, H94, and H98 play a role in the stability of the *E. coli* LSU, we wondered whether these helices play similar roles in other bacterial ribosomes. We examined the region surrounding H1 in various high resolution structures of bacterial ribosomes that contain H98 (**Table 3.1**)[154–163]. Out of the surveyed structures, the ribosomes from two organisms, *P. aeruginosa* and *E. faecalis*, have interactions between H1, H94, and H98 that form the same structure as in the *E. coli* ribosome. However, other organisms possess diverse sets of contacts between these helices that differ from the ones found in *E. coli* (**Figure S3.7**). For example, the interactions between the helices are more expansive in *M. tuberculosis* and *T. thermophilus* than in *E. coli*. *T. thermophilus* ribosomes utilize complex hydrogen bond networks and base stacking that involves both the 5′ and 3′ strands of H1, to bridge H1 with H94 and H98 (**Figure S3.7**). This

is suggestive of a stronger interaction that could be advantageous at the higher growth temperatures of *T. thermophilus*. In all the surveyed ribosome structures there are interactions between the 5′ strand of H1 and a variable nucleotide at the base of H94. However, H98 does not interact with H1 in many of the structures, such as in *B subtilis*. In these bacteria, the H1-H94 interaction or other compensating interactions may be sufficient for ribosome stability.

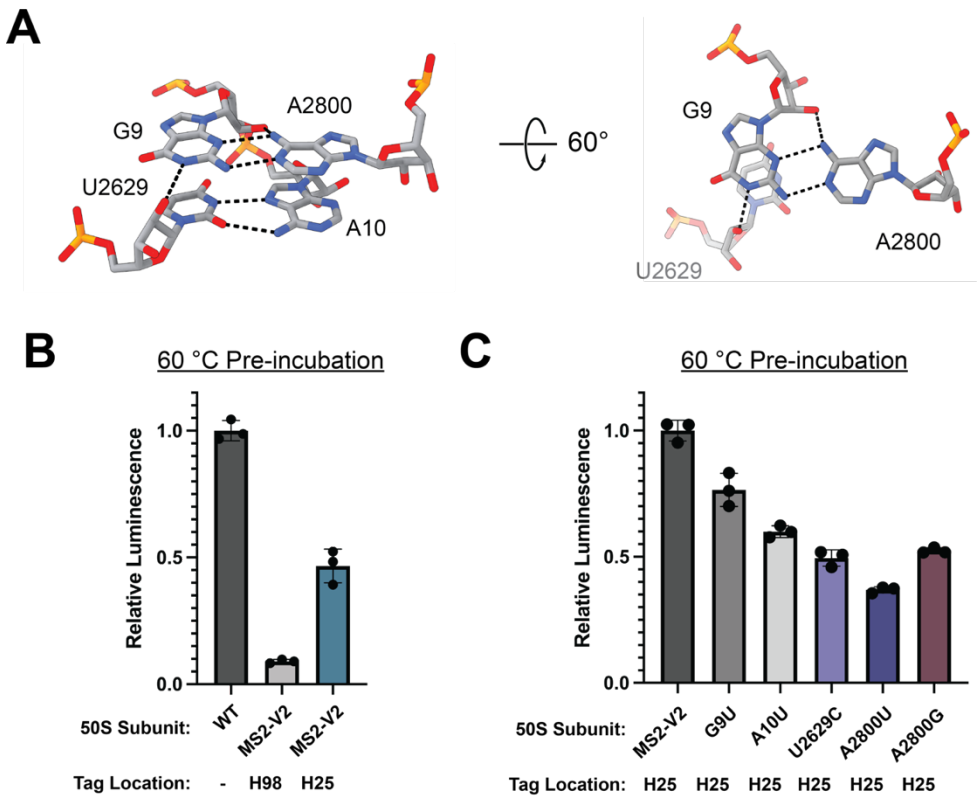


Figure 3.4. Base pairing and stacking in the H1-H94-H98 nucleotide quartet. A) Overview of the nucleotide quartet in the WT 70S ribosome. Hydrogen bonds between the bases and sugars are shown in black. B) nLuc *in vitro* translation assay for WT (no tag), MS2-V2 inserted into H98, and MS2-V2 inserted into H25 after pre-incubation of 50S subunits at 60°C. Data is normalized to untagged 50S subunits. C) nLuc *in vitro* translation assay for 50S subunits with MS2-V2 inserted into H25 and mutations in the H1-H94-H98 quartet after pre-incubation of 50S subunits at 60°C. Data is normalized to subunits with MS2-V2 inserted into H25. All error bars are the standard deviation of three experimental replicates.

Table 3.1. Interactions between rRNA helices H1, H94, and H98 from bacterial ribosomes with known structures. The identities of RNA nucleotides from these helices which interact are listed. H1 nucleotides on the 3′ strand of 23S rRNA are shown in parenthesis.

Organism	Phylum	H1 Interacting Nucleotides	H94 Interacting Nucleotides	H98 Interacting Nucleotides
Escherichia coli	Pseudomonadota	G A	U	A
Pseudomonas aeruginosa	Pseudomonadota	G A	U	A
Actinetobacter baumannii	Pseudomonadota	A A	U	U
Thermus thermophilus	Deinococcota	U G (U)	A	A
Deinococcus radiodurans	Deinococcota	U A	A	-
Bacillus subtilis	Bacillota	U A	A	-
Listeria monocytogenes	Bacillota	U A	A	-
Staphylococcus aureus	Bacillota	U A	A	-
Enterococcus faecalis	Bacillota	G A	U	A
Mycobacterium tuberculosis	Actinomycetota	G U (A)	C	G
Mycolicibacterium smegmatis	Actinomycetota	U U	C	-

3.5 Discussion

Here we show that the insertion of MS2 tags into H98 of 23S rRNA in the *E. coli* LSU using an uninterrupted RNA double helical extension[66,89] disrupts contacts between H1, H94, and H98 and destabilizes the LSU. It has been shown that affinity handles inserted into helices on the surface of the *E. coli* LSU can have negative effects on ribosome activity, assembly, and cellular growth[152,164]. The affinity tag described here builds on an MS2 tag design that does not affect cellular growth or ribosome activity[89] and now also achieves WT levels of stability. Additionally, the design principles outlined here can be applied to the placement of affinity tags in H98 of other bacterial LSUs, where maintenance of H1-H94-H98 interactions should be prioritized. Maintaining stability in the LSU could be important when studying ribosome mutations elsewhere that affect assembly, RNA folding, and global stability, since conferring additional instability from the MS2 affinity tag could lead to inactive ribosomes.

Previously it was shown that some bacteria lose H1 during the maturation of the LSU and that the loss of H1 is correlated with the evolutionary loss of H98[146]. This finding hinted at an unknown synergistic role between the two helices and that H1 became redundant after the evolutionary loss of H98. It was hypothesized that H98 may play a role in protecting H1 from RNase cleavage[146], and our data suggests that H98 plays an additional role stabilizing the ribosome through interactions with the 5′ strand of H1. As the ribosomes of many organisms lack H98 and some bacteria cleave H1 during LSU assembly, there may be compensating interactions that replace the H1-H94-H98 interaction in these ribosomes. For example, in the *Flavobacterium johnsoniae* ribosome, which lacks H1 in the mature LSU, the 5′ and 3′ ends of the 23S rRNA

interact with L22 and L32, respectively[165]. L22 and L32 form a protein-protein interaction in the *F. johnsonjae* ribosome, which may play a synonymous role to the H1-H94-H98 RNA-RNA interaction in *E. coli* as it bridges the 5′ and 3′ ends of 23S rRNA.

RNA intrinsically forms compact structures and it has been shown that the 5′ and 3′ ends of long RNAs are in close proximity[166–168], likely playing a role in RNA folding and stability. This observation has also been made for the termini of many proteins, and in certain proteins the loss of the N-terminal—C-terminal interaction leads to protein destabilization or unfolding[169]. RNAs with compact structures, such as rRNA and other ribozymes, have closer end to end distances than RNAs with less stable structures[170]. While H1 bridges the 5′ and 3′ ends of 23S rRNA, additional interactions between the 5′ end of H1 and terminal helices H94 and H98 on the 3′ end likely work to further tether the ends of the 23S rRNA. The interactions between helices on the ends of 23S rRNA likely stabilize the fold of certain bacterial ribosomal large subunits and may more broadly represent a method for stabilizing the fold of highly structured RNAs.

3.6 Supplementary Information

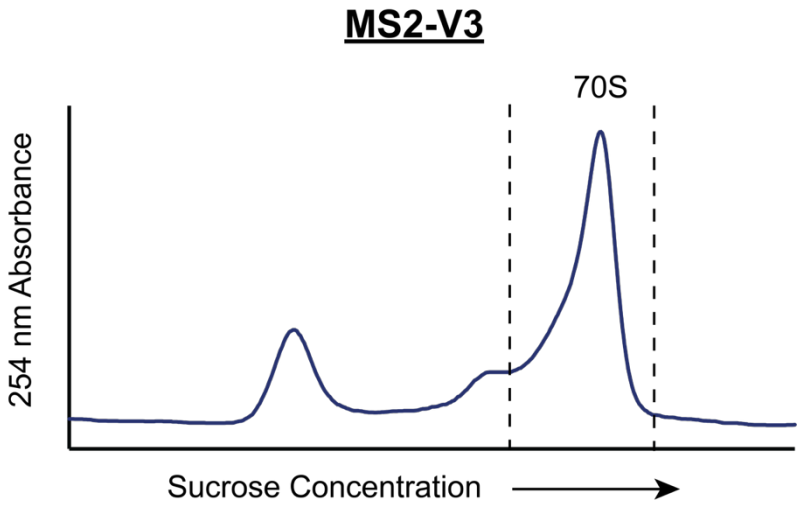


Figure S3.1. Association of 50S subunits with MS2-V3 tags inserted in H98 and untagged WT *E. coli* 30S subunits. 30S subunits (20 pmol) and 50S subunits (10 pmol) were incubated with 10 mM $MgCl_2$ and resolved on a 15-40% sucrose gradient. 70S fractions were collected between the dashed lines for cryo-EM analysis.

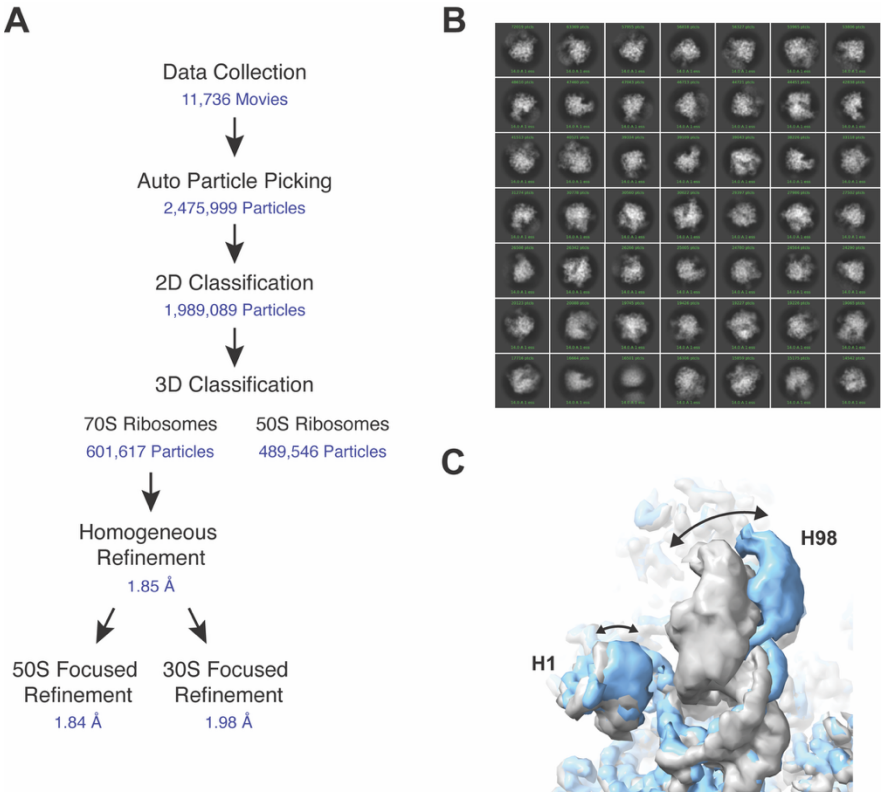


Figure S3.2. Cryo-EM data processing. A) The cryo-EM processing workflow is shown with the number of particles or half-map FSC resolution (0.143 cut-off) at each stage. B) Representative 2D classes. C) First and last frame from a component of 3D variability analysis of the region surrounding H98. Arrows demonstrate movement of H1 and H98.

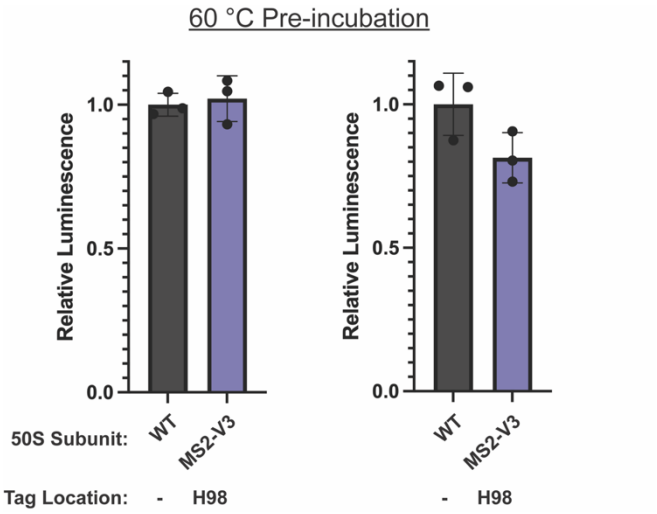


Figure S3.3. Additional replicates of nanoluciferase *in vitro* translation assays for 50S subunits with MS2-V3 tags inserted into H98. 50S subunits were preincubated at 60°C before adding to the *in vitro* translation assay. Each graph represents an independent replicate and data is normalized to WT subunits with no MS2 tag. Error bars are represented as the standard deviation of three experimental replicates.

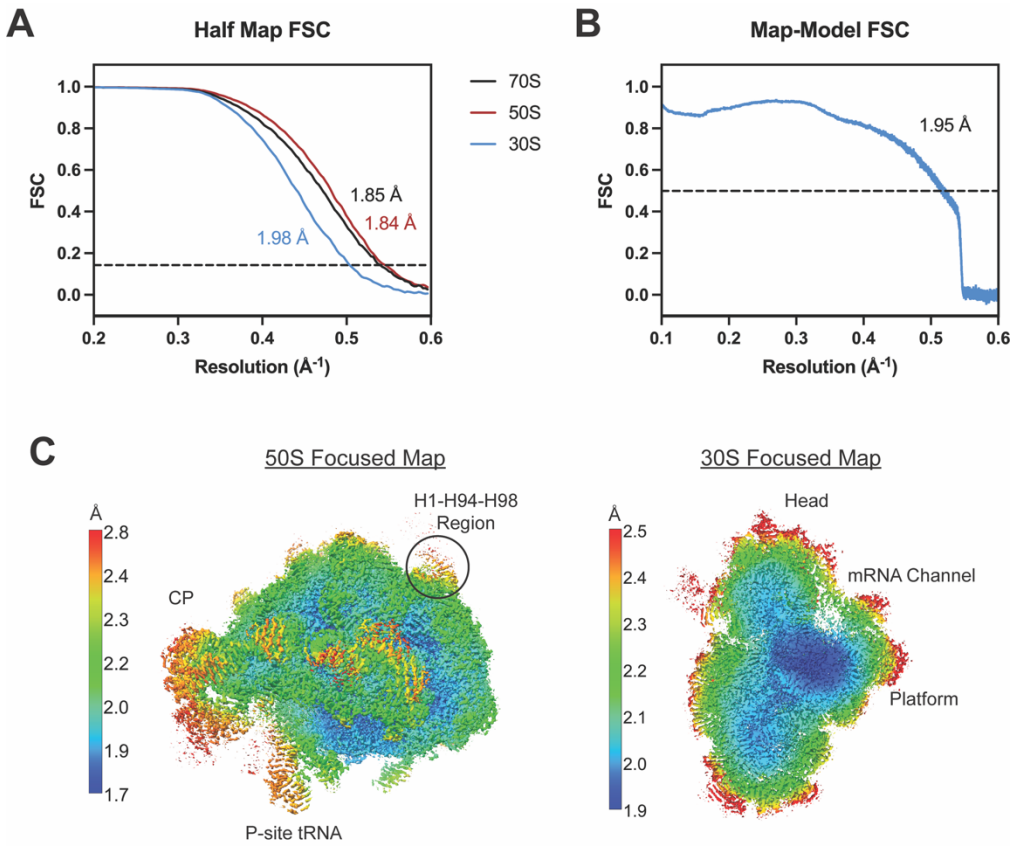


Figure S3.4: Resolutions of cryo-EM maps. A) The half map FSC resolutions (0.143 cut-off) for the global map (70S), 50S focused refinement map, and 30S focused refinement map are shown. B) The global 70S ribosome map to model FSC resolution (0.5 cut-off) is 1.95 Å. C) Local resolution is plotted on the 50S (left) or 30S (right) focused refinement maps.

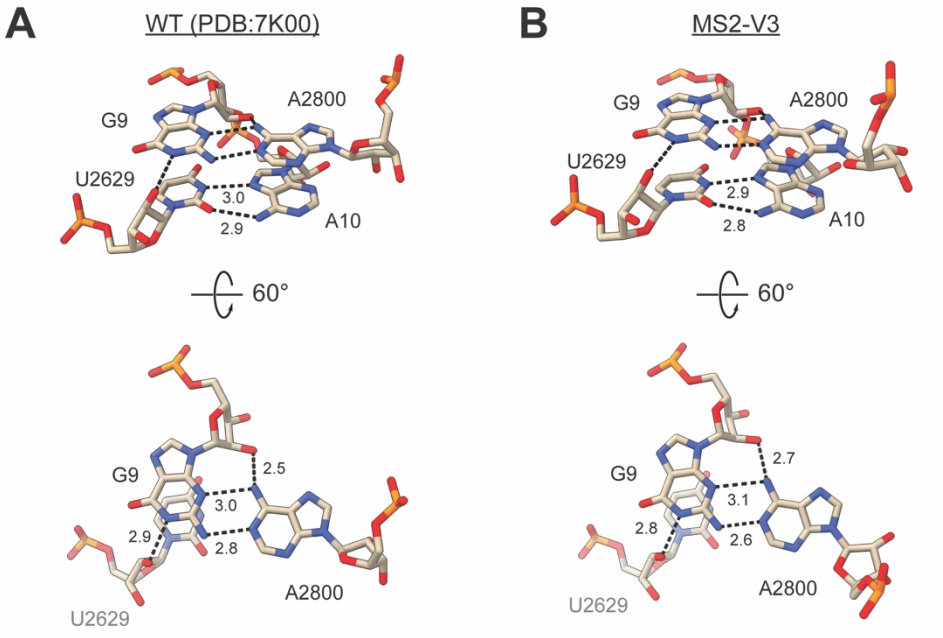


Figure S3.5. Hydrogen bonding between H1, H94, and H98 nucleotides. The nucleotides in A) WT (PDB:7K00) and B) MS2-V3 tagged ribosomes are shown, with hydrogen bonds indicated by dashed lines and distances given in Å.

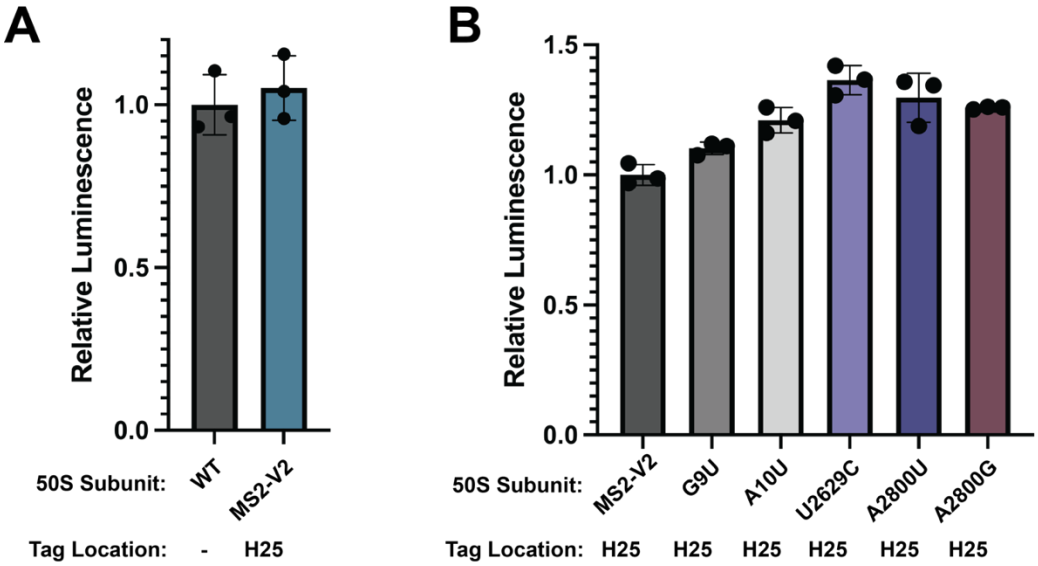


Figure S3.6. Nanoluciferase *in vitro* translation assay for 50S subunits with MS2 tags with mutations in H1, H94, and H98. A) nLuc *in vitro* translation assay for WT (no tag), and MS2-V2 inserted into H25. Data is normalized to untagged 50S subunits. B) nLuc *in vitro* translation assay for 50S subunits with MS2-V2 inserted into H25 and mutations in the H1-H94-H98 nucleotide quartet. Data is normalized to subunits with MS2-V2 inserted into H25. In these experiments, 50S subunits were not pre-incubated prior to the *in vitro* translation assay. All error bars are the standard deviation of three experimental replicates.

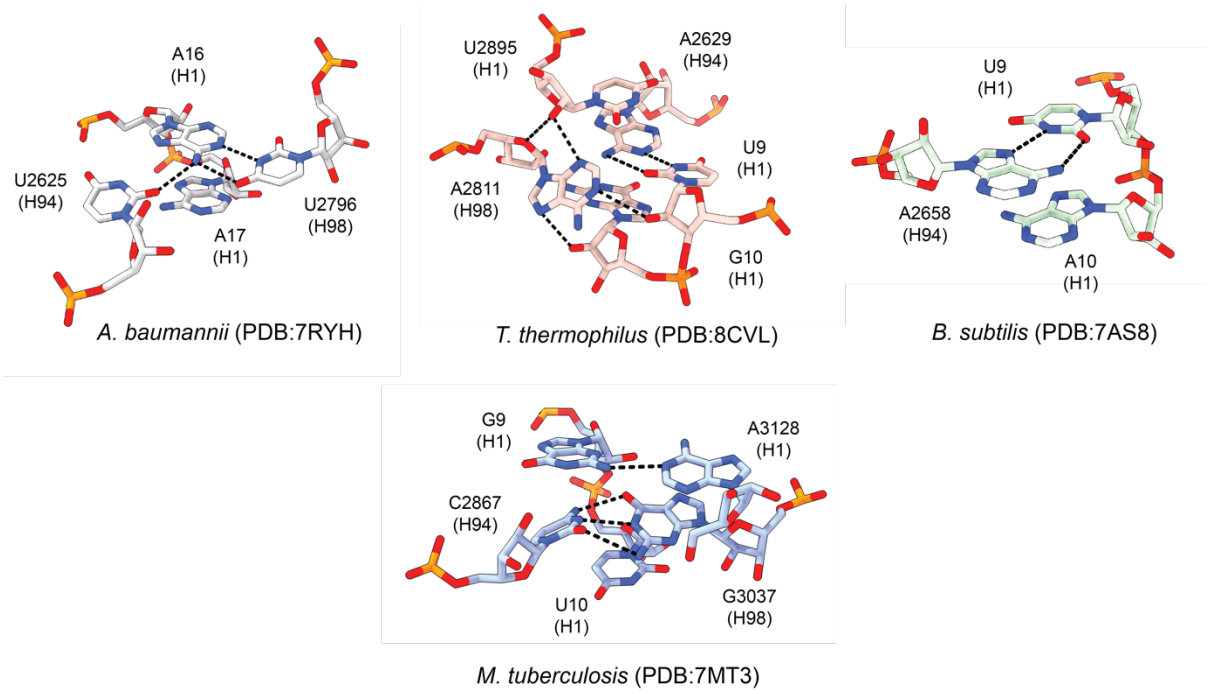


Figure S3.7. Interactions between H1, H94, and H98 in various bacterial ribosomes. Nucleotides from H1, H94, and H98 that interact with one another are displayed. Hydrogen bonds between the bases and sugars are shown in black.

Table S3.1. DNA primers used in chapter 3
(m denotes 2'-O-Me; lowercases in the sequence indicate sites where mutations are introduced)

Primer Name	Sequence	Description
Add_A2800_H98MS2_F	TTTTGATCAAGGGTCCTGAAGGAACGTTGA	Forward primer for the addition of A2800 into MS2V2 in H98 (to make MS2V3). InFusion Kit
Add_A2800_H98MS2_R	GACCCTTGATCAAAAACATGGGTGATCCTCA	Reverse primer for the addition of A2800 into MS2V2 in H98 (to make MS2V3). InFusion Kit
Delete_MS2_H98_F	TGACCCTTTAAGGGTCCTGAAGGAACGTTGA	Forward primer for the deletion of MS2V2 from H98 (restores WT 23S rRNA). InFusion Kit
Delete_MS2_H98_R	ACCCTTAAAGGGTCAGGGAGAACTCATCTCG	Reverse primer for the deletion of MS2V2 from H98 (restores WT 23S rRNA). InFusion Kit
Insert_MS2_H25_F	cacccatgtttttgatcGCGTGTGACTGCGTACCTTTTG	Forward primer for the insertion of MS2V2 into H25. Q5 Kit
Insert_MS2_H25_R	atcctcatgtaaatgatcGCGTGCTCCCACTGCTTG	Reverse primer for the insertion of MS2V2 into H25. Q5 Kit
Insert _H98MS2_V1_F	tacccatctttactagtAGGGTCCTGAAGGAACGT	Forward primer for the insertion of MS2V1 into H98. Q5 Kit
Insert_H98MS2_V1_R	atcctcatcaaaactagtAGGGTCAGGGAGAACTCAT	Reverse primer for the insertion of MS2V1 into H98. Q5 Kit
G9U_F	GAGGTTAAGCtACTAAGCGTAC	Forward primer for G9U 23S rRNA mutagenesis (H25MS2). Q5 Kit
G9U_R	ACAACCCGAAGATGTTTC	Reverse primer for G9U 23S rRNA mutagenesis (H25MS2). Q5 Kit
A10U_F	AGGTTAAGCGtCTAAGCGTAC	Forward primer for A10U 23S rRNA mutagenesis (H25MS2). Q5 Kit
A10U_R	CACAACCCGAAGATGTTTC	Reverse primer for A10U 23S rRNA mutagenesis (H25MS2). Q5 Kit
U2629C_F	CCGTGGGCGCcGGAGAACTGA	Forward primer for U2629C 23S rRNA mutagenesis (H25MS2). Q5 Kit
U2629C_R	CAGATAGGGACCGAACTGTCTC	Reverse primer for U2629C 23S rRNA mutagenesis (H25MS2). Q5 Kit
A2800U_F	TGACCCTTTAtGGGTCCTGAAG	Forward primer for A2800U 23S rRNA mutagenesis (H25MS2). Q5 Kit

A2800U_R	GGGAGAACTCATCTCGGG	Reverse primer for A2800U 23S rRNA mutagenesis (H25MS2). Q5 Kit
A2800G_F	TGACCCTTTAgGGGTCCTGAAG	Forward primer for A2800G 23S rRNA mutagenesis (H25MS2). Q5 Kit
A2800G_R	GGGAGAACTCATCTCGGG	Reverse primer for A2800G 23S rRNA mutagenesis (H25MS2). Q5 Kit
MS2_H98_quant_F	CTTGCCCCGAGATGAGTTCTCCC	RT-PCR primer for the ribosome purity assay with H98 MS2 tags
MS2_H98_quant_R	GTACCGGTTAGCTCAACGCATCGCT	Primer for amplification of cDNA in the ribosome purity assay with H98 MS2 tags
MS2_H25_quant_F	ACCGTGTACGTACAAGCAGTGGG	RT-PCR primer for the ribosome purity assay with H25 MS2 tags
MS2_H25_quant_R	CCCTTCGGCTCCCCTATTCGGTTAAC	Primer for amplification of cDNA in the ribosome purity assay with H25 MS2 tags

Table S3.2. Cryo-EM data collection and processing

Magnification	105,000
Voltage (kV)	300
Electron Exposure ($e^-/Å^2$)	40
Defocus Range (μm)	-0.5/-1.5
Pixel Size (Å)	0.8248
Symmetry Imposed	C1
Initial Particle Images	2,475,999
Final Particle Images	601,617
Map Resolution (Å)	1.84
FSC Threshold	0.143

Table S3.3. Model refinement statistics

Model component	
Model resolution (Å)	1.95
FSC threshold	0.5
Map sharpening *B* factor (Å^2)	-38.2
Model composition	
Non-hydrogen atoms	146561
Mg^{2+} ions	284
Waters	6114
Mean *B* Factors (Å^2)	
RNA	24.25
Protein	24.91
Waters	16.95
Other	21.21
R.m.s. deviations from ideal values	
Bond (Å)	0.007
Angle (°)	0.968
Molprobity score	2.11
Clash Score	6.94
Rotamer outliers (%)	3.59
Ramachandran plot	
Favored (%)	95.61
Allowed (%)	3.73
Outliers (%)	0.66
RNA validation	
Angles outliers (%)	0.001
Sugar pucker outliers (%)	0.009
Average suiteness	0.589

Chapter 4: Structure of an archaeal ribosome reveals a divergent active site and hibernation factor

Reproduced from: Nissley, A. J. *et al.* Structure of an archaeal ribosome reveals a divergent active site and hibernation factor. *Nat. Microbiol.* **10**, 1940–1953 (2025).

4.1 Abstract

Ribosomes translate mRNA into protein. Despite divergence in ribosome structure over the course of evolution, the catalytic site, known as the peptidyl transferase center (PTC), is thought to be nearly universally conserved. Here, we identify clades of archaea that have highly divergent ribosomal RNA sequences in the PTC. To understand how these PTC sequences fold, we determined cryo-EM structures of the 70S and 50S ribosomes to 2.4 Å and 2 Å, respectively, from the hyperthermophilic archaeon *Pyrobaculum calidifontis*. PTC sequence variation leads to the rearrangement of key base triples and differences between archaeal and bacterial ribosomal proteins enable sequence variation in archaeal PTCs. Finally, we identify a previously undescribed archaeal ribosome hibernation factor, Dri, that differs from known bacterial and eukaryotic hibernation factors and is found in multiple archaeal phyla. Overall, this work identifies factors that regulate ribosome function in archaea and reveals a larger diversity of the most ancient sequences in the ribosome.

4.2 Introduction

The ribosome is a ubiquitous ribonucleoprotein complex responsible for protein synthesis in the cell. While many aspects of ribosome structure have diverged through evolution, the active sites of the ribosome are thought to be nearly universally conserved[2,171,172]. The structures of ribosomes from model organisms have been well studied by X-ray crystallography[173–177], but less is known about how ribosomes differ in non-model organisms. Cryogenic electron microscopy (cryo-EM) has recently enabled the determination of ribosome structures from a diversity of organisms[11,46,178–180] and organelles[181–183] at high resolution. These ribosomes vary in structure and provide a more holistic understanding of ribosome function and regulation.

Archaea are prokaryotes that are widespread on Earth, found in diverse environments, and play important roles in biogeochemical cycling[111,184–186]. For example, methanogenic archaea are the primary driver of global methane emissions[187]. Hyperthermophilic archaea live in environments that reach extreme temperatures and have modified their translation machinery, including the ribosome, to function at these temperatures. These adaptions include post-transcriptional RNA modifications[35,123] and changes in ribosomal proteins (rProteins) and ribosomal RNA (rRNA) sequences[28,148]. However, we lack a clear understanding of how archaeal ribosomes differ in their structure and regulation as there are only high-resolution ribosome structures from a few archaeal species[35,174,188–190].

In the large subunit (LSU) of the ribosome, the peptidyl transferase center (PTC) catalyzes peptide bond formation during translation. Due to its functional importance, the PTC, which is comprised of rRNA, is one of the most ancient and conserved regions of the ribosome[171,191,192]. Extreme sequence conservation hampers our understanding of how natural changes to the PTC affect its structure and function. It also limits our understanding of how the PTC can be altered to promote new functions with widespread utility in biomanufacturing and the synthesis of novel sequence-defined polymers[51,52]. While the sequence of the PTC is broadly conserved in archaea, it was previously shown that the ribosomes from *Thermoproteus tenax*, a member of the archaeal class Thermoprotei, have rare sequence variation at otherwise highly conserved rRNA positions

in the PTC[193]. Here, we find that PTC sequence variation occurs more broadly in several clades of archaea. *Pyrobaculum calidifontis*, an aerobic hyperthermophile (T_{opt}=90-95 °C)[194], is a member of Thermoprotei and has rare variation at five rRNA positions in the core of the PTC. Using cryo-EM, we determine the structure of the *P. calidifontis* ribosome, revealing how nucleotide changes are accommodated in an archaeal PTC.

Additionally, we find a protein of previously unknown function bound to the *P. calidifontis* ribosome. We designate this protein **D**ual **R**ibosomal subunit **I**nhibitor (Dri). Dri is comprised of two ribosome binding modules that interact with the LSU and small ribosomal subunit (SSU), where it occupies the PTC and mRNA binding channel. We show that Dri inhibits protein synthesis, consistent with its role as a ribosome hibernation factor. Ribosome hibernation factors play a critical role in preserving ribosomes when translation is downregulated during stress or cellular dormancy, an important part of the microbial life cycle[195,196]. Under these conditions, ribosome hibernation factors bind to the ribosome, inhibit protein synthesis, and can protect ribosomes from damage while in an inactive state[37–39]. Dri homologs are found broadly in multiple archaeal phyla and may constitute a widely distributed family of archaeal ribosome hibernation factors.

4.3 Materials and methods

Pyrobaculum calidifontis growth

Pyrobaculum calidifontis (DSM 21063) was purchased from the DSMZ collection and grown as described[194] with modifications. For long-term storage, cells were kept at -80 °C in 40% (v/v) glycerol. Cells were grown in modified TY medium (0.1% yeast extract, 1% tryptone, 0.3% sodium thiosulphate, pH 7.0) at 90 °C without shaking. For pre-cultures, 200 mL of modified TY media in a 1 L screw top bottle was inoculated with 600 µL of a frozen cell stock. The pre-culture was placed in an oven at 90 °C without shaking for two days. Cultures (200 mL of modified TY medium in a 1 L screw top bottle) were then inoculated with 20 mL of pre-culture and incubated at 90 °C until they reached an OD_{600} of 0.17.

P. calidifontis ribosome preparation

3 L of *P. calidifontis* cell culture at stationary phase (OD_{600} of 0.17) were centrifuged at 6,000 *xg* for 20 minutes at 4 °C. The cell pellet was then resuspended in 20 mL *Pc* buffer A (20 mM HEPES-KOH pH 7.0, 100 mM NH_4Cl, 10 mM $Mg(OAc)_2$, 2 mM dithiothreitol (DTT)). Cells were then lysed by sonication and spun in an F14-14x50cy rotor (ThermoFisher) at 12,000 rpm (25,000 *xg*) for 45 minutes. The supernatant was then split evenly and layered onto two sucrose cushions containing 35 mL *Pc* buffer A with 1 M sucrose. The sucrose cushions were placed in a Ti-45 rotor (Beckman-Coulter) and centrifuged at 38,000 rpm (113,000 *xg*) for 16 hours at 4 °C. The pellets (crude ribosomes) were then resuspended in 1 mL of *Pc* buffer A. After resuspension, 0.5 mg of crude ribosomes were placed on a 15-35% sucrose gradient in *Pc* buffer B (20 mM HEPES-KOH pH 7.0, 10 mM KCl, 10 mM $Mg(OAc)_2$, 2 mM DTT). The sucrose gradient was placed in an SW-32 rotor (Beckman-Coulter) and centrifuged at 26,000 rpm (83,000 *xg*) for 16 hours. After centrifugation, the gradient was fractionated with an ISCO fractionation system. The peak corresponding to 70S ribosomes (Extended Data Fig. 1a) was isolated, buffer exchanged into *Pc* buffer C (20 mM HEPES-KOH pH 7.0, 10 mM KCl, 20 mM $Mg(OAc)_2$, 3 mM spermine, 2 mM DTT), and concentrated in a 100 kDa molecular weight cut off spin filter (Millipore). Ribosomes were then flash frozen and stored at -80 °C. *P. calidifontis* ribosomes were quantified using the approximation 1 A_{260}=40 µg/mL.

Recombinant expression and purification of Dri

E. coli Rosetta (DE3) cells were transformed with a pET-21(+) plasmid containing the Dri protein sequence with an N or C-terminal His-tag (**Table S4.1**). Overnight cultures of the transformants were diluted 1:100 into 1 L of LB media with 100 µg/mL ampicillin and incubated at 37°C. Once the OD_{600} reached 0.5, protein expression was induced using 0.5 mM Isopropyl β-D-1-thiogalactopyranosie (IPTG) and the culture was incubated at 37 °C for an additional 2 hours. The cells were then pelleted and flash frozen. Cell pellets were thawed on ice and resuspended in Dri lysis buffer (30 mM HEPES-KOH pH 7.5, 500 mM KCl, 20 mM imidazole) with a Pierce protease inhibitor tablet (ThermoFisher) and lysed by sonication. The lysate was heat treated at 90 °C for 30 minutes and clarified by centrifugation at 25,000 *xg* for 1 hour in an F14-14 x 50cy rotor (Thermo Fisher). The supernatant was collected and filtered through a 0.2 µm filter. A 5 mL His-trap column (Cytiva) was equilibrated with 5 column volumes (CV) of Dri lysis buffer, and the lysate was then loaded onto the column. The column was washed with 10 CV of Dri wash buffer (30 mM HEPES-KOH pH 7.5, 20 mM imidazole) with 1.5 M KCl for the Dri C-terminal lobe or Dri wash buffer with 2.5 M KCl for the Dri N-terminal lobe and WT Dri protein. The protein was eluted using a gradient of 0-100% Dri elution buffer (30 mM HEPES-KOH pH 7.5, 500 mM KCl, 500 mM imidazole) over 5 CV. After the elution, the Dri C-terminal lobe was buffer exchanged into Dri buffer A (30 mM HEPES-KOH pH 7.5, 500 mM KCl, 20% glycerol), concentrated in a 10 kDa cut-off spin filter (Millipore), flash frozen, and stored at -80 °C.

After elution from the His-trap column, the Dri N-terminal lobe and WT Dri protein were buffer exchanged into heparin buffer A (30 mM HEPES-KOH pH 7.5, 500 mM KCl). A 5 mL heparin column (Cytiva) was equilibrated with heparin buffer A, and the protein was loaded onto the column. The column was then washed with five columns of heparin buffer A. The protein was eluted from the column using a gradient from 0-100% of heparin elution buffer (30 mM HEPES-KOH pH 7.5, 2 M KCl) over 10 CV. Fractions containing protein were combined and buffer exchanged into Dri buffer A. The purified proteins were concentrated in 10 kDa cut-off spin filters (Millipore), flash frozen, and stored at -80°C.

P. calidifontis in vitro translation

P. calidifontis was grown in 1.6 L of modified TY medium at 90 °C without shaking until cultures reached an OD_{600} of 0.09. Cultures were then placed in an ice water bath and after cooling, cells were pelleted at 6,000 *xg* for 20 minutes at 4 °C. The cells were resuspended in 10 mL of *Pc* buffer A and transferred to a 50 mL falcon tube. Cells were then pelleted again at 6000 *xg* for 20 minutes, and the cell pellet was weighed. The pellet was resuspended with 2.5 mL *Pc* buffer C without spermine per gram of wet cell pellet. Cells were lysed by sonication for three minutes and the lysate was clarified by two rounds of centrifugation at 20,000 *xg* for 30 minutes. The lysate was then flash frozen and stored in single-use aliquots at -80 °C.

HiBiT peptide mRNA was *in vitro* transcribed with T7 RNA polymerase and purified using the RNA clean and concentrator kit (Zymo). 30 µL *in vitro* translation reactions were assembled as follows: 15 µL *P. calidifontis* lysate, 3 mM ATP, 2 mM GTP, 3 mM spermine, 100 µM amino acid mixture (Promega), 900 ng HiBiT mRNA, and 10 mM $MgCl_2$ (final concentration of 20 mM Mg^{2+}). Either 3 µL of Dri protein or Dri buffer A (control reactions) was added to *in vitro* translation reactions. Reactions were incubated at 95 °C for 10 minutes and then cooled on ice. For each reaction, 8 µL was placed in three wells of a 384-well plate. 20 µL of LgBiT buffer (20 mM HEPES pH 7.5, 50 mM KCl, and 10% glycerol) with a 1:50 dilution of NanoGlo HiBiT lytic substrate (Promega) and a 1:100 dilution of LgBiT protein (Promega) was added to each well. The

plate was incubated for 10 minutes at room temperature and then luminescence was measured in a Spark plate reader (Tecan).

Cryo-EM sample preparation and data acquisition

A *P. calidifontis* 70S ribosome aliquot was thawed and diluted to 0.12 mg/mL in *Pc* buffer C. The solution was incubated at 80 °C for 20 minutes and placed on ice. Three-hundred mesh R1.2/1.3 UltrAuFoil grids with a layer of 2 nm amorphous carbon (Quantifoil) were glow discharged in a Pelco easiGlow for 12 seconds under a 0.37 mBar vacuum with 25 mA current. 4 µL of ribosome sample was applied to the grid, incubated for one minute at room temperature, and plunge-frozen in liquid ethane using a Vitrobot Mark IV at 4 °C with 100% humidity.

Cryo-EM movies were collected with a 300 kV Titan Krios microscope with a BIO-energy filter and Gatan K3 camera (**Table S4.2**). Data was collected with a super-resolution pixel size of 0.41 Å (physical pixel size of 0.8293) over a defocus range of -0.5 to -1.5 µm with a total electron dose of 40 $e^-/Å^2$ split over 40 frames. Serial-EM[150] was used to automate data collection and image shift was used to collect movies in a 10 x 10 grid of holes with two movies collected per hole.

Cryo-EM image processing

Image processing was performed in cryoSPARC 4[103] (**Figure S4.1**). Movies were Fourier-cropped to the calibrated physical pixel size (0.8293 Å), patch motion corrected, and the CTFs of micrographs were estimated using patch CTF estimation. Micrographs were split into exposure groups based on their position in the 10 x 10 groups during image-shift collection and micrographs with poor estimated CTF fit were manually excluded from further processing. Particles were picked with the cryoSPARC template picker using ribosome 2D templates generated in cryoSPARC. Particles were extracted and Fourier-cropped to 1/8 of the box size and 2D classification was performed using 75 classes. After selecting classes corresponding to ribosomes, a second round of 2D classification was performed using 50 classes. The selected particles were reextracted and Fourier-cropped to 1/4 of the box size. A reference map was generated with an *ab initio* reconstruction of the binned particles in cryoSPARC. 3D classification was performed using heterogeneous refinement in cryoSPARC with six classes. Classes containing features consistent with 70S and 50S ribosomes were subjected to a second round of 3D classification.

3D classes consistent with 50S ribosomes were sorted into two classes based on Dri occupancy using 3D classification (without alignment) in cryoSPARC. Particles from the 50S class with stronger density for Dri were reextracted at the full box size. Particles were subjected to homogeneous refinement with the per-particle defocus optimization, per-group CTF parameter optimization, and minimization over per-particle scale options selected. Local motion was corrected using reference-based motion correction in cryoSPARC. The corrected particles were subjected to another homogeneous refinement with Ewald sphere correction to yield the final map.

3D classes consistent with 70S ribosomes were sorted into four classes using a mask on the SSU to remove isolated 50S subunits. Classes consistent with 70S ribosomes were pooled and reextracted at the full box size. Particles were subjected to homogeneous refinement with the per-particle defocus optimization, per-group CTF parameter optimization, and minimization over per-particle scale options selected. Local motion was corrected using reference-based motion correction in cryoSPARC, and a consensus 70S ribosome map was generated with homogeneous refinement. Masks were generated for Dri on the LSU, SSU, and both subunits and were used to classify 70S ribosomes based on protein occupancy. Local resolution was calculated in Relion 4[197]

using the Relion implementation. For figure presentation, cryo-EM maps were supersampled using the 'make a smoother copy' function in COOT[110].

Model Building

For modeling 70S ribosomes, composite maps were generated for the 70S-consensus reconstruction and 70S-SSU-Dri reconstruction. We aligned the focused-refined maps (SSU-focused, LSU-focused, SSU-head-focused, and LSU-CP-focused for the 70S-consensus reconstruction and SSU-focused, LSU-focused, and SSU-head-focused refined maps for the 70S-SSU-Dri reconstruction) to the global 70S ribosome map using the 'Fit in Map' tool in ChimeraX[108]. The focus-refined maps were then resampled using 'vop resample' and scaled according to their standard deviations from the 'Map statistics' tool. The scaled maps were then added sequentially using 'vop add'.

Initial models were built using ModelAngelo[198] provided with sequences for *P. calidifontis* rRNAs (NCBI database) and rProteins (Uniprot). Unknown proteins were built using ModelAngelo without provided sequences. Protein models were inspected for completeness and manually built in regions where the sequences were missing or incorrect. RNA models were manually inspected at each nucleotide for correct modeling and post-transcriptional modifications. To model Dri on the SSU, the AlphaFold prediction[199] was docked into the cryo-EM map and regions of the prediction that did not agree with the map were rebuilt manually. Magnesium ions and spermine molecules were identified using the 'unmodeled blobs' tool in COOT[110] and modeled manually. No attempt was made to systematically model potassium ions. The models were then refined in Phenix[109] with real-space refinement, and manual adjustments were made to the model in COOT[110] (**Table S4.3**). After refinement, phenix.douse[109] was used to model solvent using the default settings. For the 70S structures, solvent was modeled into the individual focused refinement maps and then docked into the composite map.

Bioinformatic analysis

23S rRNA sequences in archaea and bacteria were identified by searching all Genome Taxonomy Database (GTDB v220)[200] representative genomes using the Infernal 1.1.5 cmsearch program[201] with the corresponding Rfam 14.10[202] covariance model (RF02540 for archaea and RF02541 for bacteria) using an e-value cutoff of 1e-20. For each genome, we selected the single most significant hit, additionally filtering for hits with <10% non-GC/AU/GU base pairs in regions corresponding to helices in the Rfam consensus secondary structure to minimize hits to pseudogenes. This resulted in 23S rRNA sequences for 3,686 archaeal and 58,032 bacterial species, which were aligned to the respective Rfam model using the Infernal cmalign program.

To plot PTC nucleotide frequencies in Thermoproteota, we used WebLogo3.[203] webserver, only including 23S rRNA sequences with no gaps in the shown PTC region. To calculate the Shannon entropy of PTC positions in bacteria and archaea, we only considered 23S rRNA sequences with no gaps in the plotted PTC regions (2,435 archaeal and 40,562 bacterial species). Shannon entropy was calculated from nucleotide counts at each position with a pseudocount of 1e-10 added to each sum to avoid division by zero.

uL3 sequences were analyzed using an existing alignment[204]. The distribution of previously undescribed rProteins was established by iterative searches using the homology search tool HMMER 3.4[205] hmmsearch program against the predicted proteomes of representative genomes for all GTDB archaeal species. The first search was performed using a profile HMM built from the *P. calidifontis* sequence, keeping only the top hit per genome. Hits across all archaea were

examined manually, and a conservative set of well-aligning and full-length hits was selected within an e-value plateau. Selected sequences were aligned with mafft v7.525[206] using default settings and profile HMMs were built using HMMER hmmbuild program to use in the subsequent search. This process was repeated until no new full-length hits were recovered.

Dri homologs were identified by first using a profile HMM built from the *P. calidifontis* Dri sequence to search UniProt[207] TREMBL (release 2024_04) using the HMMER program hmmscan. From these results, an initial Dri profile HMM was built from 22 full-length hits from Thermoproteaceae with e-values <1e-90 that were aligned using mafft with default settings. This initial Dri model was used to search the predicted proteomes of representative genomes for all GTDB archaeal species using hmmsearch with an e-value cutoff of 1e-10. Each hit was individually aligned to the *P. calidifontis* Dri sequence and evaluated on the following additional properties: percent alignment to *P. calidifontis* Dri N-terminal lobe (positions 14-303), percent alignment to *P. calidifontis* Dri C-terminal lobe (positions 324-640), charge of amino acids aligning to the *P. calidifontis* Dri N-terminal lobe ribosome binding surface (positions 43-44, 76-77, 203-210, 215, 224-225, and 227-241), charge of amino acids aligning to the *P. calidifontis* Dri C-terminal lobe P-site loop including a 3 amino acid buffer on either side (positions 544-579), and length of regions aligning to the *P. calidifontis* Dri C-terminal lobe P-site loop (positions 544-579), C-terminal lobe A-site loop (positions 394-425), and the N-terminal lobe P-site loop (positions 205-236) including a 3 amino acid buffer on either side. A final set of 92 full-length Dri homologs, corresponding to 91 unique species, was selected by filtering hits on >75% N-lobe and >75% C-lobe alignment, and e-value <1e-60. All of these full-length Dri homologs had sequence features consistent with the mode of ribosome binding seen in *P. calidifontis* such as a positively charged ribosome binding region on the N-terminal lobe and the presence and positive charge of the P-site loop on the C-terminal lobe.

The 92 full-length Dri homologs were aligned using mafft with default settings, and then split into N-lobe and C-lobe only regions corresponding to the *P. calidifontis* positions 14-303 and 324-640, respectively. These alignments were used to build single-lobe profile HMMs which were used to search all GTDB archaeal species using hmmsearch. Dri N-terminal lobe-only homologs were selected by filtering based on e-value <1e-30, ≥50% N-terminal lobe and <50% C-terminal lobe alignment, P-site loop length ≥13 amino acids, ribosome binding surface net charge ≥0 and basic amino acids ≥4. E-value and lobe alignment filters alone resulted in 647 sequences with only 9 removed with the additional filters. Dri C-terminal lobe-only homologs were selected by filtering based on e-value <1e-30, ≥50% C-terminal lobe and <50% N-terminal lobe alignment, A-site loop length ≥10 amino acids, P-site loop length ≥25 amino acids, P-site loop net charge ≥0 and basic amino acids ≥4. E-value and lobe alignment alone resulted in 782 sequences with 75 removed with the additional filters.

The distribution of Dri homologs was plotted on the GTDB v220 archaeal phylogenetic tree using the Interactive Tree of Life (iTOL v6) webserver[208]. To tabulate the frequency of single-lobed Dri gene arrangements, we only considered genomes where both Dri N-terminal and C-terminal single lobe homologs were found and additionally restricted to genomes where at least one of the homologs occurs >2000 nucleotides from the edge of a contig, resulting in 388 genomes.

Methanosarcina acetivorans ribosome preparation

Methanosarcina acetivorans was grown at 37 °C without shaking in bicarbonate-buffered high salt liquid medium with 50 mM trimethylamine hydrochloride and N_2/CO_2 (80/20) in the headspace[209]. Cultures were maintained at stationary phase for four days and on the fourth day

were placed on ice for 15 minutes. Cells were pelleted at 5,000 *xg* for 15 minutes and cell pellets were flash frozen and stored at -80 °C. The cell pellet was then thawed, resuspended in 15 mL *Ma* lysis buffer (50 mM $K_xH_yPO_4$ pH 7, 10 mM $MgCl_2$) with 20 units of RQ1 DNase (Promega) and a Pierce protease inhibitor mini tablet (ThermoFisher), and incubated at room temperature for 10 minutes. After incubation, $MgCl_2$ was added to a final concentration of 20 mM and the lysate was clarified by centrifugation at 12,000 rpm (29,000 *xg*) for 45 minutes in an F14-14 x 50 cy rotor (ThermoFisher). The lysate was then loaded onto a sucrose cushion with 40 mL of *Ma* buffer B (30 mM HEPES-KOH pH 7, 60 mM KCl, 20 mM $MgCl_2$, 2 mM DTT) with 1 M sucrose, and the cushion was spun in a Ti-45 rotor at 38,000 rpm (113,000 *xg*) for 16 hours. The ribosome pellet was resuspended in 500 µL *Ma* buffer B and 1 mg of ribosomes was loaded onto a 25-40% sucrose gradient in *Ma* buffer B. The sucrose gradient was placed in an SW-32 rotor (Beckman-Coulter) and centrifuged at 26,000 rpm (83,000 *xg*) for 16 hours. The sucrose gradient was then fractionated on a BioComp fractionator and the 70S peak was collected for mass spectrometry.

Protein Mass Spectrometry

For the identification of *P. calidifontis* 50S rProteins, 5 µg of 50S subunits were buffer exchanged into 100 mM Tris-HCl, pH 8.5 with 8 M urea. TCEP was added to a concentration of 5 mM and the solution was incubated at room temperature for 20 minutes. 10 mM iodoacetamide was added to the solution, and the sample was incubated for an additional 15 minutes in the dark. The sample was then diluted with 100 mM Tris-HCl pH 8.5 until the urea concentration was 6 M. 50 units of Benzonase were added to the solution and the reaction was incubated at 35 °C for 15 minutes. The sample was then diluted again with 100 mM Tris-HCl pH 8.5 until the urea concentration was 2 M. 1 mM $CaCl_2$ and 1 µg trypsin/LysC were added to the sample and the reaction was incubated overnight at 37 °C. 5% formic acid was then added to quench the digestion reaction.

To identify *P. calidifontis* 30S or *M. acetivorans* 70S rProteins, 20 µg of 30S subunits or 70S ribosomes were dried under vacuum and the pellet was resuspended with 0.1% RapiGest SF in 50 mM ammonium bicarbonate and 5 mM DTT. The solution was incubated at 80 °C for 30 minutes and then cooled to room temperature. 15 mM iodoacetamide was added and the sample was incubated in the dark for 30 minutes. The sample was then sonicated on ice using a handheld ultrasonic homogenizer with a 2 mm probe (Shengwin) at 40% power for three 30 second cycles with a 30 second rest period in-between cycles. 50 units of Benzonase were added and the sample was incubated at 35 °C for 15 minutes. The sample was then sonicated again using the above settings. 0.5 µg of chymotrypsin (*P. calidifontis* 30S) or trypsin/LysC (*M. acetivorans* 70S) was added to the sample and the reaction was incubated at 37 °C for 1 hour. The sample was sonicated a third time using the above settings, an additional 0.5 µg of chymotrypsin or trypsin/LysC was added to the sample, and the reaction was incubated at 37 °C overnight. Finally, 5% formic acid was added to quench the digestion reaction.

Mass spectrometry was performed at the Vincent J. Coates Proteomics/Mass Spectrometry Laboratory at the University of California, Berkeley. To identify *P. calidifontis* or *M. acetivorans* rProteins, multidimensional protein identification technique (MudPIT) was performed as described[210,211]. Briefly, a 2D nano-LC column was packed in a 100-µm inner diameter glass capillary with an integrated pulled emitter tip. The column consisted of 10 cm of ReproSil-Gold C18-1.9 µm resin (Dr. Maisch GmbH) and 4 cm of strong cation exchange resin (Partisphere, HiChrom). The column was loaded and conditioned using a pressure bomb and then coupled to an electrospray ionization source mounted on a Thermo-Fisher LTQ XL linear ion trap mass

spectrometer. An Agilent 1200 HPLC equipped with a split line to deliver a flow rate of 1 µL/minute was used for chromatography. Four buffers were used to elute peptides: Buffer A (5% acetonitrile, 0.02% heptafluorobutyric acid (HFBA)), buffer B (80% acetonitrile, 0.02% HFBA), buffer C (250 mM $NH_4(OAc)$, 0.02% HFBA), and buffer D (500 mM $NH_4(OAc)$, 0.02% HFBA). Peptides were eluted in four steps, with the system equilibrated in buffer A, step 1: 0-80% buffer B in 70 minutes, step 2: 0-50% buffer C in 5 minutes and 0-45% buffer B in 100 minutes, step 3: 0-100% buffer C in 5 minutes and 0-45% buffer B in 100 minutes, and step 4: 0-100% buffer D in 5 minutes and 0-45% buffer B in 160 minutes. Collision-induced dissociation (CID) spectra were collected for each *m/z*. Protein identification and analysis were done with PEAKS Studio 12 (Bioinformatics Solutions Inc.) with the following parameters: semi-specific cleavage specificity at the C-terminal site of R and K, allowing for 5 missed cleavages, precursor mass tolerance of 3 Da, and fragment ion mass tolerance of 0.6 Daltons. Methionine oxidation and phosphorylation of serine, threonine, and tyrosine were set as variable modifications and cysteine carbamidomethylation was set as a fixed modification. Peptide hits were filtered using a 1% false discovery rate (FDR).

For quantitative mass spectrometry, 20 µg of 70S ribosomes from *P. calidifontis* cultures grown to OD_{600} 0.07 or 0.15 were digested as described for *P. calidifontis* 30S subunits. Trypsin/LysC digested peptides were analyzed by online capillary nanoLC-MS/MS using a 25 cm reversed phase column and a 10 cm pre-column fabricated in-house (75 µm inner diameter, packed with ReproSil-Gold C18-1.9 µm resin (Dr. Maisch GmbH)) that was equipped with a laser-pulled nanoelectrospray emitter tip. The pre-column used 3.0 µm packing (Dr. Maisch GmbH). Peptides were eluted at a flow rate of 300 nL/minute using a linear gradient of 2-40% buffer B over 140 minutes (buffer A: 0.05% formic acid and 5% acetonitrile in water; buffer B: 0.05% formic acid and 95% acetonitrile in water) in a Thermo Fisher Easy-nLC1200 nanoLC system. Peptides were ionized using a FLEX ion source (Thermo Fisher) using electrospray ionization into a Fusion Lumos Tribrid Orbitrap Mass Spectrometer (Thermo Fisher). Data was acquired in orbi-trap mode. Instrument method parameters were as follows: MS1 resolution, 120,000 at 200 m/z; scan range, 350−1600 m/z. The top 20 most-abundant ions were subjected to collision-induced dissociation with a normalized collision energy of 35%, activation q 0.25, and precursor isolation width 2 m/z. Dynamic exclusion was enabled with a repeat count of 1, a repeat duration of 30 seconds, and an exclusion duration of 20 seconds. RAW files were analyzed using PEAKS Studio 12 (Bioinformatics Solution Inc) with the following parameters: semi-specific cleavage specificity at the C-terminal site of R and K, allowing for 5 missed cleavages, precursor mass tolerance of 15 ppm, and fragment ion mass tolerance of 0.5 Daltons. Methionine oxidation was set as variable modifications and cysteine carbamidomethylation was set as a fixed modification. Peptide hits were filtered using a 1% FDR. Proteins with at least 2 unique peptides were filtered with a 1% FDR. Label free quantitation (LFQ) was performed using PEAKS quantitation module and default parameters with the following exceptions: Top 2 peptides for each protein with a min of 10^4 abundance was used and the TIC was used for all normalization including technical replicates. The mass spectrometry proteomics data have been deposited to the PRIDE database[212].

Total RNA Isolation and Quantitative RT-PCR

P. calidifontis cultures were grown to the stated optical density and placed in an ice water bath. Cells were pelleted at 6,000 *xg* and RNA was isolated using the quick RNA miniprep kit (Zymo research). The manufacturer protocol was used without the on-column DNase digestion. After eluting the RNA, 10 units of RQ1 DNase (Promega) was added, and the sample was

incubated at 37 °C for 30 minutes to remove residual gDNA contamination. The RNA was then purified using a second quick RNA miniprep column. RT-qPCR was preformed using the Power SYBR Green RNA-to-C_T 1-Step Kit (Applied Biosystems) and the corresponding primer sets (**Table S4.4**) and were measured with a CFX96 real-time PCR detection system (Bio-Rad).

CRISPR-Cas9 Editing

CRISPR-Cas9 editing of *E. coli* was conducted with a modified pCas/pTargetF system[213]. sgRNA sequences were inserted in the pEcgRNA plasmid using the corresponding primer set (**Table S4.4**) and the InFusion cloning kit. NEB Express I^q cells (chloramphenicol (CAM) resistant) were transformed with the pEcCas plasmid, which encodes for Cas9, the inducible λ-Red system, and kanamycin resistance (KAN). Positive transformations were grown overnight in LB with 50 μg/mL KAN and 10 μg/mL CAM (LB-KAN-CAM). 400 μL of the overnight culture was added to 40 mL of fresh LB-KAN-CAM. The culture was then grown at 37 °C with shaking until an OD_{600} of 0.4 was obtained. Expression of the λ-Red system was induced with 10 mM arabinose, and the culture was incubated for another 15 minutes at 37 °C with shaking. Cells were pelleted by centrifugation at 4,000 *xg* for 15 minutes, washed with ice-cold sterile water, pelleted again by centrifugation at 4,000 *xg* for 15 minutes, and resuspended in 400 μL of cold sterile 10% glycerol. 50 μL of cells were electroporated with 100 ng of the pEcgRNA plasmid, which contains the sgRNA (**Table S4.5**) and spectinomycin (SPEC) resistance, and 400 ng of double stranded linear donor dsDNA (**Table S4.6**). The cells were then selected on LB-KAN-CAM-SPEC agar plates with 100 μg/mL SPEC. PCR amplifications of the *rplC* gene were Sanger sequenced (Elim Bio) (Extended Data Fig. 3b) to identify positive clones.

To cure *E. coli* strains of the pEcCas and pEcgRNA plasmids, edited colonies were used to inoculate 2 mL of LB-KAN-CAM containing 40 mM rhamnose, and the culture was grown overnight at 37 °C with shaking. 10 μL of the overnight culture was then used to inoculate a 2 mL LB-CAM culture that was grown for 6 hours at 37 °C with shaking. The culture was diluted 1:300 in SOC media and 5 μL of the dilution was spread on an LB-CAM-agar plate with 1% sucrose and incubated at 37 °C overnight. Plasmid curing was confirmed by replica plating colonies onto LB-CAM, LB-KAN, and LB-SPEC agar plates.

For growth measurements of edited *E. coli* strains, an LB-CAM culture was grown overnight at 37 °C. The culture was then diluted to OD 0.01 in LB with no antibiotics, and 200 μL of the diluted cells were placed into a sterile 96-well plate. The OD_{600} was measured every 10 minutes using a Park Plate Reader (Tecan) at 37 °C with shaking.

E. coli Ribosome Expression and Purification

A modified version of the pLK35 plasmid[88], which contains an IPTG inducible tac promoter and *E. coli* 23S rRNA with the MS2-tag from Nissley et al.[214] inserted in helix H98, was used to express mutant *E. coli* ribosomes. The pLK35 plasmid was linearized with primers PTC_InFusion_F/R (**Table S4.4**), and mutations were introduced into the 23S rRNA using the InFusion cloning kit (Takara bio) and corresponding gene block (Twist) (**Table S4.6**). Sequences were confirmed with whole plasmid sequencing (Elim Bio).

Untagged *E. coli* 30S subunits were purified from *E. coli* MRE600 as previously described[148]. MS2-tagged *E. coli* ribosomes were purified as previously described with adaptions[148]. pLK35 plasmids were transformed into NEB Express I^q cells. Transformants were grown in LB media overnight, and the next morning, they were diluted 1:100 in 1 L of LB media with 100 μg/mL ampicillin. The culture was grown at 37 °C with shaking until it reached an OD_{600}

of 0.6. rRNA expression was induced with 0.5 mM IPTG and the cultures were grown for an additional three hours at 37 °C. Cells were pelleted and resuspended in 30 mL of *Ec* buffer A (20 mM Tris-HCl pH 7.5, 100 mM NH_4Cl, 10 mM $MgCl_2$) with a Pierce protease inhibitor tablet (ThermoFisher). Cells were lysed by sonication and the lysate was clarified by centrifugation at 12,000 rpm (29,000 *xg*) for 45 minutes in an F14-14 x 50 cy rotor (ThermoFisher). The lysate was then loaded onto a sucrose cushion with 24 mL of *Ec* buffer B (20 mM Tris-HCl pH 7.5, 500 mM NH_4Cl, 10 mM $MgCl_2$) with 0.5 M sucrose and 17 mL of *Ec* buffer C (20 mM Tris-HCl pH 7.5, 60 mM NH_4Cl, 6 mM $MgCl_2$) with 0.7 M sucrose. Ribosomes were pelleted by centrifugation at 27,000 rpm (57,000 *xg*) for 16 h at 4 °C in a Ti-45 rotor (Beckman-Coulter). Ribosomes pellets were then resuspended in dissociation buffer (20 mM Tris-HCl pH 7.5, 60 mM NH_4Cl, 1 mM $MgCl_2$).

10 mg of MBP-MS2 fusion protein, purified as previously described[66], was loaded onto a 5 mL MBP Trap column (Cytiva) that was pre-equilibrated with MS2-150 buffer (20 mM HEPES pH 7.5, 150 mM KCl, 1mM EDTA, 2 mM 2-mecaptoethanol). The column was washed with 5 CV of *Ec* buffer A-1 (20 mM Tris-HCl pH 7.5, 100 mM NH_4Cl, 1 mM $MgCl_2$), and the resuspended ribosomes were loaded onto the column. The column was then washed with 5 CV of *Ec* buffer A-1 and 10 CV of *Ec* buffer A-250 (20 mM Tris-HCl pH 7.5, 250 mM NH_4Cl, 1 mM $MgCl_2$). Tagged *E. coli* 50S subunits were eluted with 10 mL of *Ec* elution buffer (20 mM Tris-HCl pH 7.5, 100 mM NH_4Cl, 1 mM $MgCl_2$, 10 mM maltose). The sample was then concentrated in a 100 kDa cut-off spin filter (Millipore) and washed with *Ec* buffer A-1. 50S subunits were quantified using the approximation of 1 A_{260} = 36 nM, flash frozen, and stored at -80 °C.

Endogenous *E. coli* 50S subunit contamination was quantified using semi-quantitative RT-PCR. 50 pmol of MS2-purified 50S subunits were denatured at 95 °C for 5 minutes, and the rRNA was precipitated with 4M LiCl. 75 ng of rRNA was reverse transcribed and amplified with 8 PCR cycles using the OneStep RT-PCR kit (Qiagen) and primers MS2_quant_F and MS2_quant_R (**Table S5.4**). DNA products were resolved on a 10% TBE gel, visualized with SYBR gold stain (Thermo Fisher), and quantified using Image J software[93].

E. coli Ribosome Activity Assays

HiBiT[95] *in vitro* translation assays were conducted as previously described[214]. Briefly, an *in vitro* translation reaction was assembled with the ΔRibosome PURExpress kit (NEB): 3.2 µL solution A (NEB), 1 µL factor mix (NEB), 250 nM MS2-tagged 50S ribosomal subunit, 500 nM untagged 30S ribosomal subunit, 1 U/µL murine RNAse inhibitor (NEB), 400 nM 11S NanoLuc protein (purified as described in[148]), 1:50 (v/v) dilution of Nano-Glo substrate (Promega), and 1 ng/µL of DNA template encoding the HiBiT peptide (**Table S4.6**). 2 µL of the mixture was then placed in a well of a 384-well plate, and luminescence was measured in a Spark plate reader (Tecan) at 37 °C incubation. Ribosome activity was determined as the slope of the initial linear increase in the signal of each *in vitro* translation reaction.

4.4 Results

Cryo-EM structures of the P. calidifontis ribosome

To investigate the unique features of Thermoprotei ribosomes, we isolated ribosomes from stationary phase cultures of *P. calidifontis*. 70S ribosomes isolated from archaea in the phylum Thermoproteota (formerly Crenarchaeota) often dissociate into subunits during ultracentrifugation, even under high magnesium concentrations[190,215,216]. While most *P. calidifontis* ribosomes dissociate during ultracentrifugation, some 70S ribosomes stay associated

(**Extended Figure 4.1a**). We determined the cryo-EM structure of the *P. calidifontis* 70S ribosome to a global resolution of 2.4 Å (**Figures 4.1a** and **S4.2**). Due to the large amount of dissociated 50S subunits in the sucrose gradient, we also found a population of 50S subunits during cryo-EM processing and determined the *P. calidifontis* 50S subunit structure to a resolution of 2.0 Å.

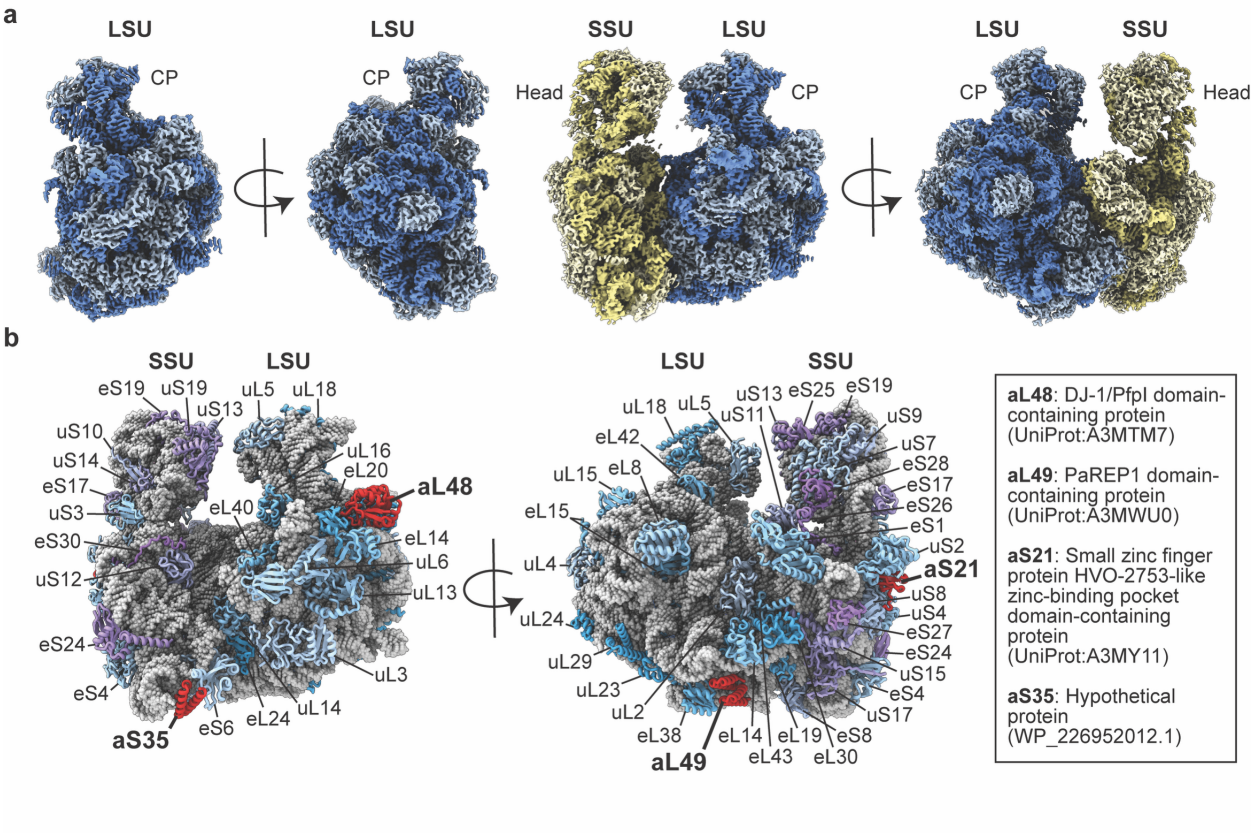


Figure 4.1. Cryo-EM structures of the *P. calidifontis* ribosome. **a,** Cryo-EM maps for the 50S subunit (LSU, left) and 70S ribosome (right) from *P. calidifontis*. The LSU central protuberance (CP) and SSU head are marked for reference. **b**, rProteins are labeled on the model of the *P. calidifontis* 70S ribosome. Archaea-specific rProteins are shown in red, and their previous annotations, including accession codes, are shown on the right.

In the cryo-EM structure of the *P. calidifontis* 70S ribosome, we were able to model all three rRNAs and 61 annotated rProteins (**Figure 4.1b**). Additionally, we found density for four proteins not annotated as rProteins in the *P. calidifontis* proteome. One of the proteins is a homolog of a previously identified archaea-specific rProtein, aS21[217]. For the other proteins, the cryo-EM maps had sufficient resolution to identify them using the automated modeling software ModelAngelo[198]. Demonstrating the strength of this technique, we were able to identify a protein that was present in the *P. calidifontis* genome but absent in the UniProt proteome (aS35 in **Figure 4.1b**). The other two rProteins were annotated as proteins with unknown function, which we designate as aL48 and aL49. We further confirmed the identities of these proteins using mass spectrometry (**Tables S4.7** and **S4.8**). These proteins are archaea-specific rProteins that are distributed in the order Thermoproteales (**Extended Figure 4.1b**).

Our high-resolution cryo-EM maps allowed us to identify magnesium and zinc binding sites (**Extended Figure 4.1c**) and putative pseudouridylation, nucleobase methylation and acetylation, and 2′-*O*-methylation sites in the *P. calidifontis* ribosome (**Extended Figure 4.1d-e**).

Previously, it was shown that N^4-acetylcytidine is a widespread modification in ribosomes from the hyperthermophilic archaea *Thermococcus kodakarensis* and that the number of N^4-acetylcytidine modifications increases with growth temperature[35]. In addition, the *T. kodakarensis* ribosome harbors numerous 5-methylcytidine sites that support growth at high temperature[36]. In *P. calidifontis* ribosomes purified from stationary phase cultures, we find very few potential N^4-acetylcytidine or 5-methylcytidine sites, whereas the predominant post-transcriptional modification is 2′-*O*-methylation. Additionally, putative post-transcriptional modifications are mainly buried in the core of the *P. calidifontis* ribosomal subunits and are less widely distributed compared to their distribution in ribosomes from *T. kodakarensis* (**Extended Figure 4.1f**). The limited distribution of post-transcriptional modifications has also been observed in the ribosomes from *Saccharolobus solfataricus*[9,35], another member of Thermoprotei.

Highly divergent PTCs from a subset of archaea

We mined genomes from the Genome Taxonomy Database (GTDB) for 23S rRNA sequences to ascertain how broadly PTC sequence variation occurs in bacteria and archaea. This resulted in alignments of 23S rRNAs from 3,686 archaeal and 58,032 bacterial species (**Figures S4.3 and S4.4**). Overall, many PTC positions are more variable in archaea than in bacteria when comparing Shannon entropy of nucleotide frequencies between the archaeal and bacterial 23S rRNA alignments (**Extended Figure 4.2a**). Within these alignments, we found nine archaeal orders that have sequence variation at more than 7 out of 30 PTC positions (**Figures S4.3 and S4.4**). Species in the archaeal order Parvarchaeales[218], phylum Nanoarchaeota, have sequence variation at up to eleven positions in the PTC, the most in archaea (**Extended Figure 4.2b**). In clades with high levels of PTC sequence variation, only species in the archaeal classes Thermoprotei and Methanomethylicia have been cultured. These organisms vary at up to eight PTC positions, six of which span the core regions 2447-2453 and 2500-2504 (*Escherichia coli* 23S rRNA numbering) (**Figure 4.2a**). The *P. calidifontis* ribosome varies at five positions in these regions, including nucleotides 2447, 2453, 2500, 2501, and 2504 (**Figure 4.2b**).

To understand how natural nucleotide variations affect PTC structure, we compared the cryo-EM structure of the *P. calidifontis* 50S subunit to the X-ray crystal structure of the *Haloarcula marismortui* 50S subunit (PDB:1S72)[219], which has a canonical PTC sequence. Here, we use *E. coli* 23S rRNA numbering and a conversion table to *P. calidifontis* numbering is in **Table S4.9**. One set of nucleotides affected by rRNA sequence variation is 2063, 2450, and 2501, which forms the canonical C2063-A2450-C2501 base triple in *H. marismortui*. In *P. calidifontis*, the base triple is disrupted by a C to A change at position 2501 and A2501 adopts a *syn*-conformation to make a Hoogsteen base pair with A2450 (**Figure 4.2c** and **Extended Figure 4.2c**).

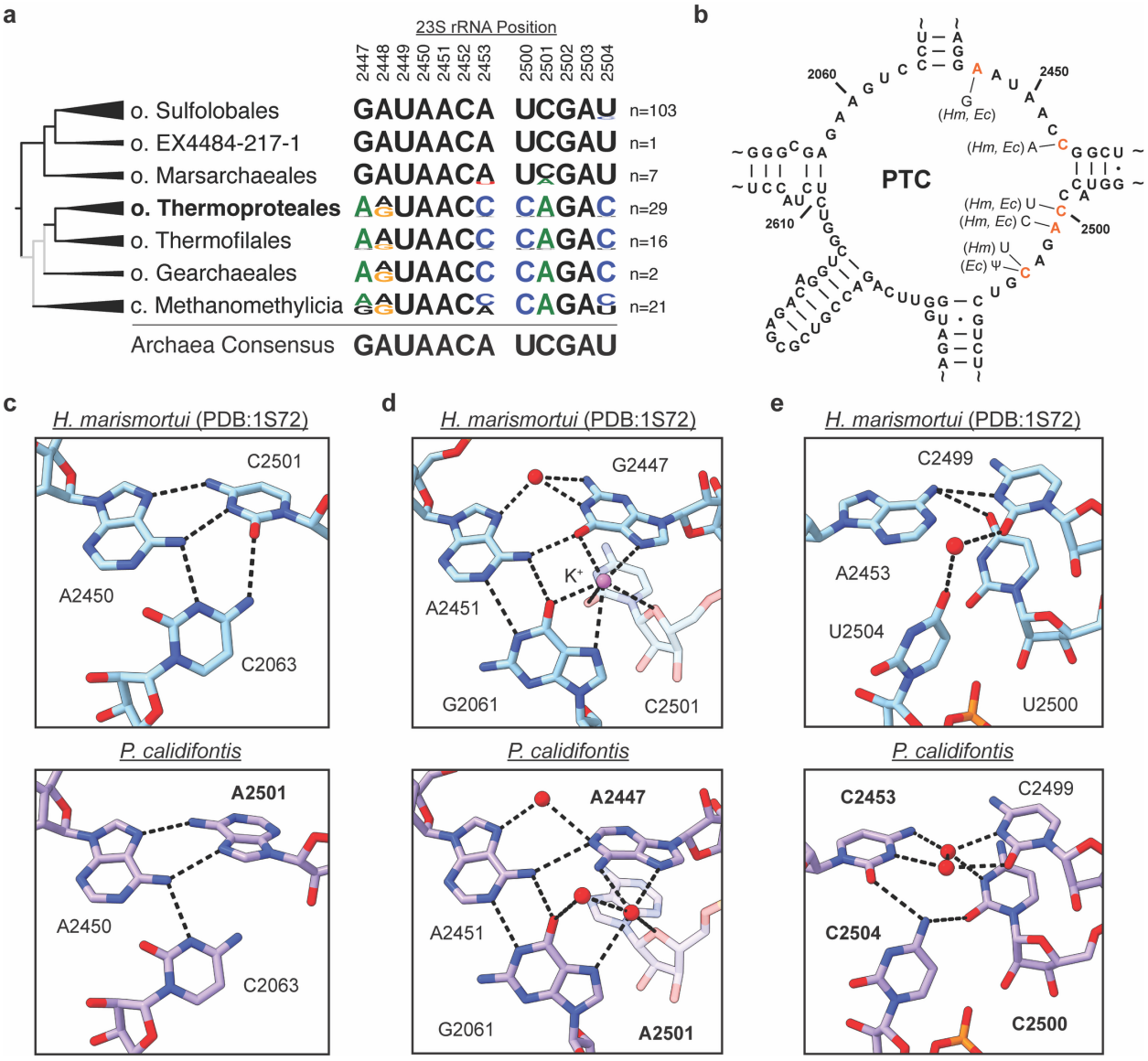


Figure 4.2. Sequence variation in the *P. calidifontis* PTC. **a**, Distribution of rare PTC sequences in archaea. The cladogram is derived from the GTDB phylogeny, where branches with bootstrap support <50% are colored in grey. o and c represent order and class respectively, and n represents the number of 23S rRNA sequences in each distribution. Nucleotides that differ from the archaeal consensus sequence are shown in color. **b**, Secondary structure of the *P. calidifontis* PTC. Positions that differ from the consensus sequence in the 2447-2453 and 2500-2504 regions are colored orange and the nucleotide identities in *H. marismortui* (*Hm*) and *E. coli* (*Ec*) 23S rRNAs are indicated. Positions are labeled according to *E. coli* 23S rRNA numbering. **c-e**, Comparison of the PTCs in *H. marismortui* PDB:1S72[219] (top) and *P. calidifontis* (bottom). Water molecules and potassium ions are shown as red and pink spheres respectively. Hydrogen bonds, shown with dashes, were calculated in ChimeraX[108].

A second region of the PTC affected by sequence variation in *P. calidifontis* involves the interaction between bases 2061, 2447, and 2451. In *H. marismortui*, G2447 hydrogen bonds with A2451 and coordinates a potassium ion that interacts with G2061 and C2501. *P. calidifontis* contains a G2447A change that preserves hydrogen bonding to A2451 (**Figure 4.2d** and **Extended Figure 4.2d**), consistent with a report that a G2447A mutation is viable in *E. coli*, and ribosomes with this mutation support cellular protein synthesis[70]. However, the A2447 change, along with

the *syn* conformation of A2501, results in loss of the potassium ion binding site seen in the *H. marismortui* ribosome, with a concomitant positioning of two water molecules that bridge bases A2061, A2447, and A2501 (**Figure 4.2d**). The third major rearrangement occurs due to three differences in the *P. calidifontis* rRNA at positions 2453, 2500, and 2504, which are all cytidines. In *H. marismortui*, these three bases interact with the base of C2499, forming sparse hydrogen bonding. In *P. calidifontis*, these four bases form a more complex hydrogen bonding network that interacts with two ordered water molecules (**Figure 4.2e** and **Extended Figure 4.2e**). Comparison of the PTCs from *P. calidifontis* and *E. coli* revealed similar differences (**Figure S4.5**).

Another difference in the rRNA from *P. calidifontis* occurs in the A loop of the LSU, which serves as the binding site for the CCA-end of the A-site transfer RNA (tRNA)[73]. We previously reported that rare uridine to cytidine sequence variation at positions 2554 and 2555 of the A loop is found in Thermoprotei archaea and this sequence variation stabilizes the LSU from thermal denaturation[148]. Comparing the A loop from *P. calidifontis* and *H. marismortui*, which has uridines at positions 2554 and 2555, cytidines at positions 2554 and 2555 in *P. calidifontis* have altered positioning so that they stack with each other and G2553 (**Extended Figure 4.2f-h**). We did not observe this conformational change in *E. coli* ribosomes with U2554C/U2555C mutations that contained an A-site tRNA, suggesting that this conformation may only exist in the apo ribosome[148]. These stacking interactions may rigidify the A loop, which is part of the last region of the 23S rRNA to fold during ribosome assembly[129], to help stabilize the LSU.

Differences in archaeal uL3 enable PTC sequence variation

P. calidifontis PTC sequence variation occurs at positions where mutations are not tolerated in the *E. coli* ribosome. Single point mutations at positions A2453C, U2500C, and U2504C inactivate or greatly decrease the activity of *E. coli* ribosomes[65] and *E. coli* ribosomes with these individual mutations cannot support growth *in vivo*[115]. Conversely, ribosomes from halophilic archaea with these point mutations can support growth *in vivo*, albeit with decreased growth rates[220,221]. It is unclear why these mutations are accommodated in archaeal ribosomes, but not in *E. coli* ribosomes.

As the *P. calidifontis* ribosome has cytidine residues at positions 2453, 2500, and 2504, we compared its structure to the *E. coli* ribosome[99]. In the *E. coli* ribosome, Ψ2504 base pairs with C2452, and A2453 base pairs with U2500, distinct from the complex hydrogen bonding network seen in *P. calidifontis* (**Figures 4.2e and 4.3a**). For the interactions to form in *P. calidifontis*, C2504 flips up 54° compared to Ψ2504 in *E. coli*, and to avoid steric clashes, A2572 moves out of the way compared to its position in *E. coli*. However, the shift in A2572 in *P. calidifontis* can only occur because rProtein uL3 is shorter in *P. calidifontis* than in *E. coli* near the PTC (**Figure 4.3b**). The region of uL3 proximal to the PTC is extended in most bacteria compared to archaea and eukaryotes (**Extended Figure 4.3a**). If uL3 were not shorter in *P. calidifontis*, A2572 would clash with *E. coli* uL3 residue Q150, which is post-translationally methylated[222]. Interestingly, the flipped conformation of nucleobase 2504 is found in other archaeal ribosomes and is not exclusive to ribosomes with sequence variation at position 2504 (**Extended Figure 4.3c**).

We wondered whether positions 2453, 2500, and 2504 are mutable in archaea, but not in *E. coli*, because of the rearrangement of base 2504 and a shorter uL3 sequence. To test this hypothesis, we used CRISPR-Cas9 editing[213] to delete Q150 from the *rplC* gene (ΔQ150-uL3) in *E. coli* (**Extended Figure 4.3b**). We find that ΔQ150-uL3 *E. coli* are viable and have no major growth defects other than a modest increase in the lag phase (**Figure 4.3c**). Next, we isolated ribosomes from WT or ΔQ150-uL3 *E. coli* strains. *E. coli* ribosomes with ΔQ150-uL3 display WT

levels of activity in an *in vitro* translation assay, indicating that the extended uL3 loop is not essential for PTC function (**Figure 4.3d**). Surprisingly, *E. coli* ribosomes with WT-uL3 and A2453C, U2500C, and U2504C (3M) 23S rRNA mutations have 18% of WT activity, suggesting there is a synergistic effect between these mutations even with the longer uL3 loop. Consistent with our hypothesis, *E. coli* ribosomes with ΔQ150-uL3 and 3M mutations have 34% of WT activity, demonstrating that the length of uL3 modulates the mutability of these rRNA positions.

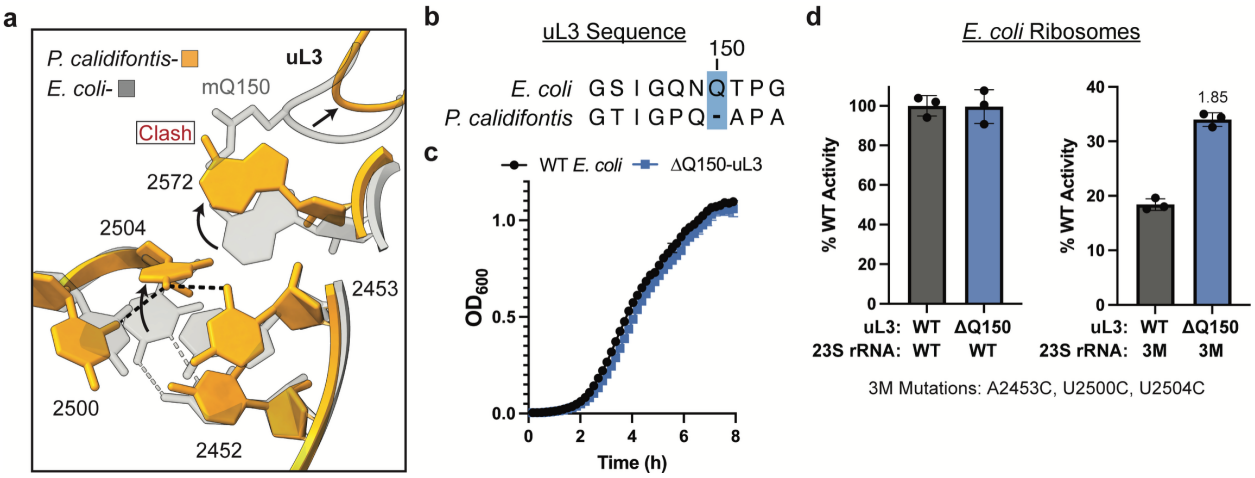


Figure 4.3. uL3 length affects the mutability of PTC rRNA. **a**, Comparison of the PTC and uL3 in *P. calidifontis* (yellow) and *E. coli* PDB:7K00[99] (grey). Positions are labeled according to *E. coli* 23S rRNA numbering. **b**, Protein alignment for *E. coli* and *P. calidifontis* uL3 loops that interact with the PTC. **c**, Growth curve of WT and ΔQ150-uL3 *E. coli*. Each data point is the average of three independent measurements and error bars represent the standard deviation of the three measurements. **d**, HiBiT *in vitro* activity assays for mutant *E. coli* ribosomes. Ribosome activity is the slope of the increase in luminescence signal in each *in vitro* translation reaction (methods) and activities were normalized to WT. Each point on the graph represents an individual measurement, and data and error bars represent the mean and standard deviation of the three measurements, respectively. The fold change from the WT uL3 control is indicated on top of the bar. A two-sided, two-sample *t*-test was used to compare values (p-values: 0.95, left panel, and $8x10^{-5}$, right panel).

Dri is an archaeal ribosome hibernation factor

In the *P. calidifontis* cryo-EM maps, we found density in both the isolated 50S subunit and the 70S complex that did not correspond to a known component of the ribosome (**Figure 4.4a**). After 3D classification (**Figure S4.1**), we were able to attribute the density to a protein of unknown function using the protein sequence predicted by ModelAngelo[198] and we verified its presence by mass spectrometry (**Tables S4.7 and S4.8**). We designate this protein **D**ual **R**ibosomal subunit **I**nhibitor (Dri) due to its positioning in the ribosome. Dri contains eight cystathionine-β-synthase (CBS) domains[223] that form two disc-shaped lobes, each comprised of four CBS domains (**Figure 4.4a**). We found that the Dri C-terminal lobe binds to the P and E sites of the SSU on the 70S ribosome (**Figure 4.4b**) and interacts with the ribosome in the rotated state (**Extended Figure 4.4a**). An extended loop of the C-terminal lobe reaches into the SSU and blocks the mRNA binding channel (**Figure 4.4b**). Additionally, there is a disordered 24 amino acid loop in the C-terminal lobe that points towards the A site and could block the binding of the A-site tRNA in the SSU. In the majority of 70S particles, the Dri C-terminal lobe is bound to the SSU. However, we also see populations of 70S particles where the N-terminal lobe is bound to the LSU and where both the N- and C-terminal lobes are bound to the ribosome concurrently (**Figure S4.1**).

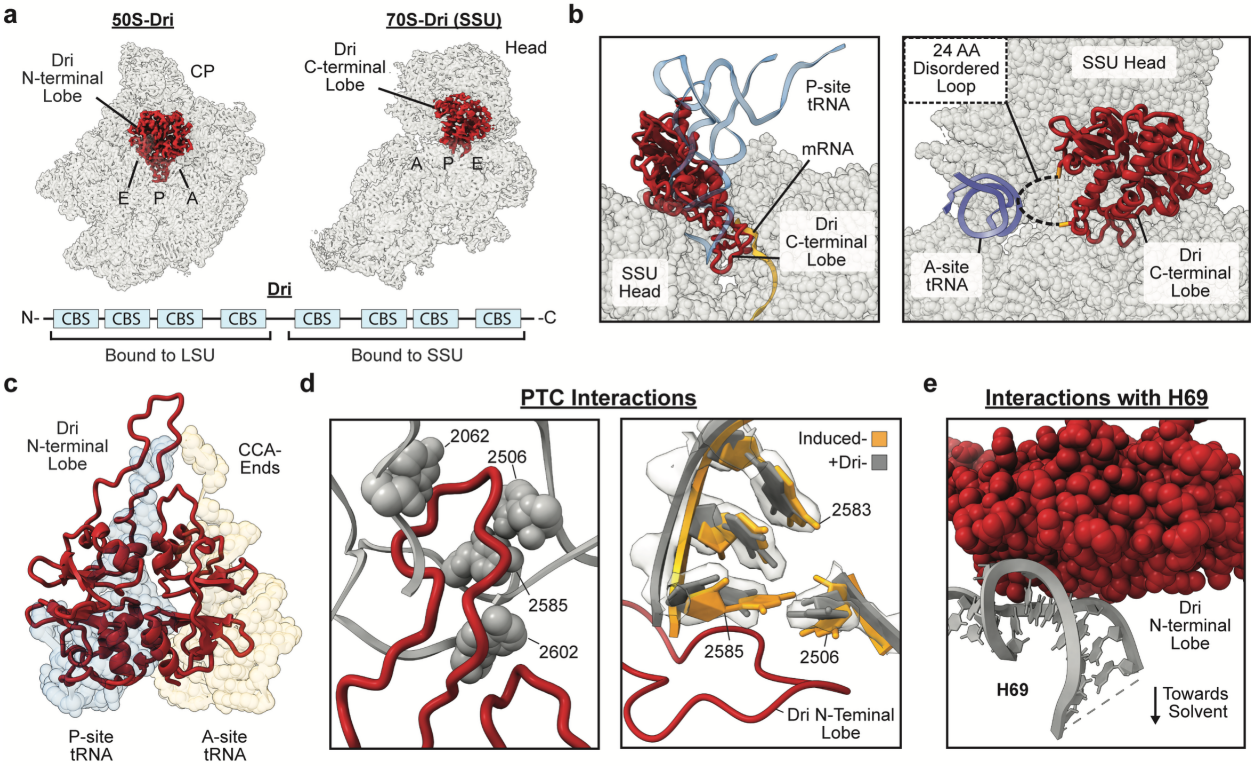


Figure 4.4. Dri binding sites on the ribosome. **a**, Cryo-EM density for the N- and C- terminal lobes of Dri on the isolated 50S (left) and SSU of the 70S ribosome (right) viewed from the subunit interface. The SSU head and LSU central protuberance (CP) are labeled. The domain architecture of Dri is shown below. **b**, (left) The Dri C-terminal lobe binds to the small subunit and blocks the mRNA channel in the P and E sites. The mRNA and P-site tRNA from PDB:7K00[99] are overlayed on the *P. calidifontis* structure. (right) A disordered loop of Dri points into the A site of the SSU. The A-site tRNA from PDB:7K00[99] is overlayed on the *P. calidifontis* structure. **c**, The Dri N-terminal lobe occupies a similar position to the A- and P-site tRNAs on the LSU from PDB:7K00[99]. **d**, (left) The P-site loop of Dri extends into the PTC and contacts key PTC nucleotides. (right) PTC nucleotides that participate in the tRNA induced fit are shown when tRNA is bound to the *Thermus thermophilus* ribosome (gold, PDB:1VY4[105]) or when Dri is bound to the *P. calidifontis* LSU (grey and cryo-EM density). **e**, The N-terminal lobe of Dri makes extensive contacts with H69 of the LSU.

The Dri N-terminal lobe is bound to the isolated 50S subunit and the LSU of the 70S ribosome (**Figure S4.1**) and occupies the A-site and P-site tRNA binding sites (**Figure 4.4c**). There is an extended loop off the N-terminal lobe that reaches into the P-site of the PTC and mimics aminoacyl-tRNA binding to the 50S subunit[105,106] (**Extended Figure 4.4b**), inducing the active conformation of the PTC[224] (**Figure 4.4d**). Dri binding also stabilizes uL16 in an ordered conformation previously observed upon P-site tRNA binding[225,226] (**Extended Figure 4.4c**). There is strong density for PTC nucleotides when the Dri N-terminal lobe is bound to the 50S subunit (**Extended Figure 4.4d**), while in its absence, several regions of the PTC are disordered. Dri further interacts with the 50S subunit by making extensive contacts with helix H69, a region of 23S rRNA that makes important bridges with the SSU during subunit joining[227] (**Figure 4.4e**).

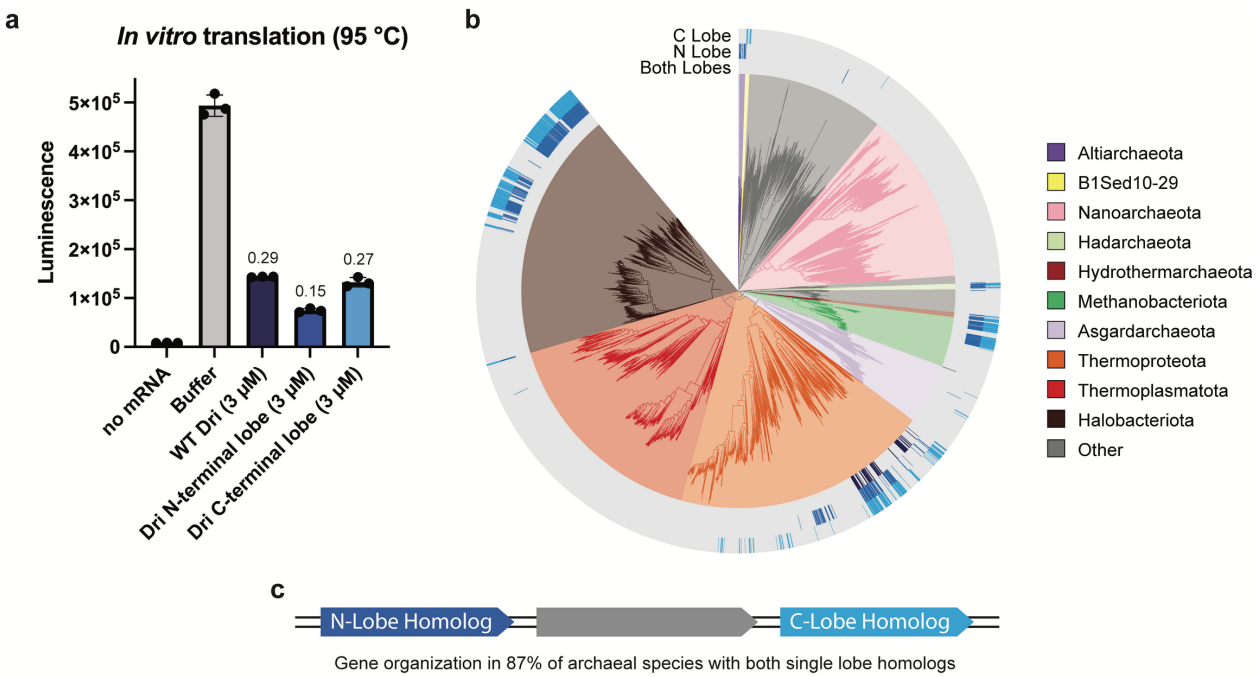


Figure 4.5. Translation inhibition and phylogenetic distribution of Dri homologs. **a**, *P. calidifontis* lysate-based *in vitro* translation assay. After translation of the HiBiT peptide, luminescence was measured from the HiBiT-LgBiT complex. For the no mRNA and buffer controls, 3 μL of Dri buffer A was added to the reaction. Each point on the graph represents an individual measurement, and data and error bars represent the mean and standard deviation of the three measurements, respectively. The fold change from the buffer control is indicated on top of each bar. A two-sided, two-sample *t*-test was used to compare values (p-values from left to right: $1x10^{-5}$, $5x10^{-6}$, $1x10^{-5}$). **b**, Phylogenetic distribution of Dri homologs indicated on the GTDB archaeal phylogeny. Dri homologs with only a C-terminal or N-terminal lobe are shaded in the outer and middle rings. Dri homologs with two lobes that align to both Dri lobes are shaded in the inner ring. **c**, Archaeal genome architecture of Dri homologs.

Since Dri occludes the tRNA binding sites on the LSU and SSU, we hypothesized that Dri is an archaeal-specific ribosome hibernation factor. We developed a *P. calidifontis* lysate-based *in vitro* translation system to translate a HiBiT peptide reporter[95] using the optimized conditions for hyperthermophilic archaeal *in vitro* translation systems[228]. Upon addition of an mRNA encoding the HiBiT peptide to the *in vitro* reaction, we observed robust translation at 95 °C (**Figure 4.5a**). We recombinantly expressed the full-length WT Dri protein and the Dri N-terminal and C-terminal lobes separately (**Extended Figure 4.5a**). Addition of full-length Dri to the *in vitro* translation reaction inhibited peptide output substantially, as did addition of the isolated N-terminal and C-terminal lobes (**Figure 4.5a**). These results show that each lobe of Dri can inhibit translation. Titrations of the full-length WT Dri protein showed that lower concentrations of Dri partially inhibit the *in vitro* translation reaction (**Extended Figure 4.5b**). In addition, the isolated N-terminal lobe shows higher levels of translation inhibition than the C-terminal lobe or full-length protein.

Ribosome hibernation factors bind to ribosomes during cellular stress or when cells reach stationary phase[41,46]. To examine if Dri was present in our cryo-EM structures because ribosomes were purified from *P. calidifontis* cultures at stationary phase, we isolated ribosomes from mid-logarithmic phase (OD_{600} 0.07) or stationary phase (OD_{600} 0.15) cultures (**Figure S4.6**) using sucrose gradients. A population of 70S ribosomes could be isolated from cells grown in both conditions (**Extended Figure 4.5c**). Using mass spectrometry, we quantified the relative

abundance of Dri in both samples and found that Dri is present at equal levels with respect to ribosomal proteins from stationary and logarithmic phase cultures (**Extended Figure 4.5d**). We also wondered if Dri binding to the ribosome occurs due to cold shock in the cell isolation and lysis steps. If Dri binding to the ribosome constitutes a fast cellular response to cold shock, we would expect Dri to be expressed at both logarithmic and stationary phase. We compared the levels of Dri mRNA and ribosomal protein uL2 mRNA in logarithmic and stationary phase cultures and found that the ratio of Dri to uL2 expression is only slightly increased at stationary phase, indicating that Dri is expressed even during active growth (**Extended Figure 4.5e**).

To determine the phylogenetic distribution of Dri, we searched the genomes of all GTDB archaeal species for Dri homologs by sequence homology. We found full length homologs (containing both the N- and C-terminal lobes) mainly in the archaeal phylum Thermoproteota (**Figure 4.5b** and **Extended Table 4.1**). These homologs contain extended loops in both the N- and C-terminal lobes that likely interact with the PTC and mRNA channel in a similar manner to Dri. Interestingly, we also found truncated Dri homologs comprised of only the N- or C-terminal lobe broadly distributed in at least seven archaeal phyla including Halobacteriota and Methanobacteriota and in archaea that have different levels of PTC variation (**Figure S4.7**). Since the Dri N- and C-terminal lobes separately inhibit *P. calidifontis* translation, we hypothesize that single-lobed Dri homologs function as ribosome hibernation factors. The single-lobed homologs frequently co-occur, as 59% of genomes that contain one homolog also contain the other, and they are typically found in the same gene order, separated by an additional gene (**Figure 4.5c**).

To further assess if single-lobed Dri homologs associate with the ribosome, we isolated 70S ribosomes from a stationary phase culture of *Methanosarcina acetivorans*, a member of Halobacteriota (**Extended Figure 4.5f**). We detected the *M. acetivorans* Dri C-terminal lobe homolog in the 70S ribosome sample with mass spectrometry, suggesting that this homolog also binds to the ribosome (**Table S4.10**). Interestingly, in the *M. acetivorans* 70S ribosome sample we also found the CBS-domain containing protein encoded by the gene located between the Dri N- and C-terminal lobe homolog genes, consistent with these proteins binding to ribosomes.

4.5 Discussion

Here, we show that one of the most conserved elements of the ribosome, the PTC, is highly divergent in certain archaeal ribosomes. Our finding that natural PTC sequence variation is more widespread in archaea than in bacteria suggests that there are differences in bacterial ribosomes that limit PTC variability. These differences could have allowed PTC variation to accumulate in archaea without major fitness effects, while limiting variation in bacteria. Additionally, large differences in growth temperatures and growth rates among microbes, such as *E. coli* (37 °C and ~20 minutes) and *P. calidifontis* (92 °C and ~5.5 hours)[194], may require different rates of protein synthesis and impose different constraints on the PTC sequence. Four of the nucleotide variations found in *P. calidifontis* were shown to confer resistance to PTC inhibitors, including linezolid[221] (A2453C, U2500C, and U2504C), anisomycin[220,229] (G2447A, A2453C, and U2500C), and chloramphenicol[230] (U2504C). This suggests that, irrespective of how PTC variation was acquired in archaea, a consequence may be the evasion of PTC inhibition by small molecules. Further studies will be needed to understand if PTC variation accumulated in archaea due to increased mutational flexibility compared to bacteria, or if it provides advantages in the native environments of these microbes.

PTC sequence variation occurs at positions in the *P. calidifontis* ribosome that cannot be mutated in ribosomes from *E. coli*[65,115]. We show that the length of rProtein uL3 and nearby PTC

rearrangements are differences between bacterial and archaeal ribosomes that contribute to the accommodation of PTC sequence variation. In further support of this, it was shown that changes in the uL3 sequence near the PTC affects the conformation of PTC nucleotides in *Saccharomyces cerevisiae*[231]. The difficulty of mutating multiple PTC positions in *E. coli* has been a challenge in efforts to engineer the PTC for novel functions[51,52,66]. However, it has been shown that epistatic interactions in the PTC can compensate for deleterious mutations[232]. Here, we show that uL3 sequence and length modulate the mutability of PTC positions and demonstrate that modified rProteins could aid in the development of ribosomes with engineered active sites.

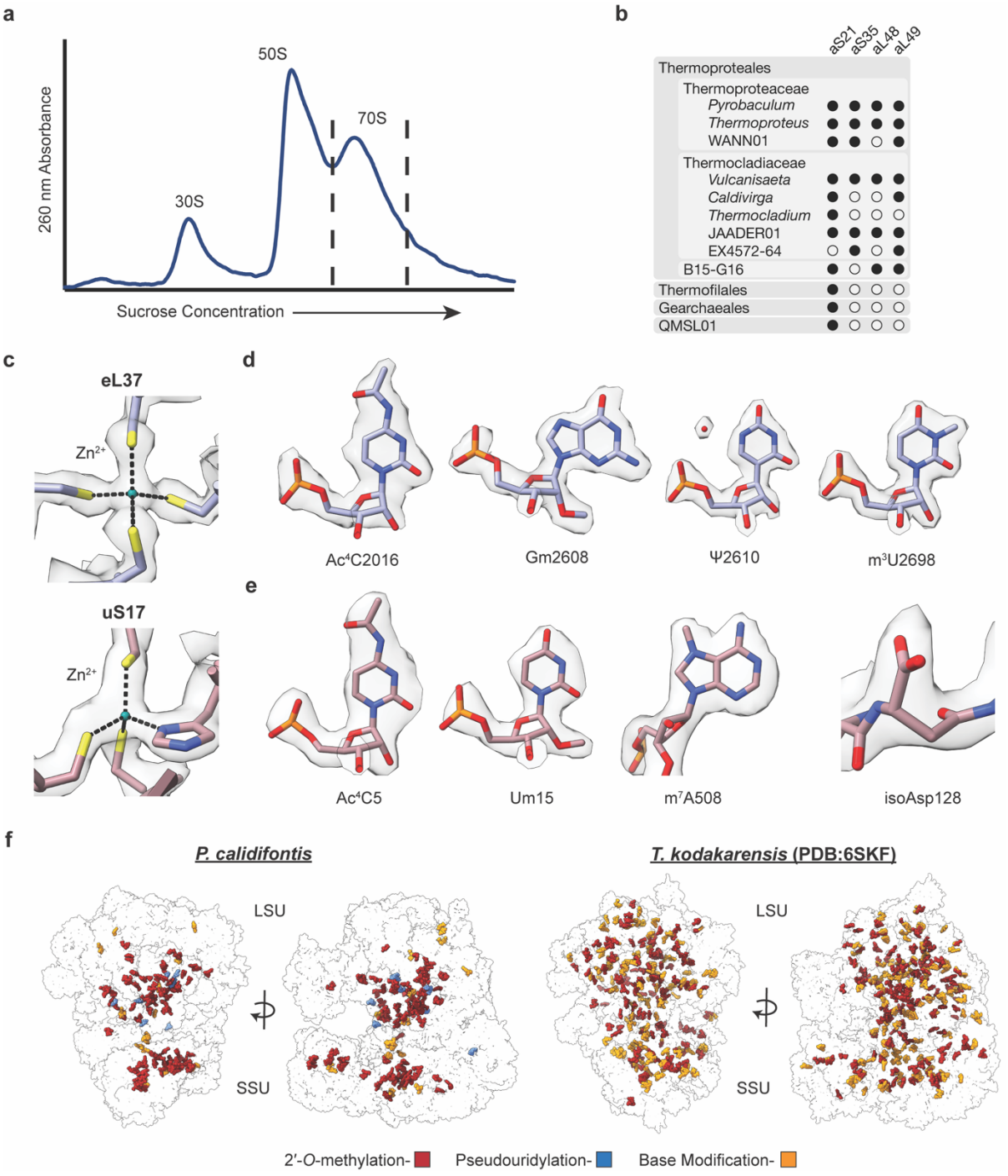
Ribosome hibernation has been well studied in bacteria and eukaryotes, but it was previously unknown what factors influence hibernation in archaea.[37,38] While a factor that dimerizes isolated 30S subunits was identified in the genus *Pyrococcus*, it remains unclear if it participates in ribosome hibernation or plays some unknown role.[233,234] Here, we describe a previously undescribed archaeal hibernation factor, Dri, that binds to the LSU and SSU of the ribosome. The Dri C-terminal lobe binds to the mRNA channel in the P and E sites, similar to known bacterial and eukaryotic hibernation factors[19,41,42]. The independent evolution of hibernation factors that target the mRNA channel in each domain of life underscores the importance of inactivating the SSU during hibernation.[37,38] The Dri N-terminal lobe binds to the LSU and makes extensive contacts in the PTC similar to some eukaryotic and bacterial hibernation factors (i.e. MDF2[19] and Balon[46]). In addition to blocking tRNA binding, the Dri N-terminal lobe may help chaperone the PTC during hibernation. Consistent with this hypothesis we find that the *P. calidifontis* PTC is disordered in the absence of Dri. Interactions between the Dri N-terminal lobe and H69 in the LSU, which makes important contacts with the SSU during subunit joining, could suggest that the N-terminal lobe may play a role in stabilizing hibernating 70S ribosomes.

We find Dri bound to ribosomes purified from stationary and logarithmic phase cultures and show that Dri is expressed in actively growing cells. As we do not expect a translation inhibitor to be bound to ribosomes during growth, Dri may bind to ribosomes once they stop translating, such as during cold shock. Dri may therefore play a role similar to the bacterial hibernation factor RaiA (protein Y), which binds to the ribosome during cold shock but not at temperatures optimal for translation[41]. At low micromolar concentrations, Dri does not fully inhibit *in vitro* translation reactions, while the reactions are inhibited by the more potent Dri N-terminal lobe, suggesting that the full length Dri is attenuated to spare actively translating ribosomes. The ability of Dri to be present in actively growing cells, while not interfering with translation, presents the opportunity for Dri to quickly bind and protect ribosomes when translation is downregulated in response to stress or cellular dormancy.

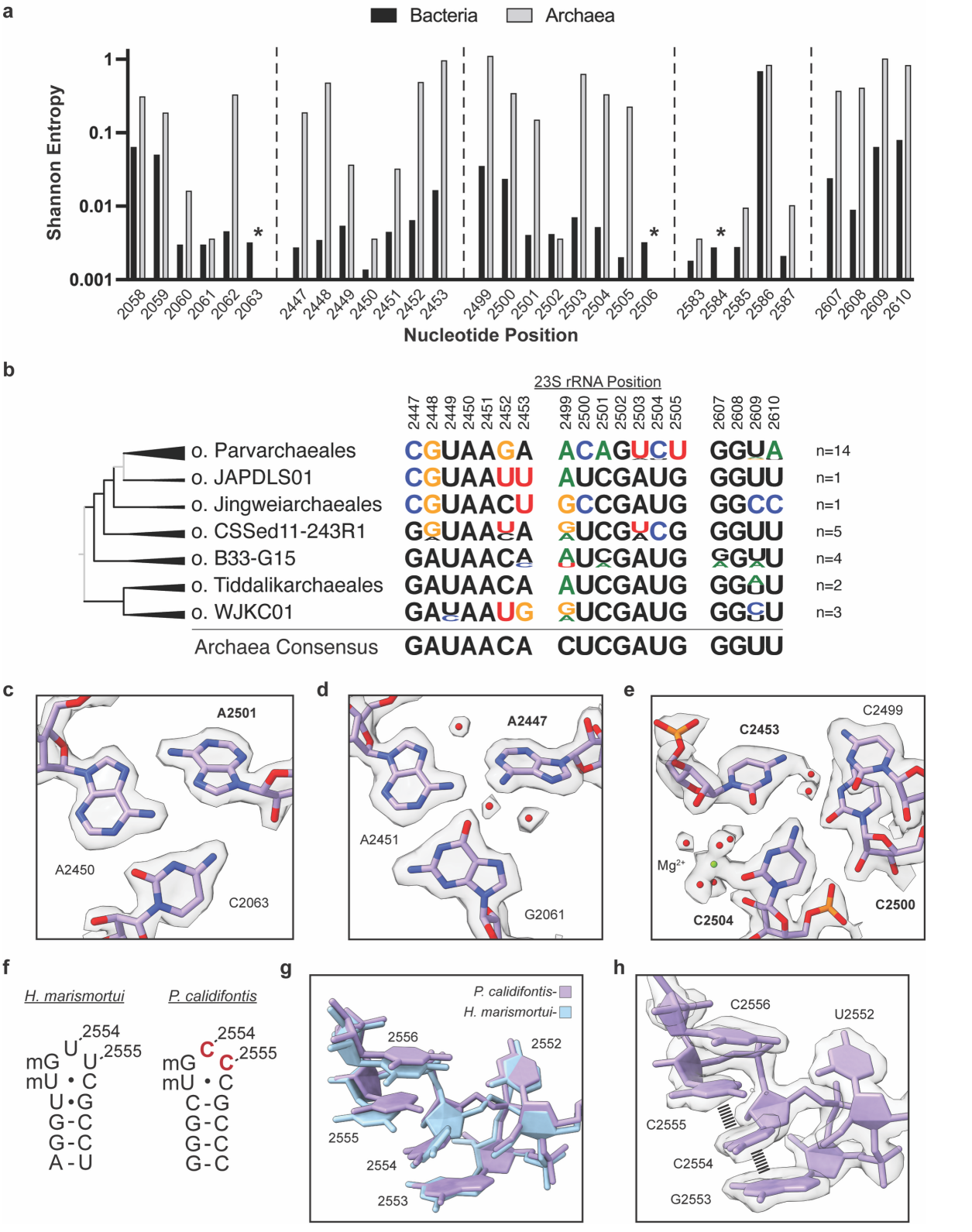
Dri is an archaea-specific ribosome hibernation factor that evolved separately from bacterial and eukaryotic hibernation factors. While some Dri homologs have two ribosome binding lobes, other homologs have a single lobe that would only interact with one of the ribosomal subunits. In many genomes, two single-lobed homologs are found in the same orientation, separated by a single gene, suggesting that full length Dri in Thermoproteota may have evolved by gene fusion of the more widely distributed single-lobed gene organization. Since the isolated N- and C-terminal Dri lobes can independently inhibit translation, the two single-lobed Dri homologs could work together to inhibit translation in a manner like the two-lobed homologs. We find that the *P. calidifontis* N-terminal Dri lobe is a more potent translation inhibitor than the C-terminal Dri lobe, suggesting that organisms could use single-lobed Dri homologs to control the levels of ribosome hibernation in response to different stimuli. Dri homologs are widespread in archaea throughout multiple phyla. While it has been suggested that hibernation factors evolved

after the split between Bacteria and Archaea/Eukaryota[38], the discovery of an archaea-specific hibernation factor suggests that ribosome hibernation may have also evolved independently in Archaea. Further studies of archaeal ribosome hibernation will help to uncover the evolution of this ubiquitous yet diverse regulatory process.

4.6 Extended Figures and Tables

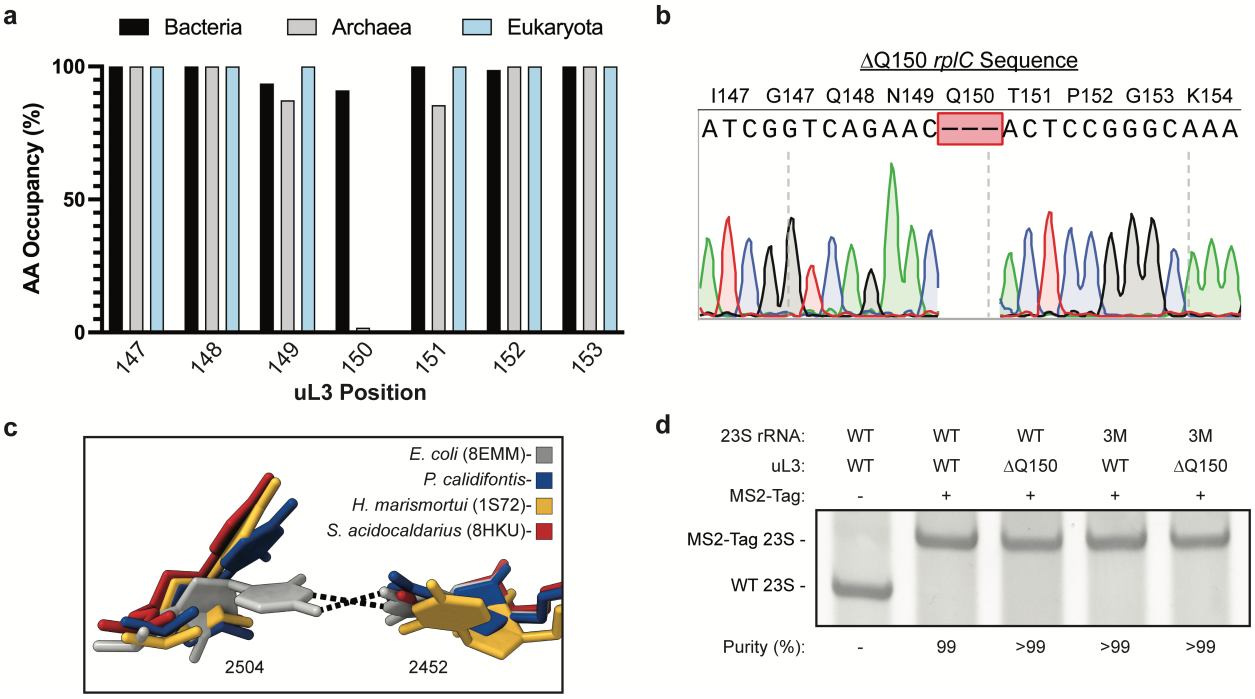


Extended Figure 4.1. Cryo-EM sample preparation and analysis of post-transcriptional modifications in *P. calidifontis*. **a**, Sucrose gradient fractionation of *P. calidifontis* ribosomes. Dashed lines bracket the sample that was collected for cryo-EM analysis. **b**, Distribution of archaea-specific rProteins across four orders and further subclades in the class Thermoprotei. Closed and open circles represent clades where rProtein homologs were or were not identified, respectively. **c**, Zinc binding sites in LSU rProtein eL37 and SSU rProtein uS17 with cryo-EM density. **d-e,** Cryo-EM density for representative post-transcriptional and post-translational modifications in the LSU (**d**) and SSU (**e**). **f**, Distribution of post-transcriptional modifications in *P. calidifontis* (left) and *T. kodakarensis* PDB:6SKF[35] (right). Note that pseudouridines are not modeled in *T. kodakarensis*.

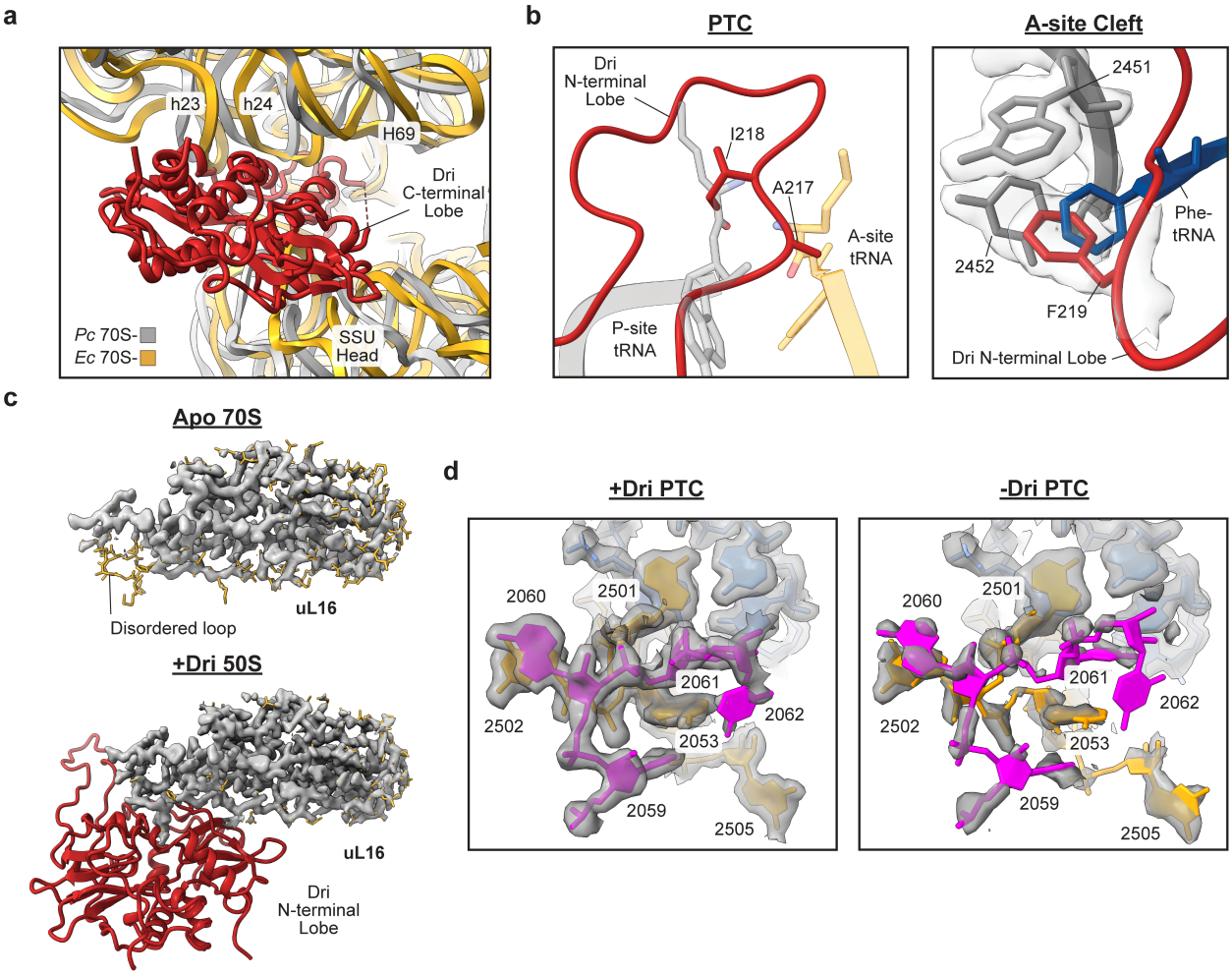


Extended Figure 4.2. Sequence and structural diversity in archaeal PTCs**. a**, Shannon entropy plot for PTC nucleotides in GTDB bacteria and archaea. Positions indicated by a * have a Shannon entropy value of zero for archaea. A Shannon entropy value of zero corresponds to complete conservation of the nucleotide, while a value of

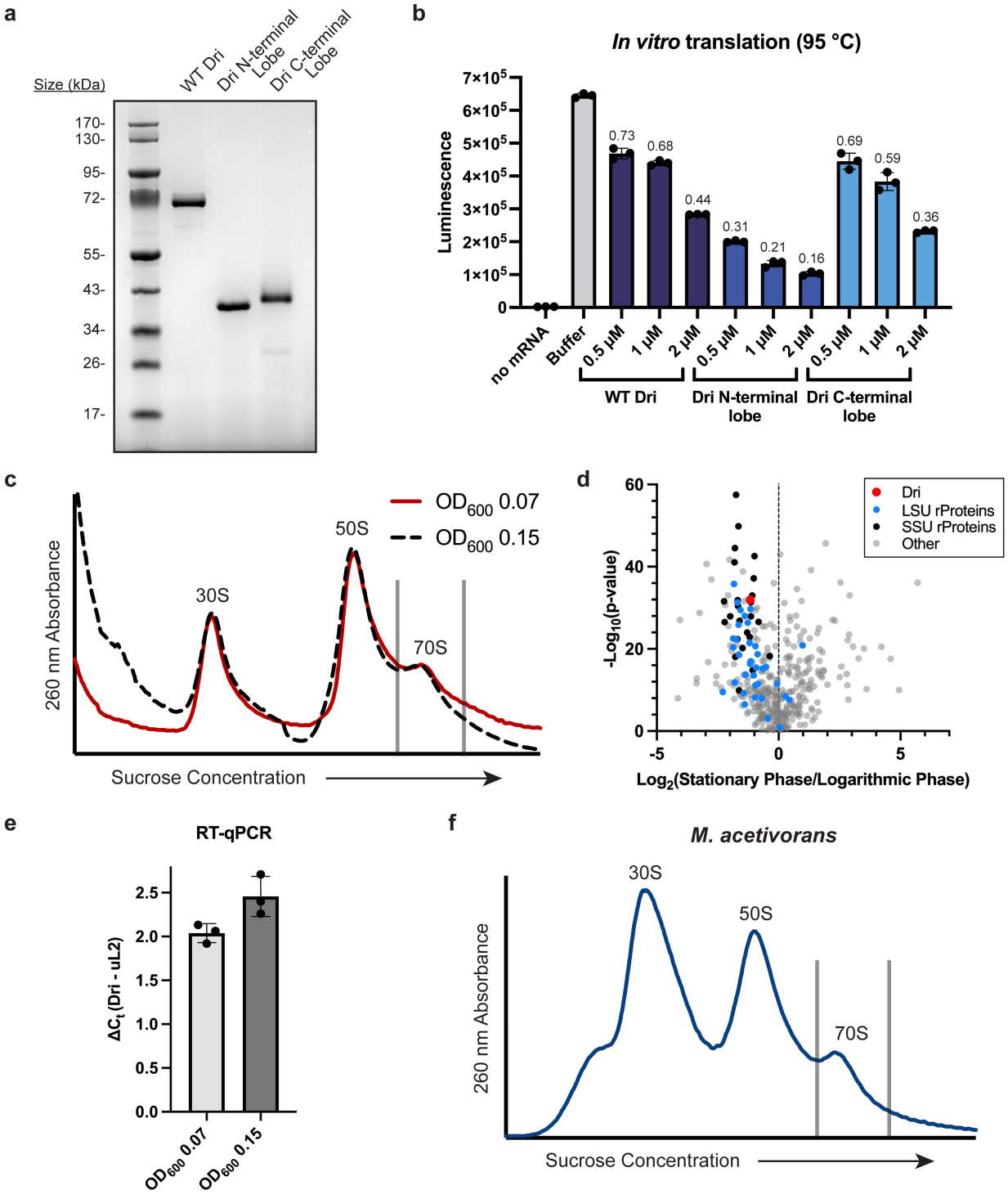
1.386 corresponds to an equal distribution of all four nucleotides. **b**, Distribution of rare PTC sequences in Nanoarchaeota archaea. The cladogram is derived from the GTDB phylogeny, where branches with bootstrap support <50% are colored in grey. The letter o represents order and n represents the number of 23S rRNA sequences in each distribution. Nucleotides that differ from the archaeal consensus sequence are shown in color. **c-e**, Cryo-EM density for regions of the PTC shown in Figure 2. Water molecules and magnesium ions are shown as red and green spheres respectively. **f**, Secondary structures of the *H. marismortui* and *P. calidifontis* A loops. Positions with rare sequence variation, 2554 and 2555, are highlighted in red in the *P. calidifontis* A loop. **g**, Comparison of the apical region of the A loop in *H. marismortui* PDB:1S72[219] (blue) and *P. calidifontis* (purple). **h**, Cryo-EM density for the *P. calidifontis* A loop. Base stacking interactions are shown as dashed lines.



Extended Figure 4.3. Differences in uL3 and the PTC between the domains of life. **a**, Amino acid occupancy in an alignment of uL3 sequences from representative species in bacteria, archaea, and eukaryotes[204]. **b**, Sequencing chromatogram for the *rplC* gene from ΔQ150-uL3 *E. coli*, showing the deletion of residue Q150. The chromatogram trace was broken at the site of deletion for clarity. **c**, Comparison of the positions of 23S rRNA nucleotides 2452 and 2504 in *E. coli* and archaeal ribosomes. **d**, RT-PCR purity assay for MS2-tagged *E. coli* ribosomes used in this study. Sample purity was quantified using the band intensities of the upper (MS2-tagged ribosome) and lower (WT ribosome) bands.



Extended Figure 4.4. Dri interactions with the ribosome. **a**, Dri (red) binds to the rotated state of the *P. calidifontis* ribosome (grey). An *E. coli* ribosome in the unrotated state (PDB:8EMM[106]) is overlayed for reference (grey). **b**, (left) Dri residues occupy the positions of the A and P-site amino acids in the PTC. The A and P-site tRNAs from PDB:8EMM[106] are overlayed on the *P. calidifontis* ribosome (right). Dri residue F219 occupies the A-site cleft in a position similar to phenylalanyl-tRNA^{Phe} (PDB: 1VY4[105]). **c**, In the absence of the Dri protein, a loop of rProtein uL16 is disordered (top). Cryo-EM density is shown in gray. Upon binding of the Dri N-terminal lobe to the LSU, the loop of uL16 becomes ordered (bottom). **d**, Cryo-EM density for PTC nucleotides in the 50S-Dri complex (left) or the composite 70S complex (right).



Extended Figure 4.5. Dri expression and association with the ribosome. **a**, Recombinantly expressed and purified Dri proteins resolved on a 4-12% polyacrylamide gel stained with Coomassie brilliant blue. **b**, *P. calidifontis* lysate-based *in vitro* translation assay. After translation of the HiBiT peptide, luminescence was measured from the HiBiT-LgBiT complex. For the no mRNA and buffer controls, 3 µL of Dri buffer A was added to the reaction. Each point on the graph represents an individual measurement, and data and error bars represent the mean and standard deviation of the three measurements, respectively. The fold change from the buffer control is indicated on top of each bar. A two-sided, two-sample *t*-test was used to compare values (p-values from left to right: $6x10^{-5}$, $3x10^{-6}$, $7x10^{-8}$, $4x10^{-8}$, $2x10^{-}$

^{7}, $4x10^{-8}$, $2x10^{-4}$, $9x10^{-5}$, $7x10^{-8}$). **c**, Sucrose gradient fractionation of ribosomes from *P. calidifontis* cultures grown to the indicated optical densities. Data was overlayed based on the 50S peak and grey lines bracket the sample that was collected for mass spectrometry. **d**, Fold change, measured by mass spectrometry, in protein levels from *P. calidifontis* 70S ribosomes samples isolated from stationary and logarithmic phase cultures. P-values were calculated with ANOVA in PEAKS Studio. **e**, The difference in Dri and uL2 mRNA C_t values from total RNA extracted from cultures at logarithmic (OD_{600} 0.07) or stationary (OD_{600} 0.15) phase, measured by RT-qPCR. Each point on the graph represents an individual measurement, and data and error bars represent the mean and standard deviation of the three measurements, respectively. A two-sided, two-sample *t*-test was used to compare values (p-value=0.046). **f**, Sucrose gradient fractionation of *M. acetivorans* ribosomes. Grey lines bracket the sample that was collected for mass spectrometry.

Extended Table 4.1. **Dri homologs in archaeal phyla**

Phylum	Species in Phylum	Species Containing a Homolog with Both Lobes	Species Containing a Homolog with Only the N-lobe	Species Containing a Homolog with Only the C-lobe
Altiarchaeota	33	0	17	0
B1Sed10-29	19	0	19	10
Iainarchaeota	101	0	0	0
Micrarchaeota	331	0	0	0
Undinarchaeota	6	0	2	0
SpSt-1190	10	0	0	0
Huberarchaeota	1	0	0	0
Nanohaloarchaeota	29	0	0	0
EX4484-52	34	0	0	0
Aenigmatarchaeota	165	0	0	1
Nanoarchaeota	847	0	0	0
Methanobacteriota_A	35	0	0	0
Hadarchaeota	27	0	0	15
Methanobacteriota_B	116	0	2	0
JACRDV01	1	0	1	1
Hydrothermarchaeota	23	0	14	15
Methanobacteriota	244	0	81	82
Asgardarchaeota	296	1	1	5
Thermoproteota	1264	90	151	173
Halobacteriota	1223	0	343	402
Thermoplasmatota	1064	0	1	0
Total	5869	91	632	704

4.7 Supplementary Information

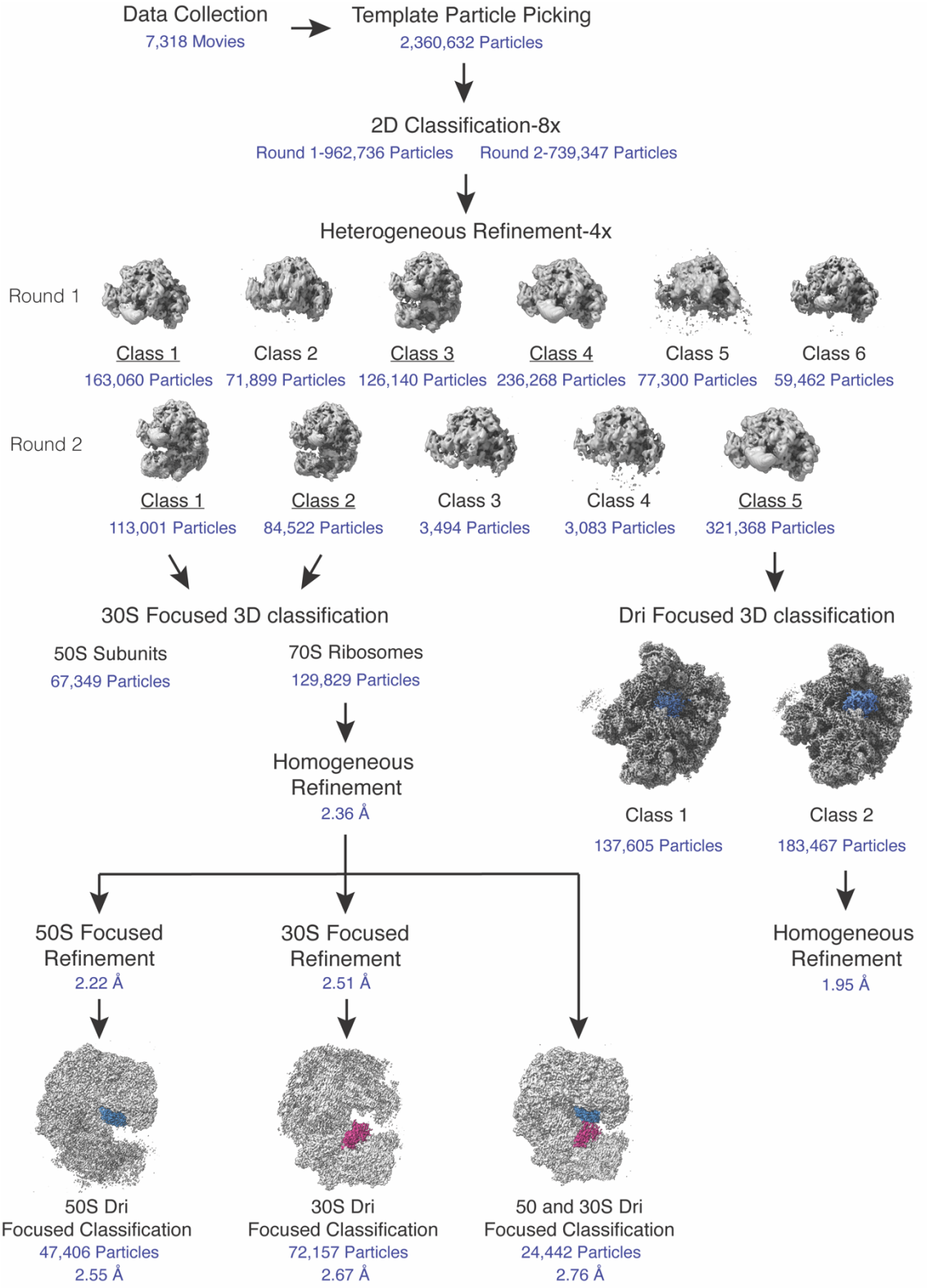


Figure S4.1. Cryo-EM processing workflow.

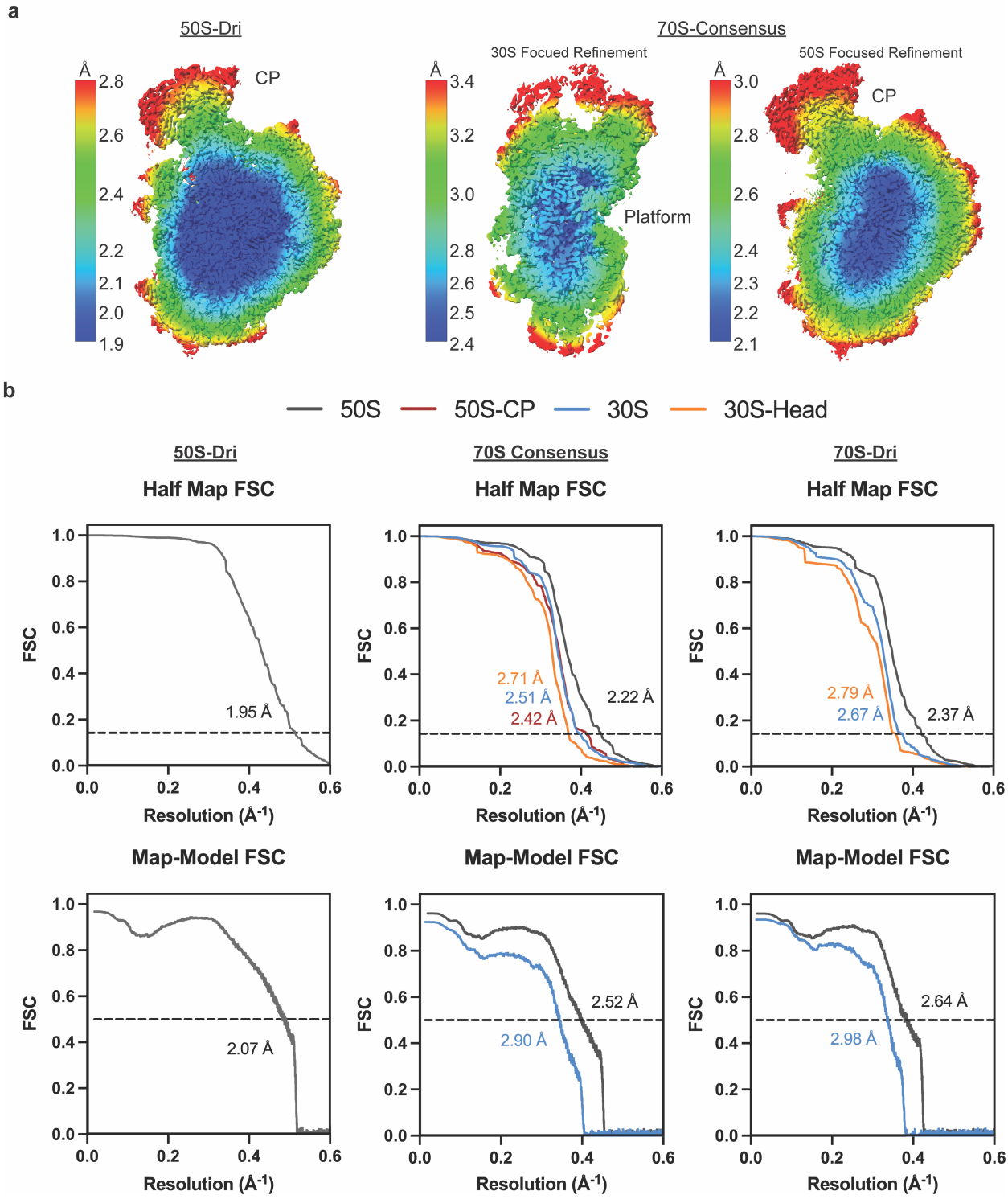


Figure S4.2. Resolution of cryo-EM maps. **a**, Local resolution plotted on the 50S (left) or 70S consensus (right) reconstructions. The 30S platform and 50S central protuberance (CP) are labelled. **b**, Half map (top) and map to model (bottom) FSCs for cryo-EM maps and models in this study.

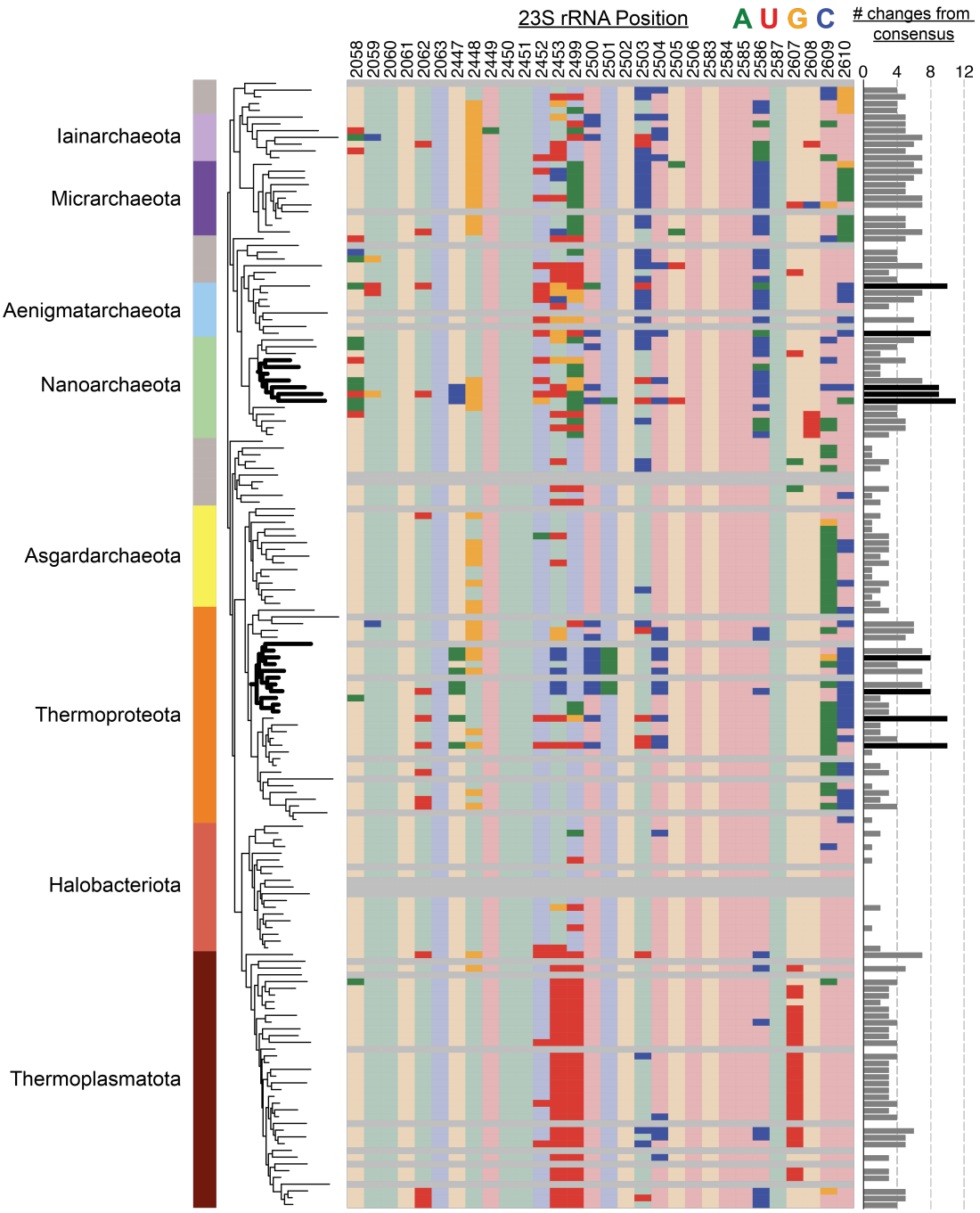


Figure S4.3. Distribution of PTC sequences from GTDB archaea. Each node in the tree represents one of 167 orders, and the corresponding sequence is the consensus sequence for species within the order, determined by taking the most frequent nucleotide at each position. A subset of archaeal phyla are represented by the bar on the left of the tree and other phyla are colored in grey. Grey nucleotides indicate that either no sequences were found, or the sequences contained gaps in the PTC nucleotides. Nucleotides that differ from the archaeal consensus sequence are colored according to nucleotide identity, and nucleotides that match the consensus are transparent. The number of nucleotides that differ from the archaeal consensus sequence are shown on the right. Branches of the tree that are bolded correspond to the tree in Fig. 2a (lower) and Extended Data Fig. 2b (upper).

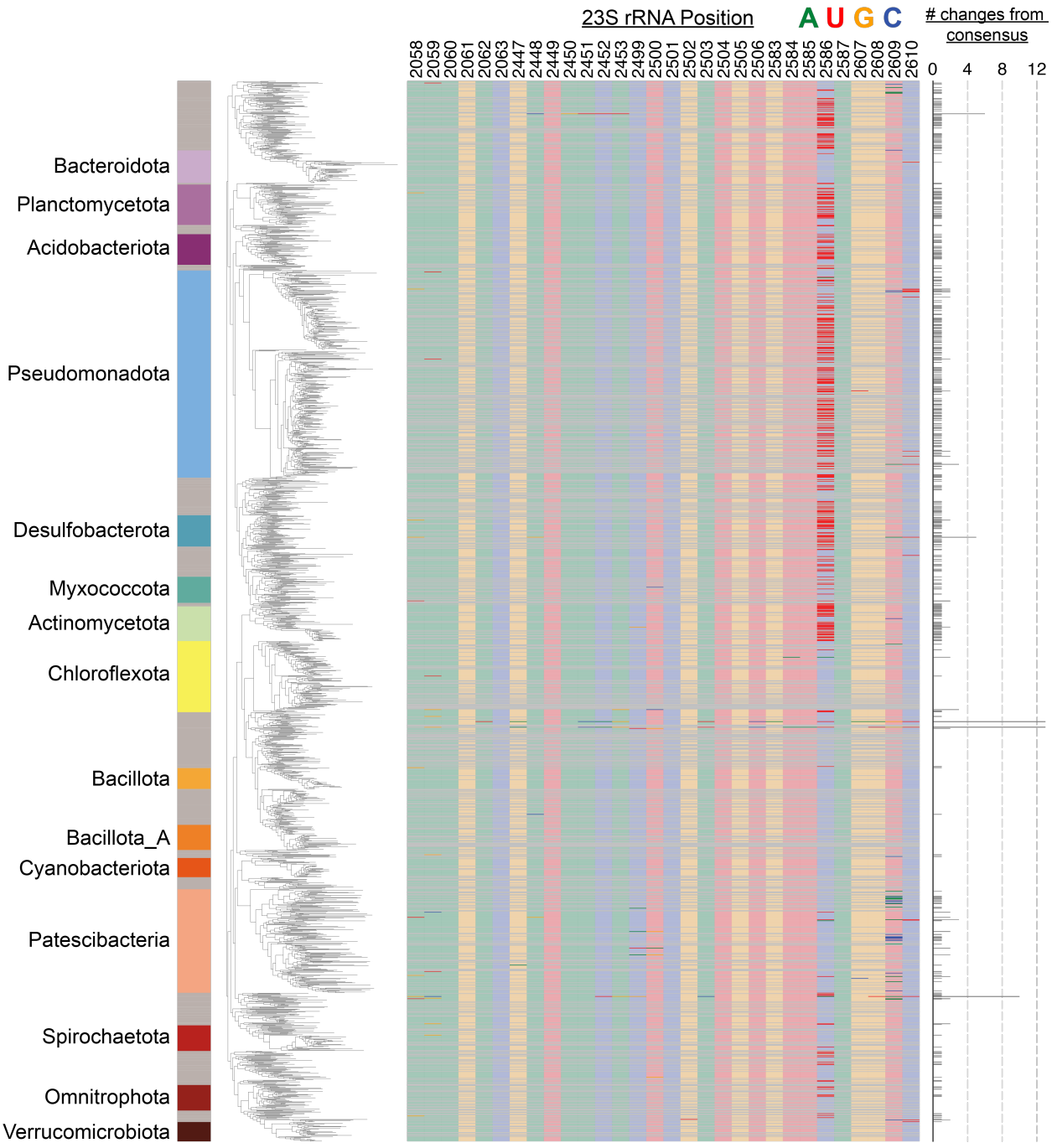


Figure S4.4. Distribution of PTC sequences from GTDB bacteria. Each node in the tree represents one of 1,863 orders, and the corresponding sequence is the consensus sequence for species within the order, determined by taking the most frequent nucleotide at each position. A subset of bacterial phyla are represented by the bar on the left of the tree and other phyla are colored in grey. Grey nucleotides indicate that either no sequences were found, or the sequences contained gaps in the PTC nucleotides. Nucleotides that differ from the bacterial consensus sequence are colored according to nucleotide identity, and nucleotides that match the consensus are transparent. The number of nucleotides that differ from the bacterial consensus sequence are shown on the right.

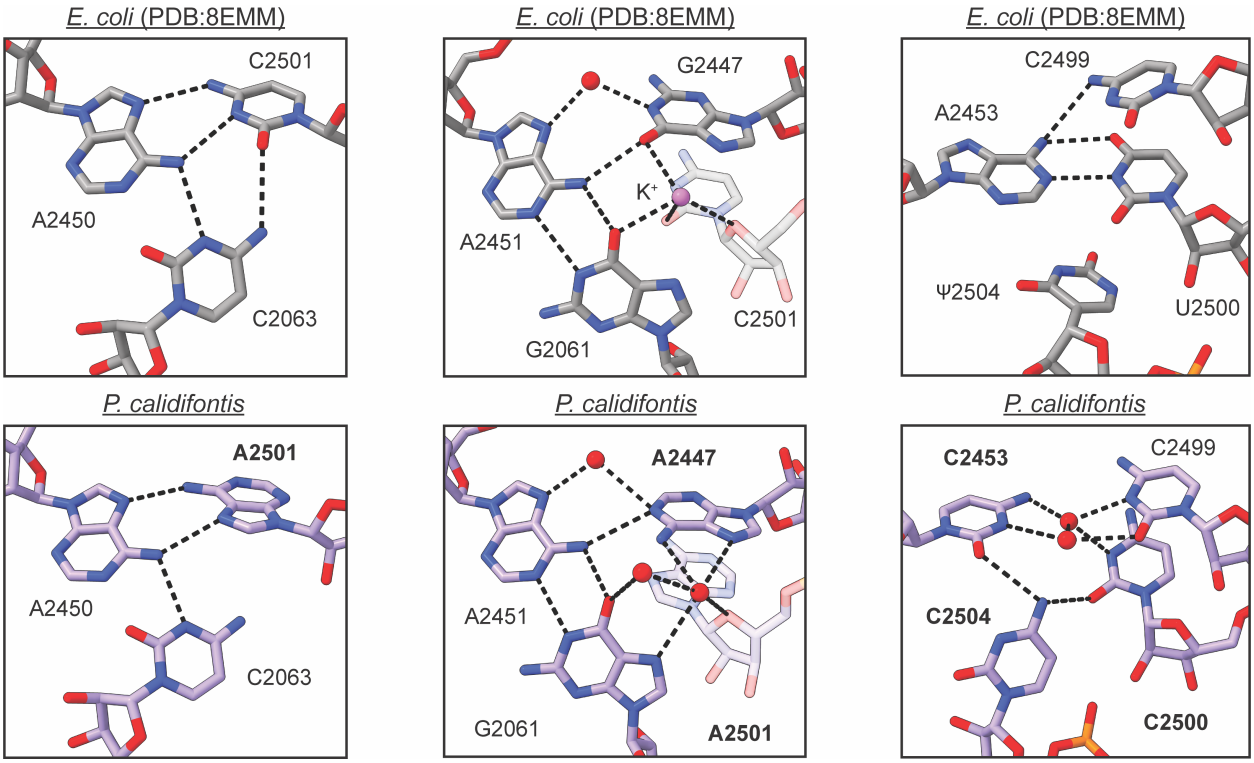


Figure S5.5. Comparison of the PTCs in *E. coli* PDB:8EMM (top) and *P. calidifontis* (bottom). Water molecules and potassium ions are shown as red and pink spheres respectively. Hydrogen bonds, shown with dashes, were calculated in ChimeraX.

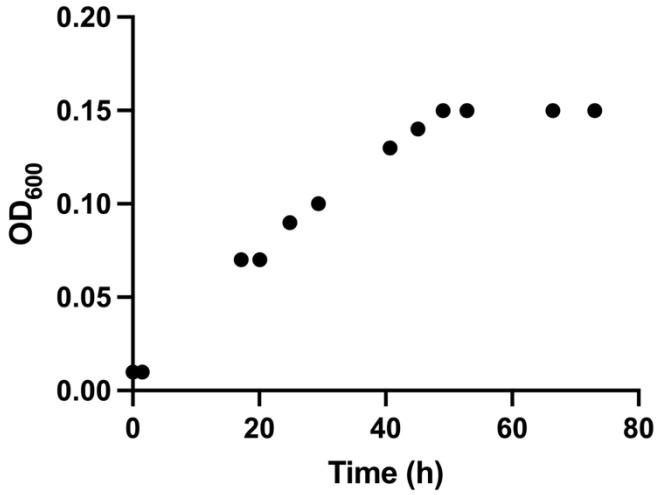


Figure S4.6. Representative growth curve for *P. calidifontis*. Ribosomes used for structure determination were isolated from cultures grown for 48 hours.

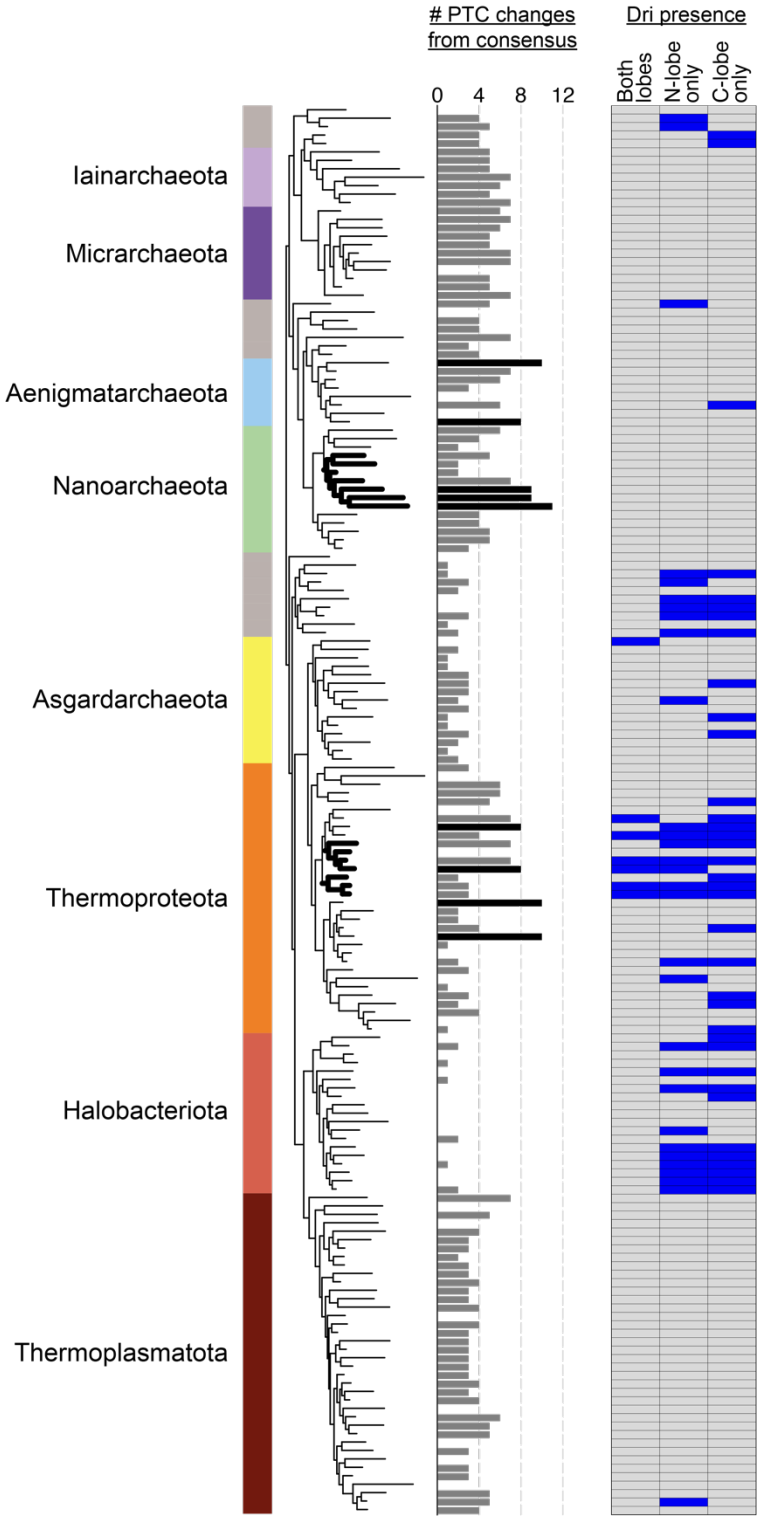


Figure 4.7. Distribution of PTC sequences and Dri homologs from GTDB archaea. Each node represents an order. The number of PTC nucleotides that differ from the archaeal consensus sequence are plotted in the middle and the presence of any Dri homologs in each order are shown on the right. Branches of the tree that are bolded correspond to the tree in Figure 5.2a (lower) and Extended Figure 5.2b (upper).

Table S4.1. Protein sequences used in chapter 4

Name	Sequence
WT Dri	MLTREELEKLAEKRVPQFVRDVVEHPPFRVTVNTTLETLAAYLRKFPVDVVPVFKSVFSD EVAGVVYPHTALLLKSKKLDAKVGEFLNQPLVVKESWRIENVAEMLISESKWGAVVVD EEGKFVGVVSLRGLLSALLLREPKAKSVAAVYTSIDEKKPRVGFVKAIEKVSKIFHKLVG GEVDGYVVLNREGGAAGILTVWNFLKSRRWFRGSGEPRAIFGTRVTRGESKPRGVARV WRIMSRGVAVANPDTPITDVARYMATFGIYVVPVVDRNGKVIGAVTAWDVLHAYLYGP KEGREDVEVKTAVEVPVSKPSMEAVIRLKPVKHVTGLRARDVMLSDVPMVNVRDPLSSI RKAFLRSKSGILAVVDDSGKVVGFITRRDFMSYIAEKSLGYWRRQKGKLLVLREEALPGE QAKLAVEEGTAGDLAKSEYPTVSESATLEEVAYKMLAAGTDYVVVIDSAGQPIGVVTKD ELVKAYKERGRSVKVGELMTPADVAAVNPFSSLMSTTRKINAFELDGVVVVEGGNIMG VVTVDDLALRPVEETLRGERVVYFTKSGVLRKATTGLSRLRYSKVGTLTALDVSRPVDH VANVNADVKEVLDKLVEQGVVPVVDEQGRLVGVLNKMDIVKDLARVYVTYAMPEKLA EVKQVEERAHHHHHH
Dri N-terminal Lobe	MLTREELEKLAEKRVPQFVRDVVEHPPFRVTVNTTLETLAAYLRKFPVDVVPVFKSVFSD EVAGVVYPHTALLLKSKKLDAKVGEFLNQPLVVKESWRIENVAEMLISESKWGAVVVD EEGKFVGVVSLRGLLSALLLREPKAKSVAAVYTSIDEKKPRVGFVKAIEKVSKIFHKLVG GEVDGYVVLNREGGAAGILTVWNFLKSRRWFRGSGEPRAIFGTRVTRGESKPRGVARV WRIMSRGVAVANPDTPITDVARYMATFGIYVVPVVDRNGKVIGAVTAWDVLHAYLYGP KEGREDVEVKTAVEVPHHHHHH
Dri C-terminal Lobe	MGSSHHHHHHAVIRLKPVKHVTGLRARDVMLSDVPMVNVRDPLSSIRKAFLRSKSGILA VVDDSGKVVGFITRRDFMSYIAEKSLGYWRRQKGKLLVLREEALPGEQAKLAVEEGTAG DLAKSEYPTVSESATLEEVAYKMLAAGTDYVVVIDSAGQPIGVVTKDELVKAYKERGRS VKVGELMTPADVAAVNPFSSLMSTTRKINAFELDGVVVVEGGNIMGVVTVDDLALRPVE ETLRGERVVYFTKSGVLRKATTGLSRLRYSKVGTLTALDVSRPVDHVANVNADVKEVL DKLVEQGVVPVVDEQGRLVGVLNKMDIVKDLARVYVTYAMPEKLAEVKQVEERA

Table S4.2. Cryo-EM data collection and processing

Reconstruction	**50S-Dri**	**70S-Consensus**	**70S-Dri**
Magnification	105,000	105,000	105,000
Voltage (kV)	300	300	300
Electron Exposure ($e^-/Å^2$)	40	40	40
Defocus Range (μm)	-0.5/-1.5	-0.5/-1.5	-0.5/-1.5
Pixel Size (Å)	0.8293	0.8293	0.8293
Symmetry Imposed	C1	C1	C1
Initial Particle Images	2,360,632	2,360,632	2,360,632
Final Particle Images	183,467	129,829	72,157
Map Resolution (Å)	1.95	2.36 (Global)	2.53 (Global)
FSC Threshold	0.143	0.143	0.143

Table S4.3. Model refinement statistics

Model	**50S-Dri**	**70S-Consensus**	**70S-Dri**
Model component			
Model resolution (Å)	2.07	2.52/2.90 (50S/30S)	2.64/2.98 (50S/30S)
FSC threshold	0.5	0.5	0.5
Map sharpening *B* factor (Å^2)	36.3	42.3/47.4 (50S/30S)	41.8/43.8 (50S/30S)
Model composition			
Non-hydrogen atoms	114588	171375	172200
Mg^{2+} ions	173	252	251
Waters	7994	7812	6387
Mean *B* Factors (Å^2)			
RNA	49.06	66.88	66.12
Protein	56.83	70.87	72.98
Waters	48.77	60.66	61.99
Other	47.58	59.46	61.04
R.m.s. deviations from ideal values			
Bond (Å)	0.008	0.006	0.007
Angle (°)	0.891	0.898	0.907
Molprobity score	1.46	2.42	2.41
Clash Score	5.79	16.77	15.02
Rotamer outliers (%)	1.31	3.59	3.65
Ramachandran plot			
Favored (%)	97.74	96.02	95.67
Allowed (%)	2.23	3.72	4.08
Outliers (%)	0.04	0.26	0.24
RNA validation			
Angles outliers (%)	0.05	0.05	0.04
Sugar pucker outliers (%)	1.14	1.53	1.32
Average suiteness	0.62	0.568	0.575

Table S4.4. DNA primers used in this study

Primer Name	Sequence	Description
PTC_InFusion_F	GGGCGCTGGAGAACTGAGG	Forward primer for pLK35 linearization
PTC_InFusion_R	GGTACACTGCATCTTCACAGCGAGTTC	Reverse primer for pLK35 linearization
uL3_sgRNA_ins_F	cggtcagaaccagactccGTTTTAGAGCTAGAAATAGCAAG	Forward primer for uL3 N20 sequence insertion into the pEcgRNA plasmid with the InFusion kit
uL3_sgRNA_ins_R	gtctggttctgaccgatACTAGTATTATACCTAGGACTGAGC	Reverse primer for uL3 N20 sequence insertion into the pEcgRNA plasmid with the InFusion kit
uL3_HDR_seq_F	GGTTAATCAGGTCATTGAGCGATTGAGAGG	Forward primer for amplification of the *E. coli rplC* gene
uL3_HDR_seq_R	TTGACTGTGGTCCTGCGGACGAG	Reverse primer for amplification of the *E. coli rplC* gene
MS2_H98_quant_F	CTTGCCCCGAGATGAGTTCTCCC	RT-PCR primer for the *E. coli* ribosome purity assay with H98 MS2 tags
MS2_H98_quant_R	GTACCGGTTAGCTCAACGCATCGCT	Primer for amplification of cDNA in the *E. coli* ribosome purity assay with H98 MS2 tags
Pc_Dri_quant_F	TCTAAGGAAATTCCCCGTGGACG	Forward primer for *P. calidifontis* Dri mRNA detection in RT-qPCR
Pc_Dri_quant_R	CTTGCTCTCGCTTATCAACATCTCG	Reverse primer for *P. calidifontis* Dri mRNA detection in RT-qPCR
Pc_uL2_quant_F	CATGAGCCAGGCCTCAATGC	Forward primer for *P. calidifontis* uL2 mRNA detection in RT-qPCR
Pc_uL2_quant_R	AACCGCTTCTCAACGTTAAACAC	Reverse primer for *P. calidifontis* uL2 mRNA detection in RT-qPCR

Table S4.5. sgRNA sequence used in chapter 4

Name	Sequence
uL3-ΔQ150 N20	AUCGGUCAGAACCAGACUCC
uL3-ΔQ150 Full sgRNA	AUCGGUCAGAACCAGACUCCGUUUUAGAGCUAGAAAUAGCAAGUUAAAAUAA GGCUAGUCCGUUAUCAACUUGAAAAAGUGGCACCGAGUCGGUGC

Table S4.6. dsDNA blocks used in chapter 4

Name	Sequence
PTC_3M	AAGATGCAGTGTACCCGCGGCAAGACGGAAAGACCCCGTGAACCTTTACTATAGCTT GACACTGAACATTGAGCCTTGATGTGTAGGATAGGTGGGAGGCTTTGAAGTGTGGAC GCCAGTCTGCATGGAGCCGACCTTGAAATACCACCCTTTAATGTTTGATGTTCTAACG TTGACCCGTAATCCGGGTTGCGGACAGTGTCTGGTGGGTAGTTTGACTGGGGCGGTC TCCTCCTAAAGAGTAACGGAGGAGCACGAAGGTTGGCTAATCCTGGTCGGACATCA GGAGGTTAGTGCAATGGCATAAGCCAGCTTGACTGCGAGCGTGACGGCGCGAGCAG GTGCGAAAGCAGGTCATAGTGATCCGGTGGTTCTGAATGGAAGGGCCATCGCTCAAC GGATAAAAGGTACTCCGGGGATAACCGGCTGATACCGCCCAAGAGTTCATATCGAC GGCGGTGTTTGGCACCCCGACGTCGGCTCATCACATCCTGGGGCTGAAGTAGGTCCC AAGGGTATGGCTGTTCGCCATTTAAAGTGGTACGCGAGCTGGGTTTAGAACGTCGTG AGACAGTTCGGTCCCTATCTGCCGTGGGCGCTGGAGAACT
uL3-ΔQ150 HDR Template	GTTACTCAGGTTAAAGACCTGGCTAACGATGGCTACCGTGCTATTCAGGTGACCACC GGTGCTAAAAAAGCTAACCGTGTGACCAAGCCTGAAGCTGGCCACTTCGCTAAAGCT GGCGTAGAAGCTGGCCGTGGTCTGTGGGAATTCCGCCTGGCTGAAGGCGAAGAGTTC ACTGTAGGTCAGAGCATTAGCGTTGAACTGTTTGCTGACGTTAAAAAAGTTGACGTA ACTGGCACCTCTAAAGGTAAAGGTTTCGCAGGTACCGTTAAGCGCTGGAACTTCCGT ACCCAGGACGCTACTCACGGTAACTCCTTGTCTCACCGCGTTCCGGGTTCTATCGGTC AGAACACTCCGGGCAAAGTGTTCAAAGGCAAGAAAATGGCAGGTCAGATGGGTAAC GAACGTGTAACCGTTCAGAGCCTTGACGTAGTACGCGTTGACGCTGAGCGCAACCTG CTGCTGGTTAAAGGTGCTGTCCCGGGTGCAACCGGTAGCGACCTGATCGTTAAACCA GCTGTGAAGGCGTAAGGAGATAGCAATGGAATTAGTATTGAAAGACGCGCAGAGCG CGCTGACTGTTTCCGAAACTACCTTCGGTCGTGATTTCAACGAAGCGCTGGTTCACCA GGTTGTTGTTGCTTATGCAGCTGGTGCTCGTCAGGGTACTCGTGCTCAGAAGACTCGT GCTGAAGTAACTGGTT
HiBit DNA Template	GCGAATTAATACGACTCACTATAGGGTTAACTTTAACAAGGAGAAAAACATGGTGA GCGGCTGGCGCCTGTTTAAAAAAATTAGCTAACTAGCATAACCCCTCTCTAAACGGA GGGGTTT

Table S4.7. *P. calidifontis* large ribosomal subunit proteins identified by mass spectrometry

Accession	-10LgP	Coverage (%)	#Peptides	#Unique Peptides	Average Mass	Description
A3MTT0|A3MTT0_PYRCJ	359.93622	76.85	20	20	11174.706	Large ribosomal subunit protein P1
A3MX83|RL1_PYRCJ	243.00838	32.88	7	7	25074.805	Large ribosomal subunit protein uL1
A3MS41|RL2_PYRCJ	249.16068	22.95	7	7	26193.252	Large ribosomal subunit protein uL2
A3MWI4|RL3_PYRCJ	375.15442	39.05	18	18	37181.547	Large ribosomal subunit protein uL3
A3MWI5|A3MWI5_PYRCJ	384.69888	56.14	21	21	31547.998	Large ribosomal subunit protein uL4
A3MXP8|A3MXP8_PYRCJ	291.17993	38.76	9	9	20116.807	Large ribosomal subunit protein uL5
A3MWV5|A3MWV5_PYRCJ	421.6866	81.12	28	28	21630.463	Large ribosomal subunit protein uL6
A3MTA9|RL7A_PYRCJ	192.32135	28.86	4	4	15990.72	Large ribosomal subunit protein eL8
A3MX84|A3MX84_PYRCJ	369.66794	45.64	18	18	37480.96	Large ribosomal subunit protein uL10
A3MX82|A3MX82_PYRCJ	140.1296	18.07	3	3	18383.375	Large ribosomal subunit protein uL11
A3MXZ7|A3MXZ7_PYRCJ	419.68018	72.58	27	27	21694.902	Large ribosomal subunit protein uL13
A3MTP8|A3MTP8_PYRCJ	317.1464	48.41	12	12	17897.012	Large ribosomal subunit protein eL13
A3MX34|RL14_PYRCJ	373.60333	72.22	20	20	15742.426	Large ribosomal subunit protein uL14
A3MS76|RL14E_PYRCJ	203.08841	30.1	4	4	11448.51	Large ribosomal subunit protein eL14
A3MUZ1|RL15_PYRCJ	303.03702	51.28	10	10	17487.32	Large ribosomal subunit protein uL15
A3MWR6|A3MWR6_PYRCJ	252.2958	23.28	6	6	22574.615	50S ribosomal protein L15e
A3MXP3|RL10E_PYRCJ	384.6988	53.37	22	22	19859.158	Large ribosomal subunit protein uL16
A3MSJ3|RL18_PYRCJ	168.60799	11.71	3	3	23374.21	Large ribosomal subunit protein uL18
A3MXZ6|A3MXZ6_PYRCJ	241.26091	40.16	5	5	13201.696	Large ribosomal subunit protein eL18
A3MSJ4|A3MSJ4_PYRCJ	345.15067	40.14	14	14	17373.215	Large ribosomal subunit protein eL19
A3MX77|RL18A_PYRCJ	313.1881	84.62	10	10	8913.517	Large ribosomal subunit protein eL20
A3MWX9|RL21_PYRCJ	263.81876	46.46	6	6	11294.232	Large ribosomal subunit protein eL21
A3MTL6|RL22_PYRCJ	314.46808	39.67	11	11	21268.16	Large ribosomal subunit protein uL22
A3MWI6|A3MWI6_PYRCJ	162.22151	25.93	2	2	9290.063	Large ribosomal subunit protein uL23
A3MWZ8|RL24_PYRCJ	294.34494	42.97	9	9	14555.221	Large ribosomal subunit protein uL24
A3MTA8|RL24E_PYRCJ	298.51492	64.52	9	9	7085.4673	Large ribosomal subunit protein eL24
A3MTL2|A3MTL2_PYRCJ	324.05475	58.23	12	12	9136.798	Large ribosomal subunit protein uL29
A3MU87|RL30_PYRCJ	113.587166	12.85	2	2	20258.785	Large ribosomal subunit protein uL30
A3MXZ2|RL30E_PYRCJ	245.51628	63.37	6	6	10871.856	Large ribosomal subunit protein eL30
A3MX75|RL31_PYRCJ	286.8368	49.45	8	8	10643.573	Large ribosomal subunit protein eL31
A3MSJ5|A3MSJ5_PYRCJ	321.42322	34.64	12	12	18131.469	Large ribosomal subunit protein eL32
A3MV68|RL34_PYRCJ	251.49355	33.33	5	5	9350.048	Large ribosomal subunit protein eL34
A3MY38|A3MY38_PYRCJ	213.66008	48.08	4	4	6156.181	Large ribosomal subunit protein eL37
A3MTT1|A3MTT1_PYRCJ	317.47028	92.54	12	12	7939.423	LSU ribosomal protein L38E
A3MUU4|RL39_PYRCJ	145.79361	35.29	2	2	6012.228	Large ribosomal subunit protein eL39
A3MX99|RL40_PYRCJ	248.84946	64.15	8	8	6339.579	Large ribosomal subunit protein eL40
A3MUV1|A3MUV1_PYRCJ	278.55612	67.47	8	8	9646.363	Large ribosomal subunit protein eL42
A3MUM7|A3MUM7_PYRCJ	403.29984	79.41	24	24	11362.385	Large ribosomal subunit protein eL43
A3MTM7|A3MTM7_PYRCJ	286.37665	39.67	8	8	20927.469	DJ-1/PfpI domain-containing protein (**aL48**)
A3MWU0|A3MWU0_PYRCJ	307.95416	49.46	11	11	10917.768	PaREP1 domain containing protein (**aL49**)
A3MX58|A3MX58_PYRCJ	223.53175	6.56	5	5	72024.73	Putative signal-transduction protein with CBS domains (**Dri**)

Table S4.8. *P. calidifontis* small ribosomal subunit proteins identified by mass spectrometry

Accession	-10LgP	Coverage (%)	#Peptides	#Unique Peptides	Average Mass	Description
A3MVE0|RS3A_PYRCJ	340.4799	65.32	21	21	24696.094	Small ribosomal subunit protein eS1
A3MS50|RS2_PYRCJ	434.48245	72.6	47	47	23798.812	Small ribosomal subunit protein uS2
A3MTL3|RS3_PYRCJ	412.854	73.61	37	36	24644.172	Small ribosomal subunit protein uS3
A3MUS9|RS4_PYRCJ	369.88324	65.41	23	23	18479.123	Small ribosomal subunit protein uS4
A3MWZ7|RS4E_PYRCJ	352.1609	53.16	19	19	26732.367	Small ribosomal subunit protein eS4
A3MU88|RS5_PYRCJ	378.48062	66.34	25	25	22123.717	Small ribosomal subunit protein uS5
A3MUD0|RS6E_PYRCJ	291.49942	51.66	13	13	16221.998	Small ribosomal subunit protein eS6
A3MS29|A3MS29_PYRCJ	250.44583	26.01	7	7	25475.637	Small ribosomal subunit protein uS7
A3MSJ6|RS8_PYRCJ	296.6819	49.23	12	11	14817.512	Small ribosomal subunit protein uS8
A3MWY2|RS8E_PYRCJ	251.13277	31.3	8	8	14415.8545	Small ribosomal subunit protein eS8
A3MXZ8|A3MXZ8_PYRCJ	183.2937	19.72	3	3	16117.1	Small ribosomal subunit protein uS9
A3MT22|RS10_PYRCJ	356.50195	62.26	20	20	12198.474	Small ribosomal subunit protein uS10
A3MX63|RS11_PYRCJ	263.05136	27.66	7	7	14963.25	Small ribosomal subunit protein uS11
A3MXZ4|RS12_PYRCJ	353.57635	80.95	22	22	16444.416	Small ribosomal subunit protein uS12
A3MUT0|RS13_PYRCJ	307.90744	62.09	15	15	16726.564	Small ribosomal subunit protein uS13
A3MSJ7|A3MSJ7_PYRCJ	273.35706	53.7	9	9	6414.726	Small ribosomal subunit protein uS14
A3MVD1|RS15_PYRCJ	200.31052	27.81	7	7	17551.531	Small ribosomal subunit protein uS15
A3MTT7|A3MTT7_PYRCJ	292.66876	45.58	10	10	16951.176	Small ribosomal subunit protein uS17
A3MS42|RS17E_PYRCJ	230.48767	57.75	6	6	8064.4707	Small ribosomal subunit protein eS17
A3MTT6|RS19_PYRCJ	241.82663	20.25	6	6	18147.479	Small ribosomal subunit protein uS19
A3MUU6|A3MUU6_PYRCJ	152.12274	17.09	2	2	17737.877	Small ribosomal subunit protein eS19
A3MSX4|A3MSX4_PYRCJ	261.62076	35.94	9	9	14820.318	Small ribosomal subunit protein eS24
A3MV37|A3MV37_PYRCJ	323.74094	68.18	17	17	12449.666	SSU ribosomal protein S25E
A3MV49|A3MV49_PYRCJ	323.6989	56	14	14	11546.789	SSU ribosomal protein S26E
A3MUV2|RS27_PYRCJ	178.86865	38.81	5	5	7434.8574	Small ribosomal subunit protein eS27
A3MSW3|A3MSW3_PYRCJ	79.18172	16.67	1	1	6098.0933	SSU ribosomal protein S30E
A3MSX5|RS27A_PYRCJ	239.32335	52.31	7	7	7573.985	Small ribosomal subunit protein eS31
A3MY11|A3MY11_PYRCJ	237.6753	63.08	8	8	6947.1035	Small zinc finger protein HVO-2753-like zinc-binding pocket domain-containing protein (**aS21**)
A3MX58|A3MX58_PYRCJ	307.99796	20.92	14	14	72024.73	Putative signal-transduction protein with CBS domains (**Dri**)
WP_226952012.1	146.96658	33.82	2	2	7837.344	Hypothetical protein (NCBI:WP_226952012.1) (**aS35**)

Table S4.9. Nucleotide numbering conversions

E. coli Numbering	*P. calidifontis* Numbering
2058	2178
2059	2179
2060	2180
2061	2181
2062	2182
2447	2561
2448	2562
2449	2563
2450	2564
2451	2565
2452	2566
2453	2567
2500	2614
2501	2615
2502	2616
2503	2617
2504	2618
2505	2619
2506	2620
2552	2666
2553	2667
2554	2668
2555	2669
2556	2670
2584	2698
2585	2699
2586	2700
2602	2716

Table S4.10. ***M. acetivorans*** **Dri homologs identified by mass spectrometry**

Accession	-10LgP	Coverage (%)	#Peptides	#Unique Peptides	Average Mass	Description
Q8TH72|Q8TH72_METAC	36.662453	4.63	1	1	31237.389	Uncharacterized protein (**Dri C-terminal lobe homolog**)
Q8TH73|Q8TH73_METAC	57.211075	6.61	2	2	36574.367	Uncharacterized protein (**CBS-domain containing protein**)

Chapter 5: Broadly distributed factors work in tandem to mediate ribosome hibernation in Archaea

5.1 Abstract

Ribosomes are molecular machines responsible for cellular protein synthesis. Under nutrient limitation or stress, ribosome hibernation factors inactivate and protect ribosomes. Ribosome hibernation plays an important role in microbes, but we lack a complete understanding of this process in Archaea. To explore archaeal ribosome hibernation, we investigated putative hibernation factors from the methanogenic archaeon *Methanosarcina acetivorans*. In *M. acetivorans*, distant homologs of a previously identified hibernation factor, Dri, are in a gene cluster with two other putative hibernation factors and we designated these proteins as SriA-SriD. We found that Sri factors inhibit protein synthesis *in vitro*. Cryo-EM structures showed that SriA and SriB simultaneously bind to the large ribosomal subunit, occluding the peptidyl transferase center and nascent polypeptide exit tunnel. Additional structures showed that SriC and SriD bind the small ribosomal subunit and form a protein-protein interface, occluding the mRNA-binding channel. We further find that *sri* genes frequently occur in gene clusters and are broadly distributed across multiple archaeal phyla. Together, these findings establish Sri proteins as a distinct group of hibernation factors that expand our understanding of ribosome hibernation in archaea.

5.2 Introduction

Ribosomes are molecular machines that translate mRNA into protein. Protein synthesis is an energetically demanding process, consuming a large fraction of the cell's energy. Under conditions of stress or adverse environmental changes, ribosomes are inactivated through ribosome hibernation.[235] This process is mediated by protein factors, known as hibernation factors, which inhibit translation by occluding functional sites on the ribosome or promoting ribosome dimerization.[37,38] In addition to suppressing protein synthesis, ribosome hibernation protects ribosomes from damage by endogenous RNases during stress.[39] Thus, hibernation preserves an intact pool of ribosomes that remain poised to resume translation once growth conditions become favorable.

Multiple ribosome hibernation factors have been identified in bacteria and eukaryotes. RMF, HPF, and RaiA (previously known as protein Y) are bacterial ribosome hibernation factors that bind to the small ribosomal subunit (SSU) and block mRNA and tRNA binding sites.[41,42] RMF and HPF also promote the formation of inactive 100S ribosome dimers.[43–45] An additional bacterial ribosome hibernation factor, Balon, is unique in its ability to bind to actively translating ribosomes.[46] Similar to their bacterial counterparts, eukaryotic ribosome hibernation factors, such as Stm1/Serbp1[47], IFRD2[48], Dapl1[49], and MDF2[19] occlude tRNA binding sites on the ribosome. Ribosome dimerization has also been observed in eukaryotes, mediated by the microsporidian hibernation factor MDF1.[50] Overall, ribosome hibernation factors share the role of preserving ribosomes under stress, yet they differ in their structure and modes of ribosome inactivation.

In Archaea, ribosome hibernation is less well understood. Archaea are widespread prokaryotes that play integral roles in biogeochemical cycling.[236,237] For example, the methanogens, a polyphyletic group of Archaea, are responsible for the majority of global methane emissions.[238] Studies of ribosome inactivation in archaea have mainly focused on factors that dimerize ribosomal subunits. These include aRDF, which dimerizes 30S subunits in the genus *Pyrococcus*[233,234], and MRDF, which dimerizes 50S subunits in *Methanosarcina acetivorans*.[239] Previously, we uncovered an archaeal ribosome hibernation factor, Dri, that is composed of two

ribosome binding lobes that target tRNA binding sites on both the large ribosomal subunit (LSU) and the SSU.[240] Dri is found predominantly in Thermoproteota. However, homologs of the two Dri ribosome binding lobes are widely distributed in Archaea, encoded as separate genes.

Here, we investigate Dri homologs from the methanogenic archaeon *Methanosarcina acetivorans*. In the *M. acetivorans* genome, Dri homologs occur in a gene cluster with two additional previously undescribed archaeal ribosome hibernation factors. We designate these four proteins as **S**ingle **r**ibosomal subunit **i**nhibitors (**Sri**A-**Sri**D). Sri proteins inhibit translation *in vitro*. Cryo-EM structures of Sri proteins bound to the *M. acetivorans* ribosome show that they act in tandem to inactivate ribosomes. Sri homologs are widespread across multiple archaeal phyla and frequently occur in gene clusters. Overall, Sri proteins represent a group of hibernation factors that expand our understanding of ribosome hibernation in Archaea.

5.3 Materials and methods

Methanosarcina acetivorans growth

M. acetivorans was cultured in high salt (HS) media with 50 mM trimethylamine; media was either buffered with either 45mM $NaHCO_3$ and N_2/CO_2 (80/20) in the headspace or 50mM PIPES (pH 6.8) and N_2 in the headspace[209].

Recombinant expression of Sri proteins

E. coli Rosetta (DE3) cells were transformed with a pET-21(+) plasmid containing a Sri protein sequence with a C-terminal His-tag (**Table S5.1**). Cultures of the transformants were diluted 1:100 in 1 L of LB media with 100 µg/mL ampicillin and incubated at 37 °C. Once the OD_{600} reached 0.5, protein expression was induced using 0.5 mM Isopropyl β-D-1-thiogalactopyranosie (IPTG) and the culture was incubated at 37 °C for an additional 2 hours. The cells were then pelleted by centrifugation at 4,000 *xg* for 15 minutes and flash frozen. Cell pellets were thawed and resuspended in Sri lysis buffer (30 mM HEPES-KOH pH 7.5, 500 mM KCl, 20 mM imidazole, and 2 mM DTT) with a Pierce protease inhibitor tablet (ThermoFisher) and lysed by sonication. The lysate was clarified by centrifugation at 25,000 *xg* for 1 hour in an F14-14 x 50cy rotor (ThermoFisher) and then passed through a 0.2 µm filter. A 5 mL His-trap column (Cytiva) was equilibrated with 5 column volumes (CV) of Sri lysis buffer, and the lysate was then loaded onto the column. The column was washed with 10 CV of Sri wash buffer (30 mM HEPES-KOH pH 7.5, 2.5 M KCl, 20 mM imidazole) and the protein was eluted using a gradient from 0-100% Sri elution buffer (30 mM HEPES-KOH pH 7.5, 500 mM KCl, 20 mM imidazole) over 5 CV. Sri proteins were buffer exchanged into Sri buffer A (30 mM HEPES-KOH pH 7.5, 500 mM KCl, 2 mM DTT, 20% glycerol) using PD-10 desalting columns (Cytiva), flash frozen, and stored at -80 °C.

M. acetivorans in vitro translation

A 1 L *M. acetivorans* culture was grown to mid-logarithmic phase (OD_{600} of ~1) and cells were harvested by centrifugation at 4,000 *xg* for 15 minutes. The cell pellet was resuspended in 2.5 mL of *Ma* lysis buffer (50 mM HEPES-KOH pH 7.0, 6 mM $MgCl_2$, and 4 mM DTT) per gram of wet cell pellet. 20 µL of RQ1 DNase (Promega) was added and the resuspension was incubated at room temperature for 10 minutes. The sample was then homogenized using a 15G needle and the lysate was clarified using two centrifugation steps at 20,000 *xg* for 20 minutes. The lysate was flash frozen and stored at -80 °C.

NanoLuc luciferase (NLuc) mRNA containing an optimized *M. acetivorans* SD sequence[241] (**Table S5.2**) was *in vitro* transcribed using T7 RNA polymerase (NEB) and purified using the RNA clean and concentrator kit (Zymo). 30 µL *in vitro* translation reactions were assembled as follows: 15 µL *M. acetivorans* lysate, 2 mM ATP, 2 mM GTP, 2 mM spermidine, 100 µM amino acid mixture (Promega), 900 ng NLuc mRNA, 30 U murine RNase inhibitor (NEB), and an additional 3 mM $MgCl_2$ (final concentration of 6 mM Mg^{2+}). Either 3 µL of Sri protein or Sri buffer A (control reactions) was added to *in vitro* translation reactions. Reactions were incubated at 37 °C for 30 minutes and then for each reaction, 8 µL was placed in three wells of a 384-well plate. 20 µL of LgBiT buffer (20 mM HEPES pH 7.5, 50 mM KCl, and 10% glycerol) with a 1:50 dilution of NanoGlo substrate (Promega) was added to each well. The plate was incubated for 10 minutes at room temperature and then luminescence was measured in a Spark plate reader (Tecan).

Ribosome purification and preparation for cryo-EM

To isolate ribosome-Sri complexes for cryo-EM, 180 µL samples were prepared as follows: 90 µL *M. acetivorans* lysate was mixed with 2 mM ATP, 2 mM GTP, 2 mM spermidine, 1 µL of RQ1 DNase (Promega), 180 U murine RNase inhibitor (NEB), and 3 mM $MgCl_2$ (final concentration of 6 mM Mg^{2+}). For data set one, 6 µM of SriA, SriB, SriC, and SriD were each added to the sample. For data set two, 10 µM SriC and SriD were each added to the sample along with 100 µM amino acid mixture (Promega). For data set three, 10 µM SriC and SriD and 100 µM amino acid mixture (Promega) were added to the sample, but ATP and GTP were not added. The samples were then incubated at 37 °C for 30 minutes. Ribosomes were purified using RAPPL.[242] After incubation, 220 µL RAPPL Buffer A (25 mM HEPES-KOH pH 7.5, 50 mM KCl, 10 mM $MgCl_2$, 2 mM DTT) and 100 µL polylysine magnetic beads (MCLAB) were added to the sample, and the mixture was rotated at room temperature for 20 minutes. The supernatant was then removed from the beads, and the beads were washed three times with 250 µL RAPPL buffer A with a one minute incubation at room temperature in between each wash. To elute ribosomes, the beads were incubated at room temperature for 10 minutes with 50 µL RAPPL elution buffer (RAPPL Buffer A with 2 mg/mL poly-L-glutamic acid (molecular weight 3-15 kDa, Sigma-Aldrich). The elution step was repeated three times. Ribosomes were then concentrated in a 100 kDa molecular weight cut off spin filter (Millipore) and washed with RAPPL Buffer A to remove the poly-L-glutamic acid. *M. acetivorans* ribosomes were quantified using the approximation 1 A_{260}=40 µg/mL.

For plunge freezing, *M. acetivorans* ribosomes were diluted to 0.42 mg/mL with RAPPL buffer A. Three-hundred mesh R1.2/1.3 UltrAuFoil grids with a layer of 2 nm amorphous carbon (Quantifoil) were glow discharged in a Pelco easiGlow under a 0.37 mBar vacuum with 25 mA current for 12 seconds. 4 µL of ribosomes was applied to the grid, incubated for three minutes at room temperature, and plunge-frozen in liquid ethane using a Vitrobot Mark IV at 4 °C with 100% humidity.

Cryo-EM data acquisition and image processing

Cryo-EM movies were collected with a 300 kV Titan Krios microscope with a BIO-energy filter and Gatan K3 camera (**Table S5.3**). Data was collected with a super-resolution pixel size of 0.41 Å (physical pixel size of 0.8293) over a defocus range of -0.5 to -1.5 µm with a total electron dose of 40 $e^-/Å^2$ split over 40 frames. Data collection was automated with Serial-EM.[150]

Cryo-EM image processing was done in cryoSPARC 4[103] (**Figure S5.1**). Movies were binned to the physical pixel size and patch motion corrected. The CTF of micrographs were estimated using patch CTF estimation and micrographs with poor CTF fit were manually excluded from further processing. Particles were picked using template picking with ribosome 2D templates generated in cryoSPARC. Particles were extracted with a box size of 512 pixels and cropped to 1/8 of the full box size. 2D classification was performed with 100 classes and 2D classes containing features consistent with ice or the foil edge were excluded. The particles were then subjected to heterogeneous refinement with 12 classes and classes consistent with 70S ribosomes were selected for further processing. 70S particles were re-extracted at the full box size and were aligned using homogeneous refinement with the per-particle defocus optimization, per-group CTF parameter optimization, and minimization over per-particle scale options selected. Local motion was then corrected using reference-based motion correction in cryoSPARC and the particles were refined a second time.

For dataset one, 70S particles containing SriA and SriB were classified using 3D classification with a mask on SriA and 3 classes. The class with SriA and SriB density was then refined.

For data set two, 70S particles were refined locally on the SSU, and particles containing SriD were classified using 3D classification with a mask on SriD and 3 classes. The class with SriD density was then subjected to a second round of 3D classification using a mask on SriD and 2 classes. The class with density for all SriD domains was then refined.

For data set three, 70S particles were classified based on SriD occupancy as described above. SriD containing particles from data sets one and two were then combined and particles also containing SriC were classified using 3D classification with a mask on SriC and 10 classes. SriD containing particles from data set three were also classified on SriC occupancy. Particles from all three datasets containing density for SriC and SriD were then combined and further classified using 3D classification with a mask on SriC and 3 classes. The class with the best density for SriC was then further refined.

After refinement, we used the 'Fit in Map' tool in ChimeraX[108] to calibrate the magnification of the cryo-EM map using the X-ray crystal structure of the *Haloarcula marismortui* 50S subunit[219], resulting in a pixel size of 0.8264. Local resolution was calculated in Relion 4[197] using the Relion implementation. For figure presentation, cryo-EM maps were supersampled using the 'make a smoother copy' function in COOT.[110]

Model building

Composite maps were generated for the 70S-Sri complexes. For the 70S-SriA-SriB and 70S-SriC-SriD complexes, we aligned the SSU-focused, SSU head-focused, and LSU-focused refined maps to the global 70S ribosome map using the 'Fit in Map' tool in ChimeraX.[108] For the 70S-SriD complex, we aligned the SSU-focused, and LSU-focused refined maps to the global 70S ribosome map. The focus refined maps were then resampled using 'vop resample', scaled according to their standard deviations from the 'Map statistics' tool, and added using 'vop add'.

Initial models were built using ModelAngelo[198] provided with sequences for *M. acetivorans* rRNAs and rProteins. The linear Rfam[202] *M. acetivorans* 23S rRNA sequence was used for modeling to maintain consistency with nucleotide numbering and because the circularized H1 extension in *M. acetivorans* 23S rRNA[243] is disordered in our cryo-EM maps. Unknown proteins were built using ModelAngelo without provided sequences. Protein models were inspected for completeness and manually built in regions where the model was incomplete. RNA

models were manually inspected at each nucleotide for correct modeling and post-transcriptional modifications. For the SriA-SriB and SriD bound ribosomes, there was strong density for the acceptor stem of an E-site tRNA, which was modeled using the sequence from *M. acetivorans* $tRNA^{Phe}$. Magnesium ions were identified using the 'unmodeled blobs' tool in COOT[110] and modeled manually. No attempt was made to systematically model potassium ions. The LSU and SSU models were then refined in their individual focused refined maps using Phenix real-space refinement.[109] Manual adjustments were made to the models in COOT[110] and ISOLDE[244] and the resulting models were docked into the composite map. For the SriA-SriB and SriD bound ribosomes, phenix.douse[109] was used to model solvent using the default settings in the individual sharpened focused refined maps and the solvent models were docked into the composite maps. The final models were validated in Phenix (**Table S5.4**).

Bioinformatic analysis

To determine the phylogenetic distribution of aS36, we used the homology search tool HMMER 3.4[205] to search the predicted proteomes of archaeal representative species in the Genome Taxonomy Database (GTDB, version 226.0)[200]. First, we built a profile HMM built from the *M. acetivorans* aS36 sequence using the HMMER hmmbuild program and then used the HMMER program hmmsearch to query all proteomes, taking all resulting hits with e-value <1e-5 as homologs of aS36. We aligned these sequences using mafft v7.525[206] with default settings and built another profile HMM to search again but no additional hits with e-value < 1e-5 were found.

To search for Dri homologs, we aligned the 92 Dri hits found in Nissley et al (2025)[240] using mafft with default settings and built a profile HMM using the HMMER hmmbuild program. After searching archaeal GTDB representative proteomes using the HMMER program hmmsearch, hits with e-value < 1e-100 and protein length greater than 500aa were used as Dri sequences for visualization on the Sri protein tree. These Dri homologs were aligned using mafft and split into N- and C-lobes, respectively, based on positions 14-303 and 324-640 in the *P. calidifontis* sequence.

To search for SriA, SriB, SriC, and SriD homologs, we built initial profile HMMs from the *M. acetivorans* sequences. After an initial search of the archaeal GTDB representative proteomes, we identified a subset of genomes where the best hits for the four models were arranged sequentially as four adjacent genes (SriA-SriB-SriC-SriD). These SriA, SriB, SriC, and SriD sequences were aligned separately using mafft and used to build another set of profile HMMs. After an additional round of searches with the final models, all hits with e-value < 1e-35 and protein lengths between 100aa and 500aa were pooled.

These protein sequences were used to construct a Sri homolog tree, also including the Dri N- and C-lobe sequences. Sequences were aligned using mafft and columns with more than 99% gaps were removed from the alignment. A phylogenetic tree was built using IQTREE v3.0.1[245] using LG model and default settings.

Upon building the tree, we identified a protein clade corresponding to a fusion of SriA and a RaiA/HPF homolog, now known as Hib[246]. Since Hib homologs hit the SriA model weakly, we separately searched for Hib homologs by building a profile HMM from sequences corresponding to this subclade on the tree, searching all GTDB representative proteomes, and including all hits with e-value <1e-35 into the final version of the tree.

We defined subtrees corresponding to each of the Sri genes where sequences predominantly hit the appropriate Sri model with the most significant e-value. All sequences falling within each subtree were considered homologs of the respective Sri gene. These subtrees

are colored in **Figure S5.2**. We further examined some Sri homologs for sequence features unique to their mode of ribosome binding. For SriB, the length of the N-terminal extension was assessed by aligning each homolog and the *M. acetivorans* SriB sequence to the SriB profile HMM using the HMMER program hmmalign and assessing the length of the homolog's sequence that aligns to positions 27-56 in *M. acetivorans* SriB, the conserved region of the extension. For SriC, we assessed the length and electrostatic charge of the ribosome binding loop by aligning each homolog and the *M. acetivorans* SriC sequence to the SriC profile HMM and assessing the length and charge of the homolog's sequence that aligns to positions 191-225 in *M. acetivorans* SriC.

To subset Sri hits based on co-occurrence with Sri genes for conservation analysis of the protein interfaces, we first selected the respective Sri gene with the most significant e-value if there were multiple hits. For SriB, we only considered sequences with long N-terminal extensions (>15aa aligning to the region specified above). Sequences were aligned using mafft and conservation scores[247] were calculated in Jalview[248].

5.4 Results

Ribosome hibernation factors in M. acetivorans

To investigate ribosome hibernation in *M. acetivorans*, we examined homologs of the previously identified archaeal hibernation factor Dri.[240] While Dri is a fusion of two ribosome binding lobes, in *M. acetivorans* the homologs of the two Dri lobes are encoded by separate genes (MA4648 and MA4650). The Dri lobe and their homologs are composed of four tandem cystathionine-β-synthase (CBS) domains. In *M. acetivorans*, an intervening gene between the two Dri homologs (MA4649) and a subsequent gene (MA4651) also encode proteins that are composed of four tandem CBS domains (**Figure 5.1A-B**). Based on their genomic proximity and domain composition, we considered all four proteins as candidate ribosome hibernation factors. We designated these proteins **S**ingle **r**ibosomal subunit **i**nhibitors (**Sri**) to differentiate them from Dri, and labeled them SriA-SriD, according to their gene order.

Having identified candidate ribosome hibernation factors, we next evaluated their expression patterns. During logarithmic growth, SriA and SriB mRNA levels were approximately half those of ribosomal proteins (rProteins) uL2 and uS2 (**Figure 5.1C**).[249] SriC and SriD had transcript levels that were near those of rProteins. Additionally, SriC and SriD had similar transcript levels, which suggests that the *sriC* and *sriD* genes are either co-transcribed, or their transcription is co-regulated. Altogether, this data showed that Sri proteins are likely expressed at levels similar to ribosomes, even during active growth. We also examined how Sri and rProtein mRNA levels change in cells with reduced levels of the critical enzyme methyl-coenzyme M reductase (MCR), which impairs *M. acetivorans* growth.[249] Under MCR limitation (linear growth), rProtein transcripts were downregulated relative to those in exponentially growing cells (WT), whereas SriA, SriC, and SriD transcripts were upregulated (**Figure 5.1D**). As the expression of MCR is increased in these cells, SriA, SriC, and SriD are no longer upregulated and rProteins are no longer downregulated (**Figure S5.3A-D**).

To assess the effect of Sri proteins on translation, we optimized an *M. acetivorans* lysate-based *in vitro* translation system and used it to test whether Sri proteins inhibit protein synthesis. In the absence of Sri proteins, we observed robust luminescence from the NLuc reporter (**Figure 5.1E**). We recombinantly expressed and purified all four Sri proteins (**Figure S5.3E**) and the addition of SriA, SriB, SriC, or SriD to the *in vitro* translation assay decreased luciferase translation. SriD was the most potent inhibitor of the four proteins and its addition to the assay resulted in a 74% reduction in translation. These results indicate that Sri proteins act as translation

inhibitors, consistent with their proposed role in occluding ribosome functional sites during hibernation.

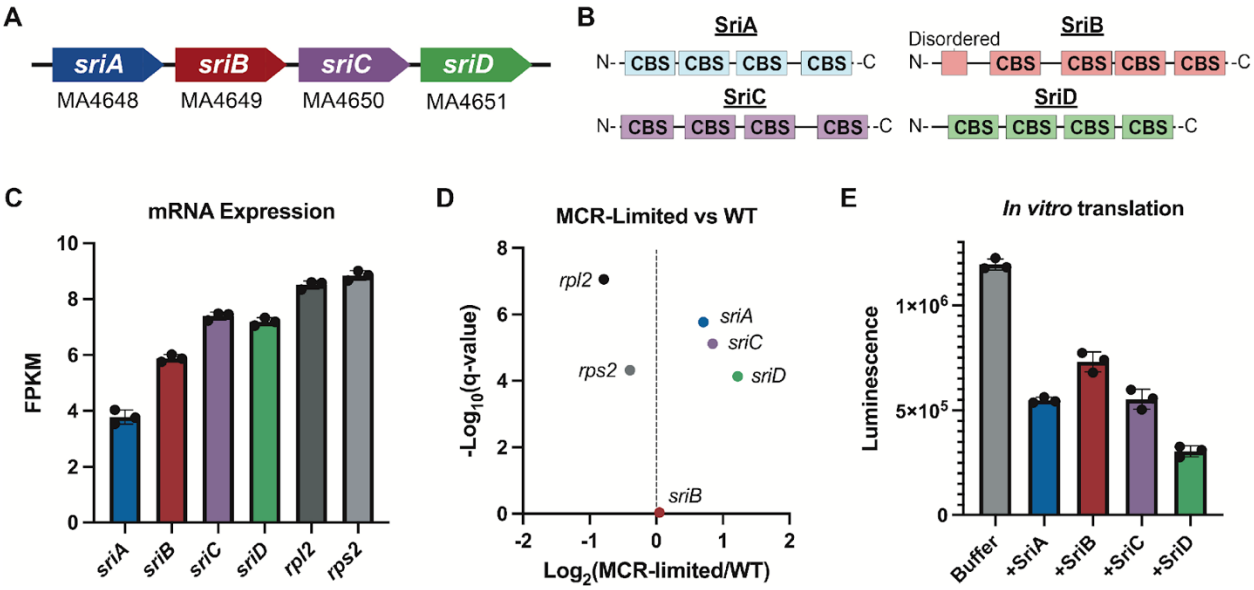


Figure 5.1. Identification of ribosome hibernation factors in *M. acetivorans*. (A) Gene organization of *sri* genes in *M. acetivorans*. (B) Domain architecture of Sri proteins, which all consist of four cystathionine-β-synthase (CBS) domains. (C) mRNA expression levels for Sri and ribosomal proteins from exponential-phase *M. acetivorans* cultures. (D) Differential mRNA expression (significance and fold change) in MCR-limited (linear growth) and WT (exponential growth) *M. acetivorans* cultures. (E) *M. acetivorans in vitro* NLuc luciferase translation assay. Sri proteins were added at a final concentration of 6 µM. For the buffer control, 3 µL of Sri buffer A was added to match the buffer of the reactions with added Sri proteins.

SriA and SriB bind to the large ribosomal subunit

To understand how Sri proteins mediate ribosome hibernation, we reconstituted Sri-ribosomes complexes and determined their structures by cryo-EM. In the structures of the *M. acetivorans* 70S ribosome, we modeled all three rRNAs, 54 annotated rProteins, and a homolog of a previously identified archaea-specific rProtein, aS21[217] (**Figure S5.4A**). We also identified density corresponding to a previously undescribed rProtein in the SSU, which we designated aS36. On the SSU, aS36 occupies a position analogous to rProtein eS30, which is found in eukaryotes and some archaea, suggesting that it has a similar structural role (**Figure S5.4B-C**). aS36 homologs are broadly distributed in the archaeal phylum Halobacteriota, including in the class II methanogens (**Figure S5.4D**). These homologs consist of a single domain of unknown function, Pfam DUF5350. In addition, our high-resolution cryo-EM maps revealed magnesium and zinc binding sites and putative ribosomal RNA (rRNA) methylation sites in the *M. acetivorans* ribosome (**Figure S5.5**).

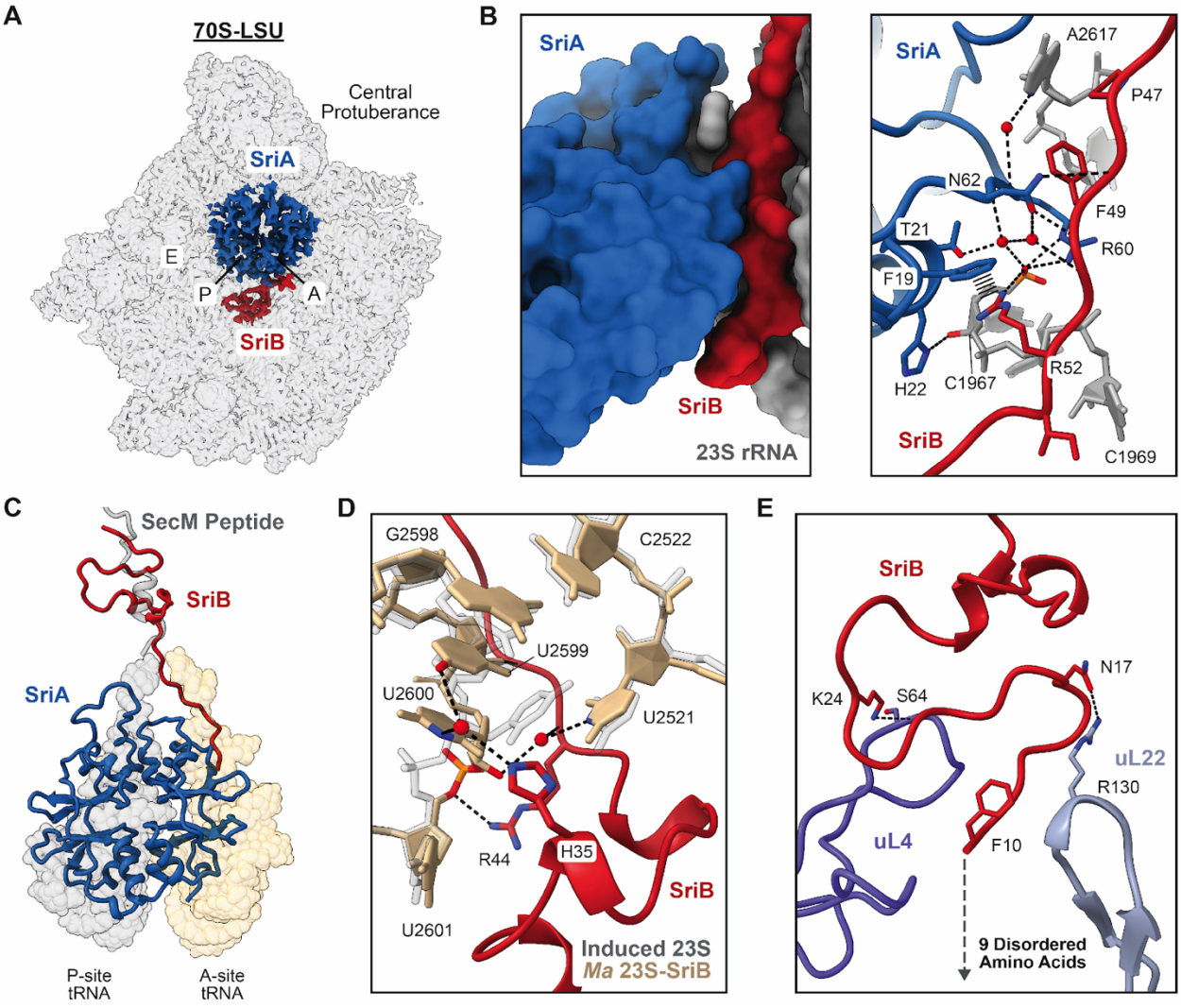


Figure 5.2. SriA and SriB in complex with the *M. acetivorans* ribosome. (A) Cryo-EM density of SriA and SriB bound to the LSU of the 70S ribosome viewed from the subunit interface. (B) Molecular surface (left) and ribbon (right) representations of the SriA-SriB interface and interactions with the 23S rRNA. (C) Overlay of SriA and SriB with the A- and P-site tRNAs and the SecM peptide from PDB:8QOA[250]. (D) PTC nucleotides involved in the tRNA-induced fit shown with tRNA bound to the *E. coli* ribosome (grey, PDB:8EMM)[106] or with SriB (red) bound to the *M. acetivorans* LSU (tan). (E) Interaction of SriB with NPET rProteins uL4 and uL22. An additional nine disordered amino acids, not resolved in the structure, extend further the NPET.

In the initial reconstitution, we added all four Sri proteins to *M. acetivorans* lysate and purified ribosomes by RNA affinity purification using poly-lysine (RAPPL).[242] After focused classification, we determined a 2.0 Å structure of the 70S ribosome (**Figure S5.6**) with densities in the LSU that correspond to SriA and SriB (**Figure 5.2A**). While we resolved the entire SriA protein, only a portion of the SriB N-terminal extension, residues 10-56, were resolved in the cryo-EM reconstruction (**Figure S5.7A**). The SriB N-terminal extension is predicted by AlphaFold[199] to be disordered. On the LSU, SriA and the SriB N-terminal extension form an interface mediated by the 23S rRNA (**Figure 5.2B**). The SriA-SriB interface consists of hydrogen-bonding networks involving ordered water molecules and the two proteins form a wedge around the conserved peptidyl transferase center (PTC) nucleotide A2617 (2602 in *E. coli*, **Table S5.5**). SriA occupies

the A- and P-site tRNA binding sites[250], and the SriB N-terminal extension interacts with SriA in the A site and extends into the PTC (**Figure 5.2C**). Overall, the SriA-SriB complex binds in a position similar to the Dri N-terminal lobe, which is homologous to SriA (**Figure S5.7B**). In the SriA-SriB-ribosome complex, we also observed strong density for the acceptor stem of an E-site tRNA, indicating that SriA binding is compatible with E-site tRNA occupancy (**Figure S5.8A**). Additionally, SriA interacts with a loop in uL16 involved in P-site tRNA binding (**Figure S5.8B**).[225,226]

In addition to its interaction with SriA, SriB extends into the PTC and the nascent polypeptide exit tunnel (NPET). In the PTC, SriB induces a conformational rearrangement that is reminiscent of, but distinct from, the active state adopted upon tRNA binding (**Figure 5.2D**).[106,224] The SriB N-terminus also extends past the PTC and interacts with NPET rProteins uL4 and uL22 (**Figure 5.2E**). In addition, nine N-terminal amino acids of SriB are unresolved in the cryo-EM map but are oriented further down the NPET. Interestingly, the path of SriB down the NPET differs from those of nascent polypeptides and other hibernation factors that target the NPET (**Figure S5.8C**).

SriC and SriD bind to the small ribosomal subunit

In the next reconstitution, we added SriC and SriD to *M. acetivorans* lysate and purified ribosomes. After focused classification, we determined a 2.1 Å structure of the 70S ribosome (**Figure S5.6**) with density in the SSU corresponding to SriD (**Figure 5.3A**). SriD occupies the A site of the SSU, where it occludes the mRNA-binding channel (**Figure 5.3B**). SriD contains two loops that engage the mRNA decoding center (DC) and interact with conserved 16S rRNA bases involved in the induced-fit mechanism of mRNA decoding (**Figure 5.3C**).[251] The presence of SriD also disrupts inter-subunit bridge B2a, formed between helices H69 of the 23S rRNA and h44 of the 16S rRNA. Upon SriD binding, the apical stem and loop of H69, which normally interact with h44, become disordered (**Figure S5.9A**). In contrast, SriA binds to the opposite face of H69 in a conformation compatible with bridge B2a formation (**Figure S5.9B**). Overlay of the SriA and SriD binding sites revealed partial overlap, and the two proteins bind to ribosomes that have distinct SSU rotational states (**Figure S5.9C-D**). Together, these differences, and the absence of SriA and SriD co-occupancy in our cryo-EM datasets, suggest that SriA and SriD cannot bind to the ribosome simultaneously.

In our cryo-EM datasets, SriC was detected only in a small portion of particles that also contained SriD. To obtain a structure of SriC bound to the ribosome, we combined particles from the first two datasets and a third dataset (methods) and determined a 2.9 Å structure of the 70S ribosome (**Figure S5.6**) with density in the SSU corresponding to SriC and SriD (**Figure 5.3D**). Relative to the Dri C-terminal lobe, the SriC ribosome-binding loop is distinct, forming a β-hairpin extension that engages uS11 (**Figure 5.3E and S5.10A**). The SriC extension also interacts with the 16S rRNA 3′-end, including part of the Shine-Dalgarno (SD) sequence (**Figure 5.3F**). This interaction sequesters the 16S rRNA 3′-end in a conformation incompatible with SD-anti SD duplex formation (**Figure 5.3G**). In the cryo-EM structure, we observed SriC and SriD binding to the SSU simultaneously. SriC lacks the A-site loop found in the Dri C-terminal lobe, which is homologous to SriC, and it is replaced with a protein face that interacts with SriD (**Figure S5.10A**). On the SSU, SriC and SriD form an extensive protein-protein interface (**Figure 5.3H**). In addition, SriC and SriD interact with the C-terminal tails of uS13 and uS19 (**Figure S5.10B-D**). The uS19 C-terminal tail lies beneath the SriC-SriD interface, where it contacts interface residues (**Figure 5.3H**).

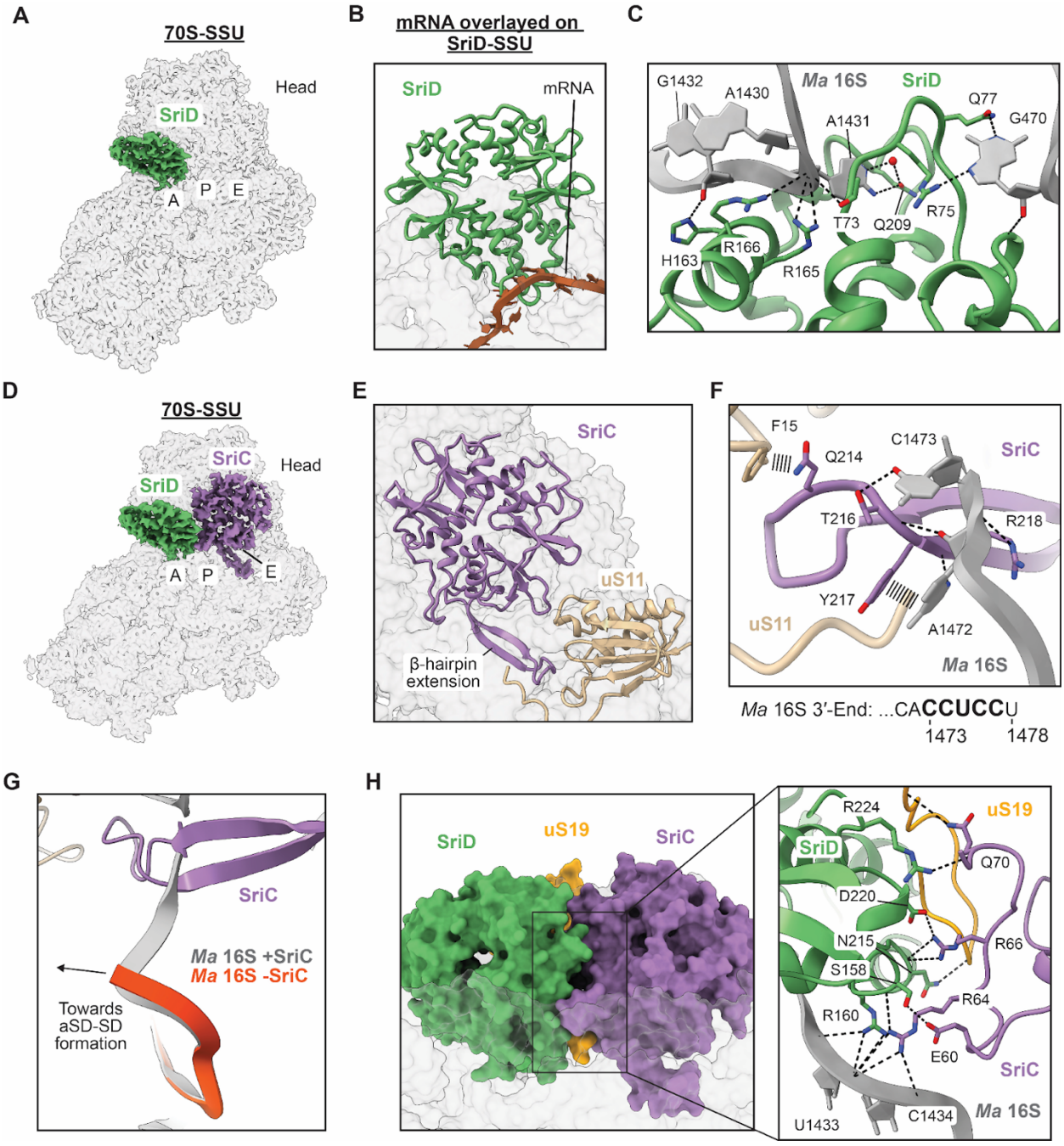


Figure 5.3. SriC and SriD in complex with the *M. acetivorans* ribosome. (A) Cryo-EM density of SriD bound to the SSU of the 70S ribosome viewed from the subunit interface. (B) Overlay of mRNA bound to the *E. coli* ribosome (PDB:8EMM)[106] with SriD bound to the *M. acetivorans* ribosome. (C) Interactions between SriD and the mRNA decoding center. (D) Cryo-EM density of SriC and SriD bound to the SSU of the 70S ribosome viewed from the subunit interface. (E) SriC binding in the P- and E-sites of SSU with extension that interacts with uS11. (F) Interaction between the SriC extension and the 16S rRNA 3′-end. The sequence of the *M. acetivorans* 16S rRNA 3′-end is shown below with the Shine-Dalgarno sequence highlighted in bold. (G) Conformation of the 16S rRNA 3′-end in the presence (grey) or absence (orange) of SriC. The direction of anti-SD (aSD)-SD duplex formation is indicated. (H) Molecular surface (left) and ribbon (right) representations of the SriC-SriD interface and interactions with uS19 and the 16S rRNA.

Sri gene clusters are broadly distributed in Archaea

To determine the phylogenetic distribution of Sri factors, we searched the genomes of all archaeal species in the Genome Taxonomy Database (GTDB) for Sri homologs using sequence homology. Because all four *sri* genes are homologous to each other through their shared CBS-domain composition, we assigned homologs of specific *sri* genes by constructing a phylogenetic tree of all Sri homologs and defining subtrees corresponding to each of the four Sri factors (**Figure S5.2**). We identified several small, but divergent Sri clades, potentially indicating divergence in function. A subgroup of SriB homologs present across multiple archaeal lineages have lost the N-terminal extension that binds the ribosome, suggesting an alternative function (referred to as SriB-short in **Figure 5.4A**). We also identified a diversification of SriC homologs predominantly in the order Nitrososphaerales, many of which have a shorter and less positively charged SSU-binding loop (referred to as SriC-short in **Figure 5.4A**). We do not consider these exceptions functional homologs in the subsequent analysis, despite their evolutionary relationship. Additionally, we found a widely distributed family of SriA homologs fused with a domain homologous to the bacterial hibernation factors HPF and RaiA. During the preparation of this report, these proteins were shown to function as ribosome hibernation factors and were named Hib.[246] The occurrence of *hib* and *sri* genes in archaeal genomes are strongly anti-correlated (**Figure 5.4A**).

Sri homologs occur in 15 archaeal phyla and frequently occur together in a gene cluster (**Figure 5.4A**). Many archaeal genomes encode SriA-D in genomic order, although some archaea encode a subset of the four Sri proteins. Additionally, several clades of archaea encode a standalone *sriD* gene, suggesting that SriD may be sufficient to mediate hibernation in these organisms. Standalone *sriD* genes occur predominantly in the phylum Asgardarchaeota, the closest archaeal relatives of eukaryotes. With the exception of standalone *sriD* genes, most other *sri* genes co-occur with their binding partner (SriA-SriB and SriC-SriD) in archaeal genomes. To evaluate whether Sri homologs cooperatively bind to ribosomes across archaea, we examined the conservation of residues[247,248] involved in Sri-Sri protein contacts on the *M. acetivorans* ribosome. In organisms that encode both SriA and SriB or SriC and SriD, residues at the protein-protein interfaces are conserved (**Figure 5.4B-C**). Conversely, in organisms that encode standalone *sri* genes, the residues at the Sri-Sri interfaces are markedly less conserved (**Figure S5.11**).

5.5 Discussion

Here, we demonstrated that Sri proteins mediate ribosome hibernation in *M. acetivorans*. Dri homologs, SriA and SriC, bind to the ribosome in similar locations to Dri and the discovery of additional factors SriB and SriD revealed that Sri proteins work in tandem to inactivate the ribosome. Sri proteins are distinct from other hibernation factors because they form protein-protein interfaces with each other upon binding the ribosome. The coordinated binding of multiple hibernation factors to the ribosome may enhance binding cooperativity or could introduce additional layers of regulation. This mode of binding is reminiscent of some hibernation factors and translation elongation factors that simultaneously bind to ribosomes.[46,48,49,239,252–255] SriA-SriB and SriC-SriD complexes cannot bind the ribosome simultaneously because the SriA and SriD binding sites overlap. This suggests that the two sets of proteins target different ribosomes in the cell.

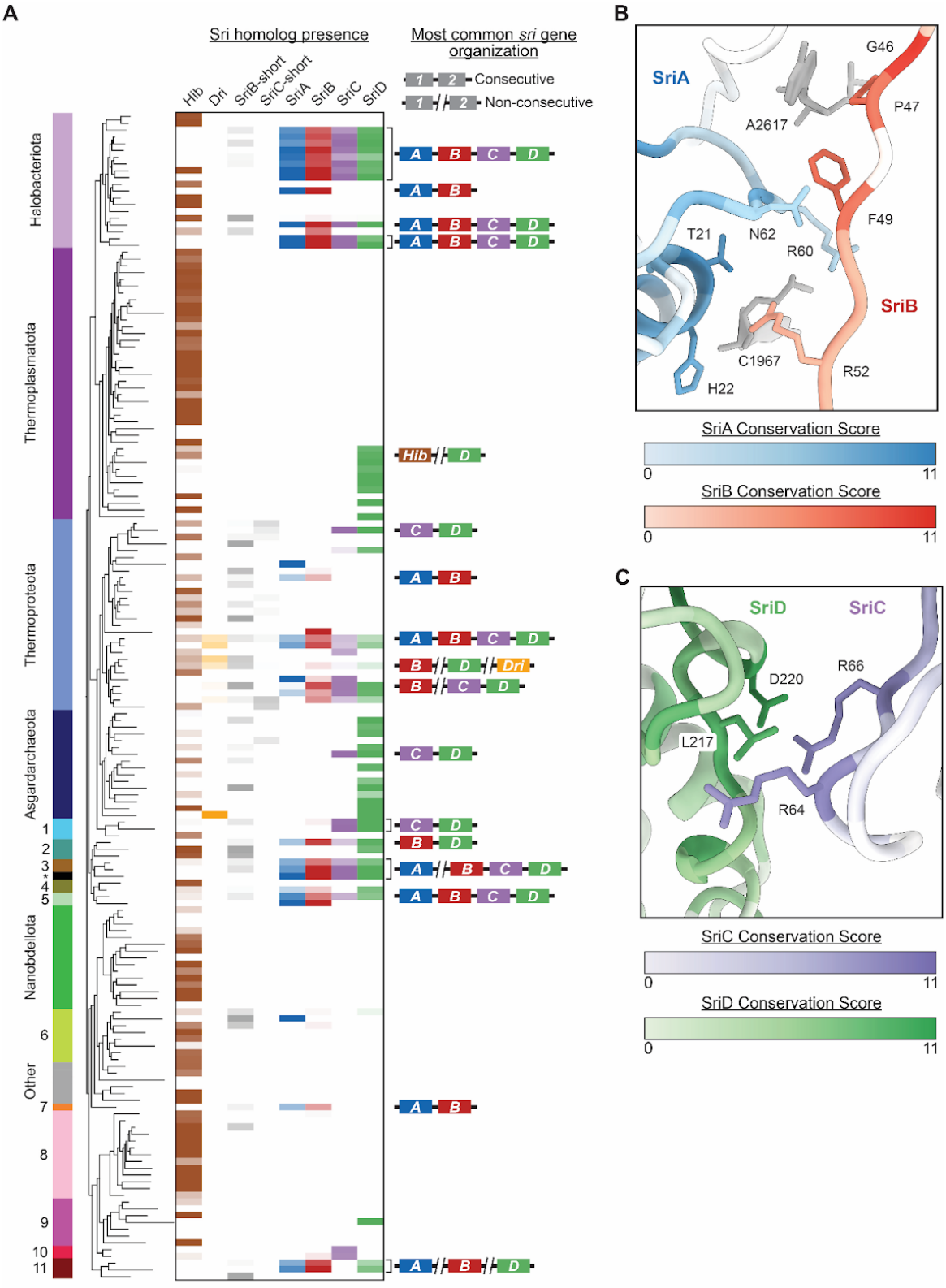


Figure 5.4. Distribution and conservation of Sri homologs in archaea. (A) Distribution of Sri homologs in GTDB archaea at the order level. Archaeal phyla are indicated on the GTDB tree (left) and Sri homologs are shaded according to their occurrence in each archaeal order. SriB homologs that lack an N-terminal extension and divergent SriC

homologs are shown in the SriB-short and SriC-short columns, respectively. The right panel depicts the most common gene organization involving *sri* genes in the indicated groups of archaea. Phylum abbreviations: 1-Korarchaeota, 2-Methanobacteriota, 3-Hydrothermarchaeota, *-JACRDV01, 4-Methanobacteriota_B, 5-Hadarchaeota, 6-Aenigmatarchaeota, 7-Undinarchaeota, 8-Micrarchaeota, 9-Iainarchaeota, 10-B1Sed10-29, 11-Altiarchaeota. (B) SriA-SriB interface residues are colored based on conservation scores from homologs in organisms that encode both proteins. 23S rRNA bases that mediate SriA-SriB interactions are shown in grey. (C) SriC-SriD interface residues are colored based on conservation scores from homologs in organisms that encode both proteins.

Sri proteins protect the SSU from degradation in stationary phase. Depletion of the SSU in Δ*sriABCD* cells during stationary phase leads to an increase in the lag phase upon growth resumption. Therefore, Sri proteins likely help archaea that inhabit nutrient-limited environments recover from dormancy. While ribosome degradation in archaea is not well understood, 3′-5′ RNA degradation is likely mediated by the exosome, though some species in Halobacteriota also encode an RNaseR homolog.[256] Our cryo-EM structures show that SriC sequesters the 16S rRNA 3′-end and could protect it from exonucleases. *M. acetivorans* 23S rRNA is circularized in the mature LSU[243], protecting it from exonucleases. This could explain why the LSU is more stable than the SSU in the absence of Sri proteins during stationary phase.

We showed that Sri proteins are expressed during active growth, suggesting that they do not bind to actively translating ribosomes, but bind to ribosomes upon translational arrest. Additional proteins or small molecules could regulate Sri binding to ribosomes. CBS-domains often function as metabolite sensors that bind to adenosine nucleotides,[257] and it remains unknown if nucleotides regulate Sri protein function. Additionally, a purine biosynthesis enzyme, PurH, and translation elongation factor 2, aEF2, dimerize 50S subunits in *M. acetivorans*.[239] It is unclear how 50S-dimerization or Sri-mediated 70S hibernation are coordinated, or if these pathways can cooperate to mediate ribosome hibernation.

Sri homologs are found across multiple archaeal phyla and represent a broadly distributed set of factors. While many clades of archaea encode all four Sri proteins, others encode only a subset, suggesting that different combinations or standalone Sri proteins can mediate ribosome hibernation in these organisms. Curiously, the occurrence of Sri and Hib (SriA-RaiA/HPF fusion)[246] genes in archaeal genomes are strongly anti-correlated, implying that these hibernation systems are either redundant or incompatible. Nearly all archaea encode either Sri, Dri, or Hib genes, and these protein families provide insight into ribosome hibernation across archaea. Our work establishes Sri proteins as a widespread set of hibernation factors and enables further investigation of ribosome hibernation in archaea.

5.6 Supplementary Information

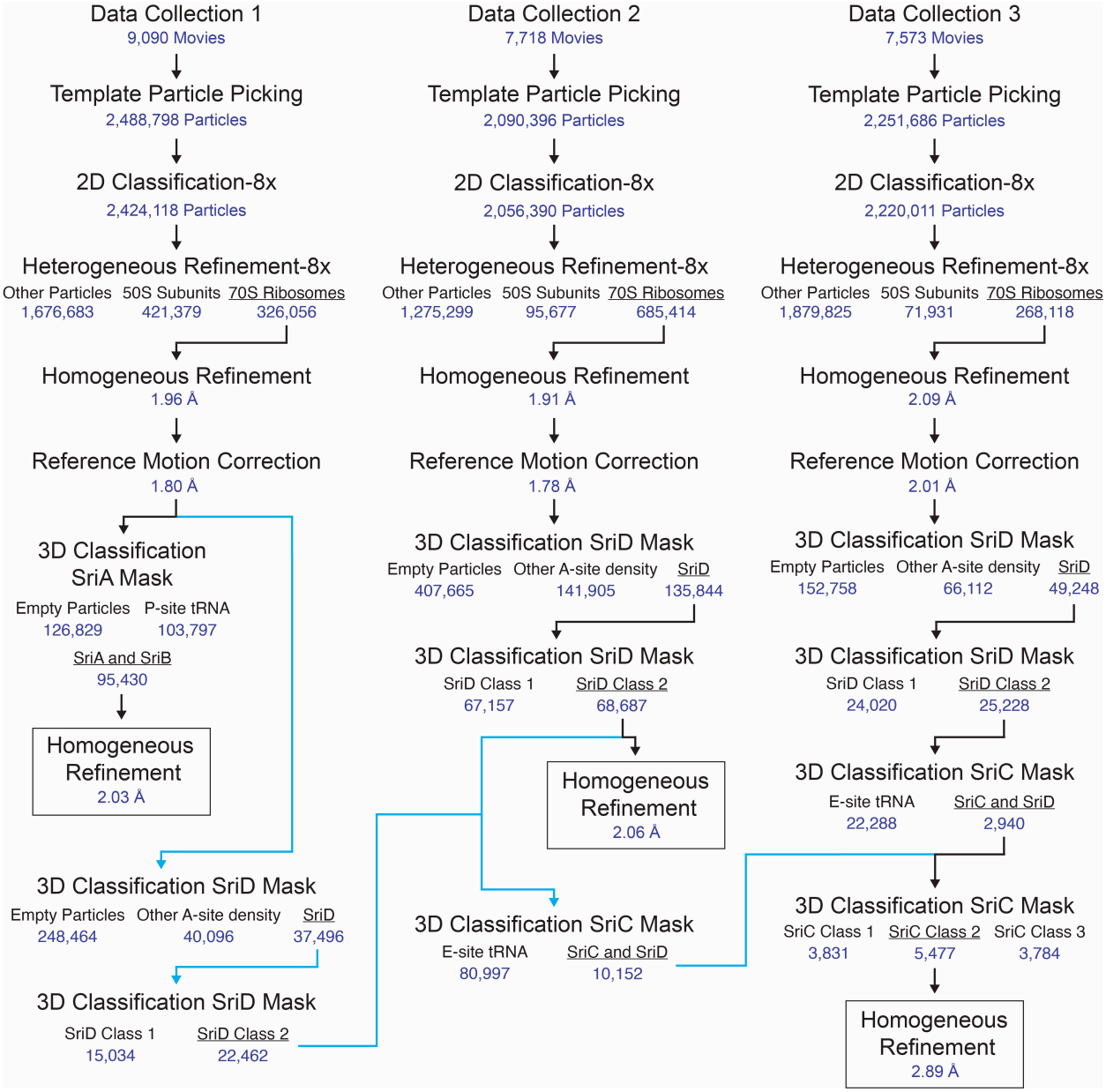


Figure S5.1. Cryo-EM processing workflow. Blue arrows show the processing path to combine SriD containing-particle from the three datasets for SriC classifications and reconstructions.

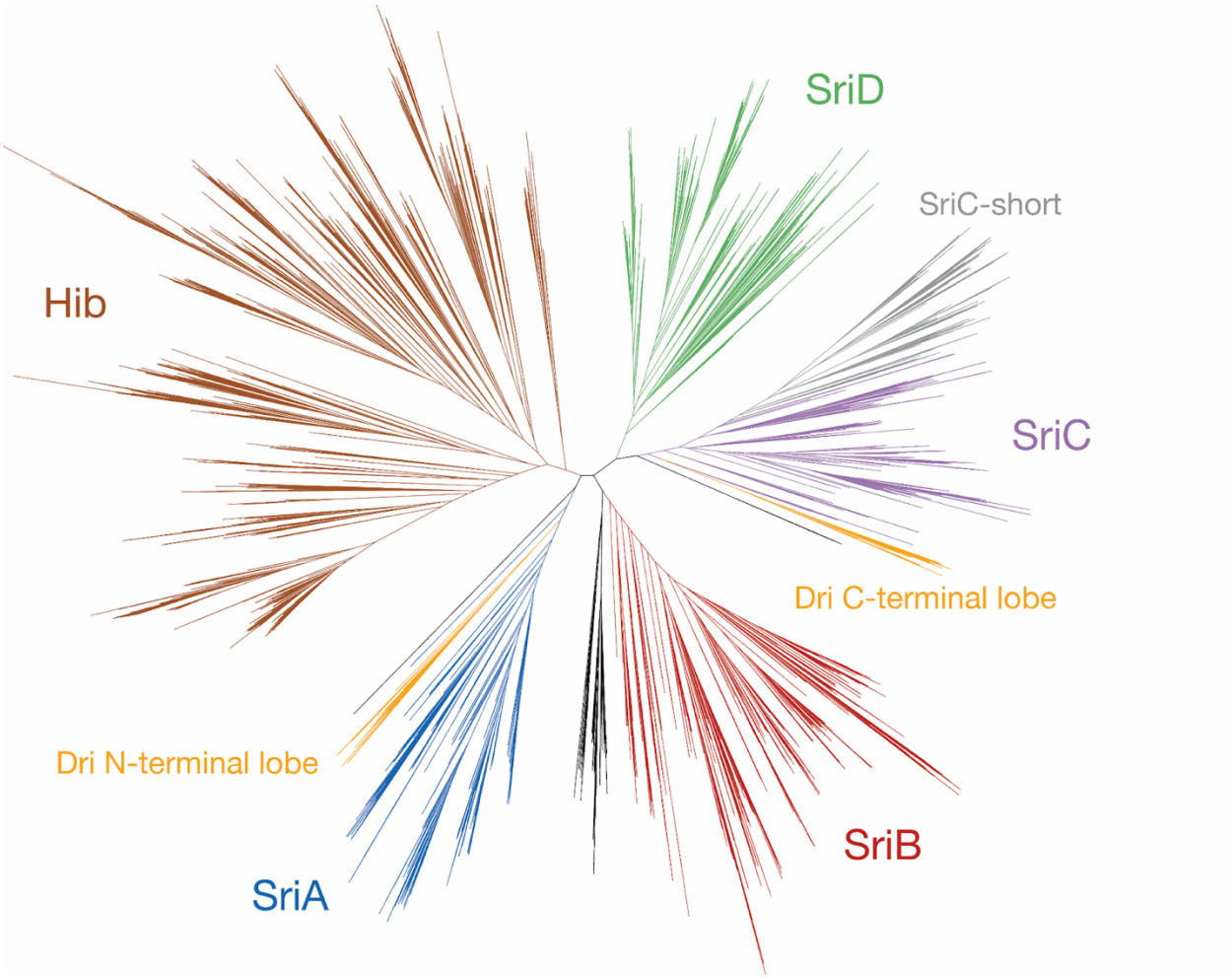


Figure S5.2. Phylogenetic tree of all Sri proteins and related homologs, including Hib and Dri (split into N- and C-terminal lobes), mined from proteomes of GTDB representative species. Subclades corresponding to SriA, SriB, SriC, SriD, and Hib were defined as regions of the tree that consistently hit the respective homology model best. SriC-short represents a diversification of SriC proteins predominantly in Nitrososphaerales that have a shorter and less positively charged loop that likely function in a different manner than canonical SriC. Clades colored black do not consistently hit one of the homolog models best and may represent related CBS domain-containing proteins.

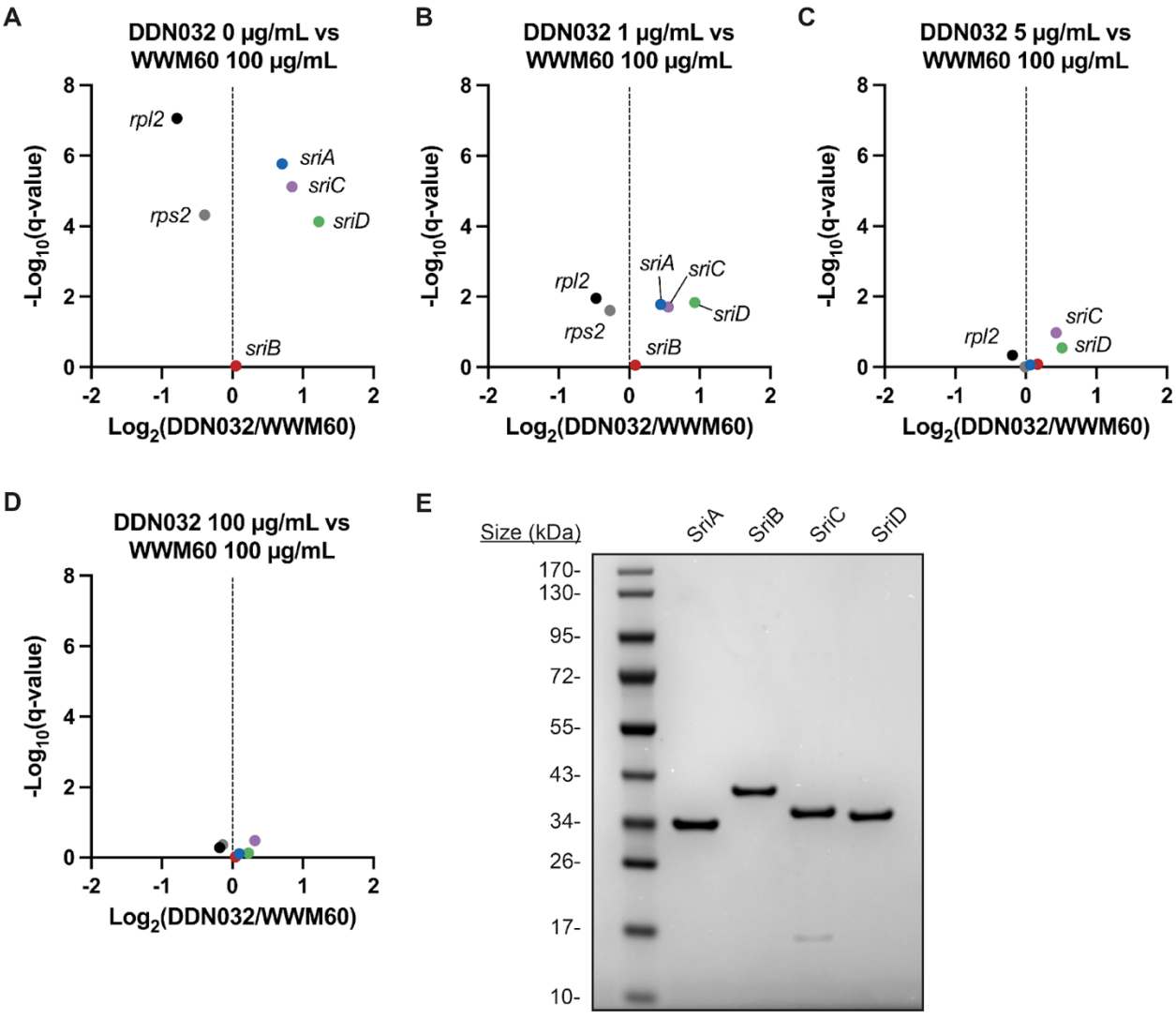


Figure S5.3. Differential expression of Sri proteins under MCR limitation and Sri protein purification. (A-D) Differential mRNA expression (significance and fold change) in DDN032 (tetracycline inducible MCR expression) and WWM60 (WT) *M. acetivorans* cultures. MCR expression was varied across panels A-D with increasing concentrations of tetracycline (concentrations are in the titles). (E) Recombinantly expressed and purified Sri proteins resolved on a 4-12% polyacrylamide gel stained with Coomassie brilliant blue.

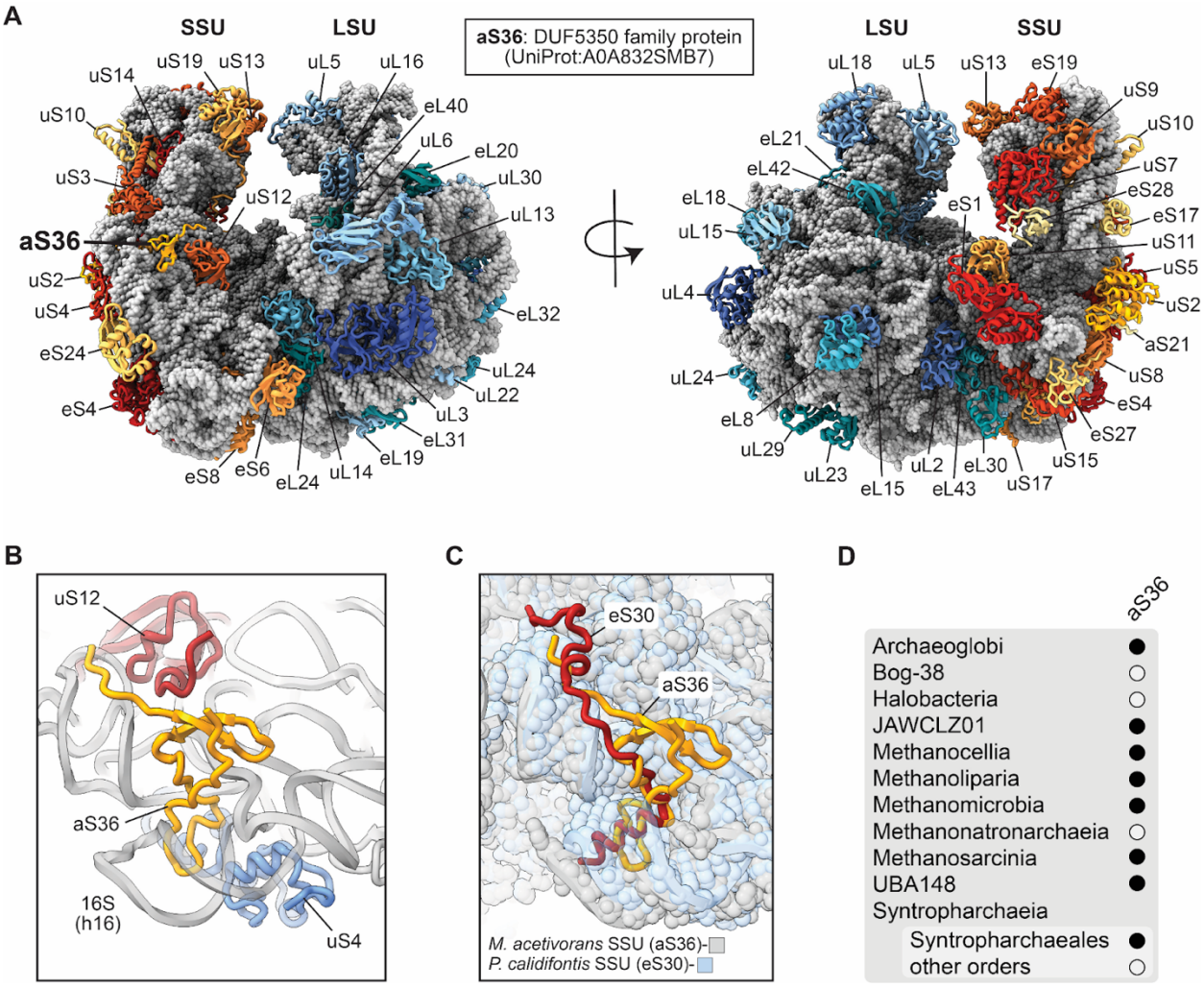


Figure S5.4. rProteins in the *M. acetivorans* ribosome. (A) rProteins are labeled on the model of the *M. acetivorans* 70S ribosome. The aS36 label is bolded and its previous annotation, including the accession code, is shown in the middle box. (B) aS36 is in proximity to uS4 and uS12 and interacts with 16S rRNA helix h16. (C) Overlay of the SSUs from *M. acetivorans* (grey) and *P. calidifontis* (blue, PDB:9E71[240]) showing the locations of aS36 and eS30, respectively. (D) Distribution of aS36 across the archaeal phylum Halobacteriota. Closed and open circles represent clades where aS36 homologs were or were not identified, respectively.

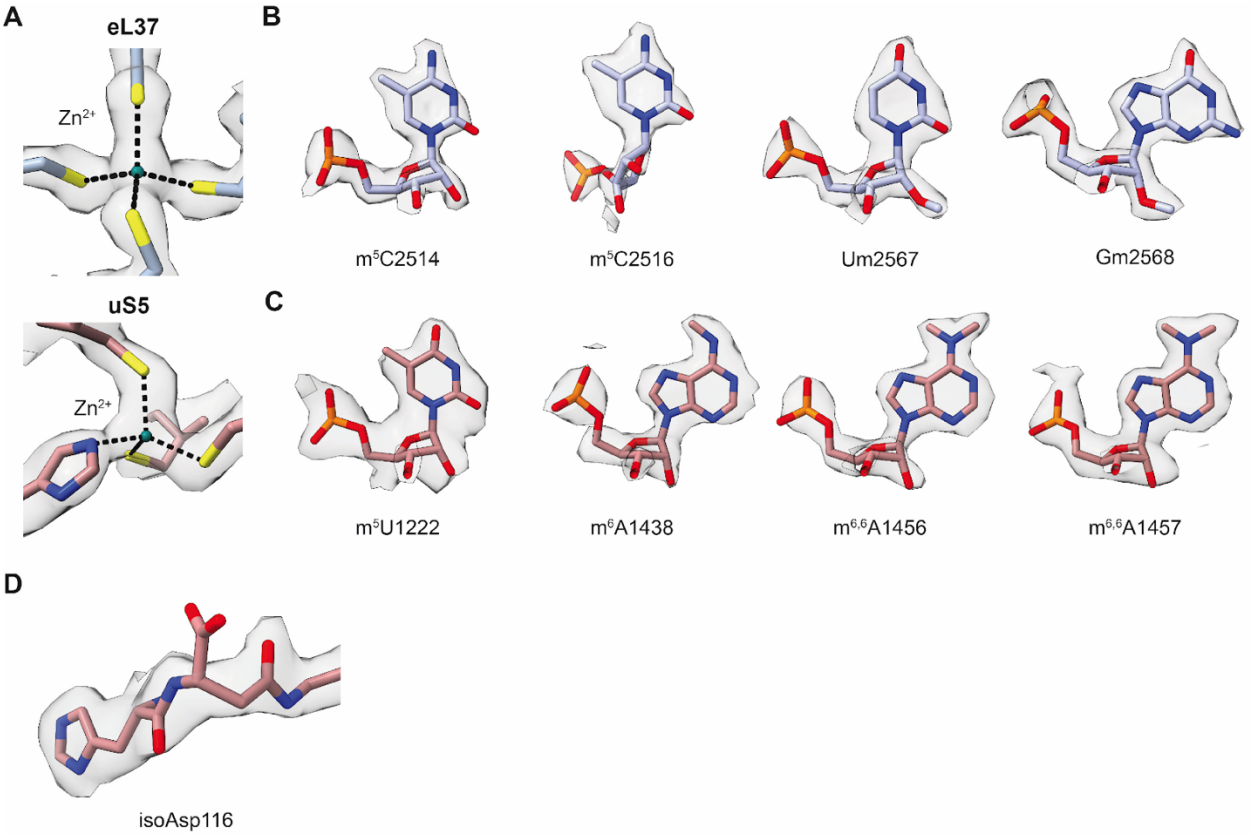


Figure S5.5. Metal binding sites and post-transcriptional and post-translational modifications in the *M. acetivorans* ribosome. (A) Zinc binding sites in LSU rProtein eL37 and SSU rProtein uS5 with cryo-EM density. (B-C) Cryo-EM density for post-transcriptional in the LSU (B) and SSU (C). (D) Cryo-EM density for isoaspartate residue 116 in uS11.

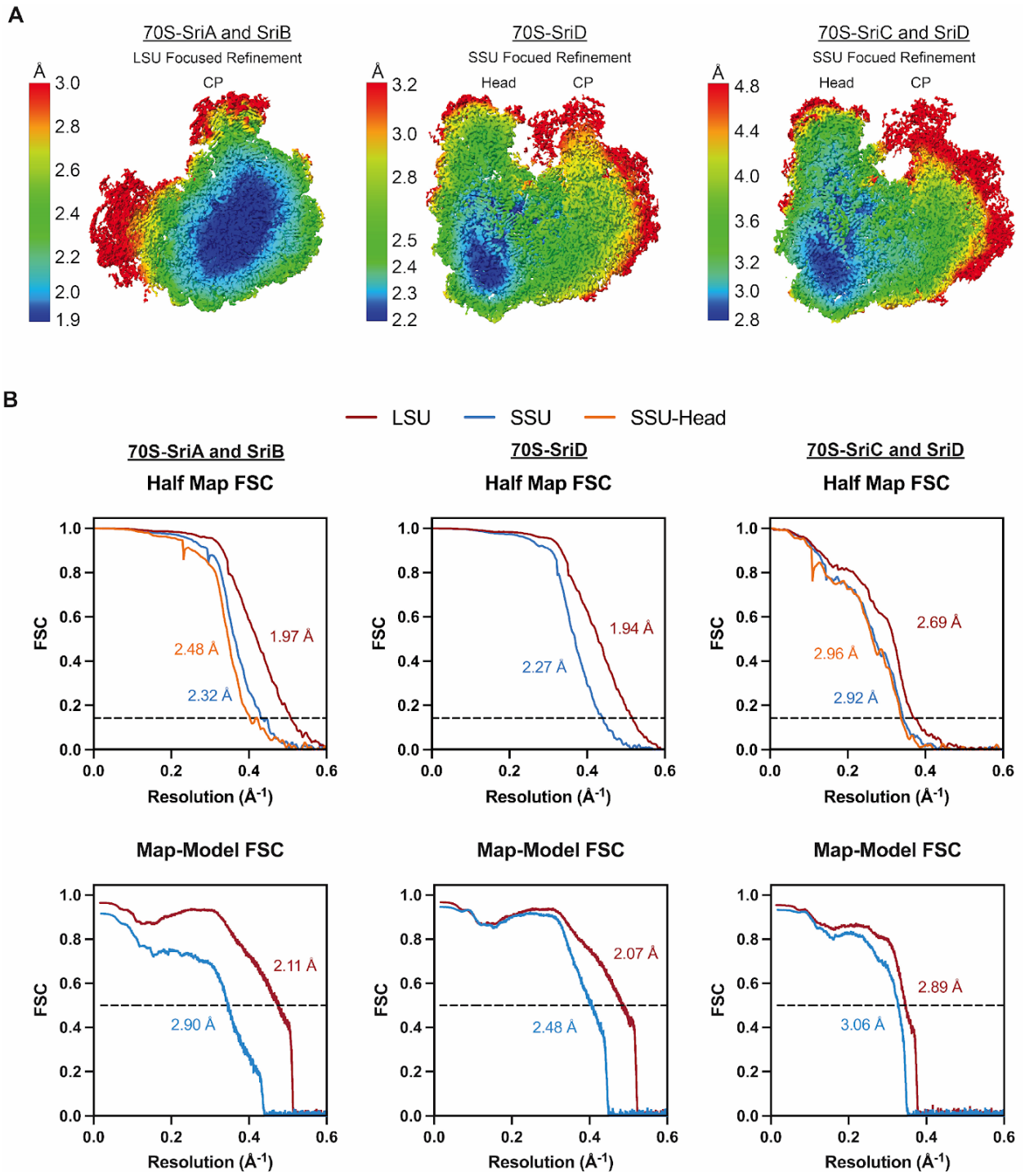


Figure S5.6. Resolution of cryo-EM maps. (A) Local resolution plotted on the LSU (left) or SSU (middle and right) focused refinement maps. The LSU central protuberance (CP) is labelled. (B) Half map (top) and map to model (bottom) FSCs for cryo-EM maps and models in this study.

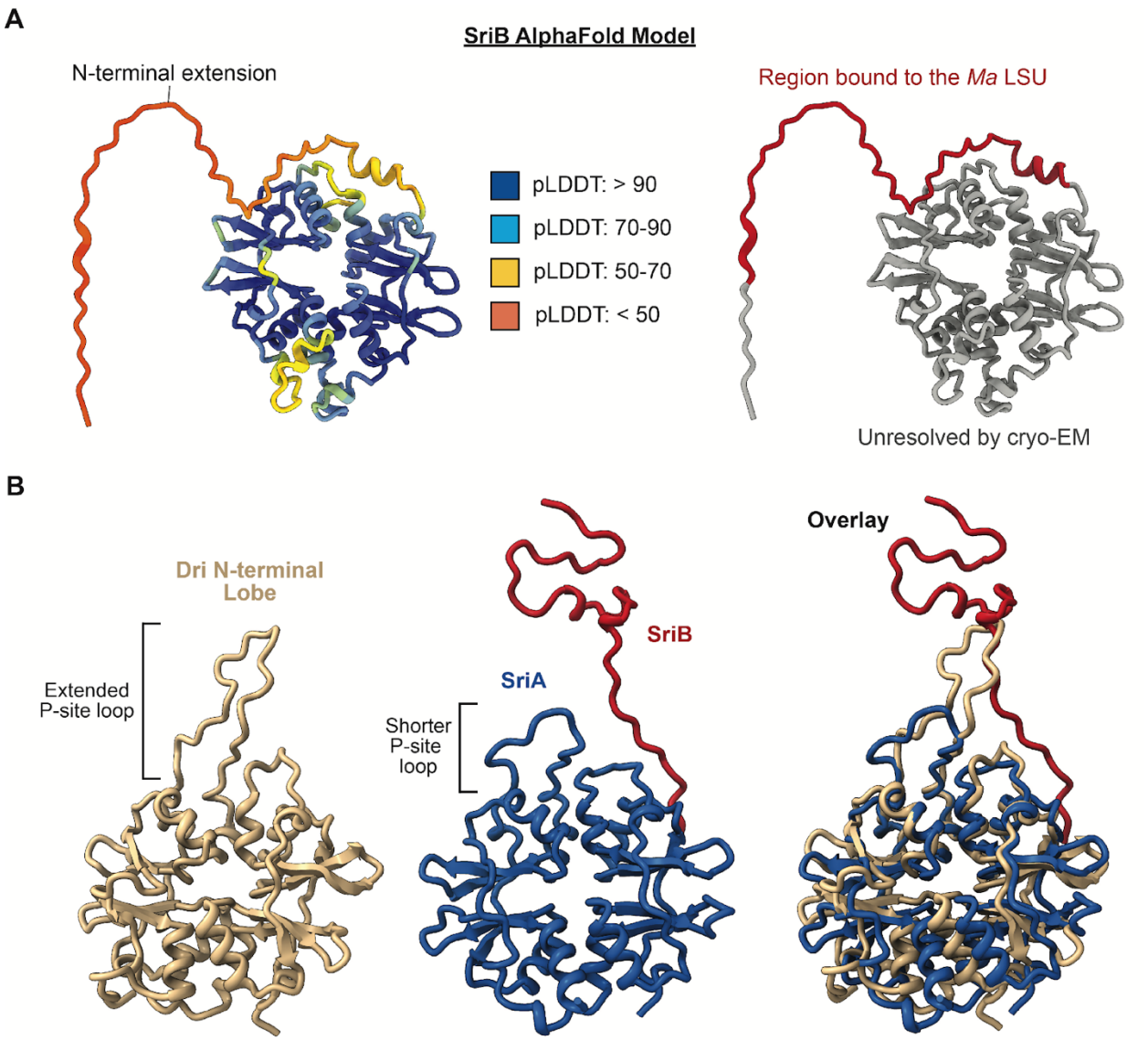


Figure S5.7. Structural features of SriA and SriB. (A) AlphaFold[2] prediction of SriB colored by (left) confidence score or (right) regions that are ordered (red) or disordered (grey) in the cryo-EM structure of SriB bound to the *M. acetivorans* ribosome. (B) Comparison of the Dri N-terminal lobe (left) with the SriA-SriB complex (middle). (right) Alignment of the *M. acetivorans* LSU in complex with SriA and SriB to the *P. calidifontis* LSU in complex with Dri (PDB:9E6Q[240]), highlighting the overlap in Sri and Dri binding sites.

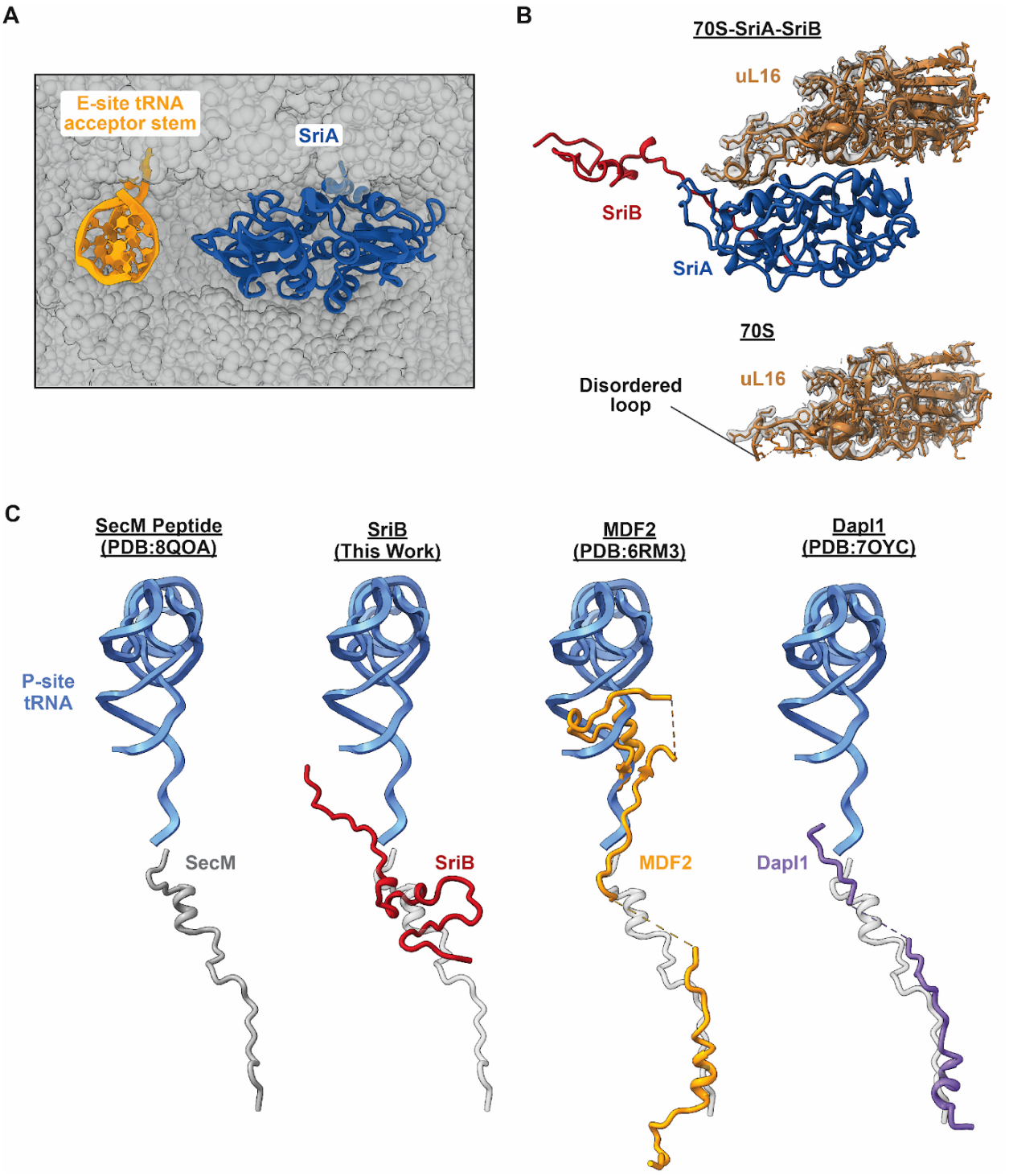


Figure S5.8. SriA and SriB interactions with the LSU. (A) SriA binding is compatible with the presence of E-site tRNA. (B) Model and cryo-EM density of uL16 in the 70S-SriA-SriB complex (top) compared with the 70S ribosome lacking SirA and SriB (bottom). In the absence of SriA and SriB, a loop of rProtein uL16 is disordered. (C) Comparison of the SriB N-terminus with a stalled nascent polypeptide chain[250] and hibernation factors MDF2[19] and Dapl1[49], which target the exit tunnel. The SecM peptide is overlaid in grey on the hibernation factors to highlight differences in their paths through the PTC and exit tunnel.

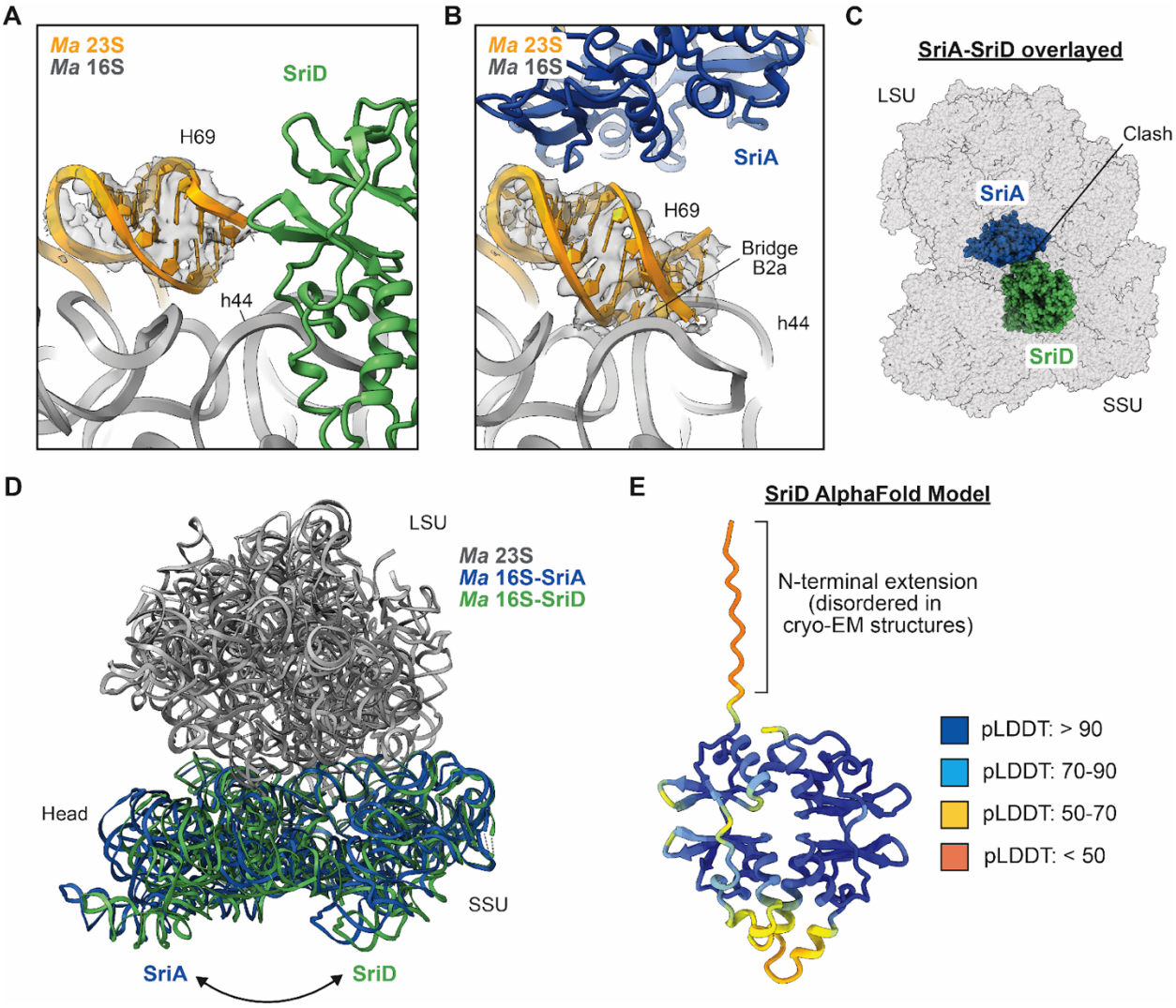


Figure S5.9. Differences in SriA and SriD binding to the ribosome. (A-B) Conformations of LSU helix H69 and SSU helix h44 in the presence of (A) SriD or (B) SriA. Bridge B2a is maintained during SriA binding but is absent in the presence of SriD. (C) Overlay of SriA and SriD binding sites on the ribosome. Simultaneous binding of SriA and SriD would result in a steric clash between the two proteins. (D) *M. acetivorans* ribosomes bound to SriA (blue) and SriD (green) aligned to their 23S rRNA (grey) to highlight differences in the rotational state of the SSU. (E) AlphaFold prediction of SriD colored by confidence score. The SriD N-terminal extension is not resolved in the cryo-EM structure of SriD bound to the *M. acetivorans* ribosome.

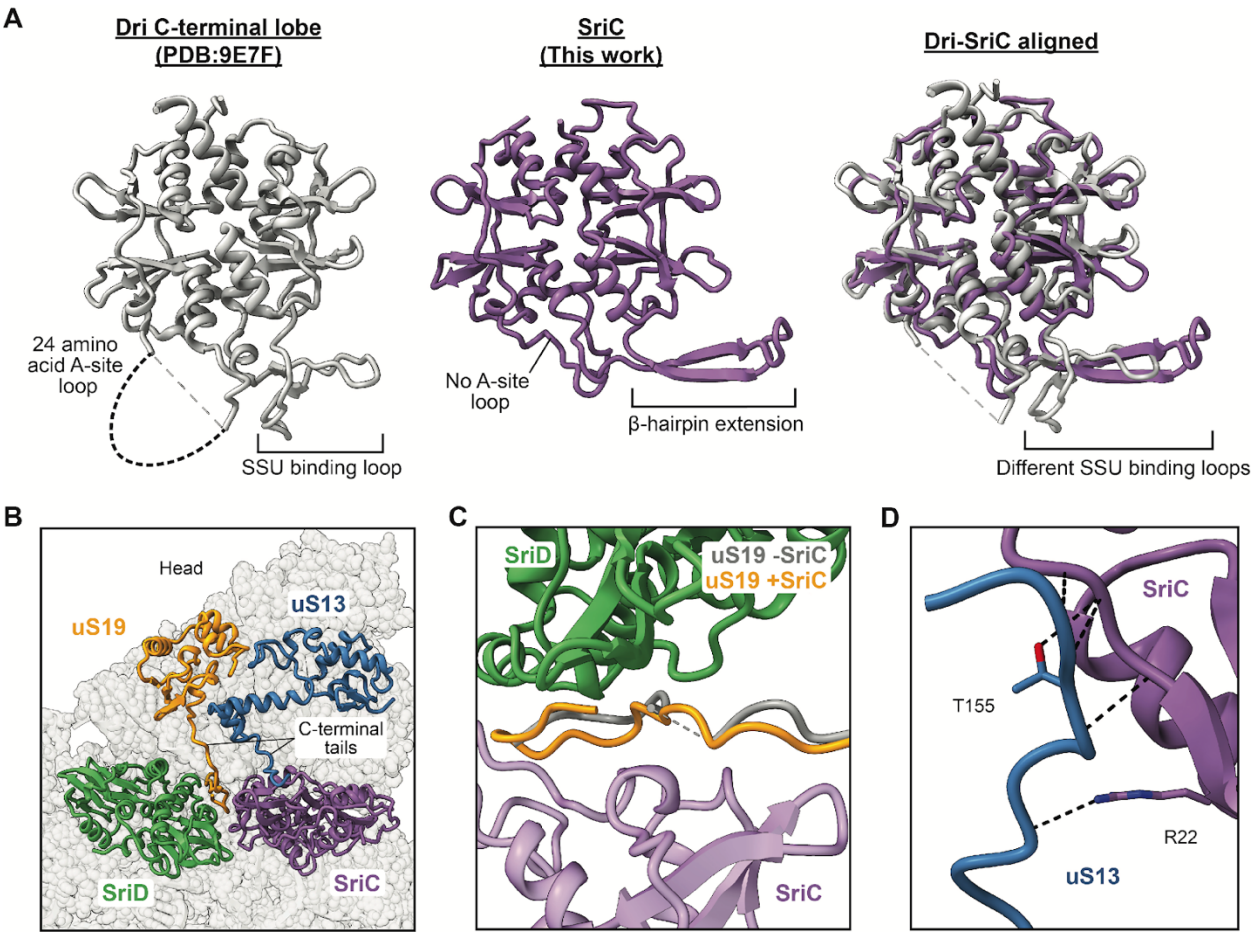


Figure S5.10. SriC and SriD interactions with the SSU. (A) Comparison of (left) the Dri C-terminal lobe (PDB:9E7F[240]) and (middle) SriC. (right) Alignment of the Dri C-terminal lobe with SriC. (B) Interactions of SriC and SriD with the C-terminal tails of uS13 and uS19. (C) Conformation of the uS19 C-terminal tail in the presence of SriD (grey) or of both SriC and SriD (yellow). (D) Interaction between SriC and the uS13 C-terminal tail.

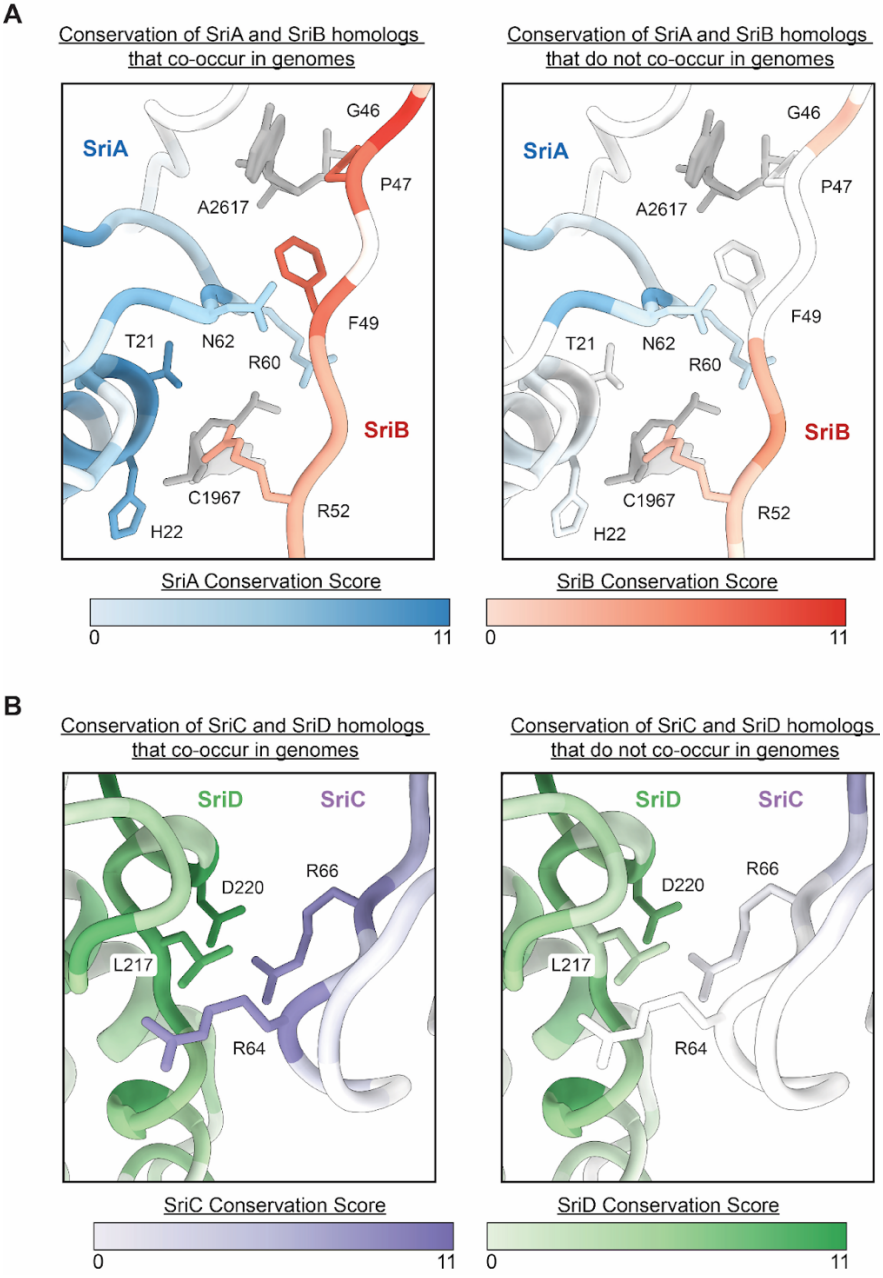


Figure S5.11. Conservation of Sri-Sri interface residues. (A) SriA-SriB interface residues are colored based on conservation scores from homologs in organisms that encode both proteins (left) or in organisms that have standalone *sriA* or *sriB* genes (right). (B) SriC-SriD interface residues are colored based on conservation scores from homologs in organisms that encode both proteins (left) or in organisms that have standalone *sriC* or *sriD* genes (right).

Table S5.1. Protein sequences used for recombinant expression in chapter 5

Name	Sequence
SriA	MNVSEIMSEGPVSIKERDFVTHARQLMRDYLFRSLVVVDEGNRLVGMLNDQDIMRV TSTRSNVTVGGYARPSPTVTPDMDVVKAAKLMVQSKQNRVPVVKSTTDHTVVGVLS DVDILRNAELPRSASKTIDMVMTKKVKTCSPDERISKVWNYMTETDYTGIPVVSKKG DPIGMITRRDIIKAGILRMSIEDERAARPNESPKVEKIMSTPAYTLSENDSVKSAIEMIIQ HDIGRVTIVNEQGKISGIADRQDLMNAFVNGWSEHHHHHH
SriB	MILLNKNTTFVPVEKMNVQPQVNKSGKKAQQKDPHSVSSMGTMRIGPSFKSRIAEHE GKILALATRDVVTLPPTAAIMEAVRIMTERRFRRIPITDAGTGRLEGVVTSVDIIDFLGG GSRNLLVENRFKGNLLAAINEEVRQIMQTDVAYLNDQADFKDAVTTMLERRTGGLPI VNDEMQVIAIFTERNAVELMGGIVTNKTVDEYMTKNVTMVTTDTPIGQAAKVMVQN RFRRLPVVKDGIFAGIVTASDIVHFLGRGDAFSKLTTGNIHEALDQPVGSIVSQELIWT SPGTDMGKAMEIMLEKKIGSLPVLEDGMLRGIITESDFLRGFDLHHHHHH
SriC	MNVADIMSSPVYAINIDEPVSRARKLMLRHRISTLLVLNEGKMVGIVTKSDISNRLAQ AEPLWRRRPIDQIPIKLLMTESVITIYPEASISQAAALMLENGVHDIPVVKNDIVGIVTR TDIVRYVAEHADEIDTKISTLMTDDIVSVHRHHTINHVIEEMNKNEIERVIVKDDAGKP VGVISKRNLALNLLTDNEGKLSTKSIKMARKSSPGGQKTYRYVKEVPLTAEDIMITPII SIDVNEKISIAAKKLIEEEITALPVSDGEEIVGILSRTDIMKSVLHHHHHH
SriD	MQRIETKTLDTHEVKCMQVKDIMVQPHKIDKSDTISHALDLMEKKDTKRLLVVHDN QVLGVLTMRGLTEQLGTRRKQSKPASSLHVATAVSDNFVKVLPDTDVKDALTLMKK KGGVIIVTDNGNAMGWVTPQELMKVNHFTGFAGEVMEKNPIIVSPSDRVSHARRLIL DKNVGRLPVIENGKLVGIIAEDDIAFAMRSFRDLVADNQQDSRIKNLLVGDIMTRSVV NVYTNTPLSDTVDTMLEYDVGGVPVLNLEEELVGFLARRNIINTIEEHHHHHH

Table S5.2. NLuc *in vitro* translation reporter mRNA sequence
The SD sequence is **bolded**; The start codon is <u>underlined</u>

Name	Sequence
NLuc mRNA	GGUCCCAAAGUGAUUUAAUAAAUU**AAAGGAGGA**AAUUAAA<u>AUG</u>GUCUUCACA CUCGAAGAUUUCGUUGGGGACUGGCGACAGACAGCCGGCUACAACCUGGACCA AGUCCUUGAACAGGGAGGUGUGUCCAGUUUGUUUCAGAAUCUCGGGGUGUCCG UAACUCCGAUCCAAAGGAUUGUCCUGAGCGGUGAAAAUGGGCUGAAGAUCGAC AUCCAUGUCAUCAUCCCGUAUGAAGGUCUGAGCGGCGACCAAAUGGGCCAGAU CGAAAAAAUUUUUAAGGUGGUGUACCCUGUGGAUGAUCAUCACUUUAAGGUGA UCCUGCACUAUGGCACACUGGUAAUCGACGGGGUUACGCCGAACAUGAUCGAC UAUUUCGGACGGCCGUAUGAAGGCAUCGCCGUGUUCGACGGCAAAAAGAUCAC UGUAACAGGGACCCUGUGGAACGGCAACAAAAUUAUCGACGAGCGCCUGAUCA ACCCCGACGGCUCCCUGCUGUUCCGAGUAACCAUCAACGGAGUGACCGGCUGGC GGCUGUGCGAACGCAUUCUGGCGUAAGGAUCCGGAGAGCUCCCAACGCGUUGG AUGCAUAGCUUGAGUAUUC

Table S5.3. Cryo-EM data collection and processing

Reconstruction	**70S-SriA-SriB**	**70S-SriD**	**70S-SriC-SriD**
Magnification	105,000	105,000	105,000
Voltage (kV)	300	300	300
Electron Exposure ($e^-/Å^2$)	40	40	40
Defocus Range (μm)	-0.5/-1.5	-0.5/-1.5	-0.5/-1.5
Pixel Size (Å)	0.8264	0.8264	0.8264
Symmetry Imposed	C1	C1	C1
Initial Particle Images	2,488,798	2,090,390	6,830,880
Final Particle Images	95,430	68,687	5,477
Map Resolution (Å)	2.03	2.06	2.89
FSC Threshold	0.143	0.143	0.143

Table S5.4. Model refinement statistics

Model	**70S-SriA-SriB**	**70S-SriD**	**70S-SriC-SriD**
Model component			
Model resolution (Å)	2.11/2.90 (50S/30S)	2.07/2.48 (50S/30S)	2.89/3.06 (50S/30S)
FSC threshold	0.5	0.5	0.5
Map sharpening *B* factor ($Å^2$)	35.5/48.6 (50S/30S)	30.7/48.3 (50S/30S)	25.1/27.9 (50S/30S)
Model composition			
Non-hydrogen atoms	157707	159420	150653
Mg^{2+} ions	305	314	314
Waters	8740	10476	0
Mean *B* Factors ($Å^2$)			
RNA	51.58	49.86	44.19
Protein	62.40	60.01	51.45
Waters	50.41	48.73	-
Other	58.21	56.95	33.33
R.m.s. deviations from ideal values			
Bond (Å)	0.005	0.005	0.006
Angle (°)	0.655	0.669	0.715
Molprobity score	1.86	1.89	2.25
Clash Score	7.91	7.50	8.64
Rotamer outliers (%)	2.59	2.82	4.87
Ramachandran plot			
Favored (%)	97.39	97.28	96.10
Allowed (%)	2.50	2.68	3.82
Outliers (%)	0.11	0.04	0.08
RNA validation			
Angles outliers (%)	0.01	0.01	0.01
Sugar pucker outliers (%)	0.9	0.7	0.7
Average suiteness	0.634	0.633	0.596

Table S5.5. Nucleotide numbering conversions

E. coli **23S numbering**	***M. acetivorans*** **23S numbering**	***E. coli*** **16S numbering**	***M. acetivorans*** **16S numbering**
1942	1967	470	530
1944	1969	1492	1430
2506	2521	1493	1431
2507	2522	1494	1432
2583	2598	1495	1433
2584	2599	1496	1434
2585	2600	1534	1472
2586	2601	1535	1473
2602	2617		

Chapter 6: Conclusion and outlook

Ribosomes are essential macromolecular machines that have been adapted to function across diverse environments. In Chapters 2 and 3 we demonstrated that changes to rRNA sequence leads to the stabilization of ribosomes at high temperature, which is likely important for the folding and stability of thermophilic ribosomes. This complements studies showing that rRNA is extensively modified in thermophiles, which further stabilizes ribosomes.[34–36] In Chapter 4 we revealed that one of the most conserved regions of the ribosome, the PTC, is highly divergent in some archaea. It remains unclear why archaeal PTCs are more divergent than bacteria and if this sequence variation represents specialized function or genetic drift made possible by differences between archaeal and bacterial ribosomes. These discoveries provide a foundation for engineering more robust ribosomes based on natural rRNA variation and exploring functional diversification of the PTC.

While ribosome hibernation has been well studied in bacteria and eukaryotes, its mechanisms in archaea were unknown. Many clades of archaea include extremophiles, which need to protect ribosomes in extreme environments. Other clades of archaea include aeonophiles, organisms with extremely slow growth rates and doubling times spanning decades, that need to preserve ribosomes over long time periods.[258] In Chapters 4 and 5 we used cryo-EM to identify a family of archaeal ribosome hibernation factors that we named Dri and Sri. We showed that these factors inactivate ribosomes by binding at functional sites. These factors are distributed across many archaeal phyla and frequently occur in gene clusters. Concurrent with the discovery of Dri and Sri, a related family of archaeal ribosome hibernation factors, Hib[246], was identified. Almost all archaea contain Dri, Sri, or Hib homologs, and these discoveries provide a more complete understanding of ribosome hibernation across archaea. Future studies of ribosome hibernation in archaea will clarify whether archaeal ribosome hibernation enables archaea to inhabit extreme environments, grow over very long time scales[259], or persist in the microbiome[260].

Decades of structural biology and biochemistry have uncovered the structure and mechanisms of the ribosome.[261] While ribosomes share many common features, they also exhibit remarkable diversity across the tree of life. Structural studies of ribosomes at high resolution were initially limited to ribosomes that were amenable to X-ray crystallography. The cryo-EM resolution revolution[15] has enabled the determination of ribosome structures from diverse organisms, revealing how ribosomes are adapted across biology. Additionally, *in silico* particle sorting has enabled the determination of many ribosome functional states from a single dataset. In the future, cryo-EM will undoubtedly enable the investigation of ribosomes across increasingly divergent forms of life. Promising advances in cryo-electron tomography (cryo-ET) and focused ion beam (FIB) milling of cells and tissues now allow ribosome structures to be explored in their native environments without the need for isolation.[262,263] For example, the *in situ* dynamics of the eukaryotic translation cycle have been measured by FIB milling cells and reconstructing ribosome structures with cryo-ET or single-particle processing.[264–267] Additionally, for cells that are sufficiently small, direct cryo-ET imaging of cells can yield ribosome structures without the need for thinning.[268] Imaging of intact or FIB-milled cells could be especially useful for studying ribosomes from organisms that cannot be cultured in the laboratory.[269] Overall, cryo-EM holds great promise for advancing our understanding of translation and ribosome structure across the tree of life.

References

1. Noller, H. F. Evolution of Protein Synthesis from an RNA World. *Cold Spring Harb. Perspect. Biol.* **4**, a003681–a003681 (2012).
2. Petrov, A. S. *et al.* History of the ribosome and the origin of translation. *Proc. Natl. Acad. Sci. U. S. A.* **112**, 15396–15401 (2015).
3. Wilson, D. N. & Doudna Cate, J. H. The structure and function of the eukaryotic ribosome. *Cold Spring Harb. Perspect. Biol.* **4**, a011536 (2012).
4. Melnikov, S. *et al.* One core, two shells: bacterial and eukaryotic ribosomes. *Nat. Struct. Mol. Biol.* **19**, 560–567 (2012).
5. Webster, M. W. Initiation of Translation in Bacteria and Chloroplasts. *J. Mol. Biol.* 169137 (2025) doi:10.1016/j.jmb.2025.169137.
6. Schmitt, E. *et al.* Recent Advances in Archaeal Translation Initiation. *Front. Microbiol.* **11**, 584152 (2020).
7. Brito Querido, J., Díaz-López, I. & Ramakrishnan, V. The molecular basis of translation initiation and its regulation in eukaryotes. *Nat. Rev. Mol. Cell Biol.* **25**, 168–186 (2024).
8. Nakagawa, S., Niimura, Y. & Gojobori, T. Comparative genomic analysis of translation initiation mechanisms for genes lacking the Shine–Dalgarno sequence in prokaryotes. *Nucleic Acids Res.* **45**, 3922–3931 (2017).
9. Bourgeois, G. *et al.* Structures of Saccharolobus solfataricus initiation complexes with leaderless mRNAs highlight archaeal features and eukaryotic proximity. *Nat. Commun.* **16**, 348 (2025).
10. Ieong, K.-W., Uzun, Ü., Selmer, M. & Ehrenberg, M. Two proofreading steps amplify the accuracy of genetic code translation. *Proc. Natl. Acad. Sci.* **113**, 13744–13749 (2016).
11. Holm, M. *et al.* mRNA decoding in human is kinetically and structurally distinct from bacteria. *Nature* **617**, 200–207 (2023).
12. Voorhees, R. M. & Ramakrishnan, V. Structural Basis of the Translational Elongation Cycle. *Annu. Rev. Biochem.* **82**, 203–236 (2013).
13. Rundlet, E. J. *et al.* Structural basis of early translocation events on the ribosome. *Nature* **595**, 741–745 (2021).
14. Choi, J. *et al.* How Messenger RNA and Nascent Chain Sequences Regulate Translation Elongation. *Annu. Rev. Biochem.* **87**, 421–449 (2018).
15. Kühlbrandt, W. The Resolution Revolution. *Science* **343**, 1443–1444 (2014).
16. Greber, B. J. & Ban, N. Structure and Function of the Mitochondrial Ribosome. *Annu. Rev. Biochem.* **85**, 103–132 (2016).
17. Suzuki, T. *et al.* Structural Compensation for the Deficit of rRNA with Proteins in the Mammalian Mitochondrial Ribosome. *J. Biol. Chem.* **276**, 21724–21736 (2001).
18. Moran, N. A. Microbial Minimalism. *Cell* **108**, 583–586 (2002).
19. Barandun, J., Hunziker, M., Vossbrinck, C. R. & Klinge, S. Evolutionary compaction and adaptation visualized by the structure of the dormant microsporidian ribosome. *Nat. Microbiol.* **4**, 1798–1804 (2019).
20. Nicholson, D. *et al.* Adaptation to genome decay in the structure of the smallest eukaryotic ribosome. *Nat. Commun.* **13**, 591 (2022).
21. Tsurumaki, M., Saito, M., Tomita, M. & Kanai, A. Features of smaller ribosomes in candidate phyla radiation (CPR) bacteria revealed with a molecular evolutionary analysis. *RNA* **28**, 1041–1057 (2022).

22. Ban, N. *et al.* A new system for naming ribosomal proteins. *Curr. Opin. Struct. Biol.* **24**, 165–169 (2014).
23. D'Urso, G., Chat, S., Gillet, R. & Giudice, E. Structural insights into the binding of bS1 to the ribosome. *Nucleic Acids Res.* **51**, 3410–3419 (2023).
24. Ferretti, M. B., Ghalei, H., Ward, E. A., Potts, E. L. & Karbstein, K. Rps26 directs mRNA-specific translation by recognition of Kozak sequence elements. *Nat. Struct. Mol. Biol.* **24**, 700–707 (2017).
25. Lanyi, J. K. Salt-dependent properties of proteins from extremely halophilic bacteria. *Bacteriol. Rev.* **38**, 272–290 (1974).
26. Fedyukina, D. V., Jennaro, T. S. & Cavagnero, S. Charge Segregation and Low Hydrophobicity Are Key Features of Ribosomal Proteins from Different Organisms. *J. Biol. Chem.* **289**, 6740–6750 (2014).
27. Tirumalai, M. R., Anane-Bediakoh, D., Rajesh, S. & Fox, G. E. Net Charges of the Ribosomal Proteins of the *S10* and *spc* Clusters of Halophiles Are Inversely Related to the Degree of Halotolerance. *Microbiol. Spectr.* **9**, e01782-21 (2021).
28. van den Elzen, A., Helena-Bueno, K., Brown, C. R., Chan, L. I. & Melnikov, S. V. Ribosomal proteins can hold a more accurate record of bacterial thermal adaptation compared to rRNA. *Nucleic Acids Res.* **51**, 8048–8059 (2023).
29. Alenko, A., Fleming, A. M. & Burrows, C. J. Reverse Transcription Past Products of Guanine Oxidation in RNA Leads to Insertion of A and C opposite 8-Oxo-7,8-dihydroguanine and A and G opposite 5-Guanidinohydantoin and Spiroiminodihydantoin Diastereomers. *Biochemistry* **56**, 5053–5064 (2017).
30. Hosseini, M. *et al.* How to fold and protect mitochondrial ribosomal RNA with fewer guanines. *Nucleic Acids Res.* https://doi.org/10.1093/nar/gky762 (2018) doi:10.1093/nar/gky762.
31. Galtier, N. & Lobry, J. R. Relationships Between Genomic G+C Content, RNA Secondary Structures, and Optimal Growth Temperature in Prokaryotes. *J. Mol. Evol.* **44**, 632–636 (1997).
32. Khachane, A. N. Uracil content of 16S rRNA of thermophilic and psychrophilic prokaryotes correlates inversely with their optimal growth temperatures. *Nucleic Acids Res.* **33**, 4016–4022 (2005).
33. López-López, A., Benlloch, S., Bonfá, M., Rodríguez-Valera, F. & Mira, A. Intragenomic 16S rDNA Divergence in Haloarcula marismortui Is an Adaptation to Different Temperatures. *J. Mol. Evol.* **65**, 687–696 (2007).
34. Garcia-Campos, M. A. *et al.* Pan-modification profiling facilitates a cross-evolutionary dissection of the thermoregulated ribosomal epitranscriptome. *Cell* S0092867425010827 (2025) doi:10.1016/j.cell.2025.09.014.
35. Sas-Chen, A. *et al.* Dynamic RNA acetylation revealed by quantitative cross-evolutionary mapping. *Nature* **583**, 638–643 (2020).
36. Fluke, K. A. *et al.* The extensive m5C epitranscriptome of Thermococcus kodakarensis is generated by a suite of RNA methyltransferases that support thermophily. *Nat. Commun.* **15**, 7272 (2024).
37. Prossliner, T., Skovbo Winther, K., Sørensen, M. A. & Gerdes, K. Ribosome Hibernation. *Annu. Rev. Genet.* **52**, 321–348 (2018).

38. Helena-Bueno, K., Chan, L. I. & Melnikov, S. V. Rippling life on a dormant planet: hibernation of ribosomes, RNA polymerases, and other essential enzymes. *Front. Microbiol.* **15**, 1386179 (2024).
39. Prossliner, T., Gerdes, K., Sørensen, M. A. & Winther, K. S. Hibernation factors directly block ribonucleases from entering the ribosome in response to starvation. *Nucleic Acids Res.* **49**, 2226–2239 (2021).
40. Blagodatskaya, E. & Kuzyakov, Y. Active microorganisms in soil: Critical review of estimation criteria and approaches. *Soil Biol. Biochem.* **67**, 192–211 (2013).
41. Vila-Sanjurjo, A., Schuwirth, B.-S., Hau, C. W. & Cate, J. H. D. Structural basis for the control of translation initiation during stress. *Nat. Struct. Mol. Biol.* **11**, 1054–1059 (2004).
42. Polikanov, Y. S., Blaha, G. M. & Steitz, T. A. How hibernation factors RMF, HPF, and YfiA turn off protein synthesis. *Science* **336**, 915–918 (2012).
43. Beckert, B. *et al.* Structure of a hibernating 100S ribosome reveals an inactive conformation of the ribosomal protein S1. *Nat. Microbiol.* **3**, 1115–1121 (2018).
44. Franken, L. E. *et al.* A general mechanism of ribosome dimerization revealed by single-particle cryo-electron microscopy. *Nat. Commun.* **8**, 722 (2017).
45. Beckert, B. *et al.* Structure of the *Bacillus subtilis* hibernating 100S ribosome reveals the basis for 70S dimerization. *EMBO J.* **36**, 2061–2072 (2017).
46. Helena-Bueno, K. *et al.* A new family of bacterial ribosome hibernation factors. *Nature* **626**, 1125–1132 (2024).
47. Ben-Shem, A. *et al.* The Structure of the Eukaryotic Ribosome at 3.0 Å Resolution. *Science* **334**, 1524–1529 (2011).
48. Brown, A., Baird, M. R., Yip, M. C., Murray, J. & Shao, S. Structures of translationally inactive mammalian ribosomes. *eLife* **7**, e40486 (2018).
49. Leesch, F. *et al.* A molecular network of conserved factors keeps ribosomes dormant in the egg. *Nature* **613**, 712–720 (2023).
50. McLaren, M. *et al.* CryoEM reveals that ribosomes in microsporidian spores are locked in a dimeric hibernating state. *Nat. Microbiol.* **8**, 1834–1845 (2023).
51. d'Aquino, A. E., Kim, D. S. & Jewett, M. C. Engineered Ribosomes for Basic Science and Synthetic Biology. *Annu. Rev. Chem. Biomol. Eng.* **9**, 311–340 (2018).
52. Ishida, S., Ngo, P. H. T., Gundlach, A. & Ellington, A. Engineering Ribosomal Machinery for Noncanonical Amino Acid Incorporation. *Chem. Rev.* **124**, 7712–7730 (2024).
53. Kofman, C., Willi, J. A., Karim, A. S. & Jewett, M. C. Ribosome Pool Engineering Increases Protein Biosynthesis Yields. *ACS Cent. Sci.* acscentsci.3c01413 (2024) doi:10.1021/acscentsci.3c01413.
54. Liu, F., Bratulić, S., Costello, A., Miettinen, T. P. & Badran, A. H. Directed evolution of rRNA improves translation kinetics and recombinant protein yield. *Nat. Commun.* **12**, 5638 (2021).
55. Krüger, A. *et al.* Community science designed ribosomes with beneficial phenotypes. *Nat. Commun.* **14**, 961 (2023).
56. Rackham, O. & Chin, J. W. A network of orthogonal ribosome·mRNA pairs. *Nat. Chem. Biol.* **1**, 159–166 (2005).
57. Schmied, W. H. *et al.* Controlling orthogonal ribosome subunit interactions enables evolution of new function. *Nature* **564**, 444–448 (2018).
58. Orelle, C. *et al.* Protein synthesis by ribosomes with tethered subunits. *Nature* **524**, 119–124 (2015).

59. Melo Czekster, C., Robertson, W. E., Walker, A. S., Söll, D. & Schepartz, A. *In Vivo* Biosynthesis of a β-Amino Acid-Containing Protein. *J. Am. Chem. Soc.* **138**, 5194–5197 (2016).
60. Maini, R. *et al.* Protein Synthesis with Ribosomes Selected for the Incorporation of β-Amino Acids. *Biochemistry* **54**, 3694–3706 (2015).
61. Dedkova, L. M., Fahmi, N. E., Golovine, S. Y. & Hecht, S. M. Enhanced D-amino acid incorporation into protein by modified ribosomes. *J. Am. Chem. Soc.* **125**, 6616–6617 (2003).
62. Maini, R. *et al.* Ribosome-Mediated Incorporation of Dipeptides and Dipeptide Analogues into Proteins in Vitro. *J. Am. Chem. Soc.* **137**, 11206–11209 (2015).
63. Davidson, A. R. Multiple Sequence Alignment as a Guideline for Protein Engineering Strategies. in *Protein Design* vol. 340 171–182 (Humana Press, New Jersey, 2006).
64. Liu, Y. *et al.* Enhancing functional proteins through multimodal inverse folding with ABACUS-T. *Nat. Commun.* **16**, 10177 (2025).
65. d'Aquino, A. E. *et al.* Mutational characterization and mapping of the 70S ribosome active site. *Nucleic Acids Res.* **48**, 2777–2789 (2020).
66. Ward, F. R., Watson, Z. L., Ad, O., Schepartz, A. & Cate, J. H. D. Defects in the Assembly of Ribosomes Selected for β-Amino Acid Incorporation. *Biochemistry* **58**, 4494–4504 (2019).
67. Bloom, J. D., Labthavikul, S. T., Otey, C. R. & Arnold, F. H. Protein stability promotes evolvability. *Proc. Natl. Acad. Sci.* **103**, 5869–5874 (2006).
68. Porse, B. T. & Garrett, R. A. Mapping important nucleotides in the peptidyl transferase centre of 23 S rRNA using a random mutagenesis approach. *J. Mol. Biol.* **249**, 1–10 (1995).
69. Gregory, S. T., Lieberman, K. R. & Dahlberg, A. E. Mutations in the peptidyl transferase region of E.coli 23S rRNA affecting translational accuracy. *Nucleic Acids Res.* **22**, 279–284 (1994).
70. Thompson, J. *et al.* Analysis of mutations at residues A2451 and G2447 of 23S rRNA in the peptidyltransferase active site of the 50S ribosomal subunit. *Proc. Natl. Acad. Sci.* **98**, 9002–9007 (2001).
71. Davidovich, C., Bashan, A. & Yonath, A. Structural basis for cross-resistance to ribosomal PTC antibiotics. *Proc. Natl. Acad. Sci. USA* **105**, 20665–20670 (2008).
72. Steitz, T. A. A structural understanding of the dynamic ribosome machine. *Nat. Rev. Mol. Cell Biol.* **9**, 242–253 (2008).
73. Kim, D. F. & Green, R. Base-pairing between 23S rRNA and tRNA in the ribosomal A site. *Mol. Cell* **4**, 859–864 (1999).
74. Terasaka, N., Hayashi, G., Katoh, T. & Suga, H. An orthogonal ribosome-tRNA pair via engineering of the peptidyl transferase center. *Nat. Chem. Biol.* **10**, 555–557 (2014).
75. Bernier, C. R., Petrov, A. S., Kovacs, N. A., Penev, P. I. & Williams, L. D. Translation: The universal structural core of life. *Mol. Biol. Evol.* **35**, 2065–2076 (2018).
76. Wang, W. *et al.* Loss of a single methylation in 23s rRNA delays 50s assembly at multiple late stages and impairs translation initiation and elongation. *Proc. Natl. Acad. Sci. USA* **117**, 15609–15619 (2020).
77. Caldas, T., Binet, E., Bouloc, P. & Richarme, G. Translational Defects of Escherichia coli Mutants Deficient in the Um2552 23S Ribosomal RNA Methyltransferase RrmJ/FTSJ. *Biochem. Biophys. Res. Commun.* **271**, 714–718 (2000).
78. Bashan, A. *et al.* Structural basis of the ribosomal machinery for peptide bond formation, translocation, and nascent chain progression. *Mol. Cell* **11**, 91–102 (2003).

79. O'Connor, M. & Dahlberg, A. E. Mutations at U2555, a tRNA-protected base in 23S rRNA, affect translational fidelity. *Proc. Natl. Acad. Sci. USA* **90**, 9214–9218 (1993).
80. Jegousse, C., Yang, Y., Zhan, J., Wang, J. & Zhou, Y. Structural signatures of thermal adaptation of bacterial ribosomal RNA, transfer RNA, and messenger RNA. *PLoS ONE* **12**, (2017).
81. Noon, K. R., Bruenger, E. & McCloskey, J. A. Posttranscriptional modifications in 16S and 23S rRNAs of the archaeal hyperthermophile Sulfolobus solfataricus. *J. Bacteriol.* **180**, 2883–2888 (1998).
82. Quast, C. *et al.* The SILVA ribosomal RNA gene database project: Improved data processing and web-based tools. *Nucleic Acids Res.* **41**, 590–596 (2013).
83. Katoh, K., Misawa, K., Kuma, K. I. & Miyata, T. MAFFT: A novel method for rapid multiple sequence alignment based on fast Fourier transform. *Nucleic Acids Res.* **30**, 3059–3066 (2002).
84. Katoh, K., Rozewicki, J. & Yamada, K. D. MAFFT online service: Multiple sequence alignment, interactive sequence choice and visualization. *Brief. Bioinform.* **20**, 1160–1166 (2018).
85. Sato, Y., Okano, K., Kimura, H. & Honda, K. Tempura: Database of growth temperatures of usual and rare prokaryotes. *Microbes Environ.* **35**, (2020).
86. Letunic, I. & Bork, P. Interactive tree of life (iTOL) v5: An online tool for phylogenetic tree display and annotation. *Nucleic Acids Res.* **49**, W293–W296 (2021).
87. Rinke, C. *et al.* A standardized archaeal taxonomy for the Genome Taxonomy Database. *Nat. Microbiol.* **6**, 946–959 (2021).
88. Douthwaite, S., Powers, T., Lee, J. Y. & Noller, H. F. Defining the structural requirements for a helix in 23S ribosomal RNA that confers erythromycin resistance. *J. Mol. Biol.* **209**, 655–665 (1989).
89. Youngman, E. M. & Green, R. Affinity purification of in vivo-assembled ribosomes for in vitro biochemical analysis. *Methods* **36**, 305–312 (2005).
90. Asai, T., Zaporojets, D., Squires, C. & Squires, C. L. An escherichia coli strain with all chromosomal rRNA operons inactivated: Complete exchange of rRNA genes between bacteria. *Proc. Natl. Acad. Sci. USA* **96**, 1971–1976 (1999).
91. Aleksashin, N. A. *et al.* A fully orthogonal system for protein synthesis in bacterial cells. *Nat. Commun.* **11**, (2020).
92. Sigmund, C. D., Ettayebi, M., Morgan, E. A. & D, A. Antibiotic resitance mutations in 16S and 23S ribosomlar RNA genes of Escherichia coli. *Nucleic Acids Res.* **12**, 4653–4663 (1984).
93. Schneider, C. A., Rasband, W. S. & Eliceiri, K. W. NIH Image to ImageJ: 25 years of image analysis. *Nat. Methods* **9**, 671–675 (2012).
94. Travin, D. Y. *et al.* Structure of ribosome-bound azole-modified peptide phazolicin rationalizes its species-specific mode of bacterial translation inhibition. *Nat. Commun.* **10**, 4563 (2019).
95. Dixon, A. S. *et al.* NanoLuc Complementation Reporter Optimized for Accurate Measurement of Protein Interactions in Cells. *ACS Chem. Biol.* **11**, 400–408 (2016).
96. Kotar, A., Ma, S. & Keane, S. C. pH dependence of C•A, G•A and A•A mismatches in the stem of precursor microRNA-31. *Biophys. Chem.* **283**, (2022).
97. Studier, F. W. Stable expression clones and auto-induction for protein production in E. coli. *Methods Mol. Biol.* **1091**, 17–32 (2014).

98. Katoh, T. & Suga, H. Flexizyme-catalyzed synthesis of 3′-aminoacyl-NH-tRNAs. *Nucleic Acids Res.* **47**, e54 (2019).
99. Watson, Z. L. *et al.* Structure of the bacterial ribosome at 2 Å resolution. *eLife* **9**, e60482 (2020).
100. Zivanov, J. *et al.* New tools for automated high-resolution cryo-EM structure determination in RELION-3. *eLife* **7**, (2018).
101. Zheng, S. Q. *et al.* MotionCor2: anisotropic correction of beam-induced motion for improved cryo-electron microscopy. *Nat. Methods* **14**, 331–332 (2017).
102. Rohou, A. & Grigorieff, N. CTFFIND4: Fast and accurate defocus estimation from electron micrographs. *J. Struct. Biol.* **192**, 216–221 (2015).
103. Punjani, A., Rubinstein, J. L., Fleet, D. J. & Brubaker, M. A. cryoSPARC: algorithms for rapid unsupervised cryo-EM structure determination. *Nat. Methods* **14**, 290–296 (2017).
104. Tang, G. *et al.* EMAN2: An extensible image processing suite for electron microscopy. *J. Struct. Biol.* **157**, 38–46 (2007).
105. Polikanov, Y. S., Steitz, T. A. & Innis, C. A. A proton wire to couple aminoacyl-tRNA accommodation and peptide-bond formation on the ribosome. *Nat. Struct. Mol. Biol.* **21**, 787–793 (2014).
106. Watson, Z. L. *et al.* Atomistic simulations of the Escherichia coli ribosome provide selection criteria for translationally active substrates. *Nat. Chem.* **15**, 913–921 (2023).
107. Zivanov, J., Nakane, T. & Scheres, S. H. W. A Bayesian approach to beam-induced motion correction in cryo-EM single-particle analysis. *IUCrJ* **6**, 5–17 (2019).
108. Pettersen, E. F. *et al.* UCSF ChimeraX: Structure visualization for researchers, educators, and developers. *Protein Sci.* **30**, 70–82 (2021).
109. Liebschner, D. *et al.* Macromolecular structure determination using X-rays, neutrons and electrons: recent developments in *Phenix*. *Acta Crystallogr. Sect. Struct. Biol.* **75**, 861–877 (2019).
110. Casañal, A., Lohkamp, B. & Emsley, P. Current developments in *Coot* for macromolecular model building of Electron Cryo-microscopy and Crystallographic Data. *Protein Sci.* **29**, 1055–1064 (2020).
111. Brochier-Armanet, C., Boussau, B., Gribaldo, S. & Forterre, P. Mesophilic Crenarchaeota: proposal for a third archaeal phylum, the Thaumarchaeota. *Nat. Rev. Microbiol.* **6**, 245–252 (2008).
112. Blöchl, E. *et al.* Pyrolobus fumarii, gen. and sp. nov., represents a novel group of archaea, extending the upper temperature limit for life to 113°C. *Extremophiles* **1**, 14–21 (1997).
113. Kashefi, K. & Lovley, D. R. Extending the upper temperature limit for life. *Science* **301**, 934 (2003).
114. Quan, S., Skovgaard, O., McLaughlin, R. E., Buurman, E. T. & Squires, C. L. Markerless Escherichia coli rrn deletion strains for genetic determination of ribosomal binding sites. *G3 GenesGenomesGenetics* **5**, 2555–2557 (2015).
115. Sato, N. S., Hirabayashi, N., Agmon, I., Yonath, A. & Suzuki, T. Comprehensive genetic selection revealed essential bases in the peptidyl-transferase center. *Proc. Natl. Acad. Sci.* **103**, 15386–15391 (2006).
116. Sokoloski, J. E., Godfrey, S. A., Dombrowski, S. E. & Bevilacqua, P. C. Prevalence of syn nucleobases in the active sites of functional RNAs. *Rna* **17**, 1775–1787 (2011).
117. Thompson, J. & Dahlberg, A. E. Testing the conversation of the translational machinery over evolution in diverse environments: Assaying Thermus thermophilus ribosomes and initiation

factors in a coupled transcription-translation system from Escherichia coli. *Nucleic Acids Res.* **32**, 5954–5961 (2004).
118. Metelev, M. *et al.* Direct measurements of mRNA translation kinetics in living cells. *Nat. Commun.* **13**, 1852 (2022).
119. Lancaster, L., Lambert, N. J., Maklan, E. J., Horan, L. H. & Noller, H. F. The sarcin–ricin loop of 23S rRNA is essential for assembly of the functional core of the 50S ribosomal subunit. *RNA* **14**, 1999–2012 (2008).
120. Uhlenbeck, O. C., Borer, P. N., Dengler, B. & Tinoco, I. Stability of RNA hairpin loops: A6-Cm-U6. *J. Mol. Biol.* **73**, 483–496 (1973).
121. Lang, K., Erlacher, M., Wilson, D. N., Micura, R. & Polacek, N. The Role of 23S Ribosomal RNA Residue A2451 in Peptide Bond Synthesis Revealed by Atomic Mutagenesis. *Chem. Biol.* **15**, 485–492 (2008).
122. Youngman, E. M., Brunelle, J. L., Kochaniak, A. B. & Green, R. The Active Site of the Ribosome Is Composed of Two Layers of Conserved Nucleotides with Distinct Roles in Peptide Bond Formation and Peptide Release. *Cell* **117**, 589–599 (2004).
123. Ohira, T. *et al.* Reversible RNA phosphorylation stabilizes tRNA for cellular thermotolerance. *Nature* **605**, 372–379 (2022).
124. Rakauskaite, R. & Dinman, J. D. rRNA mutants in the yeast peptidyltransferase center reveal allosteric information networks and mechanisms of drug resistance. *Nucleic Acids Res.* **36**, 1497–1507 (2008).
125. O'Connor, M., Willis, N. M., Bossi, L., Gesteland, R. F. & Atkins, J. F. Functional tRNAs with altered 3' ends. *EMBO J.* **12**, 2559–2566 (1993).
126. Blanchard, S. C. & Puglisi, J. D. Solution structure of the A loop of 23S ribosomal RNA. *Proc. Natl. Acad. Sci. USA* **98**, 3720–3725 (2001).
127. Frechet, D., Ehrlich, R. & Remy, P. Thermal perturbation differential spectra of ribonucleic acids. II. Nearest neighbour interactions. *Nucleic Acids Res.* **7**, 1981–2001 (1979).
128. Hayatshahi, H. S., Henriksen, N. M. & Cheatham, T. E. Consensus Conformations of Dinucleoside Monophosphates Described with Well-Converged Molecular Dynamics Simulations. *J. Chem. Theory Comput.* **14**, 1456–1470 (2018).
129. Nikolay, R. *et al.* Structural Visualization of the Formation and Activation of the 50S Ribosomal Subunit during In Vitro Reconstitution. *Mol. Cell* **70**, 881-893.e3 (2018).
130. Grasso, K. T. *et al.* Structural Robustness Affects the Engineerability of Aminoacyl-tRNA Synthetases for Genetic Code Expansion. *Biochemistry* **60**, 489–493 (2021).
131. Kofman, C. *et al.* Computationally-guided design and selection of ribosomal active site mutants with high activity. *Nucleic Acids Res.* https://doi.org/10.1101/2022.06.02.493746%0Ahttps://www.biorxiv.org/content/10.1101/2022.06.02.493746v1%0Ahttps://www.biorxiv.org/content/10.1101/2022.06.02.493746v1.abstract (2022).
132. Katoh, T. & Suga, H. In Vitro Genetic Code Reprogramming for the Expansion of Usable Noncanonical Amino Acids. *Annu. Rev. Biochem.* **91**, 221–243 (2022).
133. Bellaousov, S., Reuter, J. S., Seetin, M. G. & Mathews, D. H. RNAstructure: Web servers for RNA secondary structure prediction and analysis. *Nucleic Acids Res.* **41**, 471–474 (2013).
134. Santoro, A. E. *et al.* Genomic and proteomic characterization of 'Candidatus Nitrosopelagicus brevis': An ammonia-oxidizing archaeon from the open ocean. *Proc. Natl. Acad. Sci. U. S. A.* **112**, 1173–1178 (2015).

135. Lehtovirta-Morley, L. E., Stoecker, K., Vilcinskas, A., Prosser, J. I. & Nicol, G. W. Cultivation of an obligate acidophilic ammonia oxidizer from a nitrifying acid soil. *Proc. Natl. Acad. Sci. U. S. A.* **108**, 15892–15897 (2011).
136. Sauder, L. A., Engel, K., Lo, C., Chain, P. & Neufeld, J. D. "Candidatus Nitrosotenuis aquarius," an Ammonia-Oxidizing Archaeon from a Freshwater Aquarium Biofilte. *Appl. Enviromental Microbiol.* **84**, (2018).
137. Daebeler, A. *et al.* Cultivation and genomic analysis of 'Candidatus Nitrosocaldus islandicus,' an obligately thermophilic, ammonia-oxidizing thaumarchaeon from a hot spring biofilm in Graendalur valley, Iceland. *Front. Microbiol.* **9**, 1–16 (2018).
138. Lehtovirta-Morley, L. E. *et al.* Isolation of 'Candidatus Nitrosocosmicus franklandus', a novel ureolytic soil archaeal ammonia oxidiser with tolerance to high ammonia concentration. *FEMS Microbiol. Ecol.* **92**, 1–10 (2016).
139. Beam, J. P. *et al.* Ecophysiology of an uncultivated lineage of Aigarchaeota from an oxic, hot spring filamentous 'streamer' community. *ISME J.* **10**, 210–224 (2016).
140. Noller, H. F. RNA Structure: Reading the Ribosome. *Science* **309**, 1508–1514 (2005).
141. Shajani, Z., Sykes, M. T. & Williamson, J. R. Assembly of Bacterial Ribosomes. *Annu. Rev. Biochem.* **80**, 501–526 (2011).
142. Liiv, A. & Remme, J. Base-pairing of 23 S rRNA ends is essential for ribosomal large subunit assembly. *J. Mol. Biol.* **276**, 537–545 (1998).
143. Ginsburg, D. & Steitz, J. A. The 30 S ribosomal precursor RNA from Escherichia coli. A primary transcript containing 23 S, 16 S, and 5 S sequences. *J. Biol. Chem.* **250**, 5647–5654 (1975).
144. Nikolaev, N., Silengo, L. & Schlessinger, D. A Role for Ribonuclease III in Processing of Ribosomal Ribonucleic Acid and Messenger Ribonucleic Acid Precursors in Escherichia coli. *J. Biol. Chem.* **248**, 7967–7969 (1973).
145. Li, Z., Pandit, S. & Deutscher, M. P. Maturation of 23S ribosomal RNA requires the exoribonuclease RNase T. *RNA* **5**, 139–146 (1999).
146. Shatoff, E. A., Gemler, B. T., Bundschuh, R. & Fredrick, K. Maturation of 23S rRNA includes removal of helix H1 in many bacteria. *RNA Biol.* **18**, 856–865 (2021).
147. Peabody, D. S. The RNA binding site of bacteriophage MS2 coat protein. *EMBO J.* **12**, 595–600 (1993).
148. Nissley, A. J., Penev, P. I., Watson, Z. L., Banfield, J. F. & Cate, J. H. D. Rare ribosomal RNA sequences from archaea stabilize the bacterial ribosome. *Nucleic Acids Res.* **51**, 1880–1894 (2023).
149. Walker, S. E. & Fredrick, K. Preparation and evaluation of acylated tRNAs. *Methods* **44**, 81–86 (2008).
150. Schorb, M., Haberbosch, I., Hagen, W. J. H., Schwab, Y. & Mastronarde, D. N. Software tools for automated transmission electron microscopy. *Nat. Methods* **16**, 471–477 (2019).
151. Lowary, P. T. & Uhlenbeck, O. C. An RNA mutation that increases the affinity of an RNA–protein interaction. *Nucleic Acids Res.* **15**, 10483–10493 (1987).
152. Leonov, A. A., Sergiev, P. V., Bogdanov, A. A., Brimacombe, R. & Dontsova, O. A. Affinity Purification of Ribosomes with a Lethal G2655C Mutation in 23 S rRNA That Affects the Translocation. *J. Biol. Chem.* **278**, 25664–25670 (2003).
153. Matadeen, R. *et al.* Direct localization by cryo-electron microscopy of secondary structural elements in Escherichia coli 23 S rRNA which differ from the corresponding regions in Haloarcula marismortui. *J. Mol. Biol.* **307**, 1341–1349 (2001).

154. Basu, R. S., Sherman, M. B. & Gagnon, M. G. Compact IF2 allows initiator tRNA accommodation into the P site and gates the ribosome to elongation. *Nat. Commun.* **13**, 3388 (2022).
155. Morgan, C. E., Zhang, Z., Bonomo, R. A. & Yu, E. W. An Analysis of the Novel Fluorocycline TP-6076 Bound to Both the Ribosome and Multidrug Efflux Pump AdeJ from Acinetobacter baumannii. *mBio* **13**, e03732-21 (2022).
156. Syroegin, E. A., Aleksandrova, E. V. & Polikanov, Y. S. Insights into the ribosome function from the structures of non-arrested ribosome–nascent chain complexes. *Nat. Chem.* **15**, (2023).
157. Kaminishi, T. *et al.* Crystallographic characterization of the ribosomal binding site and molecular mechanism of action of Hygromycin A. *Nucleic Acids Res.* gkv975 (2015) doi:10.1093/nar/gkv975.
158. Crowe-McAuliffe, C. *et al.* Structural Basis for Bacterial Ribosome-Associated Quality Control by RqcH and RqcP. *Mol. Cell* **81**, 115-126.e7 (2021).
159. Crowe-McAuliffe, C. *et al.* Structural basis of ABCF-mediated resistance to pleuromutilin, lincosamide, and streptogramin A antibiotics in Gram-positive pathogens. *Nat. Commun.* **12**, 3577 (2021).
160. Halfon, Y. *et al.* Exit tunnel modulation as resistance mechanism of S. aureus erythromycin resistant mutant. *Sci. Rep.* **9**, 11460 (2019).
161. Murphy, E. L. *et al.* Cryo-electron microscopy structure of the 70S ribosome from Enterococcus faecalis. *Sci. Rep.* **10**, 16301 (2020).
162. Cui, Z. *et al.* Interplay between an ATP-binding cassette F protein and the ribosome from Mycobacterium tuberculosis. *Nat. Commun.* **13**, 432 (2022).
163. Mishra, S., Ahmed, T., Tyagi, A., Shi, J. & Bhushan, S. Structures of Mycobacterium smegmatis 70S ribosomes in complex with HPF, tmRNA, and P-tRNA. *Sci. Rep.* **8**, 13587 (2018).
164. Hesslein, A. E. Exploration of the conserved A+C wobble pair within the ribosomal peptidyl transferase center using affinity purified mutant ribosomes. *Nucleic Acids Res.* **32**, 3760–3770 (2004).
165. Jha, V. *et al.* Structural basis of sequestration of the anti-Shine-Dalgarno sequence in the Bacteroidetes ribosome. *Nucleic Acids Res.* **49**, 547–567 (2021).
166. Lai, W.-J. C. *et al.* mRNAs and lncRNAs intrinsically form secondary structures with short end-to-end distances. *Nat. Commun.* **9**, 4328 (2018).
167. Leija-Martínez, N. *et al.* The separation between the 5′-3′ ends in long RNA molecules is short and nearly constant. *Nucleic Acids Res.* **42**, 13963–13968 (2014).
168. Yoffe, A. M., Prinsen, P., Gelbart, W. M. & Ben-Shaul, A. The ends of a large RNA molecule are necessarily close. *Nucleic Acids Res.* **39**, 292–299 (2011).
169. Krishna, M. M. G. & Englander, S. W. The N-terminal to C-terminal motif in protein folding and function. *Proc. Natl. Acad. Sci.* **102**, 1053–1058 (2005).
170. Vicens, Q., Kieft, J. S. & Rissland, O. S. Revisiting the Closed-Loop Model and the Nature of mRNA 5′–3′ Communication. *Mol. Cell* **72**, 805–812 (2018).
171. Tirumalai, M. R., Rivas, M., Tran, Q. & Fox, G. E. The Peptidyl Transferase Center: a Window to the Past. *Microbiol. Mol. Biol. Rev. MMBR* **85**, e0010421 (2021).
172. Noller, H. F., Donohue, J. P. & Gutell, R. R. The universally conserved nucleotides of the small subunit ribosomal RNAs. *RNA N. Y. N* **28**, 623–644 (2022).

173. Noeske, J. *et al.* High-resolution structure of the Escherichia coli ribosome. *Nat. Struct. Mol. Biol.* **22**, 336–341 (2015).
174. Ban, N., Nissen, P., Hansen, J., Moore, P. B. & Steitz, T. A. The Complete Atomic Structure of the Large Ribosomal Subunit at 2.4 Å Resolution. *Science* **289**, 905–920 (2000).
175. Voorhees, R. M., Schmeing, T. M., Kelley, A. C. & Ramakrishnan, V. The Mechanism for Activation of GTP Hydrolysis on the Ribosome. *Science* **330**, 835–838 (2010).
176. Harms, J. *et al.* High Resolution Structure of the Large Ribosomal Subunit from a Mesophilic Eubacterium. *Cell* **107**, 679–688 (2001).
177. Ben-Shem, A., Jenner, L., Yusupova, G. & Yusupov, M. Crystal structure of the eukaryotic ribosome. *Science* **330**, 1203–1209 (2010).
178. Fromm, S. A. *et al.* The translating bacterial ribosome at 1.55 Å resolution generated by cryo-EM imaging services. *Nat. Commun.* **14**, 1095 (2023).
179. Smirnova, J. *et al.* Structure of the actively translating plant 80S ribosome at 2.2 Å resolution. *Nat. Plants* **9**, 987–1000 (2023).
180. Eiler, D. R. *et al.* The Giardia lamblia ribosome structure reveals divergence in several biological pathways and the mode of emetine function. *Struct. Lond. Engl. 1993* **32**, 400-410.e4 (2024).
181. Perez Boerema, A. *et al.* Structure of the chloroplast ribosome with chl-RRF and hibernation-promoting factor. *Nat. Plants* **4**, 212–217 (2018).
182. Singh, V. *et al.* Mitoribosome structure with cofactors and modifications reveals mechanism of ligand binding and interactions with L1 stalk. *Nat. Commun.* **15**, 4272 (2024).
183. Harper, N. J., Burnside, C. & Klinge, S. Principles of mitoribosomal small subunit assembly in eukaryotes. *Nature* **614**, 175–181 (2023).
184. Borrel, G., Brugère, J.-F., Gribaldo, S., Schmitz, R. A. & Moissl-Eichinger, C. The host-associated archaeome. *Nat. Rev. Microbiol.* **18**, 622–636 (2020).
185. Cai, M. *et al.* Ecological features and global distribution of Asgard archaea. *Sci. Total Environ.* **758**, 143581 (2021).
186. Valentin-Alvarado, L. E. *et al.* Asgard archaea modulate potential methanogenesis substrates in wetland soil. *Nat. Commun.* **15**, 6384 (2024).
187. Kohtz, A. J. *et al.* Cultivation and visualization of a methanogen of the phylum Thermoproteota. *Nature* **632**, 1118–1123 (2024).
188. Nürenberg-Goloub, E. *et al.* Molecular analysis of the ribosome recycling factor ABCE1 bound to the 30S post-splitting complex. *EMBO J.* **39**, e103788 (2020).
189. Kazan, R. *et al.* Role of aIF5B in archaeal translation initiation. *Nucleic Acids Res.* **50**, 6532–6548 (2022).
190. Wang, Y.-H. *et al.* Cryo-electron microscopy structure and translocation mechanism of the crenarchaeal ribosome. *Nucleic Acids Res.* **51**, 8909–8924 (2023).
191. Doris, S. M. *et al.* Universal and domain-specific sequences in 23S-28S ribosomal RNA identified by computational phylogenetics. *RNA N. Y. N* **21**, 1719–1730 (2015).
192. Polacek, N. & Mankin, A. S. The ribosomal peptidyl transferase center: structure, function, evolution, inhibition. *Crit. Rev. Biochem. Mol. Biol.* **40**, 285–311 (2005).
193. Kjems, J. *et al.* Gene organization, transcription signals and processing of the single ribosomal RNA operon of the archaebacterium Thermoproteus tenax. *Nucleic Acids Res.* **15**, 4821–4835 (1987).
194. Amo, T. *et al. Pyrobaculum calidifontis* sp. nov., a novel hyperthermophilic archaeon that grows in atmospheric air. *Archaea* **1**, 113–121 (2002).

195. Reeve, C. A., Amy, P. S. & Matin, A. Role of protein synthesis in the survival of carbon-starved Escherichia coli K-12. *J. Bacteriol.* **160**, 1041–1046 (1984).
196. Kolter, R., Siegele, D. A. & Tormo, A. THE STATIONARY PHASE OF THE BACTERIAL LIFE CYCLE. *Annu. Rev. Microbiol.* **47**, 855–874 (1993).
197. Kimanius, D., Dong, L., Sharov, G., Nakane, T. & Scheres, S. H. W. New tools for automated cryo-EM single-particle analysis in RELION-4.0. *Biochem. J.* **478**, 4169–4185 (2021).
198. Jamali, K. *et al.* Automated model building and protein identification in cryo-EM maps. *Nature* **628**, 450–457 (2024).
199. Jumper, J. *et al.* Highly accurate protein structure prediction with AlphaFold. *Nature* **596**, 583–589 (2021).
200. Parks, D. H. *et al.* GTDB: an ongoing census of bacterial and archaeal diversity through a phylogenetically consistent, rank normalized and complete genome-based taxonomy. *Nucleic Acids Res.* **50**, D785–D794 (2022).
201. Nawrocki, E. P. & Eddy, S. R. Infernal 1.1: 100-fold faster RNA homology searches. *Bioinforma. Oxf. Engl.* **29**, 2933–2935 (2013).
202. Kalvari, I. *et al.* Rfam 14: expanded coverage of metagenomic, viral and microRNA families. *Nucleic Acids Res.* **49**, D192–D200 (2021).
203. Crooks, G. E., Hon, G., Chandonia, J.-M. & Brenner, S. E. WebLogo: a sequence logo generator. *Genome Res.* **14**, 1188–1190 (2004).
204. Penev, P. I. *et al.* ProteoVision: web server for advanced visualization of ribosomal proteins. *Nucleic Acids Res.* **49**, W578–W588 (2021).
205. Eddy, S. R. Accelerated Profile HMM Searches. *PLoS Comput. Biol.* **7**, e1002195 (2011).
206. Katoh, K. & Standley, D. M. MAFFT multiple sequence alignment software version 7: improvements in performance and usability. *Mol. Biol. Evol.* **30**, 772–780 (2013).
207. UniProt Consortium. UniProt: the Universal Protein Knowledgebase in 2023. *Nucleic Acids Res.* **51**, D523–D531 (2023).
208. Letunic, I. & Bork, P. Interactive Tree of Life (iTOL) v6: recent updates to the phylogenetic tree display and annotation tool. *Nucleic Acids Res.* **52**, W78–W82 (2024).
209. Sowers, K. R., Boone, J. E. & Gunsalus, R. P. Disaggregation of *Methanosarcina* spp. and Growth as Single Cells at Elevated Osmolarity. *Appl. Environ. Microbiol.* **59**, 3832–3839 (1993).
210. Liu, H., Lin, D. & Yates, J. R. Multidimensional separations for protein/peptide analysis in the post-genomic era. *BioTechniques* **32**, 898, 900, 902 passim (2002).
211. Washburn, M. P., Wolters, D. & Yates, J. R. Large-scale analysis of the yeast proteome by multidimensional protein identification technology. *Nat. Biotechnol.* **19**, 242–247 (2001).
212. Perez-Riverol, Y. *et al.* The PRIDE database at 20 years: 2025 update. *Nucleic Acids Res.* **53**, D543–D553 (2025).
213. Li, Q. i *et al.* A modified pCas/pTargetF system for CRISPR-Cas9-assisted genome editing in Escherichia coli. *Acta Biochim. Biophys. Sin.* **53**, 620–627 (2021).
214. Nissley, A. J., Kamal, T. S. & Cate, J. H. D. Interactions between terminal ribosomal RNA helices stabilize the *E. coli* large ribosomal subunit. *RNA* **29**, 1500–1508 (2023).
215. Londei, P., Altamura, S., Caprini, E. & Martayan, A. Translation and ribosome assembly in extremely thermophilic archaebacteria. *Biochimie* **73**, 1465–1472 (1991).
216. Armache, J.-P. *et al.* Promiscuous behaviour of archaeal ribosomal proteins: implications for eukaryotic ribosome evolution. *Nucleic Acids Res.* **41**, 1284–1293 (2013).

217. Coureux, P.-D., Lazennec-Schurdevin, C., Bourcier, S., Mechulam, Y. & Schmitt, E. Cryo-EM study of an archaeal 30S initiation complex gives insights into evolution of translation initiation. *Commun. Biol.* **3**, 58 (2020).
218. Baker, B. J. *et al.* Enigmatic, ultrasmall, uncultivated Archaea. *Proc. Natl. Acad. Sci.* **107**, 8806–8811 (2010).
219. Klein, D. J., Moore, P. B. & Steitz, T. A. The roles of ribosomal proteins in the structure assembly, and evolution of the large ribosomal subunit. *J. Mol. Biol.* **340**, 141–177 (2004).
220. Blaha, G., Gürel, G., Schroeder, S. J., Moore, P. B. & Steitz, T. A. Mutations Outside the Anisomycin-Binding Site Can Make Ribosomes Drug-Resistant. *J. Mol. Biol.* **379**, 505–519 (2008).
221. Kloss, P., Xiong, L., Shinabarger, D. L. & Mankin, A. S. Resistance mutations in 23 S rRNA identify the site of action of the protein synthesis inhibitor linezolid in the ribosomal peptidyl transferase center 1 1Edited by D. E. Draper. *J. Mol. Biol.* **294**, 93–101 (1999).
222. Lhoest, J. & Colson, C. Genetics of ribosomal protein methylation in Escherichia coli. II. A mutant lacking a new type of methylated amino acid, N5-methylglutamine, in protein L3. *Mol. Gen. Genet. MGG* **154**, 175–180 (1977).
223. Bateman, A. The structure of a domain common to archaebacteria and the homocystinuria disease protein. *Trends Biochem. Sci.* **22**, 12–13 (1997).
224. Schmeing, T. M., Huang, K. S., Strobel, S. A. & Steitz, T. A. An induced-fit mechanism to promote peptide bond formation and exclude hydrolysis of peptidyl-tRNA. *Nature* **438**, 520–524 (2005).
225. Budkevich, T. *et al.* Structure and dynamics of the mammalian ribosomal pretranslocation complex. *Mol. Cell* **44**, 214–224 (2011).
226. Budkevich, T. V. *et al.* Regulation of the mammalian elongation cycle by subunit rolling: a eukaryotic-specific ribosome rearrangement. *Cell* **158**, 121–131 (2014).
227. Yusupov, M. M. *et al.* Crystal structure of the ribosome at 5.5 A resolution. *Science* **292**, 883–896 (2001).
228. Londei, P., Altamura, S., Cammarano, P. & Petrucci, L. Differential features of ribosomes and of poly(U)-programmed cell-free systems derived from sulphur-dependent archaebacterial species. *Eur. J. Biochem.* **157**, 455–462 (1986).
229. Hummel, H. & Böck, A. 23S ribosomal RNA mutations in halobacteria conferring resistance to the anti-80S ribosome targeted antibiotic anisomycin. *Nucleic Acids Res.* **15**, 2431–2443 (1987).
230. Kearsey, S. E. & Craig, I. W. Altered ribosomal RNA genes in mitochondria from mammalian cells with chloramphenicol resistance. *Nature* **290**, 607–608 (1981).
231. Mailliot, J. *et al.* Crystal Structures of the uL3 Mutant Ribosome: Illustration of the Importance of Ribosomal Proteins for Translation Efficiency. *J. Mol. Biol.* **428**, 2195–2202 (2016).
232. Radford, F., Rinehart, J. & Isaacs, F. J. Mapping the in vivo fitness landscape of a tethered ribosome. *Sci. Adv.* **9**, eade8934 (2023).
233. Yaeshima, C. *et al.* A novel ribosome-dimerization protein found in the hyperthermophilic archaeon Pyrococcus furiosus using ribosome-associated proteomics. *Biochem. Biophys. Res. Commun.* **593**, 116–121 (2022).
234. Hassan, A. H. *et al.* Novel archaeal ribosome dimerization factor facilitating unique 30S–30S dimerization. *Nucleic Acids Res.* **53**, gkae1324 (2025).

235. Trösch, R. & Willmund, F. The conserved theme of ribosome hibernation: from bacteria to chloroplasts of plants. *Biol. Chem.* **400**, 879–893 (2019).
236. Offre, P., Spang, A. & Schleper, C. Archaea in Biogeochemical Cycles. *Annu. Rev. Microbiol.* **67**, 437–457 (2013).
237. Baker, B. J. *et al.* Diversity, ecology and evolution of Archaea. *Nat. Microbiol.* **5**, 887–900 (2020).
238. Dean, J. F. *et al.* Methane Feedbacks to the Global Climate System in a Warmer World. *Rev. Geophys.* **56**, 207–250 (2018).
239. Fordjour, G. N. R. *et al.* Cryo-EM study and in vivo chemical mapping of the Methanosarcina acetivorans ribosome and its dimerization via a repurposed enzyme and translation factor. *J. Biol. Chem.* **301**, 110686 (2025).
240. Nissley, A. J. *et al.* Structure of an archaeal ribosome reveals a divergent active site and hibernation factor. *Nat. Microbiol.* **10**, 1940–1953 (2025).
241. Zhu, P., Molina Resendiz, M., Von Ossowski, I. & Scheller, S. A promoter–RBS library for fine-tuning gene expression in *Methanosarcina acetivorans*. *Appl. Environ. Microbiol.* **90**, e01092-24 (2024).
242. Erath, J. *et al.* A rapid, simple, and economical method for the isolation of ribosomes and translational machinery for structural and functional studies. *Nat. Commun.* **16**, 7185 (2025).
243. Shi, L.-D. *et al.* Circular 23S rRNA within archaeal ribosomes. Preprint at https://doi.org/10.1101/2025.04.27.650855 (2025).
244. Croll, T. I. *ISOLDE*: a physically realistic environment for model building into low-resolution electron-density maps. *Acta Crystallogr. Sect. Struct. Biol.* **74**, 519–530 (2018).
245. Minh, B. Q. *et al.* IQ-TREE 2: New Models and Efficient Methods for Phylogenetic Inference in the Genomic Era. *Mol. Biol. Evol.* **37**, 1530–1534 (2020).
246. Madru, C. *et al.* A new family of ribosome hibernation factors in Archaea. Preprint at https://doi.org/10.1101/2025.10.11.676729 (2025).
247. Livingstone, C. D. & Barton, G. J. Protein sequence alignments: a strategy for the hierarchical analysis of residue conservation. *Bioinformatics* **9**, 745–756 (1993).
248. Waterhouse, A. M., Procter, J. B., Martin, D. M. A., Clamp, M. & Barton, G. J. Jalview Version 2—a multiple sequence alignment editor and analysis workbench. *Bioinformatics* **25**, 1189–1191 (2009).
249. Chadwick, G. L., Dury, G. A. & Nayak, D. D. Physiological and transcriptomic response to methyl-coenzyme M reductase limitation in *Methanosarcina acetivorans*. *Appl. Environ. Microbiol.* **90**, e02220-23 (2024).
250. Gersteuer, F. *et al.* The SecM arrest peptide traps a pre-peptide bond formation state of the ribosome. *Nat. Commun.* **15**, 2431 (2024).
251. Demeshkina, N., Jenner, L., Westhof, E., Yusupov, M. & Yusupova, G. A new understanding of the decoding principle on the ribosome. *Nature* **484**, 256–259 (2012).
252. May, M. B., Lopez-Perez, G. S. & Davis, J. H. Capturing ribosomal structures in cellular extracts with cryoPRISM: A purification-free cryoEM approach reveals novel structural states. Preprint at https://doi.org/10.1101/2025.08.21.669550 (2025).
253. Anger, A. M. *et al.* Structures of the human and Drosophila 80S ribosome. *Nature* **497**, 80–85 (2013).
254. Smith, P. R. *et al.* Functionally distinct roles for eEF2K in the control of ribosome availability and p-body abundance. *Nat. Commun.* **12**, 6789 (2021).

255. Du, M., Li, X., Dong, W. & Zeng, F. Implication of Stm1 in the protection of eIF5A, eEF2 and tRNA through dormant ribosomes. *Front. Mol. Biosci.* **11**, 1395220 (2024).
256. Clouet-d'Orval, B. *et al.* Insights into RNA-processing pathways and associated RNA-degrading enzymes in Archaea. *FEMS Microbiol. Rev.* **42**, 579–613 (2018).
257. Baykov, A. A., Tuominen, H. K. & Lahti, R. The CBS Domain: A Protein Module with an Emerging Prominent Role in Regulation. *ACS Chem. Biol.* **6**, 1156–1163 (2011).
258. Lloyd, K. G. & Steen, A. D. Defining ultra-slow-growing extremophilic microorganisms as aeonophiles. *Nat. Microbiol.* **10**, 1555–1557 (2025).
259. Morono, Y. *et al.* Aerobic microbial life persists in oxic marine sediment as old as 101.5 million years. *Nat. Commun.* **11**, 3626 (2020).
260. Mohammadzadeh, R., Mahnert, A., Duller, S. & Moissl-Eichinger, C. Archaeal key-residents within the human microbiome: characteristics, interactions and involvement in health and disease. *Curr. Opin. Microbiol.* **67**, 102146 (2022).
261. Noller, H. F. The ribosome comes to life. *Cell* **187**, 6486–6500 (2024).
262. Strack, R. Structures in situ. *Nat. Methods* **17**, 21–21 (2020).
263. Berger, C. *et al.* Cryo-electron tomography on focused ion beam lamellae transforms structural cell biology. *Nat. Methods* **20**, 499–511 (2023).
264. Zheng, W. *et al.* Visualizing the translation landscape in human cells at high resolution. Preprint at https://doi.org/10.1101/2024.07.02.601723 (2024).
265. Rickgauer, J. P., Choi, H., Moore, A. S., Denk, W. & Lippincott-Schwartz, J. Structural dynamics of human ribosomes in situ reconstructed by exhaustive high-resolution template matching. *Mol. Cell* **84**, 4912-4928.e7 (2024).
266. Xing, H. *et al.* Translation dynamics in human cells visualized at high resolution reveal cancer drug action. *Science* **381**, 70–75 (2023).
267. Hoffmann, P. C. *et al.* Structures of the eukaryotic ribosome and its translational states in situ. *Nat. Commun.* **13**, 7435 (2022).
268. Xue, L. *et al.* Visualizing translation dynamics at atomic detail inside a bacterial cell. *Nature* **610**, 205–211 (2022).
269. Steen, A. D. *et al.* High proportions of bacteria and archaea across most biomes remain uncultured. *ISME J.* **13**, 3126–3130 (2019).